UNIVERSIDADE DE SÃO PAULO
INSTITUTO DE ASTRONOMIA, GEOFÍSICA E CIÊNCIAS ATMOSFÉRICAS
DEPARTAMENTO DE GEOFÍSICA

GRASIANE LUZ MATHIAS

Enviromagnetic response of marine sediments off NE Brazil to paleoclimatic and paleoceanographic changes in the last 85 kyr BP

(Resposta magnética de sedimentos marinhos da margem adjacente ao NE do Brasil às mudanças paleoclimáticas e paleoceanográficas nos últimos 85.000 anos BP)

SÃO PAULO
2015

GRASIANE LUZ MATHIAS

Enviromagnetic response of marine sediments off NE Brazil to paleoclimatic and paleoceanographic changes in the last 85 kyr BP

(Resposta magnética de sedimentos marinhos da margem adjacente ao NE do Brasil às mudanças paleoclimáticas e paleoceanográficas nos últimos 85.000 anos BP)

Tese apresentada ao Instituto de Astronomia, Geofísica e Ciências Atmosféricas da Universidade de São Paulo para obtenção do grau de Doutora em Ciências Geofísicas.

Área de Concentração: Geofísica

Orientador: Prof. Dr. Ricardo Ivan Ferreira da Trindade

SÃO PAULO

2015

To Wilbor, my partner in crime.

AKNOWLEDGEMENTS

I would like to thank my advisor professor Dr. Ricardo Ivan Ferreira da Trindade for his orientation, patience and friendship. Thanks also to my advisor in Germany, professor Dr. Tilo von Dobeneck, for his guidance, serenity, friendship and long discussions.

During my PhD I had the support from Conselho Nacional de Desenvolvimento Científico e Tecnológico (CNPq) with scholarships in Brazil and Germany (SWE) and from MARUM with additional support from a PhD guest student grant.

The Instituto de Astronomia, Geofísica e Ciências Atmosféricas (IAG-USP) provided the necessary support for my PhD. I particularly thank Teca for making everything easier. The work has benefited from the excellent infrastructure from Laboratório de Paleomagnetismo (USPmag) and the expertise of technicians Daniele Bradt, Plínio Jaqueto, Giovanni Moreira, who are also friends.

The thesis has also befitted from the amazing infrastructure from the Research Group of Marine Geophysics of University of Bremen and the IODP Bremen Core Repository. They granted me with full access to equipments, helped me with measurements and sample preparation and made available the cores used in my work. XRF analyses were performed in the Center for Marine Environmental Science (MARUM) with the invaluable help of Vera Lukies and Ursula Röhl. The members of the Laboratory for Paleo-, Rock and Environmental Magnetics, received me so friendly and made my life abroad pleasant. Thanks particularly to: Liane Brück, Heike Piero, Martina Braun, Christian Hilgenfeldt, Sebastian Razik, Benjamin Baasch. I would like to thank Dr. Janna Just, Dr. Thomas Frederichs, MSc. Sophie Roud and Dr. André Paul for the important and fruitful discussions that contributed immensely not only for the thesis but for my general backround in paleoceanography.

I would like to thank the professor Dr. Cristiano Chiessi for making the contact with the German workgroup possible, and also for his friendship and support during difficult moments in my PhD.

Thanks to Prof. Dr. Igor Ivory Gil Pacca who followed my work from the beginning as an internal reviewer for the important comments about my research.

Many thanks to my friends from the workgroup of Paleomagnetism: Elder Yokoyama, Filipe Terra-Nova, Gelvam Hartmann, Jairo Savian, Janine Carmo, Mariana Rossafa, Karine Carvas, Pedro Franco.

Thanks to my family, always present, always supporting me.

Finally, and most importantly, I would like to thank my husband Wilbor Poletti. His patience, support, encouragement, discussions and mainly love were prime to make this thesis possible. His forbearance to my recurrent bad mood in these final months was a solid prove of his love and respect for me. Thanks also to our little star Alice that is so calm and sweet, and put so many smiles on our face, even in the toughest days.

“Study the past if you would define the future.”

Confucius

RESUMO

O NE do Brasil é uma região semi-árida influenciada pela migração para sul da Zona de Convergência Intertropical (ITCZ), que é a principal sistema atmosférico que controla o aumento sazonal da precipitação nessa região. É bem estabelecido que esses períodos úmidos se correlacionam temporalmente com os Eventos Heinrich (EH) – períodos em que ocorre um aumento da deposição de *ice-rafted debris* no Atlântico Norte. Entretanto, a resposta oceanográfica local a essa descarga de água doce no Atlântico Norte e como isso influencia o transporte de sedimentos ao longo da margem adjacente ao NE do Brasil s"ao ainda motivo de debate na literatura. Este trabalho apresenta dados magnéticos e geoquímicos para quatro testemunhos coletados na parte sul do Oceano Atlântico equatorial, para os últimos 85 ka BP. Os testemunhos estão distribuídos entre as longitudes 38°W and 36°W. Além disso, nós fizemos um estudo de *end-members* baseado nas curvas de aquisição de IRM, a partir do qual elucidamos as possíveis fontes dos sedimentos. Os parâmetros magnéticos revelam um aumento significativo na concentração de minerais magnéticos durante os *stadials*, que é acompanhado por uma mudança na proporção relativadas fases magnéticas. Os picos de concentração de minerais magnéticos coincidem com picos nos indicadores geoquímicos utilizados para traçar a intendidade de intemperismo no continente. Portanto, os aumentos no aporte de material magnético para a plataforma coincidem com um aumento na precipitação no continente no NE do Brasil durante os EH. Além da variação da quantidade de material magnético observada, a contribuição relativa de cada fase magnética muda de oeste para leste. Durante os *stadials*, fases de alta coercividade (como hematita e goetita) são dominantes na porção oeste da região estudada e as fases de baixa coercividade são dominantes a leste. Essa diferença é devida, principalmente, à oxidação diferencial no continente, mas secundariamente nós sugerimos um transporte W-E de material coercivo, causado pelo enfraquecimento da Corrente Norte do Brasil (NBC) durante os stadials logo a leste da desembocadura do Rio Parnaíba, como previsto em alguns modelos paleoclimáticos.

Palavras-chave: NE Brasil, Heinrich Events, magnetismo ambiental

ABSTRACT

NE Brazil is a semi-arid region influenced by the southward displacement of the Intertropical Convergence Zone (ITCZ), which is the main atmospheric system that modulates the seasonal increasing in precipitation over this region. It is well established that these wet periods correlate temporally with Heinrich Events (HE) – periods of higher input of ice-rafted debris in the North Atlantic. However, the local oceanographic response to fresh water pulses in the North Atlantic and how this process influences sediment transport along the margin off NE Brazil are still a matter of discussion. We present here rock magnetic and geochemical element data for four marine cores collected in the south equatorial Atlantic Ocean, covering the last 85 ka. The cores are distributed between longitude 38°W and 36°W. We also performed end-member analysis based on the IRM acquisition curves bringing a better understanding about sediment sources. Magnetic proxies show a marked increase in concentration of magnetic minerals during stadials, with a concomitant change in the proportion of magnetic mineral types. Peaks in magnetic concentration parameters coincide with peaks in geochemical proxies for weathering intensity on land, being thus compatible with an increase in precipitation in NE Brazil during HE. Yet, the relative contribution of magnetic phases across the NE Brazil margin changes from west to east. During stadials the high-coercive phases (like hematite and goethite) are dominant for cores located in the western part of the study area and low-coercive phases are dominant for the core located further east. This difference is due mainly to differential oxidation over land, but secondarily we suggest a transport from W-E of high coercive material, possibly caused by the weakness of NBC during stadials just to the east of the mouth of the Parnaiba River as predicted in some paleoclimate models.

Keywords: NE Brazil, Heinrich Events, environmental magnetism

SUMMARY

LIST OF FIGURES

1 INTRODUCTION

In the last decades, a big effort has been done aiming to understand the relationship between north and south hemispheres during the last glacial period (10 to 110 kyr BP). Climate changes over annual and decadal scales that take place over the tropics can affect climate in high latitude, but such climate teleconnections over millennium time-scales and the relationship between local and regional oscillations and global forcing are still poorly known (Baker *et al*., 2001). Climate records show an out-of-phase relationship between north and south hemispheres, which revels a transmission mechanism of temperature and salinity related to changes in thermohaline circulation (THC). This mechanism, defined as 'bipolar seesaw', is governed by the fresh water discharge in the North Atlantic (Broecker, 1998), and it has been the target of many paleoclimatic and paleooceanographic studies in the tropics. Changes in the Atlantic Meridional Overturning Circulation (AMOC), a branch of the THC in the Atlantic Ocean, are the direct causes of temperature oscillation in Greenland (McManus *et al*., 2004). These decreases in temperature over Greenland result in fresh water discharge into North Atlantic from ice sheet melting, accompanied by massive discharges of ice rafted debris on the North Atlantic Ocean, named Heinrich Events (HE; Heinrich, 1988). Ruddiman (1977) was the first to identify these detritic rich layers (ice-rafted debris) in the North Atlantic, but it was Heinrich (1988) who related these massive discharges of continental material to changes in climate. He attributed the provenance of this material to the Laurentide Ice Sheet (LIS). This relationship between HE and temperature oscillation over Greenland is widely accepted and many studies performed in the tropics revealed that local changes in climate in the past are a response to these changes in the North Atlantic (e.g. H. W. Arz *et al*., 1999; Gutiérrez *et al*., 2009; Jennerjahn *et al*., 2004; Sifeddine *et al*., 2008).

NE Brazil is a semi-arid region affected nowadays by severe droughts, which interferes directly on the local agriculture and, consequently, on the regional economy. The southward displacement of the Intertropical Convergence Zone (ITCZ) – a convective belt that controls precipitation in the tropics, is the main process that modulates the seasonal increasing in precipitation over this region (e.g. Garreaud *et al*., 2009). These wet periods (Dupont *et al*., 2009; Jennerjahn *et al*., 2004) correlate temporally with the HE. Changes in paleoclimate recorded remotely by marine sequences and related temporally to HE are locally named as Heinrich Stadials (HS). The synchronicity between the southward displacement of the ITCZ and the expansion of ice-sheets in the North Atlantic have been reported by many paleo- climate

and oceanographic records (Wang *et al*., 2004; Weldeab *et al*., 2006) and were also depicted in climatic models (Chiang *et al*., 2008; Kageyama *et al*., 2013b; Kageyama *et al*., 2009).

The enhanced precipitation over NE Brazil resulting from the remote forcing of cold sea temperatures in North Atlantic (Heinrich Stadials – HS) is widely accepted (Arz *et al*., 1998; H. W. Arz *et al*., 1999; Behling *et al*., 2000; Jennerjahn *et al*., 2004). However, the local oceanographic response to the fresh water pulses in North Atlantic is still a matter of discussion. During low sea-level stands that took place in the last glacial (about 120 m below the present day sea-level) most of the continental shelf was exposed and the small rivers that presently cross the NE Brazil fed the continental slope (Knoppers *et al*., 1999). Addressing the ocean response to the southward migration of the ITCZ in the west Atlantic, Arz *et al*. (1998) related short-term changes in flow patterns and intensity of the North Brazilian Current (NBC) to global climate and oceanic circulation. The NBC dominates the dynamic circulation and sediment transport along the NE Brazilian margin (*Figure 5.1*). Some authors have shown that the southward migration of the ITCZ is connected to a weak Atlantic Meridional Overturning Circulation (AMOC; McGee *et al*., 2014; Weldeab *et al*., 2006). This weakness of the AMOC could affect the strength of the NBC and, consequently, the local circulation in NE Brazil margin.

Magnetic minerals are present in rocks and sediments in minor concentrations, but still they are very sensitive to oscillations in environmental conditions over the past and provide clues about the connection between continent and ocean basins. The use of changes in concentration, grain size and kind of magnetic minerals along marine sedimentary sequences is now a widely used technique for paleoclimatic and paleoceanographic studies (e.g. Just *et al*., 2014; Kissel *et al*., 2008), being widely known as "environmental magnetism" or "enviromagnetics" (Evans and Heller, 2003). Magnetic susceptibility is a classical proxy for detrital input, but much more information can be obtained from additional magnetic proxies (Liu *et al*., 2012). Rock magnetic techniques applied to marine cores may provide evidence about processes that take place over the continent (physical and chemical weathering, pathways – rivers suspended material or dust, etc.) and in the marine depositional environment (sediment re-distribution by currents, diagenesis - reduction of iron oxides, biogenic minerals, etc.). Detailed characterization of the magnetic minerals present in marine sediments is of utmost importance, since in the marine environment the formation of a new magnetic assembly from the detritic iron oxides is ubiquitous and sometimes the primary magnetic assembly is entirely dissolved. Reductive

conditions, with oxygen depleted and the presence of sulphate, are propitious to the dissolution of iron oxides and formation of iron sulphides (e.g. Kasten *et al*., 2004). Magnetic reduction compromises the primary signal, and hence the record of the past geomagnetic field and the original record of paleoclimate and source sediment signatures. When the primary magnetic assembly is not completely dissolved, magnetic minerals become a suitable tool to unveil the past history of the climate and oceanography systems and also in identifying sediment sources.

The terrigenous fraction entering continental margins contain iron oxides (i.e. magnetite, hematite), which composes the primary magnetic assembly of the sedimentary sequence. These minerals can provide useful information about the climate of the adjacent continental areas. As an example, the identification of pedogenic magnetic minerals (goethite and hematite) has proven to be very effective to detect changes in moisture availability during soil formation and consequently to infer about continental chemical weathering. In tropical regions, increasing moisture in soils can be generally related to a higher abundance of goethite over hematite (Abrajevitch *et al*., 2009). During extreme paleoclimatic events, precipitation in the continental area of NE Brazil is well defined (Jennerjahn *et al*., 2004) and interdigitating layers of magnetic minerals originated during wet (stadial) and dry (interstadial) conditions could be a hint to identify river supply changes. Variations on the magnetic mineralogy respond to changes in precipitation over land and deposition spots on the continental shelf can be a clue about pathways and source areas. Changes in the detrital magnetic minerals go along with variations in chemical element content (e.g., Govin *et al*., 2012). Fe/Ca and Ti/Al are normally used to track changes in detrital input, the Al/Si ratio can be sensible to continental chemical weathering, and coeval changes with magnetic parameters that are indicative of goethite increment (*i.e.* Hard-IRM and S-Ratio$_{[2.7\text{-}0.3]}$) suggest intense pedogenesis in river's catchment area. Fe/K ratio is also a proxy for changes in soil moisture availability, since K originates mostly from potassium feldspar or illite that typically are preserved or form in dry regions. In the same way, high Al/Si ratios are a tool to track soil alteration, since Al-rich minerals (mostly clay) are a product of intensive chemical weathering (Govin *et al*., 2012).

For a better comprehension about local forcings that influence sediment transport along the margin off NE Brazil, we present here detailed rock magnetic characterization and element data from marine cores collected in the south equatorial Atlantic ocean. We performed magnetic investigation and chemical analysis over four cores collected in the margin off NE Brazil, covering the last 85 kyr BP. The following magnetic parameters were used in this study:

magnetic susceptibility (κ), anhysteretic remanent magnetisation (ARM), isothermal remanent magnetisation (IRM) a 2700 mT e -300 mT [IRM_{2700mT}, IRM_{-300mT}], HIRM [Hard IRM= $IRM_{2700mT} - IRM_{-300mT})/2$], S-Ratio [$IRM_{-300mT}$/ IRM_{2700mT}], ARM/IRM and Fe/ κ. To improve the sediment source study we used X-Ray Fluorescence (XFR) measurements with spectrum operating at 10 kV for detecting major elements (*i.e.* Fe, Ca, Ti) and 30 kV spectrum in order to obtain trace elements data (*i.e.* Ni, Cu, Zn) for cores GeoB3913-3, GeoB3912-1 and GeoB3911-3. In addition, we compared geochemical data previously obtained from core GeoB3910-2 with our magnetic data.

The magnetic inventory and soil characterization over NE Brazil has showed significant differences between Parnaíba Basin (west) and Borborema Province (east; Archanjo *et al*., 2002; Journet *et al*., 2013; Roud, 2014; WRB, 2006). The identification of climatic pulses along the coast of NE Brazil using enviromagnetic tools permitted us to investigate a possible relationship between rivers supply/longitudinal transport and precipitation enhancement caused by cold events over the North Atlantic. Here we present new magnetic data for four cores recovered from the continental margin off NE Brazil (GeoB3913-3, GeoB3912-1, GeoB3911-3 and GeoB3910-2). In previous studies performed in NE Brazil margin, Fe/Ca and Ti/Ca have been published for cores GeoB3912-1 (Arz *et al*., 1998; Jennerjahn *et al*., 2004), GeoB3911-3 (H. Arz *et al*., 1999) and core GeoB3910-2 (Jaeschke *et al*., 2007). We complemented this data with new geochemical data for core GeoB3913-3 and some additional ratios (Al/Si, Fe/K and Ti/Al) for cores GeoB3912-1, GeoB3911-3 and GeoB3910-2. These four cores are located along a transect from west to east alongside the NE Brazilian coast under direct influence of ITCZ and NBC.

The thesis comprises this introduction, seven additional chapters, and VII annexes. The second chapter describes the climate in South America. The third chapter provides a detailed description of methods used, including magnetic and geochemical methods, and the end-member analysis technique. The fourth chapter reviews the application of magnetic methods to the study of past climate and oceanography. The fifth chapter describes the study region and provides a basic description of materials used in the thesis. The sixth chapter describes all experimental results. In the seventh chapter, results are discussed addressing changes in sea-level, climate and sources in the region for the last 85 kyr. The eighth chapter announces the main conclusions and perspectives. In annex, the magnetic and geochemical data are presented in the form of tables. Some tables (Annex V) are presented only in electronic form.

2 CLIMATE

2.1. Present day in South America

South America shows several climate processes and systems, with quite complex patterns, as a result of its wide latitudinal extension (10°N-55°S) and peculiar orographic configuration. The largest atmospheric systems are the Intertropical Convergence Zone (ITCZ) and the South Atlantic Convergence Zone (SAZC; *Figure 2.1*).

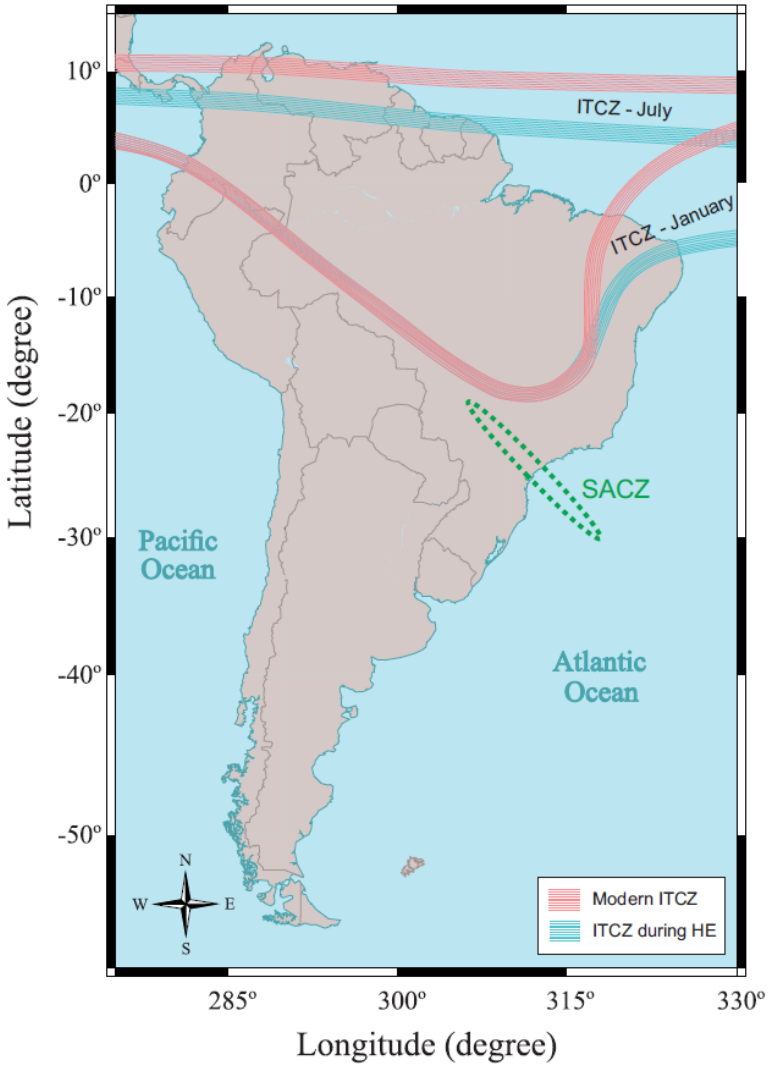

Figure 2.1: Main climate features in South America: South Atlantic Convergence Zone (SACZ) and Intertropical Convergence Zone (ITCZ): modern situation (red) and during the Heinrich Events (HE; blue).Configuration during HE from Jennerjahn et al. (2004).

These systems act in interannual timescale (Garreaud *et al*., 2009) and affect the whole South America, changing precipitation patterns over the continent and sea surface temperatures (SST) over the adjacent oceans (McGee *et al*., 2014; Robertson and Mechoso, 2000). The southward displacement of the ITCZ – a convective belt that controls precipitation in the tropics – is the main process that nowadays modulates the seasonal increasing in precipitation over this region (e.g. Garreaud *et al*., 2009). The SACZ is a convective summertime system that extends from Amazonia to the southeast forming a moisture belt, characterized by a meridional seesaw in upper-level (Robertson and Mechoso, 2000). According to Nogués-Paegle and Mo (1997) changes in the intensity of SACZ depend on humidity over tropical and subtropical South America. Higher precipitation over high latitudes of South America are associated to intensification of the SACZ (Robertson and Mechoso, 2000).

In addition to these large-scale seasonal systems, some leading modes of global atmospheric variability also present interannual variability, like El Niño Southern Oscillation (ENSO), Antarctic Oscillation (AAO) and Pacific Decadal Oscillation (PDO). ENSO is a large-scale coupled ocean-atmospheric system that takes place over the Pacific Ocean. It affects strongly the west-east temperature gradient over equatorial Pacific, and directly influence the west coast of South America and the temperature over the continent (Garreaud *et al*., 2009). The ENSO system fluctuates between warm (El Niño) and cold (La Niña) phases, which last about 2-7 yrs and bring forth, respectively, increase or decrease in precipitation in southern South America (Grimm, 2003; Poveda *et al*., 2006). The high latitude forcing AAO acts south of 20°S over tropospheric level, and presents pressure anomalies with opposite signals centred in Antarctica and on a circumglobal band at about 40-50°S (Garreaud *et al*., 2009). AAO varies in intermonthly and interannual timescales, but it plays a role in precipitation only in middle latitudes and southward (Gillett *et al*., 2006). PDO mode causes fluctuations in precipitation over South America under decadal and interdecadal timescales (Garreaud *et al*., 2009), and despite its smaller amplitude relative to AAO, it is important for our study since it is associated with interdecadal variability over NE Brazil and SST anomalies in Tropical Atlantic (Nogués-Paegle and Mo, 2002).

The asymmetrical heating of land and sea affects seasonally changes in atmospheric circulation and precipitation. Over South America, the warm season shows features that are typical of a monsoon climate. Zhou and Lau (1998) defined a monsoon as "a seasonal reversal in the large-scale circulation system driven by differential heating of the continent and the oceans."

Contrasts between winter and summer seasons exhibit a monsoon-like precipitation cycle over most of South America. Considering the existence of a regional summer monsoon circulation over South America, precipitation is strongly modulated by South America Summer Monsoon (SASM). The geographical extension of the SASM includes the core monsoon region and its areas of influence (*i.e.* low-pressure system over Chaco region and seasonal precipitation over tropical latitudes; Grimm *et al*., 2005).

As we mention before, all these systems (ITCZ, SACZ, SASM) can influence climate in South America and cause variability in SST of the adjacent oceans. However, it is important to say that global changes also affect these systems in a way that can impact climate in South America in different ways in low, middle and high latitudes. For instance, Cruz *et al*. (2009) found a phase difference between northern and southern South America, that was related to high temperature periods in the Atlantic Ocean tropical sector, a weakness of the temperature gradient between the hemispheres and the drift of ITCZ and ENSO systems. Baker *et al*. (2001) hypothesized that cooling Atlantic tropical waters intensifies the land-sea contrast, which in turn, due its influence over SASM, leads to an increase in precipitation and moisture in the Andean region. Such disconnection between north and south America was related by Robertson and Mechoso (2000) to SST anomalies in tropical and subtropical regions over South Atlantic, which strengthen the meridional temperature and intensifies trade winds.

2.2. Holocene in South America

The Holocene in South America is marked by dry conditions and high sea-level. Decrease of summer insolation in the Southern Hemisphere from late to mid-Holocene is one of the key points to explain the increasingly dry conditions in South America. Based on a multiproxy reconstruction, Prado *et al*. (2013) suggested less important precipitation in the mid Holocene in comparison to the late Holocene due to low austral summer insolation, which would reduce the land-sea temperature contrast and consequently weaken SASM. Increased land-sea temperature gradients during austral summer would enhance the transport of water-vapor to Amazonia (Baker *et al*., 2001). In more detail, differences between different regions of South America during the Holocene can be delineated. Precipitation in Amazonia south of the equator correlates with interannual and seasonal cycles recorded in Lake Titicaca, which shows maximum aridity between 8 and 5.5 ka BP (Baker *et al*., 2001). On the other hand, oxygen

isotopes data from speleothems recorded dry conditions in NE Brazil, whereas the southern tropical South America experienced humid conditions (Cruz *et al*., 2009). This was assigned to insolation-driven changes in monsoon circulation. These drier conditions are also expressed in the remarkable diminution of terrigenous input after 11 kyr BP (Arz *et al*., 1998).

2.3. Last Glacial Period

The main differences between the Last Glacial Period (110 to 12 kyr BP) and the present-day climate conditions are the ice sheet volume, CO_2 levels and changes in seasonal insulation (Ruddinam, 2008). Glacial periods are marked by large and well-defined millennial oscillations, which superimpose on the orbital-scale climate cycle. Orbital control of climate over NE Brazil, has been recorded in the final phase of the last glacial period (Cruz *et al*., 2009). However, changes in precipitation over NE Brazil recorded by high-resolution marine records, respond well to temperature changes over the North Atlantic (Arz *et al*., 1998; Jaeschke *et al*., 2007; Jennerjahn *et al*., 2004). An important characteristic of these short-time climate changes is that they begin and end up abruptly. In contrast, during interglacial periods such fluctuations are negligible or absent. Many records from ice and marine cores show synchronicity in such millennium fluctuations and result essentially from the coupling between the outer envelopes of the Earth (*i.e.* air and sea-surface temperatures). Marine records from low latitudes of the South Atlantic Ocean show a clear link between cold events in the North Atlantic and changes in precipitation patterns over the tropics (Arz *et al*., 1998; Mulitza *et al*., 2008).

The migration of the ITCZ to the south during the southward expansion of ice-sheets in the North Atlantic has been reported by many paleoclimate and paleooceanographic records (Wang *et al*., 2004; Weldeab *et al*., 2006) and were also depicted in climatic models (Kageyama *et al*., 2013a). Some works have shown that a southward migration of the ITCZ is also connected to a weaker AMOC in the past (McGee *et al*., 2014; Weldeab *et al*., 2006). This connection between different components of the climate reinforced the need for a better understanding of the link between abrupt climate changes in the North Atlantic and climate in the tropics.

Ice cores, sedimentary sequences, tree rings, and other sources have shown potential in unveiling climate events that took place in the past. Such high-resolution records made possible to investigate temporal features in detail and reveal extreme changes that occurred in a relatively short time. Abrupt climate event is a rapid change in comparison to the climate forcing, and

reaches a breaking point (Rahmstorf, 2001). In light of this definition, one could consider the transition between glacial/interglacial intervals, which lasts a few hundred or thousand years, as an abrupt climate change, once temporal scale of Milankovich Cycles is much higher. Concerning this thesis, abrupt events will be considered short-term oscillations (few thousand years) that superimpose on orbital-scale climatic cycles. Following the purposes of this thesis, here we will stick to millennial scale abrupt events (*i.e.* Heinrich Events, Younger Dryas) in the description that follows.

2.3.1. Heinrich Events

The German Hartmut Heinrich (1988) was the first to describe Heinrich Events (HE) after identifying layers anomalously rich in ice-rafted debris (IRD) in marine cores recovered from the North Atlantic. Heinrich (1988) took the ratio of lithic and total entities (fraction >150μm – 3mm) to show that the amount of IRD increased significantly in the Heinrich Layers, reaching almost 100%. IRD are detrital material transported by icebergs that detach from ice sheets and melt over the ocean depositing this grained material on the deep sea, between pelagic layers. Massive discharges of terrigenous detritus intercalated with marine sediments have been observed before by Ruddiman (1977), which identified an area between latitude 40-55°, named Ruddiman Belt, but its correlation to important changes in climate and oceanographic features on the North Atlantic was done only years later. Heinrich (1988), using $\delta^{18}O$ in foraminifera shells found an increase in the relative abundance of planktonic foraminifers typical of cold and low salinity waters (Neogloboquadrina pachyderma) during the HE. The source for detrital material in the Ruddiman Belt is linked to the detachment of icebergs from the Laurentide Ice Sheet (LIS), which were transported by the Gulf Current to deep regions of the North Atlantic Ocean (e.g. Bond *et al*., 1993; Heinrich, 1988).

Remarkable characteristics of HE are an abrupt termination marked by a sudden increase in temperature, and an inset after a gradual decrease in temperature (*Figure 2.2*). Some papers have suggested, based on models and records from Greenland and Antarctic ice cores, that weakness of North Atlantic Deep Water (NADW) starts with the input of fresh water on the North Atlantic Ocean (e.g. Blunier and Brook, 2001; Bond and Lotti, 1995; Stocker, 2000), whose origin is the LIS. According to Stocker and Marchal (2000), weakness of NADW would imply in cooling of the North Atlantic Ocean, and consequent decrease in icebergs melting rate. As HE took

place during periods of low temperature at the atmosphere and ocean surface, they reflected an increase in the resistance of icebergs at the cold ocean surface. After these periods, the NADW was re-established causing rapid warming in high latitudes of the northern hemisphere. *Figure 2.2* shows a flowchart with the scheme suggested by Stocker and Marchal (2000).

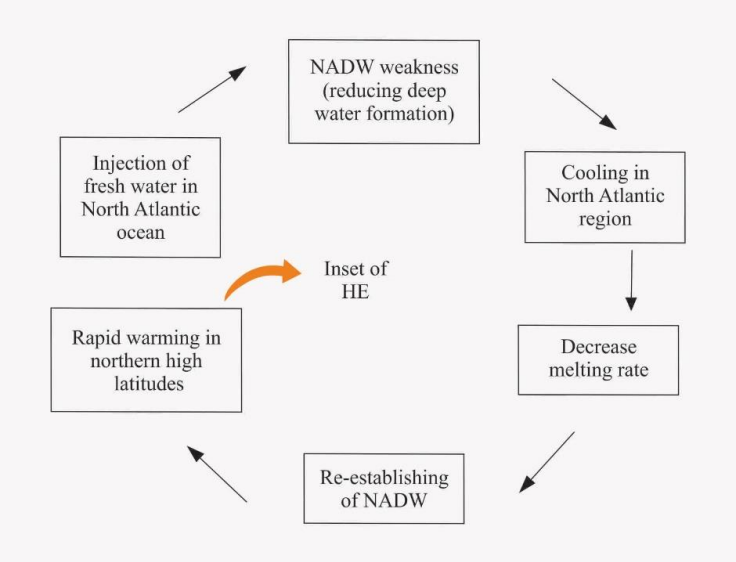

Figure 2.2: Scheme showing processes that control North Atlantic temperatures, NADW formation and inset of HE, according to Stocker and Marchal (2000).

The HE are associated to cold climate periods over the North Atlantic (e.g. Hemming, 2004). Some papers have shown an anti-phase relationship between climate over north and south Atlantic, and reveals the significance of correlating the HE to climate changes on southern Hemisphere (e.g. Broecker, 1998; Stocker, 2000). Abrupt millennial changes in climate over South America have been related to HE by many papers. When this abrupt changes take place on other regions out of North Atlantic Ocean, like the tropics, they are named stadials, and the interval in between is called interstadial. Following this conceptual assumption, we refer to the abrupt events we recorded here as Heinrich Stadials (HS).

The eastern portion of equatorial South Atlantic show that arid conditions are a reflect from HE during the last glacial period (e.g. Itambi *et al*., 2009; Just *et al*., 2012a; Mulitza *et al*., 2008). The last 85 kyr in Central America was marked by arid periods during HE due to southward migration of ITCZ (Hodell *et al*., 2008). On the other hand, in NE Brazil, wet periods were

identified by many studies, on the basis of drastic changes on geochemical data, stable isotopes and palynology in sediments, and linked to HE during the last glacial, especially during abrupt climate events (Arz *et al*., 1998; H. W. Arz *et al*., 1999; Behling *et al*., 2000; Jennerjahn *et al*., 2004).

2.3.2. Younger Dryas (YD)

The Weichselian late glacial, also referred to as last glacial-interglacial transition or last termination (15–10 kyr BP), was a period characterized by rapid climate changes. During the last termination, cold periods were interdigitated by interstadials (warm periods), that will be described in the next sub-chapter. Mangerud *et al*. (1974) were the first to propose a sub-division of the last termination (Weichselian) and the Flandrian (Holocene). Based on a sequence of glacials/interglacials events, these authors divided these two stages in chronozones, named: Bølling, Older Dryas, Allerød, Younger Dryas, Preboreal, Boreal, Atlantic, Subboreal, Subatlantic. Among these warm and cold events, the ones that have important expression globally are the B-O (item 2.3.3) and the YD. The YD was the last abrupt climate response to the transition between the last glacial and the present warm interglacial, therefore it arouse interest and has been largely studied. The last termination is classically sub-divided into a series of stadials named after the occurrence of the characteristic pollen from arctic-alpine plant species *Dryas octopetala* in lakes of Sweden and Denmark (Carlson, 2013). After that, ice cores from North Atlantic recorded with high resolution the decrease in $\delta^{18}O$ (reflecting cooling temperature), marking sharply the inset and termination of the YD (Alley, 2000). Records from Greenland are quite precise in determining timing for abrupt climate changes, like YD. At the time of the YD, the insulation was at its maximum (almost the peak) and the sea-level was at about 60-70 m below the present day configuration (Carlson, 2013). The connection between the tropics and the cold-water formation over North Atlantic Ocean is widely accepted nowadays (e.g. Kissel *et al*., 2013; Weldeab *et al*., 2006). McManus *et al*. (2004) identified a collapse in the AMOC during the YD. Due to this strong connection between North and South hemispheres throughout the Atlantic Ocean, it is possible to find the fingerprint of YD in many places around the world. During YD, wet conditions were identified in NE Brazil (H. W. Arz *et al*., 1999; Jennerjahn *et al*., 2004), concurrent with higher levels in Lake Titicaca (Baker *et al*., 2001), both consistent with migration to south of the ITCZ. Conversely, dry conditions were

identified in the eastern margin of tropical Atlantic (Just *et al*., 2012b; Mulitza *et al*., 2008). Still in the tropics, increase in sea surface temperature (about 0.25-1.2°C) in the margin off NE Brazil was recorded by alkenone analysis (Jaeschke *et al*., 2007).

Although the agreement in literature about ocean reorganization and deep-water formation, there is no consensus about what triggered the YD. The YD is sometimes referred to as Heinrich Event 0 and discussed in the same context as the Heinrich Events. However, YD cold event has not relationship with ice-rafting event. Thiagarajan *et al*. (2014) show that the structure of the water column in the North Atlantic is very different from the Heinrich-like water masses concerning temperature, $^{13}\delta C$ and $\Delta^{14}C$. According to Broecker *et al*. (2010), most of the covenant accept that YD started from a released of fresh water from Lake Agassiz, which shut down the deep-water formation. These authors consider the YD necessary for the process of transition between glacial and interglacial, as they compared YD with similar events that took place in the context of the last four terminations.

2.3.3. Bølling-Allerød (B-O)

The Bølling-Allerød (~14,7 kyr BP) interstadial is the initial warm phase during the last termination (Weichselian) that is followed by the cold stadial Younger Dryas. This warm climate event comes from the name of the localities Bølling and Allerød, in Denmark. The division of these layers has been widely used to correlate with biostratigraphic, climatostratigraphic and lithostratigraphic records that present the expression of the B-O.

The start of B-O warming is marked by both abrupt temperature rises (~9°) in high latitudes of Northern Hemisphere (Chiessi *et al*., 2008) and the restart of the AMOC (McManus *et al*., 2004). The characteristic increase in temperature in Northern Hemisphere during the B-O was concomitant with rise in CO_2 in the atmosphere, and some works show that this is probably released from deep ocean carbon reservoirs (Schmitt *et al*., 2012). On the other hand, Kohler *et al*. (2014) noticed a dramatic change in the process responsible for CO_2 rise in the beginning of B-O and suggest as a source of carbon a long-term immobile permafrost layer, whose abrupt release worked as a positive feedback to warming in Northern Hemisphere. The mechanism that triggered the onset of the B-O is still a matter of discussion. Thiagarajan *et al*. (2014) showed that B-O event was caused by discharge of warm water in the deep North Atlantic

Ocean, which also restored the AMOC. Using $231^{Pa}/230^{Th}$ ratio from a sediment core from the subtropical North Atlantic, McManus *et al*. (2004) recorded an abrupt increase at about 14.7 kyr ago, and attributed it to a rapid resumption of the AMOC, corresponding to the onset of the Bølling–Allerød warm period. Chiessi *et al*. (2008) using planktic and benthic foraminiferal records suggested the exchange between Atlantic and Indian oceans as the trigger for the resumption of the AMOC and the cause for the B-O event. Liu *et al*. (2009) addressed the B-O warming to the superposition of climate responses to the transient CO_2 forcing, the AMOC recovery from HE1, and an AMOC overshoot. Maybe a better comprehension of the temperature and salinity stratification of North Atlantic before and during B-O is prime to unveil process behind the onset of this abrupt warm period.

3 METHODS

3.1. Rock magnetism

All substances exhibit a magnetic behaviour. A sediment can be viewed as a pool of diamagnetic and paramagnetic minerals, the matrix, containing ferromagnetic minerals. The ferromagnetic behaviour is the only one that is able to preserve the magnetisation acquired during its formation. This magnetisation is named Natural Remanent Magnetisation (NRM) and it holds information about the direction and intensity of the Earth magnetic field (EMF) in the past (e.g. Tauxe, 2008). The magnetization of a sediment can vary according to the strength and direction of the ancient EMF, but is also controlled by sedimentary processes and composition of the sources. Magnetic mineralogy techniques consist on fast and non-destructive laboratory methods that enable one to characterize the different magnetic fractions in a sediment or rock. The first technique involves applying an alternated magnetic field (AF) on the samples, so that each step of the imparted AF consists of a gradually crescent field and when it reaches a peak, it decreases gradually down to zero. This oscillatory behaviour makes the magnetic moments of the low coercivity minerals become random and consequently the NRM falls away. When the intensity of the NRM is too high, (*i.e.* for volcanic or igneous rocks) the AF demagnetisation is not enough and thermal demagnetisation is required. For marine sediments, in most of the cases the AF demagnetisation is sufficient. After the NRM decreased to zero it was initiated the procedures aiming to obtain magnetic parameters for environmental magnetism analysis.

Some magnetic parameters obtained from artificial magnetic fields imparted on ferromagnetic materials are able to track changes in grain size, concentration and type of the magnetic particles. In this work, we used two remanent magnetisations for this purpose: Anhysteretic Remanent Magnetization (ARM) and Isothermal Remanent Magnetization (IRM). The ARM is a magnetisation obtained by applying an alternating field (AF) on the magnetic material simultaneously to a low intensity (0.5-1μT) direct field (DC; Evans and Heller, 2003). It provides a parameter efficient in the identification of fine magnetite (e.g. Thompson and Oldfield, 1986). The IRM is acquired in laboratory trough imparting a direct magnetic field in constant temperature, about 23-25°. Curves of IRM acquisition are obtained by imparting progressively higher fields. After each step of high intensity magnetic field induction, the magnetisation of the sample is measured. IRM acquisition curves permit the identification of magnetic minerals with different coercivities (*i.e.* hematite). In combination with the ARM, the

IRM can be used as a ratio to differentiate between small (single-domain, SD) and large particles (multi-domain, MD), so that high values of ARM/IRM indicate the presence of SD grains.

Other ratios can be obtained from these parameters and are useful in identifying proportional changes in the coercivity of magnetic minerals. The characterization of different magnetic types is useful to ensure a better quality of the paleomagnetic data and also for distinguishing between different detrital sources of sediments. The ferromagnetic particles comprise two main sub-behaviours, ferrimagnetic and anti-ferromagnetic, which correspond to the most important iron oxides present in the crust, respectively, magnetite (Fe_3O_4) and hematite (Fe_2O_3). Goethite is another anti-ferromagnetic phase usually present in sediments. Hematite and goethite are formed in the soils due to pedogenic processes during Fe-oxide oxidation (*e.g.* Abrajevitch *et al*., 2009). The S-Ratio is very effective in detecting proportional amounts of hematite/goethite (high coercivity) regarding magnetite (low coercivity). The ratio between IRM acquired at 300 mT and saturated IRM (SIRM) is defined according to the following formula:

$$0.5*[\frac{IRM_{300mT}}{IRM_{1500mT}}] \qquad \text{(Bloemendal } et\ al.\text{, 1992)} \quad (1)$$

Another useful ratio to quantify the high-coercivity magnetic minerals (*i.e.* hematite, goethite) is the HIRM (Hard-IRM), expressed by the equation:

$$0.5*[SIRM - IRM_{-300mT}] \qquad \text{(Stoner } et\ al.\text{, 1996)} \quad (2)$$

The HIRM ratio can also be used to detect changes in concentration of the ferrimagnetic minerals (Rowan *et al*., 2009), and together with the magnetic susceptibility (χ) is able to track the input of detrital material. The magnetic susceptibility is defined by the relationship between applied magnetic field (**H**) and magnetisation (**M**):

$$\mathbf{M} = \chi\mathbf{H} \qquad \text{(}e.g.\text{ Dunlop and Özdemir, 1997)} \quad (3)$$

It is dimensionless and usually simplified as a scalar (in fact, it is a second-rank tensor). Apart from the ferromagnetic behaviour, the susceptibility embraces also the contribution of diamagnetic, paramagnetic and superparamagnetic (SP) minerals. Changing frequencies during

the measurement of the magnetic susceptibility it is possible to detect the presence of SP grains (Dunlop and Özdemir, 1997).

For a better characterization of the magnetic mineralogy we used detailed techniques that make use of analysis in the crystallographic level of magnetic minerals. Changes in the temperature and applied magnetic field can show important transitions inside the structure of the grains and reveal details of magnetic minerals present in the sediments. To do so, we performed hysteresis loops (curves of induced magnetization against the inducing field). to obtain the contribution of all the magnetic particles present in the sample. The width of the curve along the inducing field axis (x-axis) is indicative of the coercivity of the ferromagnetic minerals and presence of paramagnetic grains is detected by using the slope of the curve at its very end, when the magnetisation is saturated (*e.g.* Dunlop and Özdemir, 1997). Moreover, four magnetic parameters can be extracted from the hysteresis loop and they are very important in accessing information about the size and coercivity of magnetic minerals: saturation magnetization (*Ms*), saturation remanent magnetization (*Mrs*), coercivity (*Bc*) and coercivity of remanence (*Bcr*). The ratios *Bcr/Bc* and *Mrs/Ms*, originally proposed by (Day *et al*., 1977) for titano-magnetites and displayed in the widely used Day Diagram, are quite useful in identifying different grain sizes of magnetic minerals (Dunlop, 2002). The so-called grain size in magnetics is based in the classification of magnetic minerals according to their domain structure. Thus, very diminute nanometric particles are superparamagnetic (SP), small particles are single-domain (SD), particles with intermediate grain-size are pseudo single-domain (PSD), and large particles are multi-domain (MD). Magnetite, for example has the SP-SD transition at about 0.03 μm, and SD-MD limit higher than 10 μm (Dunlop and Özdemir, 1997). For hematite, the limits are significantly different, with SP-SD threshold size of 0.025-0.03 μm (Özdemir and Dunlop, 2014) and SD-MD > 15 μm (Özdemir, 2002). Oxidation degree and changes in composition can also change the limits given above (Dunlop and Özdemir, 1997).

Low temperature curves are useful to identify characteristic transitions in the magnetization due to changes in the crystallographic lattice of some ferromagnetic minerals. These minerals undergo magnetic order/disorder below room temperature that promotes a rearrange of the atoms present in their crystallographic lattice. Certain iron oxides have specific transitions, such as the Verwey transition of magnetite (~122 K), the Morin transition of hematite (~ 262 K; Dunlop and Özdemir, 1997), and the Besnus transition of pyrrhotite (~ 32 K; Rochette *et al*., 1990). Low temperature studies investigating greigite has gained a lot of attention recently (e.g.

Roberts *et al*., 2011), after its identification on a broad set of marine sediments. However, until now no low temperature order/disorder transition has been identified for this metastable iron sulphide, but Chang *et al*. (2009) using synthetic samples found a strong dependency between remanent magnetization intensity at low temperatures and grain size for this mineral.

3.2. Unmixing magnetic remanences using IRM acquisition curves

The remanence of sediments is a linear combination of the magnetic contribution of all sources or ferromagnetic minerals. End-member (EM) analysis is an inverse technique used to numerically unmix such components (Just *et al*., 2012a). The unmixing procedure is used to separate distinct magnetic coercivities of mixed assemblages of minerals, attempting to decompose the magnetic signal into parts representing distinct minerals with specific characteristics. It provides information on different environmental processes that took place during magnetic minerals formation. Assuming that bulk IRM acquisition curves could be modelled using a linear mixture of cumulative log-Gaussian (CLG) functions (Robertson and France, 1994), the unmixing procedure intend to represent the independent coercivity components with different origins (Heslop and Dillon, 2007). Magnetostatic interactions can produce a non-linear behaviour in enviromagnetic processes, but some experimental work have shown that the deviation from a linear behaviour in natural materials is minor (e.g. Heslop *et al*., 2006). The unmixing model assumes that the measured magnetisation results from a linear mixture of a fixed number of end-members. The model uses a matrix $\mathbf{S}_{mxl}$ to represent the remanence curve of each end-member, with *m* end-members and *l* steps of applied field, and a second matrix $\mathbf{A}_{nxm}$ for the abundance ($A \geq 0$), where *n* represents the number of remanence curves or samples, and *m* represents the number of end-members. The data matrix **X** is described by:

$$\mathbf{X} = \mathbf{AS}$$

where $\mathbf{X}_{nxl}$ shows *n* lines with remanence curves for each sample and *l* columns with measurement fields. It is important to note that the contribution from each end-members, from the abundance matrix, represents the total magnetization (SIRM), and cannot be interpreted as volume or mass percentages (Just *et al*., 2012a).

The characteristic IRM acquisition curve for each specific magnetic mineral must also be defined. The magnetic grain size distribution in a natural material is logarithmic. Therefore it is approximated in IRM acquisition curves by a cumulative log-Gaussian (CLG) function (Robertson and France, 1994). In a sample with mixed magnetic minerals, the contribution of individual magnetic grains add linearly and the final result is a cumulative curve (Kruiver *et al.*, 2001). This is the basic principle of the IRM-CLG fitting program developed by Kruiver *et al.* (2001), a tool that quantifies the magnetic coercivity components through the analysis of acquisition curves. We used this tool to separate the different contributions present in each EM. This program assumes that the IRM acquisition curve resulting from contributions of different magnetic minerals can be described as a combination of different CLGs. According to this assumption, (i) filed values are converted to their logarithmic values and (ii) the linear ordinate scale is converted to a probability scale (Kruiver *et al.*, 2001).

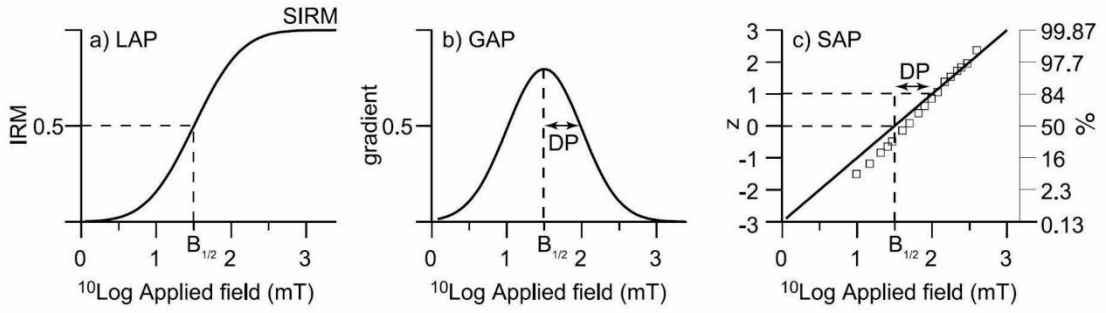

Figure 3.1: (a) Linear acquisition plot (LAP); (b) Gradient of acquisition plot (GAP); (c) Standardised acquisition plot (SAP), the IRM acquisition curve on a probability scale (right-hand ordinate) and corresponding z-score scale (left-hand ordinate). Figure from Kruiver et al. (2001).

The different components of IRM acquisition curves are obtained from their SIRM, mean coercivity ($B_{1/2}$) and dispersion (DP, Figure 3.1). $B_{1/2}$ represents the field at which half of the SIRM is reached, and DP is the standard deviation of the logarithmic distribution. In the standardised acquisition plot (SAP) z = 0 corresponds to fifty per cent of the cumulative distribution, at field $B_{1/2}$. Increasing *z* values correspond to $B_{1/2}$ + DP.

3.3. X-Ray Fluorescence (XRF) and bulk elemental composition (EDP-XRF)

Increase in the intensity or number of counts in XRF has being vastly used to trace the supply of terrestrial material to the ocean (Weltje and Tjallingii, 2008). However, since XRF core scanning data is considered to be semi-quantitative (Weltje and Tjallingii, 2008), elemental ratios have been used rather than direct counts, the most common being iron/calcium (Fe/Ca), titanium/calcium (Ti/Ca), titanium/aluminium (Ti/Al), iron/potassium (Fe/K) and aluminium/silicon (Al/Si) (Govin *et al*., 2012). Elemental ratios are more useful than single elements to reconstruct the climate in the past because they can eliminate undesirable effects. For example, the element Ca is amongst the most commonly used denominators since it accounts for the marine contribution and in this way, elements that reflect purely terrigenous contribution will be better represented. It is also important to stress that several factors, such as sediment colour, water content or instrumental settings, can interfere in the final XRF counting. In this way, the use of element count ratios is useful in comparing trends between different cores, but cannot be interpreted as the absolute values of elemental ratios.

Changes in the content of major elements along marine sedimentary sequences are sensitive to climate variability. In addition to the inorganic material produced in the oceans (*i.e.* carbonate), marine sediments are composed of terrigenous inputs, which reach the ocean via fluvial and eolian pathways. While arid conditions can be more propitious to dust transport and provide some clues about wind direction and strength, enhanced precipitation and sea level changes affect the amount and quality of the material carried into the oceans by fluvial processes. Ti and Fe contents are related to siliciclastic components and therefore represent changes in terrigenous material in the sediment, whereas Ca represents the marine contribution (carbonate content). Ti/Al ratio is associated with wind intensity and eolian contribution since coarse sediments are enriched in Ti, and Al is mostly associated with fine-particle clay minerals (Govin *et al*., 2012).

Major elements have been used also as a signature of weathering processes. In marine sediments K derives from minerals typical from dry regions, where chemical weathering is less intense, such as potassium feldspar or illite (Zabel *et al*, 2001). So, high Fe/K values suggest less chemical weathering. Conversely, Al/Si ratio is a tracker for intensive weathering, since Al is mostly associated with fine-grained clays minerals, in particular kaolinite, which is a product of chemical weathering under wet conditions. Higher contents of suspended river material were

tracked through higher values of Al/Si ratio in the margin off Senegal river (Mulitza *et al*., 2008).

In addition to the usefulness of using element ratios for recording the past climate, the comparison of geochemical data with rock magnetic parameters is helpful for the identification of redox layers present in marine sequences. In margins with high productivity and degradation of organic matter, it is not rare to find redox zones (Kasten *et al*., 2004). Drops in magnetic parameters to values close to zero can be compared with sulphur or molybdenum data in order to define such redox layers.

4 ENVIRONMENTAL MAGNETISM ON CLIMATE STUDIES

Detailed characterization of magnetic minerals as a proxy for reconstructions of climate, ocean circulation and sediment source is called environmental magnetism. The environmental magnetism comprises the characterization of the magnetic inventory when transport, deposition and transformation of magnetic grains are influenced by environmental processes in the atmosphere, lithosphere and hydrosphere (Verosub and Roberts, 1995). Magnetic mineralogy characterization makes possible to unveil processes that took place in the past and identify distinct magnetic contributions. Iron is one of the most abundant minerals in the terrestrial crust, but even considering that ferromagnetic particles are present in minor concentration, the methods for magnetic investigation are highly sensitives in detecting the presence of soil minerals, atmospheric particles and biogenic material and many areas in science use this tool, like geophysics, oceanography, climatology, sedimentology, etc. Thus, the characterization of different magnetic contributions is useful in the identification of magnetic particles present in small amounts in sediments, concerning mineralogical types, relative proportion between them, granulometry and preferential orientation. The magnetic parameters are a good tool in monitoring changes in many order of magnitude that occur even for small differences in concentration of the magnetic carriers (Verosub and Roberts, 1995). Such changes can be result of variation in depositional environment, and makes environmental magnetism an effective tool in the characterization of climate and ocean circulation in the past.

The pathways between source area and the spot for deposition has crucial impact over magnetic properties. The oceans are a natural repository for particulate and dissolved materials originated from land weathering, and marine sedimentary sequences are very important to preserve the history of processes that took place over continents and oceans. Therefore, quantitative and qualitative analyses of the magnetic carriers in sediments makes possible to separate magnetic grains in autochthone or allochthonous. Depositional (*e.g.* transport, source area, selection, reworking) and post-depositional (*e.g.* compacting, diagenesis, fluid migration) processes are determinant during building of sedimentary sequences. The classification of marine sediments is based on different criteria, like source area, grains size, chemical characteristics of its constituents, minerals assembly, etc. Considering its source area and mineralogical composition, marine sediments can be divided in: lithogenic, which are detrital particles transported to the oceans and classified as terrigenous or volcanogenic; biogenics, the ones

formed by organisms or by shell accumulation; autigenic, that precipitate direct in the solution and cosmogenic, which are not considered in this study (Schulz and Zabel, 2006). The source of magnetic minerals present in a marine sedimentary sequences can be land weathering (primary assembly) or in situ from biogeochemistry processes (secondary assembly), which can erase the primary carriers partially or totally.

The investigation about the properties of magnetic minerals along sedimentary sequences is being widely used in the last decades for paleo-climatic and -oceanographyc studies (e.g. Just *et al*., 2012a; Kissel *et al*., 2008). According to Bloemendal *et al*. (1992), the study of environmental magnetism in marine sediments can be divided in four categories: (i) investigation of origin of NRM to certify the reliability of data for earth magnetic field studies; (ii) the use of techniques for rock magnetism to investigate about diagenesis and magnetic minerals formation; (iii) study of biogenic minerals; and (iv) the use of magnetic properties as an indicator of content variations in terrigenous and for correlation between different cores from the same site. Since eight's, when the first works have been done (Henshaw and Merril, 1980; Thompson and Oldfield, 1986) many techniques of magnetic mineralogy has been developed aiming to characterize the origin of magnetic carriers in rocks and sediments, and better understand the primary magnetisation acquired by these geological material. (Grousset *et al*., 1993) published the first study using magnetic mineralogy techniques to identify distinct patterns during HE. On this study, the authors analysed the distribution of HE in time and space and they found significant differences between magnetic susceptibility for cores inside and outside of Ruddiman Belt. Susceptibility peaks were attributed to high abundance of detrital material from melting icebergs. Magnetic parameters have been useful in sediments that covers the Marine Isotope Stage 3 (MIS 3) due to some geochronological problems inherent to this period (*e.g.* Spötl *et al*., 2006). An example for that is the correlation between susceptibility and ARM with $\delta^{18}O$ data from foraminifer shells, in which Kissel *et al*. (1999) identified four HE during MIS 3. Magnetic particles can be transported by deep currents and thus, magnetic parameters provide clues about ocean circulation. Kissel *et al*. (2008) used ARM oscillations to track the pathway of the North Atlantic Deep Water (NADW) and infer about strength of the convective process and deep water formation. These authors studied also the link between NADW strength and climate changes of short term.

The use of environmental magnetism pointed previously, has shown effectiveness in studies about paleo-climate and –oceanography, and sediment source/transport. Thus, we make use

here of the parameters presented in sub-chapter 3.2 (***Rock magnetism***) aiming to understand past environmental processes that took place in our study sites. In addition to these magnetic parameters, with the purpose of better understand climate changes, we use Fe/κ ratio, which is useful to check the proportion of Fe bulk regarding the ferromagnetic contribution. According to Razik *et al*. (2013), in sediments that does not show signal of diagenetic magnetite dissolution, Fe/κ ratio can be used as a tool to track changes in sediment source and weathering conditions. Thereby, this ratio bring forth also some evidence about the presence of hematite/goethite concerning magnetite grains.

5 NE BRAZIL – STUDY AREA

5.1. Geomorphology of the continental shelf, rivers supply and geology

The Northeast Coast is about 3300 km long and stretches from latitude 3º to 13º S between the Parnaíba River to the west and the São Roque Cape to the east (*Figure 5.1*). It has a complex geomorphology as result of pre-Cenozoic geological structuring and morphoclimatic evolution, combined with climatic and eustatic fluctuations that took place during the Pleistocene (Gomes and Vital, 2010; Vital *et al*., 2010b; Vital *et al*., 2008). The continental shelf off NE Brazil is narrow (40 km width), and dominated by biogenic carbonates sedimentation (Vital *et al*., 2010ba). Its shelf break was defined by the same authors at about 70-80 m around Touros High (*Figure 5.1*), with smaller values (40-50 m) westwards. Based on its complex geomorphology, and on sedimentological and bathymetric data, Gomes and Vital (2010) and Gomes *et al*. (2014) divided the continental shelf off NE Brazil into three sectors with different gradients: inner, from 0-15 m (1:1400); middle, from 15-25 m (1:1000); and outer, from 25-40 m (1:250). In the boundary between middle and outer shelves, Gomes and Vital (2010) identified an extensive line marked by old beach rocks. Towards the open sea, steep gradient was found in the continental slope, with 1:4 at the upper slope above 300 m depth, and 1:11 below 300 m (Gomes *et al*., 2014). Moreover, important incised-valley systems draw up the margin off NE Brazil. These channels reflect the presence of relevant rivers that reached the break of the present day continental shelf and deposited sediments directly into the outer continental shelf, like incised-valley system of Piranhas-Açu River (Vital *et al*., 2010b) and estuary-incised valley system of Apodi-Mossoró River (Vital *et al*., 2010a).

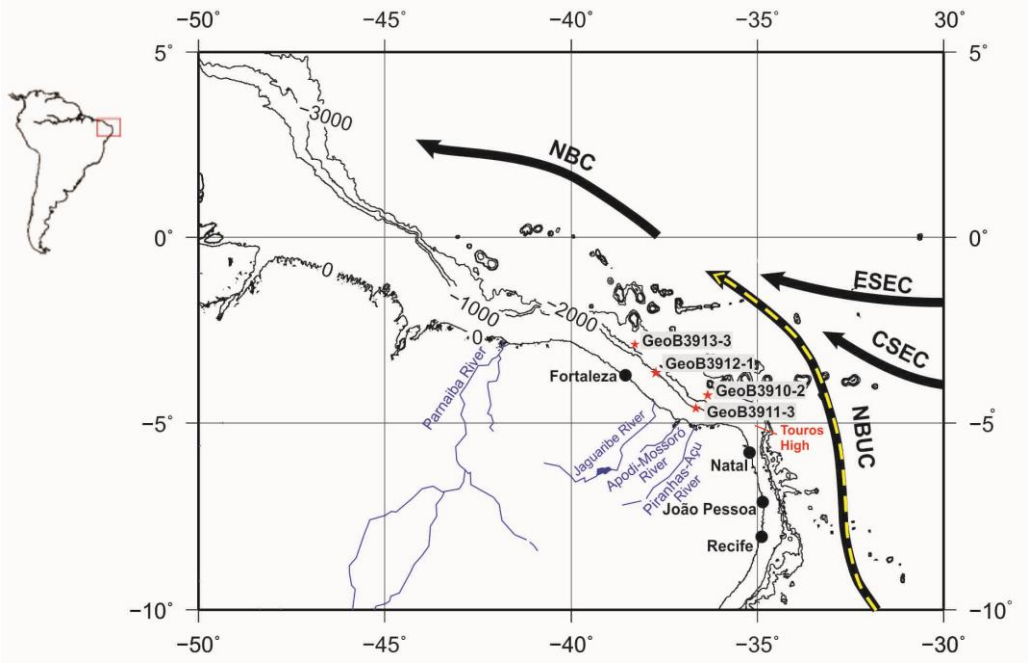

Figure 5.1: Location of the studied cores in the margin off NE Brazil. The arrows are a schematic representation of the layers 0-100 m (central and equatorial branches of the SEC and NBC), 100-500 m (SEC, NBUC and NBC) and 500-1200 m (NBC and EIC (flowing at about 0°S).

Among the rivers that debouch into NE Brazilian continental shelf, the Parnaíba River represents the second most important hydrographic region, embracing an area of 333.056 km^2 (3.9% of the Brazilian territory). According to the National Water Agency of Brazil (ANA, 2014), the Parnaíba River is 1400 km long and drains 99% of Piauí State. To the east, the Jaguaribe River is the main terrigenous supplier to the continental shelf adjacent to Ceará State (*Figure 5.1*). It is responsible for about 50% of the total fluvial outflow to this adjacent region (Dias *et al*., 2013). The drainage basin of Jaguaribe River covers an area of 75.669 km^2 and its extension is about 610 km (Gatto *et al*., 1999). Further east, the Piranhas-Açu and the Apodi-Mossoró Rivers also debouch in the continental shelf off NE Brazil. Their drainage basins are quite smaller than Parnaiba's one, but geomorphological studies performed in the adjacent margin have showed that the presence of important submarine channels cutting the continental shelf, suggesting their importance in the past (Gomes *et al*., 2014; Vital *et al*., 2010a). Apodi-Mossoró drainage basin occupies an area of 14.276 km^2, totalling a volume of 469.714.600 km^3, and the geology over its course is divided in 6.500 km^{2}of crystalline rocks to the south and 4.500 km^2 of sediments to the north (Souza *et al*., 2012). The drainage basin of Piranhas-

Açu River, to the east, embraces an area of 43.681.5 km^2, and along its course the main soil units are neosol, vertisol and argisol (ANA, 2010).

Geological domains of NE Brazil change dramatically from west to east. The western domain comprises essentially the Paleozoic to Cenozoic sediments of the Parnaíba basin (dark green, *Figure 5.2*). The eastern sector correspond to the Borborema Province (red, *Figure 5.2*), a crystalline basement constituted of Precambrian igneous and metamorphic rocks with granitic intrusions and patches of Cretaceous basaltic flows and dykes (Meju *et al*., 1999; Oliveira and Medeiros, 2012). The magnetic inventory of basement rocks and granites comprise essentially coarse-grained multi-domain magnetite (Archanjo *et al*., 2002), whereas the mafic dikes on the eastern part of Borborema Province contain mainly single-domain (SD) and multi-domain (MD) (titano)magnetite (Knesel *et al*., 2011; Trindade *et al*., 2006). Soils in the area are highly weathered and enriched in Fe-oxides hematite and goethite (Roud, 2014). In NE Brazil chromic luvisols are common; in the Parnaiba basin red and yellow ferrasols and (ferralic) arenosols are the dominant soil groups (WRB, 2006). A global data compilation of soil mineralogy from Journet *et al*. (2014) suggests generally high abundance of goethite with concentrations above 5% in the Parnaiba Basin and lower concentrations of 2-3% in most areas of the Borborema Province. In contrast, hematite is less abundant in large parts of the Parnaiba Basin (concentrations below 1%) and higher (between 1-5 %) in the Borborema Province and at the eastern border of the Parnaiba Basin (Journet *et al*., 2014).

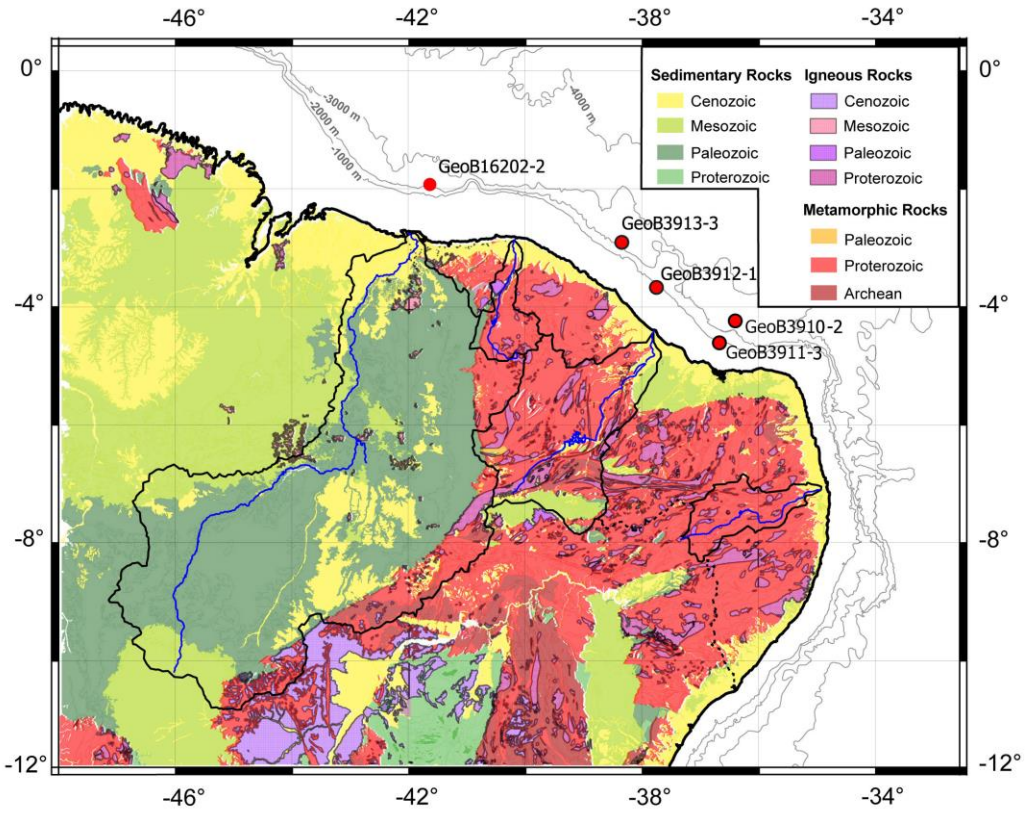

Figure 5.2: Geological map of NE Brazil. Light and dark green areas correspond to Parnaíba Basin, and pink and red ones are the Borborema Province. Modified from Roud (2014).

5.2. Oceanographic and Climatologic settings

5.2.1. Oceanic Currents

Narrow and open to sea, the NE Brazilian continental shelf is a typical example of passive margin governed by western boundary currents with extreme oligotrophic character (Knoppers *et al*., 1999; Vital *et al*., 2010b). The highly complex current circulation of the equatorial Atlantic comprises mainly the water transport from east to west by the North Brazilian Current (NBC) in surface waters and a southward transport driven by the Deep Western Boundary Current (DWBC; *Figure 5.1*). The NBC is a strong, up to 300 km wide, northwestward flowing surface current. It is one of the main water flows that cross the equator and is the major source of warm water transfer from the Southern to the Northern hemisphere (Knoppers *et al*., 1999; Stramma and England, 1999). Still according to the same authors, it is formed by the merging of equatorial and central branches of the South Equatorial Current (ESEC and CSEC, respectively) with the southerly North Brazilian Under Current (NBUC; *Figure 5.1*).

5.2.2. Sea-level

Differences in the sea-level position along the time result from changes in the volume and shape of the oceans, redistribution of water within the oceans, and to local vertical movement along the coast (Fleming *et al*., 1998). These three factors operate at different temporal and spatial scales. Redistribution of water during glacial cycles has regional and global influence, and a time scale between 10^3 and 10^5 years (Fleming *et al*., 1998). Reconstruction of eustatic sea-level curves takes into account ice distribution, considering contribution from glacio- and hydro-isostatic components and estimate sea-level curves for places close or distant from ice sheets. Aiming to show a realistic sea-level curve to represent transgression after the termination of the last glacial cycle, we used the eustatic curve from Fleming *et al*. (1998), which used data from intermediate and low latitudes, including two sites close to our study area: Jamaica and Barbados. Their data show a gradual increase in sea-level during the last 20 kyr BP (*Figure 5.3*). Sea-level for Barbados (dark blue dots) at about 18 kyr BP is about 120 m below the present-day position. In Jamaica (light green dots), the sea-level was about 10 m below present-day, and kept increasing up to mid-Holocene, when it increases slightly up to the present position.

During the last 20 kyr BP, changes in relative sea-level are a response to the transition from glacial to interglacial stages (Milne *et al*., 2005). A Holocene curve constructed from observations from many sites along the Atlantic margin off South America and the Caribbean Sea (*Figure 5.4*), shows a fast increase in sea-level between 8 and 7 kyr BP (Milne *et al*., 2005). Since 7 kyr BP, sea-level varied much less (Fleming *et al*., 1998). Spatial variations of sea-level along the Atlantic margin off South America where attributed to ice and ocean mass redistribution along the last 10 kyr BP (Milne *et al*., 2005).

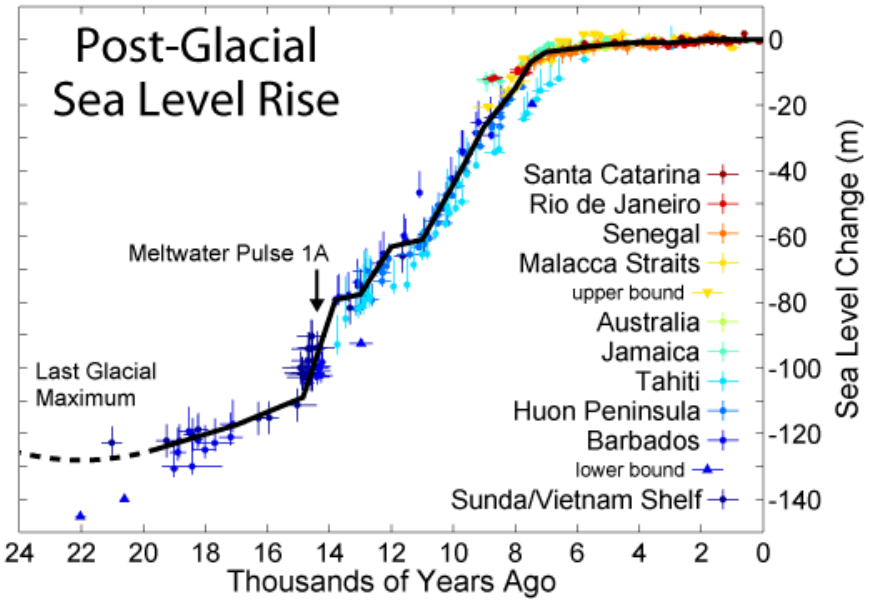

Figure 5.3: Sea-level evolution since the Last Glacial Maximum. Modified from Fleming et al. (1998).

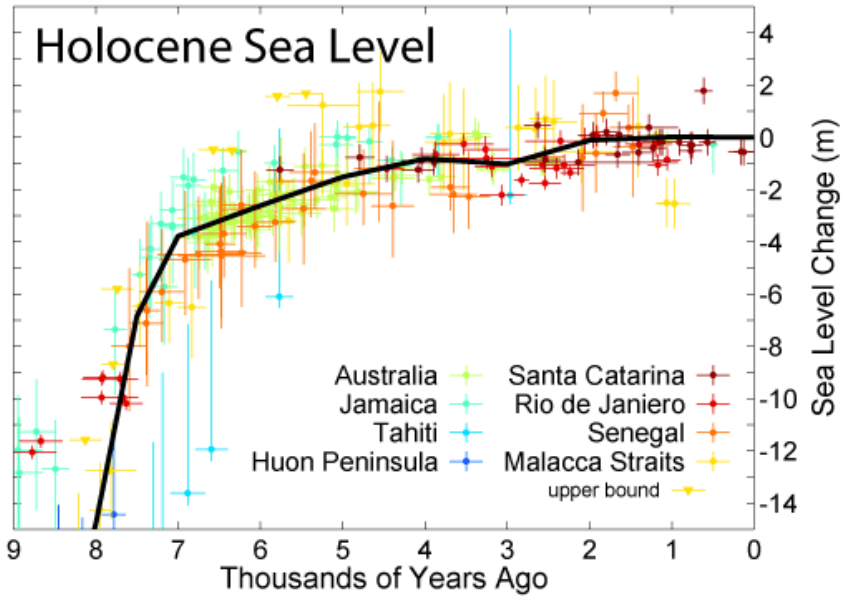

Figure 5.4: Sea-level observations from sites in the Atlantic margin off South America and the Caribbean Sea. Modified from Milne et al. (2005).

5.2.3. Climate

In the eastern part of NE Brazil region, the semi-arid climate dominates and "caatinga" vegetation prevails. In addition to the semi-arid climate, the region also presents tropical climate

in its more western portion. This region experiences between 4-5 months of dry weather (no rain), whilst in the "caatinga" region the dry season can reach six month. The annual mean precipitation over NE Brazil is only a third of the inland values at the same latitude, restricted to austral fall (Nobre and Shukla, 1996). Seasonal changes in the rain regime on this region are widely controlled by the latitudinal displacement of the ITCZ and its displacement southward during austral summer brings forth rainy season in NE Brazil (Garreaud *et al*., 2009). The ITCZ is a belt of minimum pressure and low-level convergence of the trade winds over the equatorial oceans, and its meridional shift determines the seasonality, intensity and spatial distribution of precipitation throughout the tropics (Garreaud *et al*., 2009).

5.3. Core sites and Lithology

The 7 meters long gravity-core GeoB3912-1(03°40'S, 37°43'W) was recovered at 772 m water depth (*Figure 5.1*) and its uppermost part (top 200 cm) consists of yellowish brown foraminiferal nannofossil ooze. Below, alternating sections of olive gray and very dark gray sediment occurs, indicating fluctuations in terrigenous and marine (nannofossil) components. Over the whole core length, and especially the lower part, the sediment is bioturbated (Fischer *et al*., 1996). Core GeoB3913-3 (2°53,8' S 38°18,5' W) is also a gravity core, with 6.45 meters length and recovered from 2288 m water depth. Its location is to the most west of the study area. In the upper half, core GeoB3913-3 is composed predominantly of strongly bioturbated, light olive brown to gray foraminiferal nannofossil ooze. From 300 to 350 cm two graded beds with foraminiferal sands at the base and below, down to 525 cm, the layers are tilted by 30° and are marked by nannofossil ooze with slightly enhanced clay content. From 525 cm to the end of the core the sediment consists of gray to greenish gray nannofossil ooze with varying content of foraminifera and clay (Fischer *et al*., 1996). In the east portion of the study area, two gravity cores were analysed. The 693 cm length gravity core GeoB3910-2 (4°14,7' S 36°20,7' W) was collected from the continental slope, at 2362 m water depth. It is composed of yellowish brown coloured foraminiferal nannofossil ooze in the top 30 cm and below it consists of grayish clayey nannofossil ooze. In the top 250 cm interdigitated layers of Fe-oxyhydroxides with 2-3 mm thick were found. The last 50 cm show disturbed sediments, with shell fragmente in the bottom end (Fischer *et al*., 1996). The 685 cm-long core GeoB3911-3 (4°36,8' S 36°38,4' W) was recovered from 828 m water depth and consists of light brownish foraminiferal nannofossil

ooze on its upper 50 cm. Between 200 and 460 cm there is an increasing content of terrigenous silt and clay with the sediment color turning to almost black. At about 460 cm and at the bottom end of the core layers with slightly increased content of nannofossils occur. The core is overall slightly bioturbated (Fischer *et al*., 1996). The previously mentioned cores were recovered during the METEOR-Cruise M 34/4.

5.4. Material and methods

5.4.1. Geochronology

The age model for core GeoB3912-1 for the last 40,000 yr was obtained from 12 calibrated radiocarbon accelerator mass spectrometry (AMS) ages from planktonic foraminiferal tests of *Globigerinoides sacculifer*. For ages bigger than 40,000 yr it was used three SPECMAP age control points (for detail see Arz *et al*., 1998). The ages of the top most part of the core were correlated with AMS ages of another core (GeoB3104-1) recovered from the same site in a previous cruise. To estimate the ages for core GeoB3913-3 we have made a correlation with the timescale of core GeoB3912-1. Based on the Fe/Ca ratio, we stablished 76 tie points for correlation between ages and depth (Annex I). For so, we used the software Bremen correlator, built by F. Thomas, using National Instruments LabView facilities. Dating for core GeoB3910-2 is based on 20 AMS radiocarbon ages, mainly monospecific samples of *Globigerinoides sacculifer* (for detail see Jaeschke *et al*., 2007). The stratigraphic framework of core GeoB3911-3 is exclusively based on reservoir-corrected, U/Th-calibrated, and linearly interpolated ^{14}C ages (H. W. Arz *et al*., 1999). For the four cores a global time-dependent ocean reservoir correction of about 400 years was used.

5.4.2. Magnetic minerals characterization

For magnetic measurements we sampled the cores GeoB3913-3, GeoB3912-1, GeoB3911-3 and GeoB3910-2 in 5 cm intervals, using 6,2 cm^3 plastic cubes.

The volume magnetic susceptibility (κ) for cores GeoB3913-3, GeoB3912-1 and GeoB3911-3 was measured at each centimetre using a Bartington M.S.2 susceptometer for discrete samples. Aiming to obtain the frequent dependent susceptibility, we performed in the cores from NE

Brazil (GeoB-3911-3, GeoB3912-1 and GeoB3913-3) and it involves frequencies values of 0.465 kHz (Low Frequency) and 4.65 kHz (High Frequency) ± 1%. We obtained the susceptibility using average value from three measurements intercalated with measurements of the empty space in order to minimize the errors related with the low sensibility of the equipment. For core GeoB3910-2 the volume magnetic susceptibility was measured in 694 data points using a Multi-Sensor Core Logger device, at a measurements frequency of 920 Hz with a 125 mm loop sensor and a non-magnetic core conveyor system (Fischer *et al*., 1996).

The natural remanent magnetisation (NRM) of the sediment, anhysteretic remanent magnetisation (ARM) and isothermal remanent magnetisation (IRM) were obtained step-by-step using a 2G u-channel cryogenic magnetometer 755 R at the Department of Geosciences (FB5), University of Bremen (for details, please see annex II). The ARM is a magnetisation obtained from applying an alternated field (AF) on the magnetic material simultaneously to a low intensity (0.5-1 mT) direct field (DC; Evans and Heller, 2003). It provides a parameter efficient in the identification of fine magnetite (e.g. Thompson and Oldfield, 1986). In this work, we used an axial bias field of 0.05 mT. The IRM is acquired imparting high intensity fields under constant temperature – in this work we used room temperature, about 23-25°. It permits the identification of magnetic minerals with high coercivity (*i.e.* hematite). These artificial magnetisations are useful to generate some magnetic ratios for the environmental magnetism study. In combination with the ARM, the IRM can be used as a ratio to differentiate between small (single-domain) and large particles (multi-domain), so that high values of ARM/IRM indicates the presence of grains SD. Relating the IRM in different magnetisation steps with the SIRM parameter is useful to track proportional changes in the coercivity of the magnetic minerals. In this work we obtained the Hard-IRM (HIRM; [SIRM-IRM_{-300mT}]) and the S-Ratio ([IRM_{300mT}/IRM_{2700mT}]) according to Stoner *et al*. (1996) and Rowan *et al*. (2009), respectively. The S-Ratio is very effective in detecting proportional amounts of hematite regarding magnetite, even as the HIRM is useful to identify the presence of high coercivity magnetic minerals.

Hysteresis loops were obtained in the PMC Alternating Gradient Magnetometer MicroMag 2900 at the Department of Geosciences (FB5), University of Bremen. Low (0.3T/-0.3T) and high (1 T/ -1 T) fields were used, with increment of $5x10^{-3}$ mT. Backfield and high field measurements were also made to obtain parameters Ms, Mrs, Bc and Bcr. All measurements were performed in room temperature (~23°C). A total 12 samples were measured. They were

prepared in the form of spheres with about 3-4 mm diameter and 20 mg weight using a special non-magnetic glue.

Low temperature measurements were performed in the Quantum Design Magnetic Properties Measurement System MPMS-XL7 at the Department of Geosciences (FB5), University of Bremen. Temperature ranges from 1.9 up to 400 K and DC fields vary between plus or minus 7 T. We ran five samples in strategic depths along the core GeoB3912-1. The samples were prepared in gel caps with 5 mm in diameter and 9 mm in length. We performed magnetic hysteresis loops in room temperature (300 K) and in low temperature (5 K), field-cooling (FC) and zero field-cooling (ZFC) curves, SIRM warming curves (300-400 K) and SIRM cooling/warming (0-300 K). Please find in Annex II the detailed protocols used in our samples, including the steps performed during acquisition and demagnetisation of each remanent magnetisation adopted.

5.4.3. X-Ray Fluorescence (XRF) scanning

Towards a better understanding of the weathering processes that took place during enhanced rainfall in NE Brazil, we performed XRF scanning on cores GeoB3911-3, GeoB3912-1 and GeoB3913-3. XFR measurements were performed with spectrum operating at 10 kV for detecting major elements (*i.e.* Fe, Ca, Ti), and with 30 kV spectrum in order to obtain trace elements data (*i.e.* Ni, Cu, Zn). We scanned entire sections of the cores GeoB3913-3, GeoB3912-1 and GeoB3911-3 at high resolution (1 cm) with a down-core slit size of 10 mm at the split surface of the archive half with XRF Core Scanner III (AVAATECH Serial No. 12) at the Center for Marine Environmental Sciences (MARUM), University of Bremen. In cores GeoB3913-3 and GeoB3911-3, we performed the XRF scanning using both spectrum ranges and obtained trace and major elements data. For core GeoB3912-1 we used the previously measured data, with a 2 cm resolution (Arz *et al*., 1998). The elements Ti, Fe, Si, K, Ca, Al were measured using X-ray tube settings of 10 kV, a current of 0.2 mA, and a sampling time of 20 seconds. Chemical data for core GeoB3910-2 was obtained previously at intervals of 0.4 cm for elements K, Ca, Ti and Fe (for details see Jaeschke *et al*., 2007).

Major elements (Al, K, Si, Fe, Ti) measurements from cores will be helpful in elucidating about the differences between soil contributions from the drainage basins of local rivers (Jaguaribe, Apodi-Mossoró and Piranhas-Açu). Chemical data from bulk sediment is a semi-quantitative

method (Weltje and Tjallingii, 2008), so here we used elemental ratios rather than direct counts. Either way, we compare only the trend of the different curves, not the absolute values. Moreover, other problems may affect the single-element concentration, as dilution processes (Govin *et al*., 2012), and according to Weltje and Tjallingii (2008) elemental ratios are insensitive to dilution effects. In this work, we used the ratios Fe/Ca, Al/Si, Fe/K, Ti/Al and Ti/Fe.

Aiming to check the presence of possible slumps we used a line-scan camera linked to the Super-Slit XRF-core scanner we obtained digital image for the cores GeoB3913-3, GeoB3912-2 and GeoB3911-3. The camera is a color line scan 3 CCD device using 3 x 2048 pixel CCD arrays and a beam-splitter. As we observed lamination along the three cores we will not show the data here.

5.4.4. End-member analysis

We obtained IRM acquisition curves, cumulative coercivity distributions of the integral magnetic mineral assemblage using an in-line pulse magnetizer and an external pulse magnetizer (Automated 2G Superconducting Rock Magnetometer 755 R) with 30 steps up to 2700 mT using the device from the Center for Marine Environmental Sciences (MARUM), in the Bremen University. Were obtained 138 IRM acquisition curves for core GeoB3910-2, 68 for core GeoB3911-3, 134 curves for core GeoB3912-1 and 109 curves for core GeoB3913-3. We applied a combined end-member (EM) unmixing analysis to 449 IRM acquisition curves aiming to separate the different magnetic contributions according to distinct coercivities. Using the distinct magnetic coercivities of the mixed assemblages, we applied the unmixing procedure attempting to decompose the magnetic signal into parts representing specific provenances that provide information on different environmental processes. We modelled each magnetic contribution using a linear mixture of cumulative log-Gaussian (CLG) functions to represent independent magnetic coercivity components using a software developed by Heslop and Dillon (2007). After that, we used the IRM-CLG fitting program of Kruiver *et al*. (2001) to quantifying the magnetic coercivity components present in each end-member. In other words, we took the output from IRM-CLG fitting software, which are “synthetic” IRM acquisition curves, and identified the different types of magnetic minerals.

6 RESULTS

6.1. Age model

The time range for core GeoB3912-1 is between 2.44 and 85.1 kyr BP (*Figure 6.1*b, Annex I). Correlation with core GeoB3912-1 enabled to establish the age model for core GeoB3913-3 (*Figure 6.1*a, Annex I). This core has smaller temporal resolution, with an average sedimentation rate of 5 cm/kyr. Hence, from the 6.45 m long core GeoB3913-3, we used only the topmost 3.5 m, which comprises the time interval between 1.29 and 84.6 kyr BP. Sedimentation rates vary significantly for cores GeoB3913-3 and GeoB3912-1 between ~ 5 cm/kyr and 25 cm/kyr. Intervals of increased sedimentation rates (~ 15-25 cm/kyr) coincide with the climatic events Younger Dryas (YD) and the last eight Heinrich Events (HE). Core GeoB3911-3 has higher average sedimentation rate (~ 41 cm/kyr) with two remarkable peaks between 11.1 and 11.3 kyr BP and 12.1 and 12.2 kyr BP, when sedimentation rates reach about 200 and 530 cm/kyr, respectively (*Figure 6.1*c, Annex I). The temporal range for core GeoB3911-3 comprises the period between 0.43 and 22.3 kyr BP and includes the YD and HS1. The YD coincides with the peak about 11 kyr BP, but the HS1 exhibits lower sedimentation rate of about 57 cm/kyr. The enhanced sedimentation rate observed at about 12 kyr BP suggests a remarkable terrestrial input, and it was related to Bølling-Allerød. Core GeoB3910-2 (*Figure 6.1*d, Annex I) has intermediate average sedimentation value of 9.6 cm/kyr, with coeval peaks of high sedimentation during the HS. Between 16 and 18 kyr the sedimentation rate showed its higher values (higher than 20 cm/kyr), and intervals of about 1000 years of sedimentation rates higher than 15 cm/kyr were found at 47, 43 and 23 kyr BP. The topmost interval, which comprises the Holocene, presents the lowest sedimentation rates for the four cores, with values smaller than 5 cm/kyr for cores GeoB3912-1 and GeoB3913-3, and about 11 cm/kyr for core GeoB3911-3. Core GeoB3910-2 shows high sedimentation rate in the lower Holocene (~ 10 cm/kyr) and smaller values during upper Holocene (~ about 4 cm/kyr). It is important to notice that during Holocene the further east cores GeoB3911-3 and GeoB3910-2 exhibits gradually higher sedimentation rates than cores in the west, but during Pleistocene this trend does not apply to core GeoB3910-2, which shows sedimentation rate smaller than core GeoB3913-3 and higher than GeoB3912-1.

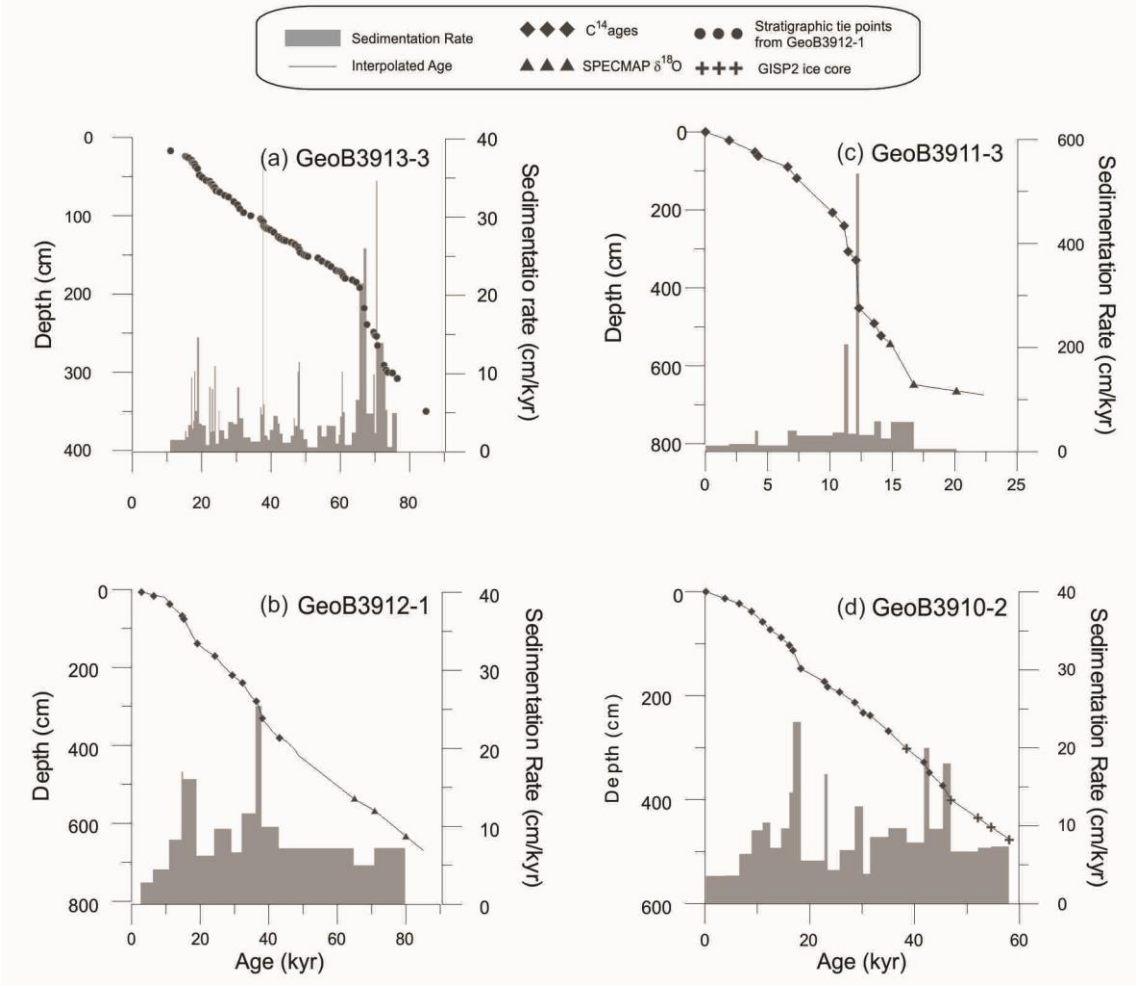

Figure 6.1: Age model (black curves) and sedimentation rate (gray step plots) for cores (a) GeoB3913-3, (b) GeoB3912-1, (c) GeoB391-3 and (d) GeoB3910-2. Diamonds represent calibrated ^{14}C ages, circles represent stratigraphic correlation tie points (GeoB3913-3 was correlated with GeoB3912-1), triangles show SPECMAP $\delta^{18}O$ (GeoB3912-1 and GeoB3911-3) and crosses represent GISP2 ice core correlation (GeoB3910-2).

6.2. Downcore Magnetic parameters

The most significant features we can observe in the rock magnetic parameters for cores GeoB3913-3, GeoB3912-1, GeoB3911-3 and GeoB3910-2 are the remarkable changes in the ferromagnetic content related to the abrupt climate changes, which were related to HE and YD (*Figure 6.2* - *Figure 6.5*). In our four cores, these abrupt events are well defined and magnetic parameters tells us about changes in the concentration, type and size of the magnetic minerals in such periods. Rock magnetic data is in annex III, and is available also in editable format in the digital media.

Core GeoB3913-3

All concentration dependent parameters - magnetic susceptibility (κ), IRM_{300mT} and HIRM - show baseline values during Pleistocene higher than in Holocene. These are the main recorders for terrestrial input in our cores, and tell us how drastically it dropped during Holocene (*Figure 6.2*a, b and d). Especially for core GeoB3913-3, this drop happens thousands of years before the inset of Holocene, just after the end of HS1. During YD we does not observe increase in the concentration dependent parameters for this core. The ratio ARM_{100mT}/IRM_{100mT} is useful in identifying changes in the grain size of the magnetic fraction comprised by (titano)magnetite.

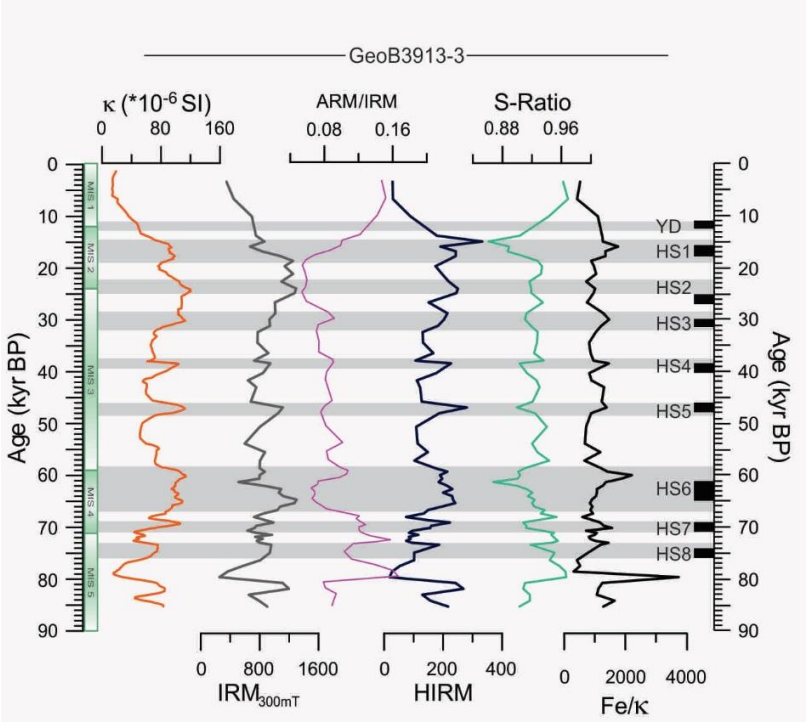

Figure 6.2: Rock magnetic parameters for core GeoB3913-3. Greyish areas mark the Heinrich Stadials (HS) that we matched with Younger Dryas (YD, Fairbanks, 1989) and Heinrich Events (H6 to H8, McManus et al., 1994; H1 to H5, Vidal et al., 1997), represented by the black squares. Greenish areas show the Marine Isotope Stages (Sarnthein et al., 2001).

Changes in ARM_{100mT}/IRM_{100mT} suggest a coarsening trend (MD-like behavior) before to 50 kys BP, during HS6, HS7 and HS8, but for late HS and YD there is a gradual increase, suggesting the prevalence of fine-grained magnetite (*Figure 6.2*c). In addition to the use of HIRM to detect changes in the concentration of the ferromagnetic particles, together with S-Ratio, this parameter track variation in the types of magnetic minerals concerning their

coercivity. S-Ratio decreases and HIRM increases during HS, suggesting the presence of high coercivity minerals (*Figure 6.2*d and e). Along the Pleistocene, the Fe/κ ratio shows peaks during the YD and HS events, reflecting a more remarkable increment in the bulk iron contribution related to the ferromagnetic contribution (*Figure 6.2*f). Up to the first half Holocene, we can see gradually small values of Fe/κ ratio.

Core GeoB3912-1

Likewise, abrupt climate events are well marked by concentration dependent parameters in core GeoB3912-1 (*Figure 6.3*a, b and d). The parameters κ and HIRM decrease significantly up to middle Holocene; however, IRM_{300mT}, differently to the other concentration dependent parameters, reaches higher values. The parameter IRM_{300mT} is effective to verify changes in the concentration of magnetic minerals, but in second instance, it is a grain size dependent. Thus, here it suggests the presence of fine-grained magnetite in late Holocene. The parameter ARM_{100mT}/IRM_{100mT} shows a coarsening of the magnetic fractions during all HS, and especially during Holocene, it reaches the highest values, suggesting the dominance of MD grains (*Figure 6.3*c). S-Ratio and HIRM also here suggest the presence of high coercivity minerals during HS, yet during Holocene, low/high values of HIRM/S-Ratio reflects the presence of less coercive phases (*Figure 6.3*d and e). Fe/κ ratio along this core exhibits sharper peaks, marking very well the inset of the HS, and just after YD it drops gradually and reaches smaller baseline values.

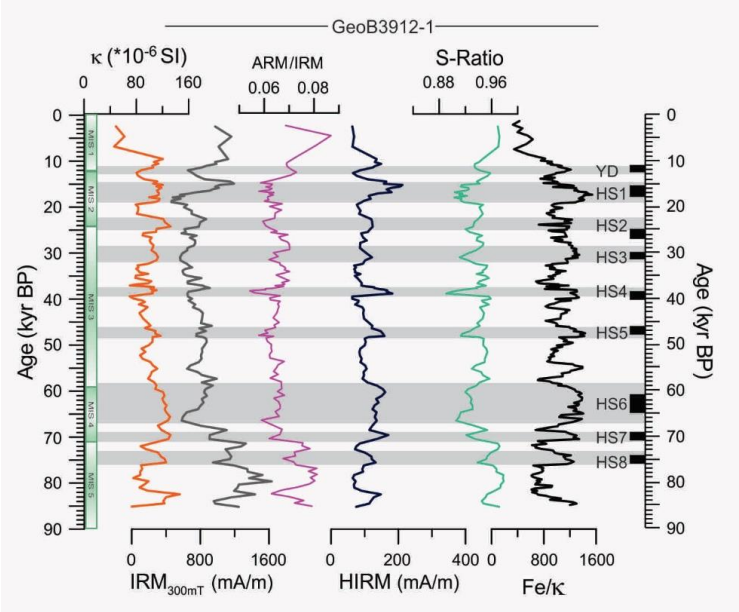

Figure 6.3: Rock magnetic parameters for core GeoB3912-1 (for details see subtitle in Figure 6.2).

Core GeoB3911-3

Differently to the other cores, concentration dependent parameters (κ, IRM_{300mT} and HIRM) here present significant drops in the upper part of HS1 and during YD (*Figure 6.4*a, b and d). It suggests that diagenetic dissolution of magnetite took place in this core. Grain size dependent parameters (IRM_{300mT} and ARM_{100mT}/IRM_{100mT}) also goes to small values in the upper part of HS1 and during YD, confirming a lost in the primary magnetic content at these depths. Between YD and HS1, the presence of SD-like magnetite is suggested by ARM_{100mT}/IRM_{100mT} ratio (*Figure 6.4*c). In addition, high values of HIRM were observed during warm period over North Atlantic region Bølling-Allerød (B-A), just before the inset of YD, and suggests the increase in the concentration of magnetic particles. High values of Fe/κ parameter are not source indicator during the abrupt climate events, due the diagenetic processes. During Holocene, decreasing values of Fe/κ ratio suggests the presence of more ferrimagnetic material (*Figure 6.4*f).

In late Holocene, decrease in κ and HIRM reveal a diminution in ferromagnetic concentration; yet IRM_{300mT} mirrors susceptibility curve, going to higher values up to about 5 kyr BP. After that, it decreases gradually. Maybe in Holocene, this parameter is working more as a grain size indicator than a parameter for changes in concentration.

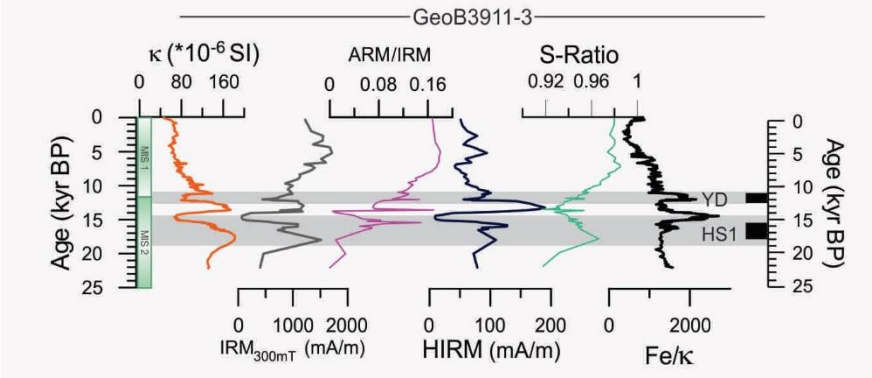

Figure 6.4: Rock magnetic parameters for core GeoB3911-3 (for details see subtitle in Figure 6.2).

Core GeoB3910-2

Along this core, IRM_{300mT} resembles susceptibility behavior, exhibiting higher values during the HS and prominent peaks during some events. HIRM also peaks during the abrupt events, suggesting increase in concentration of magnetic minerals. In the upper half of core GeoB3910-

2 (after 35 ka BP), during HS2 and HS3, parameter ARM_{100mT}/IRM_{100mT} suggests the presence of SD-grains. In the lower half, MD-like behaviour was detected in HS4 and HS5. During YD and HS1 ARM_{100mT}/IRM_{100mT} shows a variable behaviour, with an abrupt decrease in the beginning and an increase towards the end (*Figure 6.5*). Core GeoB3910-2 displays a different behaviour before about 35ka BP; curves for parameters S-Ratio and HIRM does not show an anti-coeval behaviour, as expected for anti-phase magnetite vs. hematite (*Figure 6.5*). During HS5 and HS4, differently of the behaviour in the other abrupt events, S-Ratio increases. Moreover, HIRM increases gradually during HS2 and keeps baseline values during HS3. HS1 in core GeoB3910-2 shows a singular behaviour, with an abrupt decrease of the HIRM parameter in the beginning of this event, followed by an abrupt increase and a gradual decrease towards the end. S-Ratio parameter exhibits the opposite behaviour in the HS1 for core GeoB3910-2. Differently from the other cores, Fe/κ ratio during Holocene in core GeoB3910-2 exhibits higher baseline values than in the Pleistocene. Fe/κ peaks at 9 kyr BP, and then it decreases gradually. Any signal of diagenesis was detected along this core, so here Fe/κ ratio can be used as a source or weathering indicator.

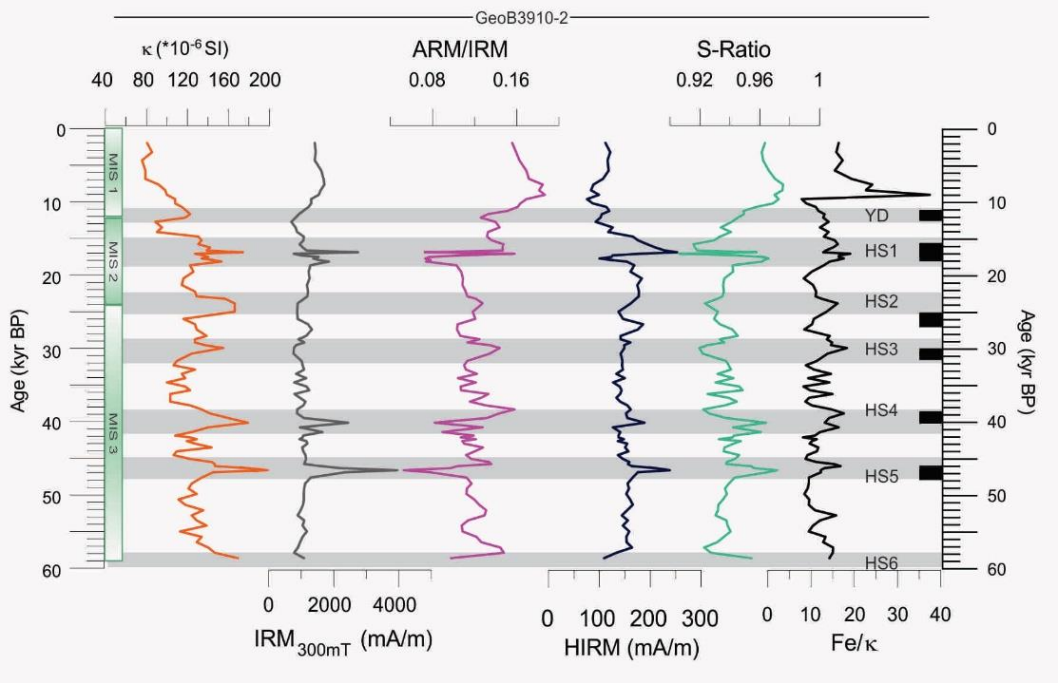

Figure 6.5: Rock magnetic parameters for core GeoB3910-2 (for details see subtitle in Figure 6.2).

6.3. Downcore element data

Similar to the rock magnetic parameters, the element data show remarkable changes during the YD and the HS 1-8 (*Figure 6.6 - Figure 6.9*). Element data is in annex IV, and is available also in editable format in the digital media.

Core GeoB3913-3

Fe/Ca ratio is the most outstanding and peaks abruptly during the HS, but in core GeoB3913-3 this ratio shows only a slightly during the YD. Al/Si ratio (*Figure 6.6*a) shows a gradual increase during HS and YD, with values slightly higher than baseline values. During Holocene, both ratios aforementioned show smaller baseline values, especially Fe/Ca, suggesting drastic reduce in terrigenous input. Fe/K ratio show noticeable peaks during the HSs, mainly during HS1. It is important to note that baseline values of Fe/K up to HS1 are smaller than in the period between about 14 and 5 kyr BP. Fe/K ratio shows the highest values recorded during the middle Holocene (4-7 ka BP). After that, this ratio shows an abrupt decrease. Ti/Al ratio shows a remarkable trend to higher values at about 54 kyr BP, when it clearly assumes higher baseline values. Before this time, slight changes are observed in the Ti/Al ratio during the HS, but afterwards, a sharp increase in this ratio marks the HS; during YD it increases smoothly. A drop in this ratio is observed at middle Holocene. After the inset of the Holocene, all major element exhibits a coeval behaviour, dropping to small values, except Fe/K ratio (purple curves), that drops after its main peak (7-4 ka BP).

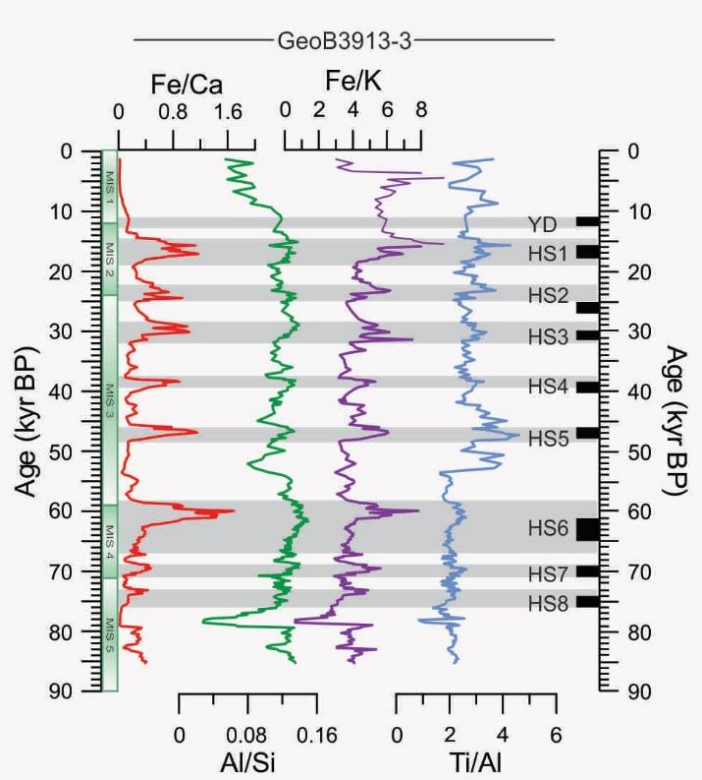

Figure 6.6: Element ratios [cps] for core GeoB3913-3 (for details see subtitle in Figure 6.2).

Core GeoB3912-1

Core GeoB3912-1 shows the most outstanding peaks in Fe/Ca ratio during HS and YD, confirming an increase in terrigenous input. Al/Si ratio from core GeoB3912-1 shows a sharp increase in the very beginning of the HS and YD and a gradual decrease towards the end (*Figure 6.7*b). Fe/K shows a very abrupt increasing in the beginning of the climatic events, but unlike the Al/Si ratio, it holds high values until the very end, when it goes down also sharply. The exception is only for the HS1, when after a sharp increase in the beginning, Fe/K ratio decreases gradually up to the end of the event. Ti/Al ratio increases mildly during HS7 and HS8 and displays an abrupt increase followed by a gradual decrease during YD, HS2, HS3, HS4 and HS5. Distinct behavior is observed during the HS6 and HS1, in which it increases smoothly after the inset of the events and decreases gradually towards the end.

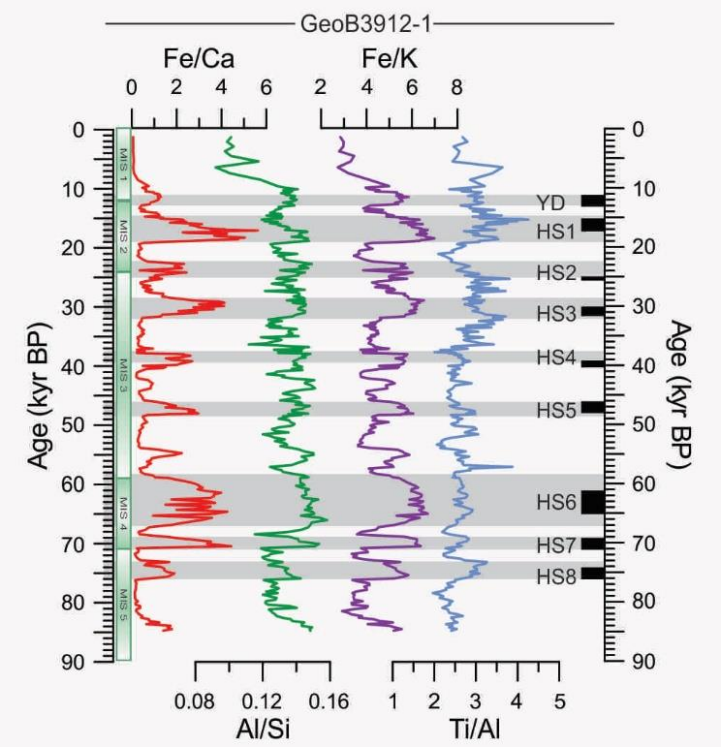

Figure 6.7: Element ratios [cps] for core GeoB3912-1 (for details see subtitle in Figure 6.2).

Core GeoB3911-3

High peaks of Fe/Ca are also observed in core GeoB3911-3 during HS1 and YD. However, the most outstanding feature in this core is the peak during B-A. This prominent peak also shows up in ratio Al/Si, and in the opposite way of the other cores, here we observe an abrupt decrease in Al/Si ratio during YD. This ratio exhibits more gentle increase during HS1 and a drop to small values in the middle of the stadial. Ti/Al ratio in core GeoB3911-3 (*Figure 6.8*c) increases smoothly after the inset of YD and HS1, but keeps almost the same baseline values along the core. The most noticeable change in Ti/Al ratio along this core happens after 5 kyr BP, when it increases slightly. Detrital phases decrease contribution during Holocene, as showed by Fe/Ca ratio, and also Al/Si and Fe/K. Fe/Ca ratio trend to zero during the whole Holocene. Al/Si exhibits decrease that is more evident after middle Holocene, between about 6-2 kyr BP, when it keeps the same values towards the top. Fe/K decreases gradually during the Holocene, up to aout 2 kyr BP, when it increases slightly.

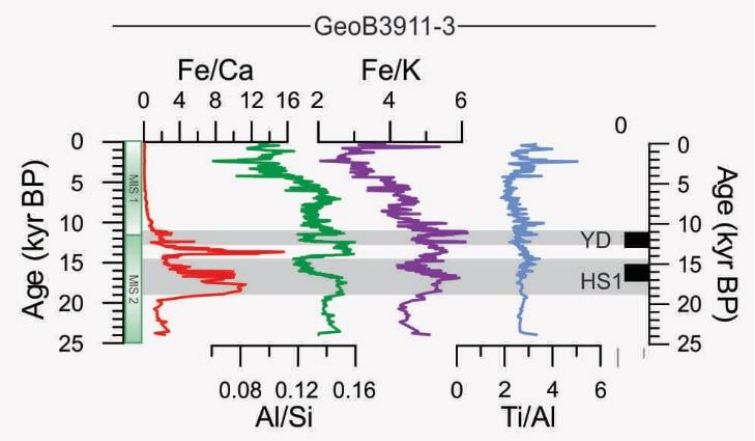

Figure 6.8: Element ratios [cps] for core GeoB3911-3 (for details see subtitle in Figure 6.2).

Core GeoB3910-2

For core GeoB3910-2, we have only Fe/Ca and Fe/K element ratios. Both shows remarkable peaks during HS1-HS5 and during YD. After the inset of Holocene these terrigenous indicators drops to almost zero, just like the other cores.

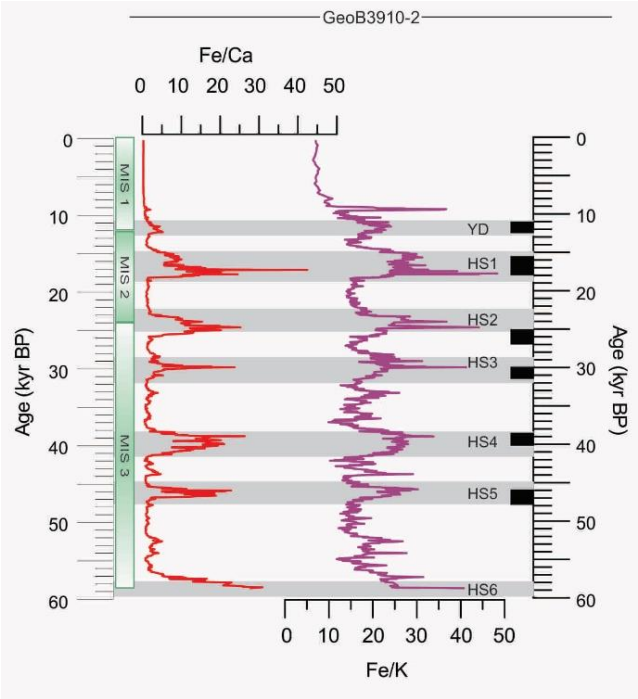

Figure 6.9: Element ratios [cps] for core GeoB3910-2 (for details see subtitle in Figure 6.2).

6.4. Magnetic contribution from end-members (EM)

6.4.1. Number of end-members

Before performing the end-member analysis, we investigated the parameters of environmental magnetism, in order to identify secondary magnetic minerals and magnetic mineral diagenesis. A remarkable lost in magnetization can indicate magnetic mineral dissolution related to diagenetic process. Core GeoB3911-3 shows an important decay in magnetization between about 515 and 605 cm (equivalent to ages 16 and 14 kyr BP in *Figure 6.4*). Even considering the possibility of diagenesis in core GeoB3911-3, we ran the IRM-unmixer model for this core too. Input data (IRM acquisition curves) for end-member analysis is available in editable format in the media (Annex V). IRM-unmixer calculates a coefficient for the fitting (R^2) between the matrix of data (**X**) and the matrices with the model (**A** and **S**) for each field step. R-Square provides a measure of how well a given model explains the data variance across the applied field range (Heslop and Dillon, 2007). *Figure 6.10* shows R^2 values for our cores (data available in Annex VI). Parameter R^2 shows high values for all end-members options (>0.92), indicating that our data can be modelled by the end-members approach with good quality. We can observe that the highest improvement in R^2 takes place between two and three end-members, when values increase from 0.92-0.97 to 0.94-0.98. For a higher number of end-members, R^2 values increase smoothly until EM = 9, when almost all cores show R^2 values as high as 0.9.

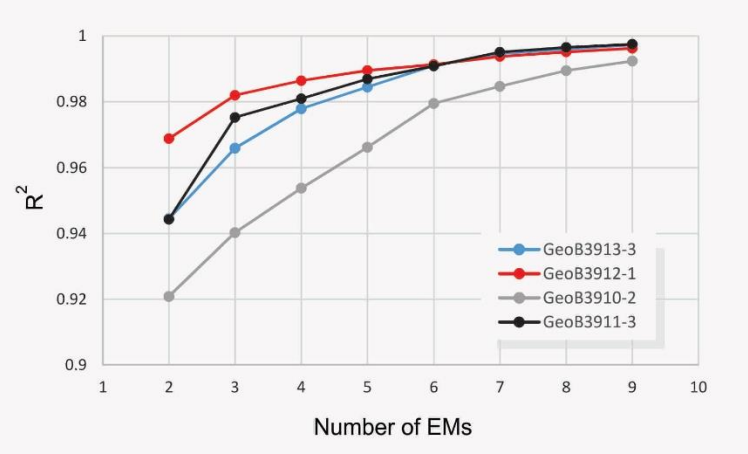

Figure 6.10: Coefficient of determination (R^2) for our four cores.

The IRM-unmixing models also provide the parameter "convexity at termination", that should be as close to "-6" as possible to assure the quality of the end-member modeling. For our four

cores, but GeoB3911-3 that is partially affected by diagenesis, the model with three end-members showed convexity closer to -6 (Table 6-1). Therefore, the combination to parameters R^2 and convexity suggest that 3 end-members is the best choice for cores GeoB3913-3, GeoB3912-1 and GeoB3910-2. The three end-members model also accounts better for the geological context of the study region (local geology, riverine inputs, etc) and matches the previous qualitative analysis of the magnetic mineralogy. Thus, based on the end-member contributions along the cores we decided to use the three end-members model to represent sediment sources on our study area.

Table 6-1: Convexity values for each end-member calculated during the unmixing process for our four cores.

Core	Number of end-members	Convexity at termination
GeoB3913-3	2	-6.0222
	3	***-6.002***
	4	-3.3562
GeoB3912-1	2	-6.0232
	3	***-6.0069***
	4	-5.345
GeoB3910-2	2	-4.8053
	3	***-5.0134***
	4	-3.5305
GeoB3911-3	2	-6.0044
	3	-4.5253
	4	-3.6865

The unmixing process using three end-members for core GeoB3911-3 shows an end-member that does not match any of the end-members from other cores, that we attributed to a diagenetic phase, based on the magnetically depleted interval mentioned before. Considering this diagenetic phase and the higher convexity value for the three end-member analysis of core GeoB3911-3 (Table 6-1), we decided to exclude this core from the sediment source study. The shape of IRM curves for each end-member and their relative abundance for core GeoB3911-3 are presented in the supplementary material, Annex VII.

6.4.2. Shape of the IRM acquisition curves from the unmixing

The unmixing method produces IRM-acquistion curves for each end-member from the analysis of all IRM-acquisition curves (input data to the model). In total, we obtained, respectively: 109, 134 and 138 curves from cores GeoB3913-3, GeoB3912-1 and GeoB3910-2. In *Figure 6.11* we show all IRM acquisition curves obtained for our cores and the end-member "synthetic" curves generated by the model (data in annex VIII). As expected, the end-member curves define an envelope that encloses all IRM-acquisition curves. Comparing the shape of end-member acquisition curves among the cores GeoB3913-3, GeoB3912-1 and GeoB3910-2 we also observe a good resemblance between EM1, EM2 and EM3 defined for each core (*Figure 6.12*).

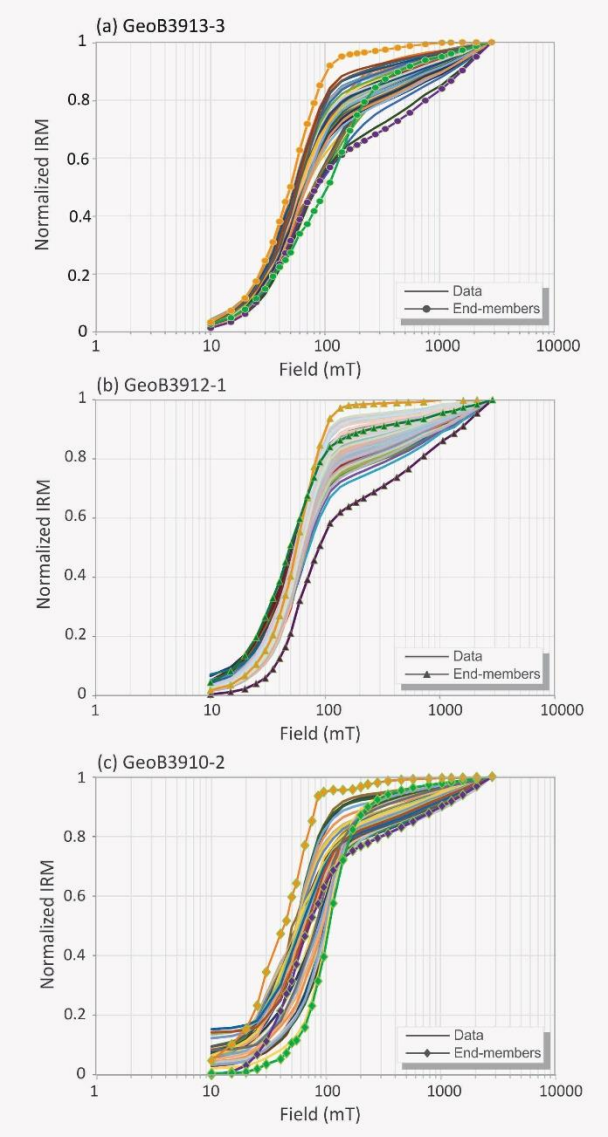

Figure 6.11: Comparison between the shape of the acquisition curves from the end-member analysis and the input data for cores (a) GeoB3913-3, (b) GeoB3912-1 and (c) GeoB3910-2.

Acquisition curves for EM1 (purple) suggest a mixture of a low coercivity magnetic phase saturated at about 20 mT (*i.e.* magnetite), and highly coercive phases, which do not reach saturation until 2.8 T (*i.e.* goethite and hematite; *Figure 6.12a*).

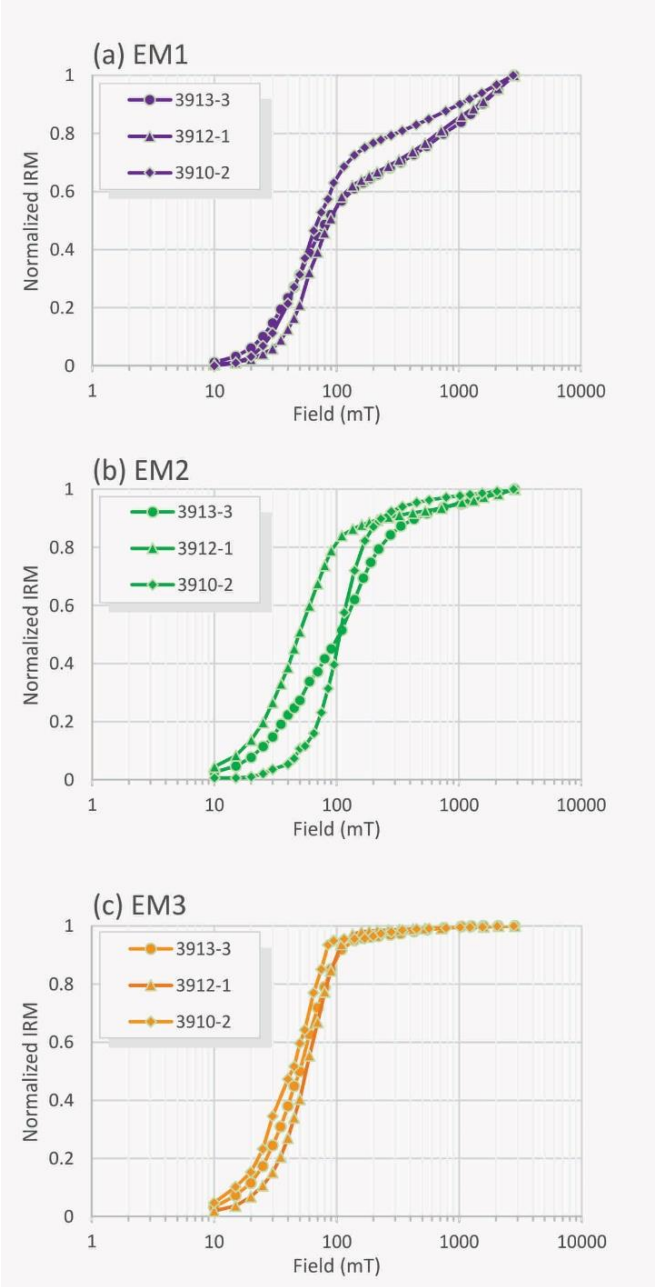

Figure 6.12: Comparison between the shape of the acquisition curves from the end-member analysis from cores GeoB3913-3, GeoB3912-1 and GeoB3910-2. (a) EM1, (b) EM2 and (c) EM3.

EM2 curves (green) show slight differences between cores, but in general these end-members are composed of low coercivity magnetic phases (*Figure 6.12b*). In cores GeoB3913-3 and GeoB3912-1, EM2 curves start acquisition at about 20 mT, whilst for core GeoB3910-2,

acquisition starts later at ~40 mT. These dissimilarities in the shape of the curves were attributed to the presence of low-coercivity grains with different sizes (SD and MD). For core GeoB3912-1, the faster acquisition is likely due to the presence of MD phases. The slower the IRM acquisition, the higher the relative contribution of SD grains.

EM3 curves (orange) showed the highest similarity among cores. In the synthetic IRM curves for EM3 magnetization started to be acquired in very low fields below 20 mT, and before 100 mT the curves reached complete saturation (*Figure 6.12c*).

6.4.3. Magnetic contributions from end-members

Each end-member provided by the IRM-unmixing shows variations in its relative contribution along the core, as described below.

GeoB3913-3

EM1 is present along the whole core, comprising about 50% of the magnetic signal (*Figure 6.13*). Remarkable peaks in EM1 are observed for core GeoB3913-3 during the HS, with values twice higher than baseline values. It is possible to observe sharper peaks in HS5 and HS4 in comparison to the other HS events. Moreover, HS1 exhibits two peaks of high intensity of magnetization, mimicking the behaviour of the environmental magnetic parameters (*Figure 6.2*). The EM2 is present along the entire core in small amounts. During the Holocene it is higher than in the last glacial. Between 25 and 15 kyr BP the EM2 increases significantly, comprising more than a half of the contribution; it reflects the dominance of (titano)magnetite in this sector of the core (*Figure 6.13*). The contribution from EM3 does not change significantly along the core but for some marked decrease during HS1 and at the bottom core, at about 78 kyr BP.

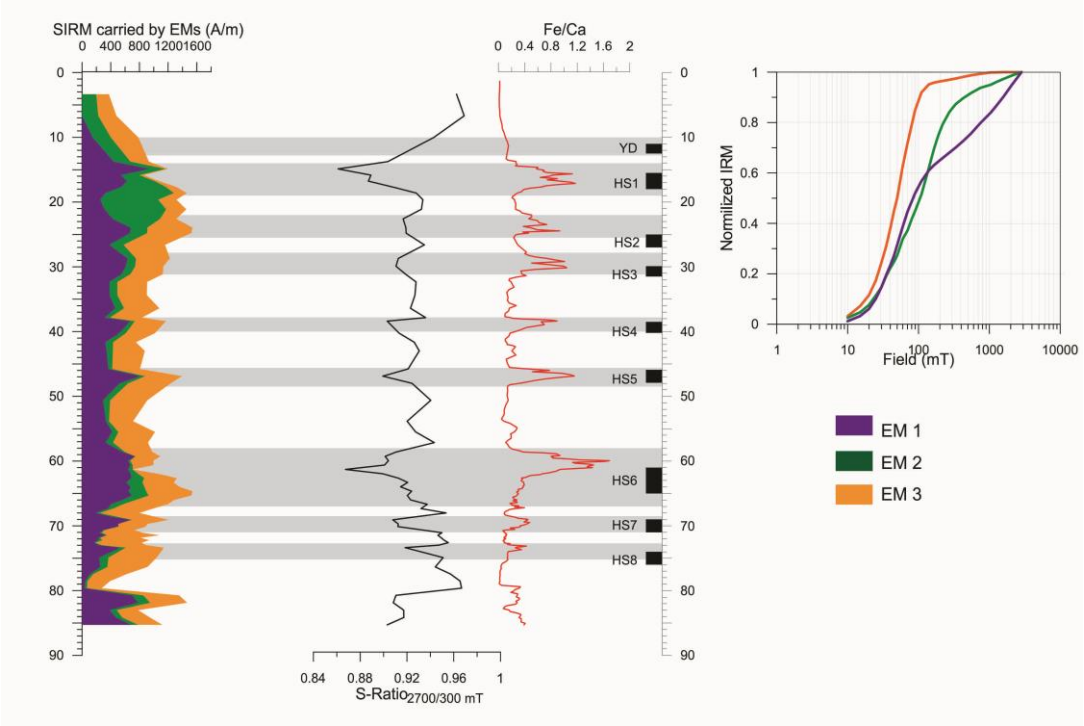

Figure 6.13: (a) downcore contribution and (b) IRM acquisition curves from the end-members calculated for core GeoB3913-3.

GeoB3912-1

EM1 shows significant peaks during HS in core GeoB3912-1 (*Figure 6.14)*. The intensity of the magnetization increases sharply during the stadials, except for HS3 and HS2. The contribution of EM2 is very important in the base of the core, and decreases smoothly towards the top, whereas the abundance of EM3 shows an opposite behaviour, being smaller at the base and higher at the top of the core, especially during the Holocene. This end-member also shows a decrease during the stadials.

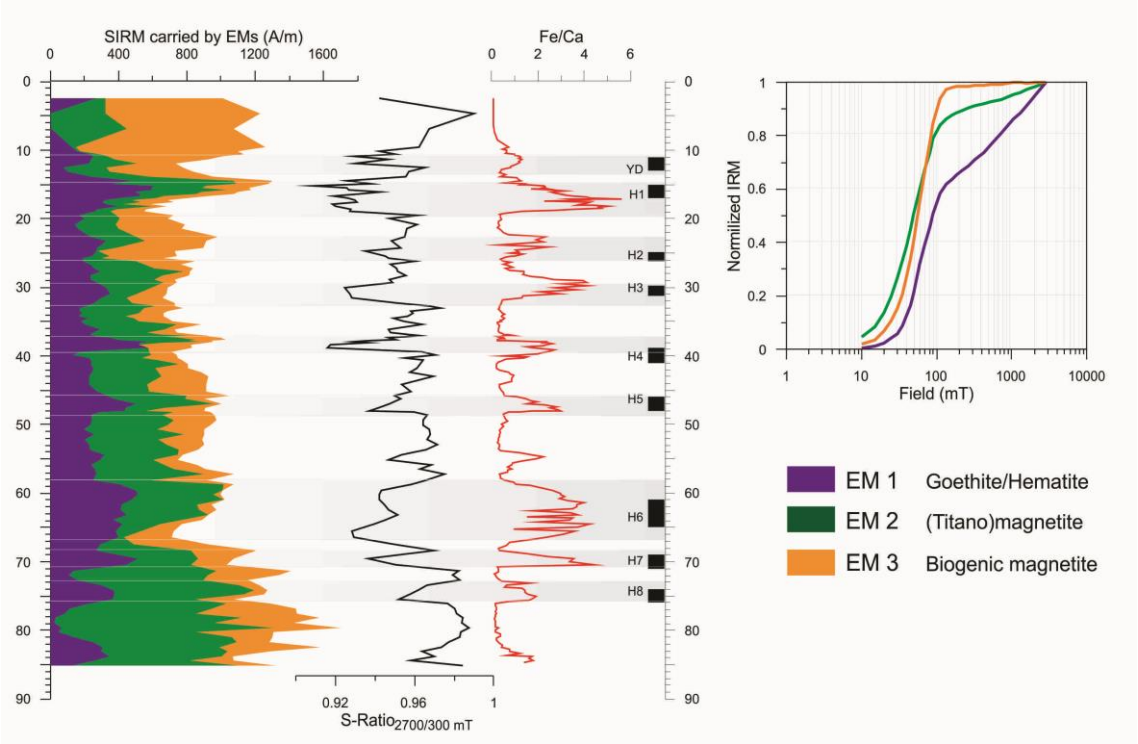

Figure 6.14: (a) downcore contribution and (b) IRM acquisition curves from the end-members calculated for core GeoB3912-1.

GeoB3910-2

EM1 is the dominant contribution to the magnetic signal along core GeoB3910-2 (*Figure 6.15*). However, differently from the other cores, this end-member does not peak during stadials. During HS3 and HS2 it does not vary significantly, whereas during HS5, HS4 and HS1 its contribution decreases. The EM1 only peaks remarkably during the younger stages of HS1. In contrast, EM2 increase during the stadials and show significant contribution at these extreme events. The contribution of EM3 along the core is small, but almost constant during the last glacial. EM3 decreases during the stadials, and increases significantly during the Holocene.

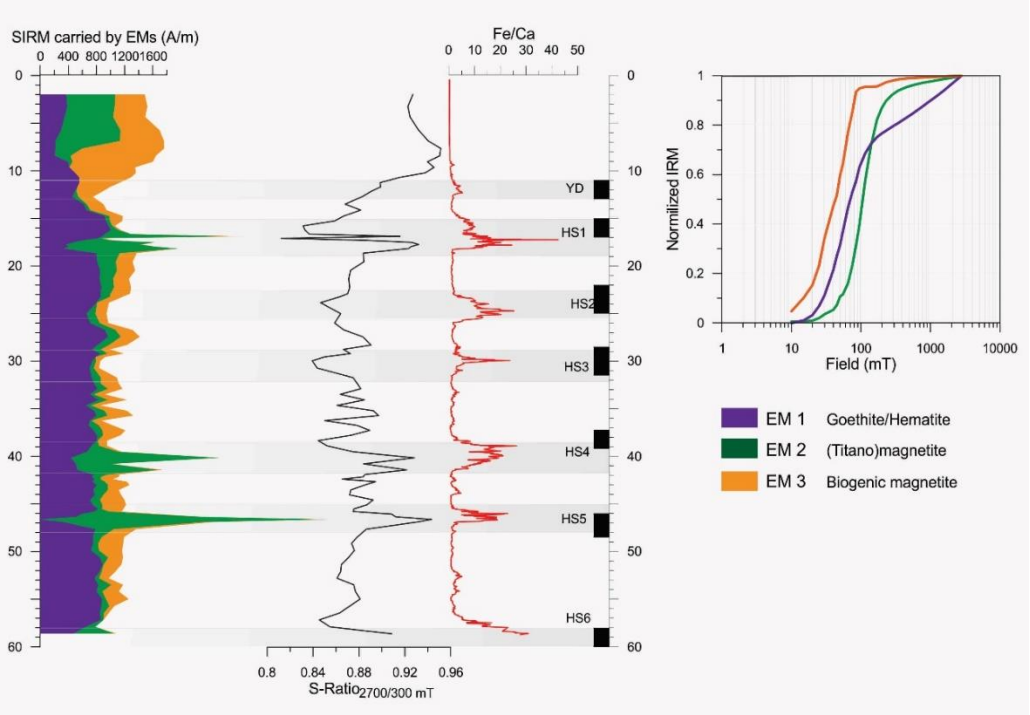

Figure 6.15: (a) downcore contribution and (b) IRM acquisition curves from the end-members calculated for core GeoB3910-2.

6.4.4. Significance of each end-member

Here the magnetic mineralogy content is discussed for our end-members according to the shape of the IRM acquisition curves of EM1, EM2 and EM3. Each end-member was deconvolved in individual IRM acquisition curves by direct modelling each EM synthetic curve using the IRM-CLG fitting of Kruiver *et al*. (2001). For each component parameters SIRM, $B_{1/2}$ and DP were obtained. *Figure 6.16* (EM1), *Figure 6.17* (EM2) and *Figure 6.18* (EM3) show the component analysis results for each end-member for the three cores. Table 6-2 shows the values of the parameters for each component and for each EM. The assembly of magnetic minerals present in our cores exhibit five components with increasing magnetic hardness, that are combined in different proportions in our three end-members.

Initially, to identify the magnetic minerals present in each of our five components, we used the values of $B_{1/2}$ and DP (Kruiver *et al*., 2001). The magnetically soft phases correspond to components 1 and 2 and were interpreted as magnetite, due to their $B_{1/2}$ values < 60 mT. Component 1 has a consistent peak of $B_{1/2}$ between 13 and 33 mT and DP between 0.12 and 0.30 and correspond to the limits observed by Geiss *et al*. (2008) for pedogenic magnetite. For end-members 1 and 2 this component is interpreted as related to pedogenic processes. We note,

however, that component 1 obtained for EM3, that presents a low $B_{1/2}$ < 18 mT and low DP of 0.18-0.25, could be an artefact from the IRM-CLG modeling. The approach of Kruiver *et al*. (2001) cannot fit left-skewed distributions (Egli, 2003), and an additional low-coercivity component is sometimes needed to fit the data (Just *et al*., 2012a). Thus, we are cautious about attributing such component to a very soft magnetic mineral, MD magnetite, for end-member 3. The coercivity of our component 2 is between ~47 and ~57 mT. We attributed it to magnetossomes with intermediate coercivity following (Egli, 2004). Component 3 presents an intermediate hardness (~100-200 mT) and was attributed to fine-grained titano(magnetite). According to Geiss *et al*. (2008), these values of $B_{1/2}$ suggest the presence of parental material from crystalline rocks. Components 4 and 5 are simple to identify because of their characteristic high values of $B_{1/2}$. Component 4 exhibits $B_{1/2}$ between ~500-700 mT and can be ascribed to hematite. Component 5 shows up $B_{1/2}$ higher than ~1500 mT and was interpreted as goethite.

EM1 is a mixture of magnetic minerals with low and high coercivities. In EM1 of cores GeoB3913-3 (*Figure 6.16*) and GeoB3912-1 (*Figure 6.17*) two soft components are present: component 1 (pink curve) and component 2 (green curve), with $B_{1/2}$ of ~30 and ~70 mT, respectively. Moreover, two magnetically hard components are present: components 4 (grey curve) and 5 (black curve), with $B_{1/2}$ of about ~600 and ~1800 mT. In core GeoB3910-2 (*Figure 6.18*), component 1 is absent, but we observed components 2, 4 and 5. Components 1 and 2 account for about 62% of SIRM in cores GeoB3913-3 and GeoB3912-1, whilst in core GeoB3910-2 the contribution from these magnetically soft phases is of 78%. Component 4 accounts for about 24%, 28% and 15% of the total SIRM in cores GeoB3913-3, GeoB3912-1 and GeoB3910-1, respectively. The most coercive component 5 has minor contribution in cores GeoB3912-1 and GeoB3910-1 (~9.8% and 7%, respectively); and in core GeoB3913-3 it has the most significant contribution in SIRM, to ~14%. Even considering that the percentage contribution to the total magnetization of hematite/goethite is small in comparison with that of magnetite, these hard phases correspond to an important fraction of the magnetic inventory of the sediments. That is because the intrinsic remanent magnetization of magnetite is about 200 times higher than that of hematite and goethite (Dunlop and Özdemir, 1997).

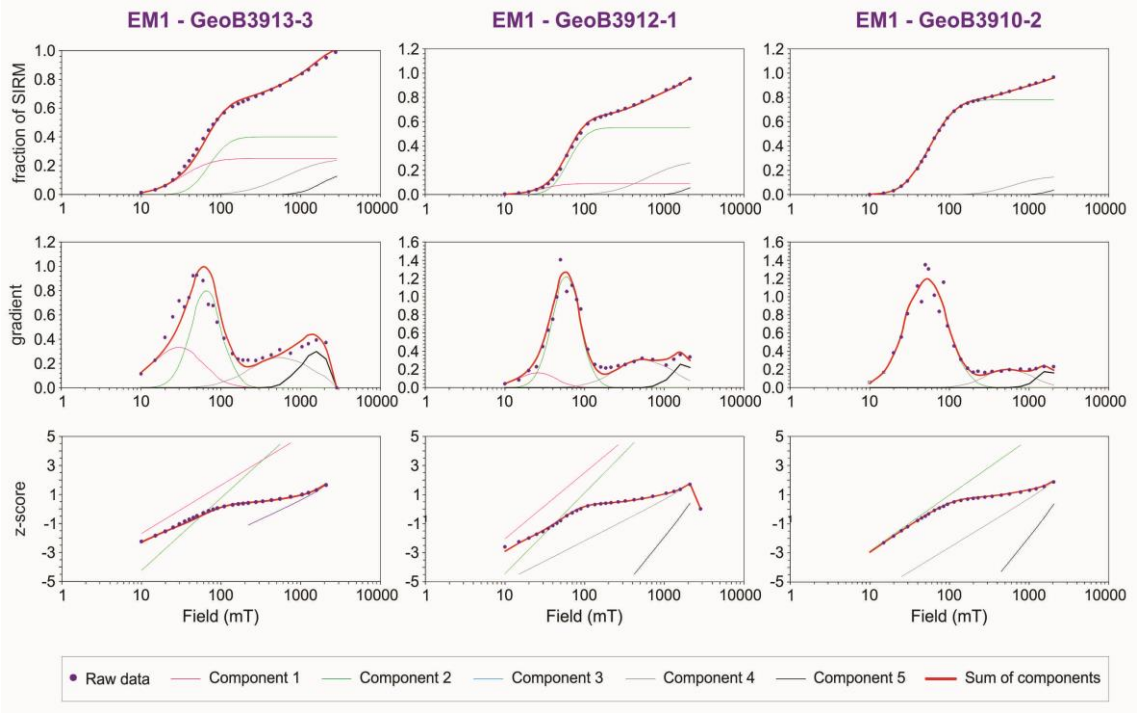

Figure 6.16: IRM component analyses of EM1 (hematite/goethite). Each column corresponds to one core: GeoB3913-3 (left), GeoB3912-1 (middle), GeoB3910-2 (right). Different colors indicate the components needed to fit the sum of the components (red curve). Purple dots corresponds to the IRM acquisition curve from the "synthetic" data. (top row) Linear acquisition plot; (middle row) gradient acquisition plot; and (bottom row) standardized acquisition plot.

For EM2 the softer component 1 ($B_{1/2}$ between ~ 25-32 mT) is present in cores GeoB3913-3 (~35%) and GeoB3910-2 (~6%) but it is absent in core GeoB3912-1. Component 2 contributes to 90% of the SIRM in core GeoB3912-1, and the remaining 10% are made up by component 5 ($B_{1/2}$ ~1500 mT). A component with intermediate hardness, component 3 (blue curve), is present in EM2 and has a contribution of ~52% and ~88% in cores GeoB3913-3 and GeoB3910-2, respectively. The component 4 of EM2 is present only in core GeoB3913-3, but the hardest one is absent. In core GeoB3910-1 the magnetically hard component 5 accounts for ~6% of the SIRM.

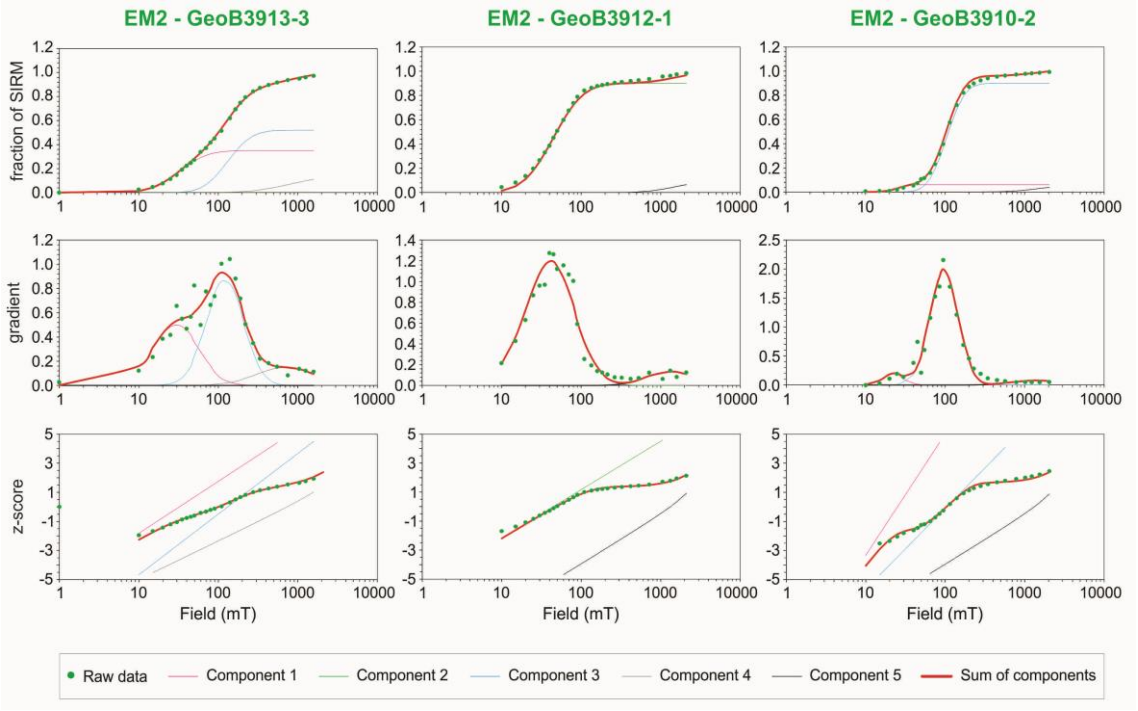

Figure 6.17: IRM component analyses of EM2 ((titano)magnetite). Each column corresponds to one core: GeoB3913-3 (left), GeoB3912-1 (middle), GeoB3910-2 (right). Different colors indicate the components needed to fit the sum of the components (red curve). Green dots corresponds to the IRM acquisition curve from the "synthetic" data. (top row) Linear acquisition plot; (middle row) gradient acquisition plot; and (bottom row) standardized acquisition plot.

EM3 comprises essentially the soft components. Magnetically hard components 4 ($B_{1/2}$ of 795 mT) and 5 ($B_{1/2}$ of 1778 mT) were introduced with very small contributions of 0.5% in core GeoB3912-1, to model the high-coercivity part of the SAP diagram of Kruiver *et al*. (2001). The same was done for core GeoB3913-3, with a contribution of ~3% of a component 4 ($B_{1/2}$ of ~500 mT). These components in EM3 with very low contribution to the total SIRM are interpreted as artefacts from right-skewed distributions as suggested by Egli (2003). The intermediate component 3 is present only in core GeoB3910-2, comprising ~5% of the SIRM with $B_{1/2}$ of ~200 mT. The magnetically soft components are present in EM3 in the three cores with important contributions. Component 2 accounts for 89% of SIRM in EM3 for core GeoB3912-1, ~88% of the SIRM ($B_{1/2}$ ~ 50 mT) for core GeoB3913-3, and ~75% of the SIRM for core GeoB3910-2. Contributions of component 1 vary between ~9% and ~20%.

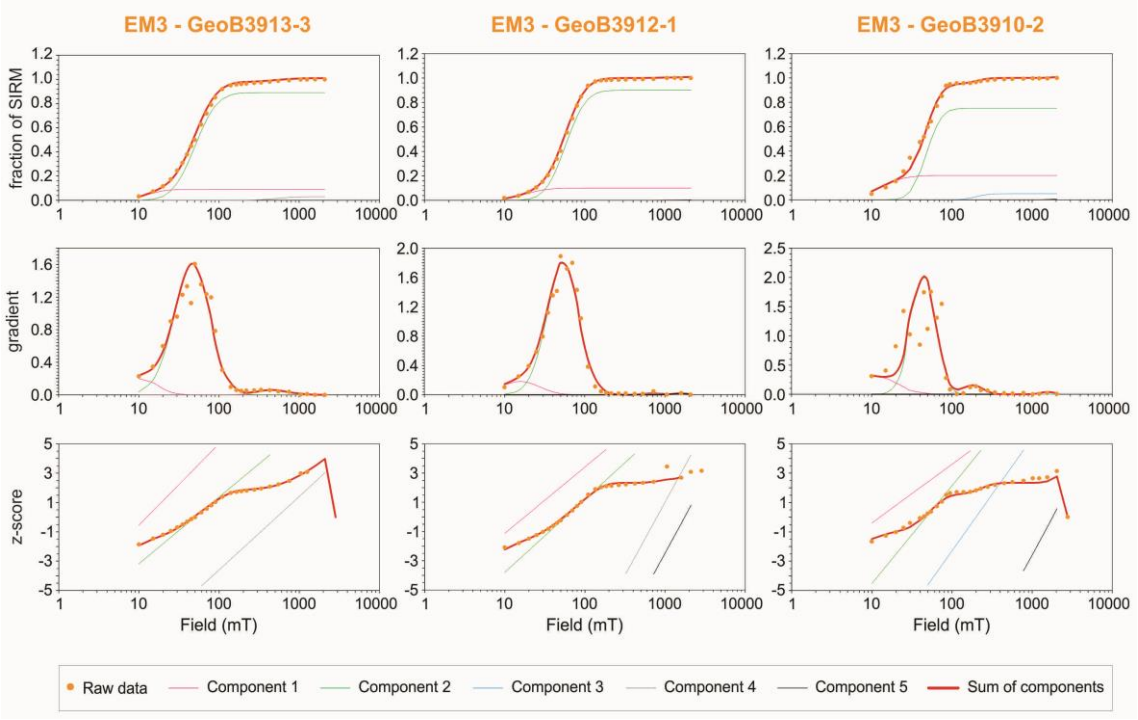

Figure 6.18: IRM component analyses of EM3 (biogenic magnetite). Each column corresponds to one core: GeoB3913-3 (left), GeoB3912-1 (middle), GeoB3910-2 (right). Different colors indicate the components needed to fit the sum of the components (red curve). Orange dots corresponds to the IRM acquisition curve from the "synthetic" data. (top row) Linear acquisition plot; (middle row) gradient acquisition plot; and (bottom row) standardized acquisition plot.

Table 6-2: Parameters from IRM component analysis (Kruiver et al., 2001) of end-members derived by the unmixing.

	IRM Component 1				IRM Component 2				IRM Component 3				IRM Component 4				IRM Component 5			
	Contrib. (%)	SIRM	$B_{1/2}$ (mT)	DP (mT)	Contrib. (%)	SIRM	$B_{1/2}$ (mT)	DP (mT)	Contrib. (%)	SIRM	$B_{1/2}$ (mT)	DP (mT)	Contrib. (%)	SIRM	$B_{1/2}$ (mT)	DP (mT)	Contrib. (%)	SIRM	$B_{1/2}$ (mT)	DP (mT)
GeoB3913-3																				
EM1	23.81	0.25	32.36	0.30	38.10	0.40	70.79	0.20	-	-	-	-	23.81	0.25	630.96	0.40	14.29	0.15	1778.28	0.20
EM2	34.65	0.35	32.36	0.28	-	-	-	-	51.49	0.52	131.83	0.24	13.86	0.14	794.33	0.38	-	-	-	-
EM3	8.91	0.09	12.59	0.18	88.12	0.89	50.12	0.22	-	-	-	-	2.97	0.03	524.81	0.20	-	-	-	-
GeoB3912-1																				
EM1	8.82	0.09	28.18	0.22	53.92	0.55	63.10	0.18	-	-	-	-	27.45	0.28	616.60	0.36	9.80	0.10	1995.26	0.15
EM2	-	-	-	-	90.00	0.90	44.67	0.30	-	-	-	-	-	-	-	-	10.00	0.10	1584.89	0.30
EM3	9.90	0.10	17.78	0.22	89.11	0.90	57.54	0.20	-	-	-	-	0.50	0.01	794.33	0.10	0.50	0.01	1778.28	0.10
GeoB3910-1																				
EM1	-	-	-	-	78.00	0.78	56.23	0.26	-	-	-	-	15.00	0.15	616.60	0.30	7.00	0.07	1995.26	0.15
EM2	5.88	0.06	25.12	0.12	-	-	-	-	88.24	0.90	104.71	0.18	-	-	-	-	5.88	0.06	1584.89	0.30
EM3	19.80	0.20	12.59	0.25	74.26	0.75	47.86	0.15	4.95	0.05	199.53	0.13	-	-	-	-	-	-	-	-

6.5. *Magnetic characterization: hysteresis and low temperature curves*

Hysteresis curves and low temperature measurements were obtained for core GeoB3912-1, and brought some hints about magnetic size and type. We selected three samples along the core that represent sections with different behaviour in the "enviromagnetic" parameters (*Figure 6.3*) and end-members (*Figure 6.14*). *Figure 6.19* shows hysteresis loops corrected for paramagnetic effect for top (G088, 10.5 cm), middle (G093, 321.5 cm) and base (G099, 620 cm) of the core. The dominant end-members in theses intervals are EM3, EM1 and EM2, respectively.

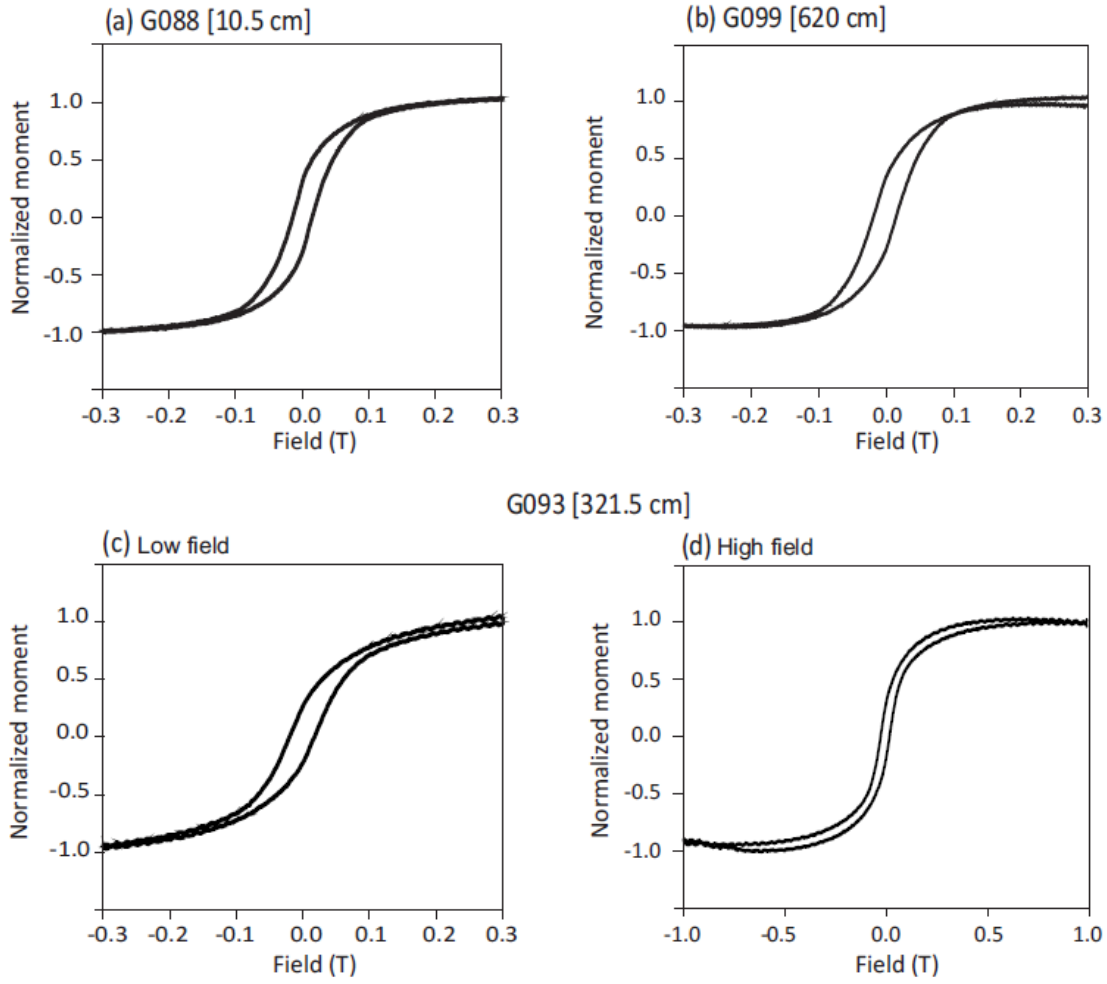

Figure 6.19: Low field (-0.3/0.3T) hysteresis loops for (a) top (b) base and (c) middle, and high field (-1T/1T) hysteresis loop for (d) middle part of core GeoB3912-1.

Low field loops (*Figure 6.19* a, b and c) show narrow waist especially in sample G088. High field loops were performed for all samples, but here we show only the example for sample G093 (middle of the core, *Figure 6.19*d). Loops obtained from induced measurements up/down to

+1/-1 T for our samples saturate fast and do not suggest the presence of highly coercive phases. The high field curve for sample G093 was the only one that exhibited a "wasp-waist" behaviour, suggesting a mixture of magnetic grains with contrasting coercivities (Liu *et al*., 2012). The different coercivities we identified here can be attributed to magnetic grains with distinct sizes or two types of magnetic minerals with contrasting coercivities, like hematite or goethite and magnetite.

Low temperature measurements were obtained for five samples distributed along the core GeoB3912-1: 20, 75, 335, 510.5 and 630 cm. The corresponding ages for these samples are present in the plots (*Figure 6.20*).

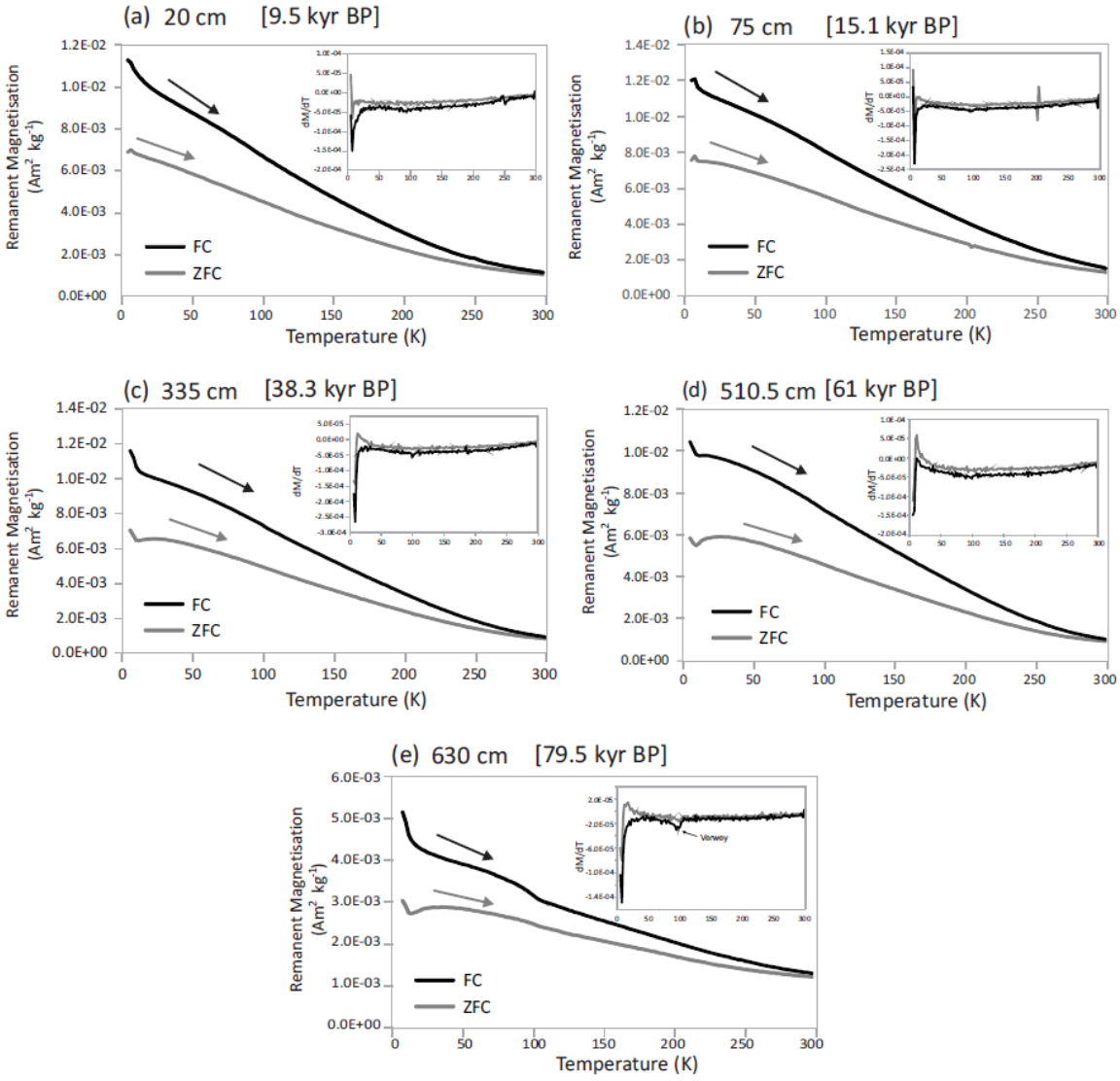

Figure 6.20: Low temperature measurements of samples obtained in intervals with dominant end-member contribution of (a) EM3, (b) EM1 + EM2, (c) EM1, (d) EM1 + EM2 and (e) EM2.

All our samples exhibit ZFC and FC curves that converge at higher temperatures. The convergence between FC and ZFC warming curves was attributed previously to the presence of goethite (Just *et al*., 2012a). Sample 630 cm (EM2) is the only one that shows the Verwey transition at 120 K (*Figure 6.20*). It confirms the presence of (titano)magnetite, inferred before based on IRM acquisition curves (*Figure 6.17*).

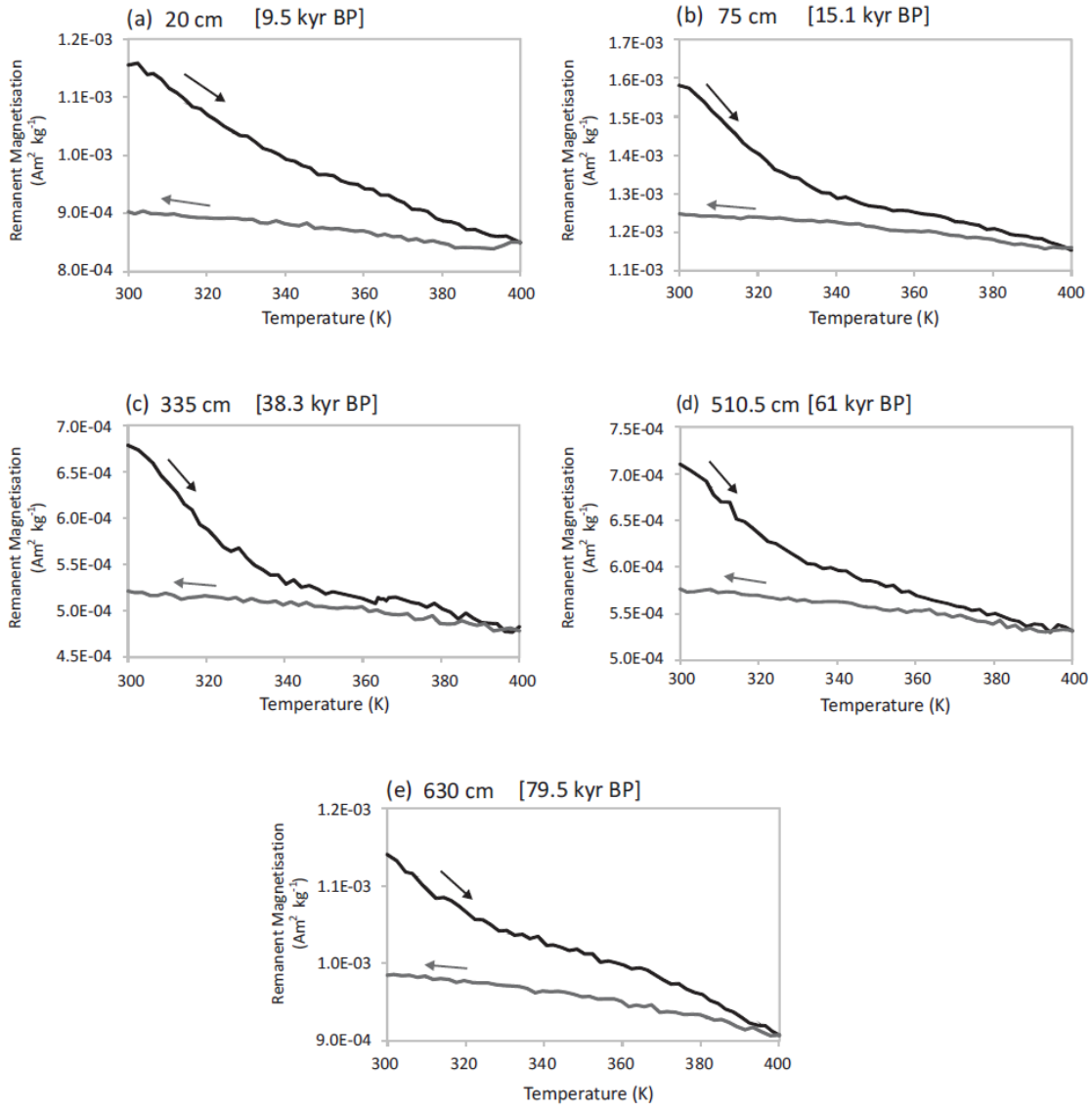

Figure 6.21: High temperature measurements of samples obtained in the intervals with dominant end-member contribution of (a) EM3, (b) EM1 + EM2, (c) EM1, (d) EM1 + EM2 and (e) EM2.

SIRM warming is presented in *Figure 6.21*, with heating between 300 and 400 K (black curve), and cooling back (gray curve). Samples 75, 335 and 510.5 cm (*Figure 6.21*b, c and d) show a

significant loss in magnetization after heating up to about 340 K. The Curie temperature for pure goethite is about 120°C (or 390 K), but in pedogenically formed goethite Al-substitution is quite normal and it would decrease Curie temperature, as well as the presence of water in the structure (Just *et al*., 2012a) explaining the transition temperatures observed. It is important to notice that these samples with sharper lost in magnetization have dominance of EM1 (*Figure 6.14*).

7 DISCUSSION

7.1. Deglacial sea-level and hydrographic control on sediment supply

Magnetic and chemical data for the Holocene contrast with patterns and baseline values recorded during part of the Last Glacial Period (85 up to 12 kyr BP) in our four cores (*Figure 6.1* - *Figure 6.9*). After the onset of Holocene, all indicators of detrital input show a marked decrease, including magnetic susceptibility, HIRM and Fe/Ca, indicating less terrigenous material being delivered to the continental margin. H. W. Arz *et al*. (1999) presented previously element data for core GeoB3911-3 and showed a remarkable diminution of terrigenous input after 11 ka BP. These authors attributed this change to the flooding of riverine systems at high sea-level stand, which retained detrital sediments on the continental shelf. In all cores studied here, there is an increase in S-Ratio parameter during the Holocene, with values higher than 0.96, indicating a clear predominance of low-coercivity phases, *i.e.* magnetite. This increased S-Ratio reflects the presence of SD-magnetite, and suggests the inception of the marine dominance in the margin off NE Brazil. Susceptibility, HIRM and S-Ratio confirm the scenario already described before for NE Brazil margin. However, we observed compositional differences between our cores using some magnetic parameters. For example, IRM_{300mT} increases in cores GeoB3912-1 (*Figure 6.3*), GeoB3911-3 (*Figure 6.4*) and GeoB3910-2 (*Figure 6.5*) during the Holocene (gray curve), suggesting the presence of an additional phase of highly-magnetic material in the eastern cores. This additional phase does not appear in core GeoB3913-3, as we observe from its low values of IRM_{300mT} (< 800 mA/m; *Figure 6.2*a).

Major element ratios were used as a signature for weathering processes in the source regions. The Al/Si ratio tracks weathering intensity, since Al is mostly associated with fine-grained clay minerals, in particular kaolinite, which is product of chemical weathering under wet conditions (Govin *et al*., 2012). Smaller baseline values of Al/Si in the Holocene for cores GeoB3913-3, GeoB3912-1 and GeoB3911-3 indicate the dominance of a dry climate over the continent during this epoch (*Figure 6.6* - *Figure 6.8*). Additional information can be provided by the Fe/K ratio. In marine sediments K is provided by minerals typical from dry regions, such as potassium feldspar or illite (Zabel *et al*., 2001), thus low Fe/K values suggest a decrease in chemical weathering. Mulitza *et al*. (2008) used Fe/K ratio to distinguish between dust and river supply, the high values of this ratio indicating higher riverine input. A drop in Fe/K ratio during the Holocene is observed in cores GeoB3912-1, GeoB3911-3 and GeoB3910-2 (*Figure 6.7* -

Figure 6.9), attesting to the increasingly drier climate in NE Brazil. Crossplots between Ti and K, show much higher values for K in core GeoB3910-2 when compared to the other cores during the Holocene, suggesting drier conditions in the eastern part of NE Brazil, where the continental sources for this core are located (*Figure 7.1*d, bottom panel). Conversely, in core GeoB3913-3, which is sourced from the west, the Fe/K ratio increases up to the middle Holocene and just after that it starts to drop attesting to the complex climate dynamics at the studied region.

Sea level has increased along the NE Brazilian coast by ~120 m after its minimum low-stand that took place in the last glacial period. Such sea-level rise lead to the drowning of river mouths, and consequently limited the sourcing of sediments to the continental shelf (Knoppers *et al*., 1999). Recent studies have delineated changes in the geomorphology of the continental shelf off NE Brazil and revealed important features that mark the coast line in the past and the direction of paleo-channels (e.g. Gomes *et al*., 2014; Vital *et al*., 2010a; Vital *et al*., 2010b). It confirms previous works that indicate continental sediment delivery deeper than today (H. W. Arz *et al*., 1999; Knoppers *et al*., 1999). The geometry of the coast affected directly the debouching of detrital material to the continental slope off NE Brazil by the incised-valley system of Piranhas-Açu River (Vital *et al*., 2010b) and estuary-incised valley system of Apodi-Mossoró River (Vital *et al*., 2010a), being therefore relevant to explain the longitudinal distribution of sediment along the continental margin by the NBC.

In our cores, the high input of magnetite (increase in S-Ratio parameter) reflects the marine influence (*Figure 6.2* - *Figure 6.5*). During the high stand sea-level, sediments that would reach the continental slope and the abyssal plain are transferred northwestward by the NBC. In this configuration, Apodi-Mossoró and Piranhas-Açu rivers would have been the main source of detrital material to cores GeoB3910-2 e GeoB3911-3, and the Jaguaribe river (or occasionally the Parnaíba river) would feed cores GeoB3912-1 and GeoB3913-3. Differences recorded among the cores in the last 12 ka BP are correlated to their longitudinal position along the coast and in consequence to their riverine supply. Low IRM_{300mT} in the westernmost core GeoB3913-3 (*Figure 6.6*), recording the lesser amounts of fine-grained magnetite, is probably associated to a higher degree of chemical weathering on land at least until the middle Holocene. The same would be expected for core GeoB3912-1, if one assumes it has the same source. However, the high IRM_{300mT} values observed in core GeoB3912-1 are more compatible with the input of less coercive material from Apodi-Mossoró and/or Piranhas-Açu River that could have reached core

GeoB3912-1 during that time, but not the westernmost core GeoB3913-3. The magnetic minerals present in the soils of the NE Brazil differs significantly from west, in Parnaíba Basin, to east, in Borborema Province. Journet *et al*. (2014) in a global study for soil mineralogy have shown that coercive magnetic minerals (*i.e.* hematite and goethite) are dominant in the western part of our study area, whilst in the east the prevalence of (titano)magnetite was reported (Archanjo *et al*., 2002; Knesel *et al*., 2011; Trindade *et al*., 2006). The increase in sedimentation rates during the Holocene would be modulated by changes in precipitation over the source areas, and its consequent impact on rivers supply.

In general, EM1 and EM2 are strongly controlled by continental sources. EM1 is composed mainly by a mixture between highly coercive magnetic phases (*i.e.* goethite and hematite) originated from mature soils from humid regions (*Figure 6.20* and *Figure 6.21*). EM2 is composed dominantly by fine-grained low-coearcive pedogenic magnetic phases (*i.e.* magnetite, *Figure 6.20*e). We attributed the third end-member (EM3) to biogenic magnetite, formed *in-situ*.

For the late Holocene there is a clear partition between end-members distributions from west to east. Core GeoB3913-3, the westernmost core, shows a gradual decrease in all magnetic contributions after ~15 kyr BP (*Figure 6.13*). After about 7 kyr BP, EM1 drops to zero and both EM2 and EM3 present even contributions up to almost 3 kyr BP. In core GeoB3912-1 contribution of EM1 also drops significantly at about 7 kyr BP concomitant with a sharp increase in contributions of EM2 and EM3 (Figure 6.14). In this core, EM3 is dominant for the last 10 kyr. In the easternmost core GeoB3910-2, EM1 never reaches zero. EM2 and EM3 show a significant increase in EM2 and EM3 at ~8 kyr BP and ~13 kyr BP, respectively. Differences in the timing of delivery increase in EM2 and EM3 as recorded in cores GeoB3912-1 and GeoB3910-2 may be attributed to the gradual sea-level increase, with the deepest core (GeoB3910-2) experiencing stronger variations in their detrital inputs first. Significant changes recorded in all cores at ~7 kyr BP are likely due to the rapid increase in sea-level recorded globally between 8-7 kyr BP. In core GeoB3912-1, there is a marked inverse correlation between EM2 and EM3, with an increase of EM3 concomitant to a decrease in EM2. This trend suggests an increase in marine sources, as we expect from the high stand sea-level in Holocene (*Figure 5.3*).

7.2. Climate driven sediment pulses, in relation to precipitation

Conditions prevailing during the last glacial period contrasted significantly with those dominating in the Holocene (*e.g.* H. W. Arz *et al*., 1999; Baker *et al*., 2001; Fleming *et al*., 1998). All four marine cores we present here show wetter climate between 85-12 kyr BP in comparison to the Holocene. This is visible from the baseline values of some magnetic and geochemical parameters, which indicate higher terrestrial input (susceptibility, HIRM, Fe/Ca) and intensive weathering (S-Ratio, Fe/K and Fe/κ) during the glacial period (*Figure 6.2* - *Figure 6.9*). Peaks in concentration indicators, such as susceptibility (orange curves) and HIRM (dark blue curves), reflect higher terrigenous input to the continental shelf and slope during HS. The most remarkable changes in magnetic types are observed in parameters that reflect humid conditions on land, like drops in S-Ratio (black curves) and peaks in HIRM (dark blue curves); both suggesting the presence of more coercive magnetic phases, which are formed during weathering (*i.e.* hematite and goethite). In most of HS, both S-Ratio and HIRM peak in the beginning of the events and then drop gradually towards the end, suggesting changes in the weathering processes and a gradual change in the source of sediments during HS. High values of Fe/κ ratio (light green curves) during HS also confirm the presence of antiferrimagnetic minerals (hematite and goethite). It fits the S-Ratio drops mentioned before. IRM_{300mT} values (gray curves) are mirrored by the S-Ratio parameter, showing the expected decrease in magnetite regarding hematite and goethite during the stadials. The grain-size indicator ARM_{100mT}/IRM_{100mT}, does not show coeval changes between the cores during the eight HS recorded here, but it shows smaller values during the Pleistocene in comparison to the Holocene for all cores (pink curves). Core GeoB3913-3 (*Figure 6.2*) exhibits a ARM_{100mT}/IRM_{100mT} increment from the beginning of HS1, whereas in cores GeoB3912-1 (*Figure 6.3*) and GeoB3911-3 (*Figure 6.4*) it starts to increase from the end of HS1, while in core GeoB3910-2 (*Figure 6.5*) it reaches high values after the middle of HS1. Magnetic parameters for core GeoB3911-3 show some signals of dissolution due its high sedimentation rate (*Figure 6.1*), with significant terrigenous input. The expected high values of concentration parameters susceptibility and HIRM show an abrupt decrease towards the end of HS1 and during the YD (orange and dark blue curves). High coercivity magnetic minerals would be expected during these wet events, but S-Ratio increases coevally, suggesting the presence of newly formed fine magnetic minerals (Rowan *et al*., 2009). For the same core, Fe/Ca ratio also shows dissolution of iron towards the end of HS1 and during YD, and the increase in Fe/κ confirms the dissolution

of ferromagnetic iron in these redox layers (*Figure 6.8*). During B-A, the parameters that indicate an increase in the concentration of magnetic minerals peak abruptly and the S-Ratio drops, suggesting humid condition over land (*Figure 6.4*).

Changes in weathering conditions recorded by magnetic indicators were identified also through geochemical proxies. Element data for core GeoB3913-3 exhibit remarkable peaks which are synchronous to HE (*Figure 6.6*). Cores GeoB3913-3 and GeoB3912-2 (*Figure 6.7*) recorded an increase in Al/Si values during HS, suggesting intensified chemical weathering during humid periods (green curves). We observed more prominent peaks in the eastern core (GeoB3912-1) during HS than in those located to the west (GeoB3913-3). This can be related to differences in precipitation regimes from west to east during the Pleistocene, with a more humid climate in the west during the interstadials (GeoB3913-3) and a more contrasted climate to the east (core BeoB3912-1), with drier interstadials and more humid stadials resulting in the stark contrast in the geochemical signals in core GeoB3912-1.

Well-documented wet conditions prevailing over NE Brazil region resulted in significant terrestrial input triggered by increased precipitation during HE (e.g. Arz *et al*., 1998; H. W. Arz *et al*., 1999; Behling *et al*., 2000; Dupont *et al*., 2009; Jennerjahn *et al*., 2004). These changes are the most remarkable climate signature of our records, which show well defined peaks/drops during Heinrich Stadials (HS). Changes in detrital sediments that reach the continental margin off NE Brazil has been recorded previously for some of the cores presented here. Arz *et al*. (1998), for example, related peaks in Fe/Ca ratio for core GeoB3912-1 to the Heinrich Events (HE) and attributed higher terrigenous input to humid conditions in the continent and resedimentation processes related to short-term sea-level changes. Still for core GeoB3912-1, Jennerjahn *et al*. (2004) found an asynchronicity between marine and terrestrial signals during the cold events of the North Atlantic, based on a multiproxy record. Element data for core GeoB3911-3 also showed higher terrigenous sediment influx caused by enhanced precipitation and increased riverine input (Figure 6.8; H. W. Arz *et al*., 1999). Jaeschke *et al*. (2007) identified peaks in detrital sediments using Ti/Ca ratio for core GeoB3910-1, which they related to HE. In paleoclimate studies, Ti/Al ratio is associated with wind intensity versus riverine supply (Itambi *et al*., 2009); coarse sediments are enriched in Ti, and Al is mostly associated with fine-particle clay minerals (Govin *et al*., 2012). In NE Brazil, the winds blow from NE, following the north-south displacement of the ITCZ, and especially during the HS the trade winds are remarkably intensified (Weldeab *et al*., 2006). Even with an intensified ITCZ over

NE Brazil, riverine supply seems to be more important during HS, due to the concurrent humid conditions on land. In core GeoB3912-1 (*Figure 6.7*), Ti/Al increases during HS as expected during wet stadials, but in core GeoB3911-3 only slight changes were detected (*Figure 6.8*). The most remarkable change in Ti/Al ratio was observed in core GeoB3913-3, at about 54 ka BP. At this time, Ti/Al values increase significantly to higher baseline values. We attributed this abrupt increase that lasted up to the Holocene to a decrease in the intensity of trade winds.

Differences between stadials and interstadials are noticeable in downcore plots, but we show here some crossplots for our four cores using magnetic and geochemical parameters (*Figure 7.1*) aiming to make it clearer. Using two magnetic parameters (S-Ratio versus susceptibility; *Figure 7.1*a) it is possible to see the increase in concentration of magnetic minerals (high susceptibility) concurrent with the increment of low coercive phases (low S-Ratio). In tropical and subtropical regions, where organic carbon content and moisture availability are generally related, the abundance of goethite over hematite can be used as an indicator of higher precipitation, whereas low values imply drier/warmer conditions (Abrajevitch *et al*., 2009). Jennerjahn *et al*. (2004) found this correlation between organic carbon and humid conditions during HE in NE Brazil. Thus, during the Pleistocene, a high amount of coercive magnetic minerals in periods of enhanced precipitation can be associated to soil formation, with oxidation of magnetite and formation of hematite and goethite. Crossplotting geochemical and magnetic parameters Fe/Ca and HIRM, we observe a linear correlation, reflecting an increase in detrital influx from interstadials to stadials (*Figure 7.1*, middle panels). HIRM for the western core GeoB3913-3 show the highest values, suggesting higher contribution of oxidized phases from the Parnaíba Basin (*Figure 7.1*a). Note that this scenario requires that during stadials at least part of the sediments sourcing core GeoB3913-3 to be provided by the Parnaiba river located to the west of the sampling site, and consequently implies either a reversal of the North Brazilian Current (NBC) or a significant reduction in its intensity locally.

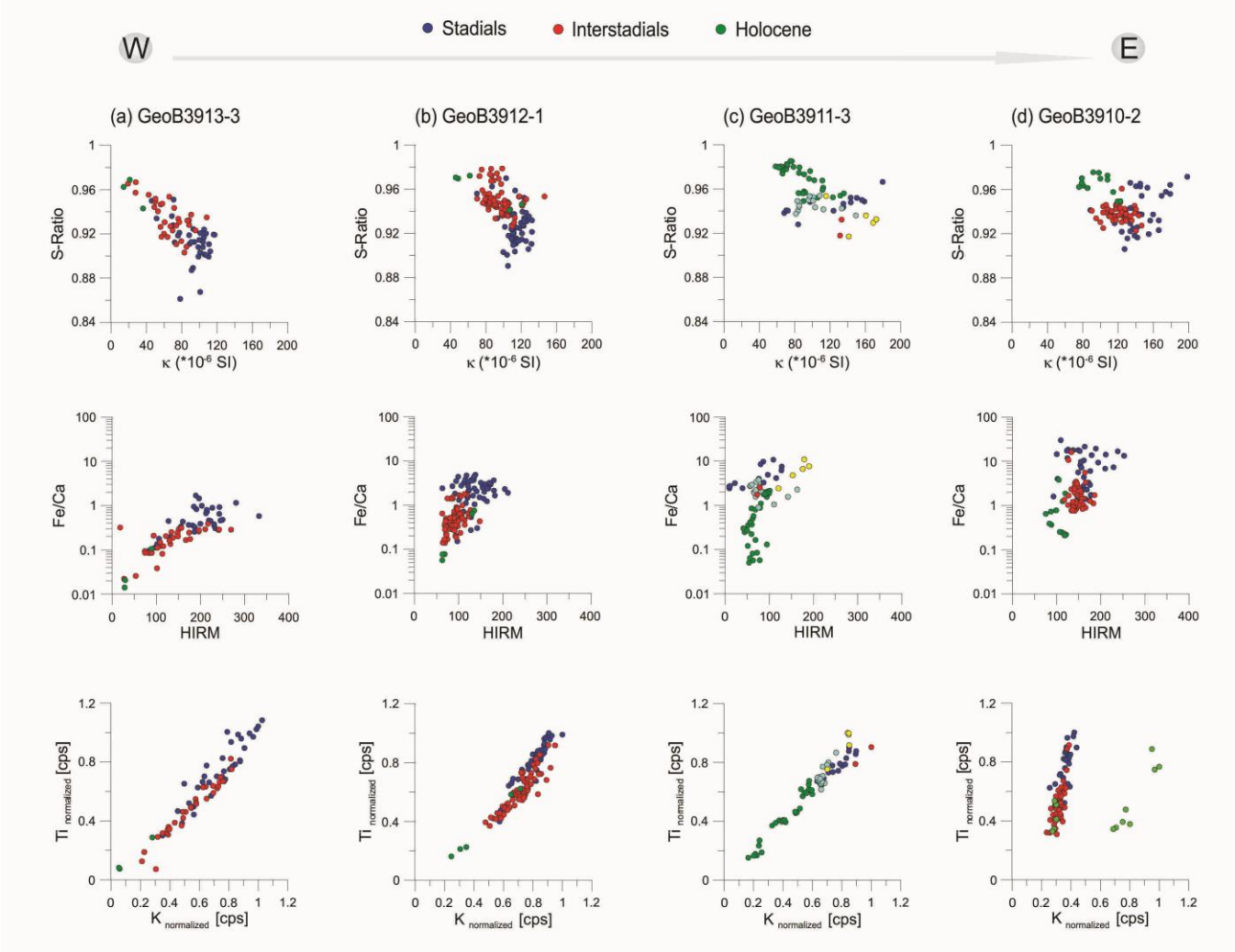

Figure 7.1: Crossplots using magnetic and geochemical parameters for the different cores: (a) GeoB3913-3, (b) GeoB3912-1, (c) GeoB3911-3, and (d) GeoB3910-2.

The increase in precipitation over NE Brazil during HE is widely accepted and also its link to the enhanced terrigenous input. This is clearly demonstrated by the magnetic parameters reported here. The end-member analysis, just like magnetic and geochemical proxies, also indicates drier conditions during the Holocene in the margin of NE Brazil. Peaks in high-coercive EM1 component during HS in cores GeoB3913-3 (*Figure 6.13*) and GeoB3912-1 (*Figure 6.14*) are remarkable, especially for core GeoB3912-1, where these peaks are very sharp and reinforce the presence of low-coercive pedogenic magnetite during humid events. In core GeoB3913-3, the same component is absent during the YD, as expected from the rock magnetic parameters S-Ratio and HIRM for the same interval (*Figure 6.2*). Core GeoB3910-2 shows a very different behaviour in terms of distribution of end-members along the HS. EM1 decreases

for HS1, HS4 and HS5, and EM2 becomes important at the same intervals (*Figure 6.15*). The high contribution of EM2 during HS4 and HS5 suggests that the transport of (titano)magnetite from the Borborema Province was more important during these events. They are coeval with a sharp increase in S-Ratio (*Figure 6.5*), that is compatible with the dominant presence of magnetite and represents an enrichment of a distinct phase during stadials, when compared with the coeval peaks in high-coercive EM1 observed for the other cores. In addition, core GeoB3910-2 shows a contrasting behaviour for HS2 and HS3 when compared to HS1, HS4 and HS5. Suppression of HS2 and HS3 records has also been marked in other proxies in the same region and elsewhere ($\delta^{18}O$ in Hulu cave, Cariaco basin reflectance), and has been attributed to periods of lower precipitation during H2 and H3, which correspond to periods of low austral autumn insolation (Wang *et al*., 2004). Another possibility is that HS2 and HS3 represent periods of dislocation of the precipitation dipole between Amazon and NE Brazil (Cheng *et al*., 2013), when HS would correspond to drier intervals over the eastern sectors of NE Brazil. Note that HS for cores GeoB3913-3 and GeoB3912-1, located in central and western sectors of the studied transect do not show significant differences between HS2 and HS3, and HS1, HS4 and HS5 (*Figure 6.13* and *Figure 6.14*).

7.3. The W-E source area pattern

The complex circulation pattern in the western equatorial Atlantic is a response to surface and intermediated waters exchanges between austral and boreal hemispheres, which play an important role in the sea surface temperature (SST) gradient throughout the equator. Droughts in Amazonia and NE Brazil, for instance, have been linked to anomalously warm surface waters in the tropical North Atlantic (Cruz *et al*., 2009). Likewise, humid periods over NE Brazil during HE have been connected to the southward migration of the ITCZ (e.g. Arz *et al*., 1998; H. W. Arz *et al*., 1999; Behling *et al*., 2000; Dupont *et al*., 2009; Jennerjahn *et al*., 2004; Wang *et al*., 2004). This connection between North Atlantic and tropical Atlantic waters, has been also observed in climate simulations, which suggest that the AMOC almost collapsed during fresh water input over the North Atlantic Ocean (Kageyama *et al*., 2013a) and could also cause a reversion of the NBC (Chiang *et al*., 2008). Considering a change in direction of NBC, a difference in sediment sources feeding the continental shelf would be expected. Yet, the magnetic and geochemical parameters reported here do not corroborate a NBC inversion at least

for the last 85 kyr BP. Our cores show some differences in geochemical and magnetic signals along the coast (*Figure 7.2*), but we attribute these longitudinal dissimilarities to the weathering degree of different sources associated to the W-E precipitation patterns. Variation in concentration of magnetic minerals from west to east are clear in the crossplots using mean values for S-Ratio versus susceptibility during Holocene, stadials and interstadials (*Figure 7.2*a). This plot shows higher availability of ferrimagnetic minerals (*i.e.* magnetite, with high susceptibility values) in the eastern cores; and smaller amounts of this magnetic mineral further west. On this plot, the separation between wet (stadials) and dry (interstadials) trends amid Holocene and Pleistocene epochs is quite clear. S-Ratio values suggest that the oscillation between periods when magnetite dominates and periods when more coercive phases (hematite and goethite) dominate is likely controlled by the climate conditions over the continental source basins rather than by core location. During humid periods (HS) the entire margin off NE Brazil was affected in the same way by increased precipitation over the continent, with only slight differences (*Figure 7.2*a). Blue symbols, which show samples from stadials, exhibit similar mean values for all the cores. Conversely, during interstadials or in the Holocene epoch (red and green symbols, respectively), mean values for different cores plot more apart from each other. This suggests that during HS, changes in the W-E sediment deposition were more similar along the coast than during interstadials and the Holocene.

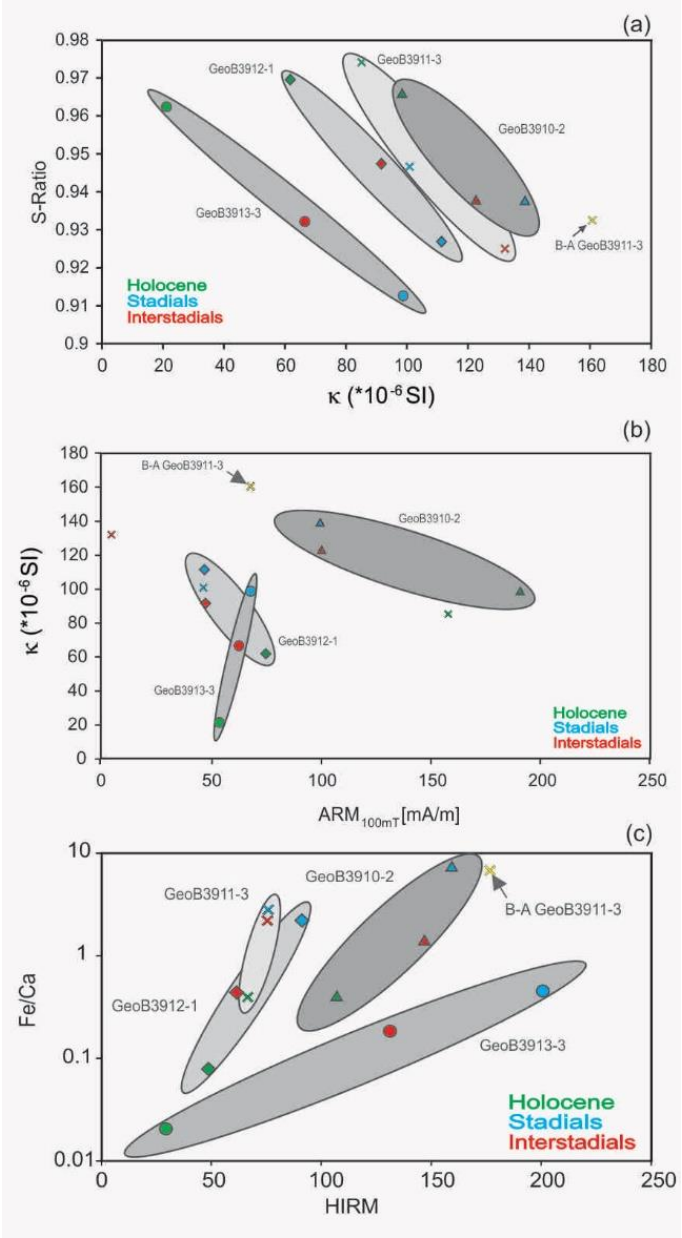

Figure 7.2: Crossplots using the mean value of magnetic and geochemical parameters for wet (stadials, blue) and dry (interstadials, red) condition in NE Brazil, and during Holocene (green). Yellow dots represent Bølling-Allerød (B-A) oscillations.

The dominance of fine-grained magnetite in the eastern cores is also evident, based on the parameter ARM_{100mT} (*Figure 7.2*b). High values of ARM_{100mT} in core GeoB3910-2 suggest the dominance of titano(magnetite), probably related to the source areas in the Borborema Province, whilst in the west there is a clear dominance of coercive phases marked by lower values of parameters such as susceptibility and ARM_{100mT}. Studies in soils and bedrocks from

Parnaíba Basin (Journet *et al*., 2014) and Borborema Province (Archanjo *et al*., 2002; Knesel *et al*., 2011) suggest the presence of more coercive phases in the west and less coercive phases to the east. This tendency is further reinforced by recently published magnetic susceptibility and geochemistry data of a marine sediment core collected to the west of the Parnaíba River's mouth (Nace *et al*., 2014). In this study, core CDH-86 systematically shows high values of Ti/Ca associated to low values of susceptibility for the last 120 ka BP, and the authors attribute this pattern to the prevalence of high coercive magnetic phases hematite and goethite sourced from the Parnaíba Basin. We observed peaks of susceptibility in our four cores during stadials (*Figure 6.2* - *Figure 6.5*, orange curves), but it is remarkable that these peaks are less intense in the cores collected to the west (*Figure 7.2*a and 7.2b). The fact that Nace ey al. (2014) did not report a more detailed magnetic study prevents us to go further in such a comparison. Still, considering gradually higher values of susceptibility and S-Ratio from west to east, we suggest a change in the main magnetic phase being sourced from the continent.

The main W-E difference among the end-members in our three cores is their contribution during HS. In western cores GeoB3913-3 and GeoB3912-1, EM1 peaks during HS, whilst in core GeoB3910-2 it drops during HS1, HS4 and HS5 (*Figure 6.15*). During HS2 and HS3 no significant changes are observed between end-member contributions on this core. Sharp peaks of EM1 along core GeoB3912-1 may be a response to intense precipitation over NE Brazil, as suggested before (Jennerjahn *et al*., 2004). The absence of peaks in H2 and H3 along core GeoB3910-2 could be a reflex of the different sourcing in this point. H2 and H3 are typically less intense and shorter events, and in this way not necessarily affected the river catchment area significantly to provide a detectable increase in sediment supply in the eastern region.

7.3. Climate and paleoceanographic models

Enhanced precipitation over NE Brazil has been previously attributed to a southward migration of the ITCZ during cold periods recorded in the North Atlantic Ocean. Kageyama *et al*. (2013a) simulating the input of freshwater in North Atlantic, obtained a consistent response to increased precipitation over tropical Atlantic, related to southward migrations of the ITCZ. The authors based the simulation on six different models, all considering ocean-atmosphere interaction with a resolution between 1^{o}-3^{o}, and most of them accounting for free-ocean surface. Analysing three glacial coupled atmosphere-ocean simulations, Kageyama *et al*. (2009) found a reduction from

18 Sv to 15 Sv in the AMOC after a decrease of 0.08 Sv in the flux of fresh water into the North Atlantic Ocean. Model results are corroborated by geochemical data obtained on foraminifer shells from core GeoB3911-3 by Weldeab *et al*. (2006). These authors show that NBC play a crucial role in the inter-hemispheric heat and salinity exchange. This large current (~300 km) could have played less important role during the last glacial period, enabling the deposition of terrigenous material far from the coast, in the continental slope (H. W. Arz *et al*., 1999). Thus, stadials, which are periods with clear prevalence of terrigenous input over the continental slope off NE Brazil, are coincident with AMOC weakness, and consequently, with a decrease in the intensity of the NBC. Chiang *et al*. (2008), by their turn, proposes that the weakness of the AMOC would promote an abrupt transition in the North tropical Atlantic, reversing the NBC.

Recently, Liedtke (2014) proposed a series of circulation models using the Regional Ocean Model System (ROMS; Shchepetkin, 2003; Shchepetkin and McWilliams, 2005). ROMS is a 3D ocean model that solves the free-surface hydrostatic equations on vertical coordinates that follow the bottom topography (Shchepetkin and McWilliams, 2005). Liedtke (2014) ran four models off NE Brazil: Models 1 and 2 simulate the present-day conditions using wind shear models CODES and Trace21ka project, respectively; and models 3 and 4 simulated paleoceanographic conditions during Heinrich Events (16,000 years BP) and are therefore of great interest to our work. Both used wind stress models from Trace21ka project (50 years average, monthly) but model 4 also used a different shoreline, equivalent to a 120 m sea-level drop to emulate glacial times (e.g. Knoppers *et al*., 1999). Oceanographic currents and SST outputs from models 1 and 2 match present-day observations attesting to the robustness of the models. These models show the South Equatorial Current (SEC) along the equator and its countercurrent at around 5° N with higher intensity in July (*Figure 7.3*a). The North Brazilian current (NBC) runs along the coast from southeast to northwest. Model 2 shows current rings around the Ceará Rise that were described previously by Fratantoni and Richardson (2006) and Wilson *et al*. (2011). Interestingly, for 16,000 years ago there is a significant northward shift of the SEC (*Figure 7.3*b). In January simulations, it runs at around 4° N, hits the coast at longitude 44° W close to the Parnaiba river mouth, and strongly influences the intensity of the NBC. Right to the east of the Parnaiba mouth, the intensity of the NBC is significantly reduced or, at some points, vectors show reversed directions (flow lines point to the east and southeast). In the present day condition, the SEC is much weaker. It does not affect the NBC, which runs towards the northwest until 56° W.

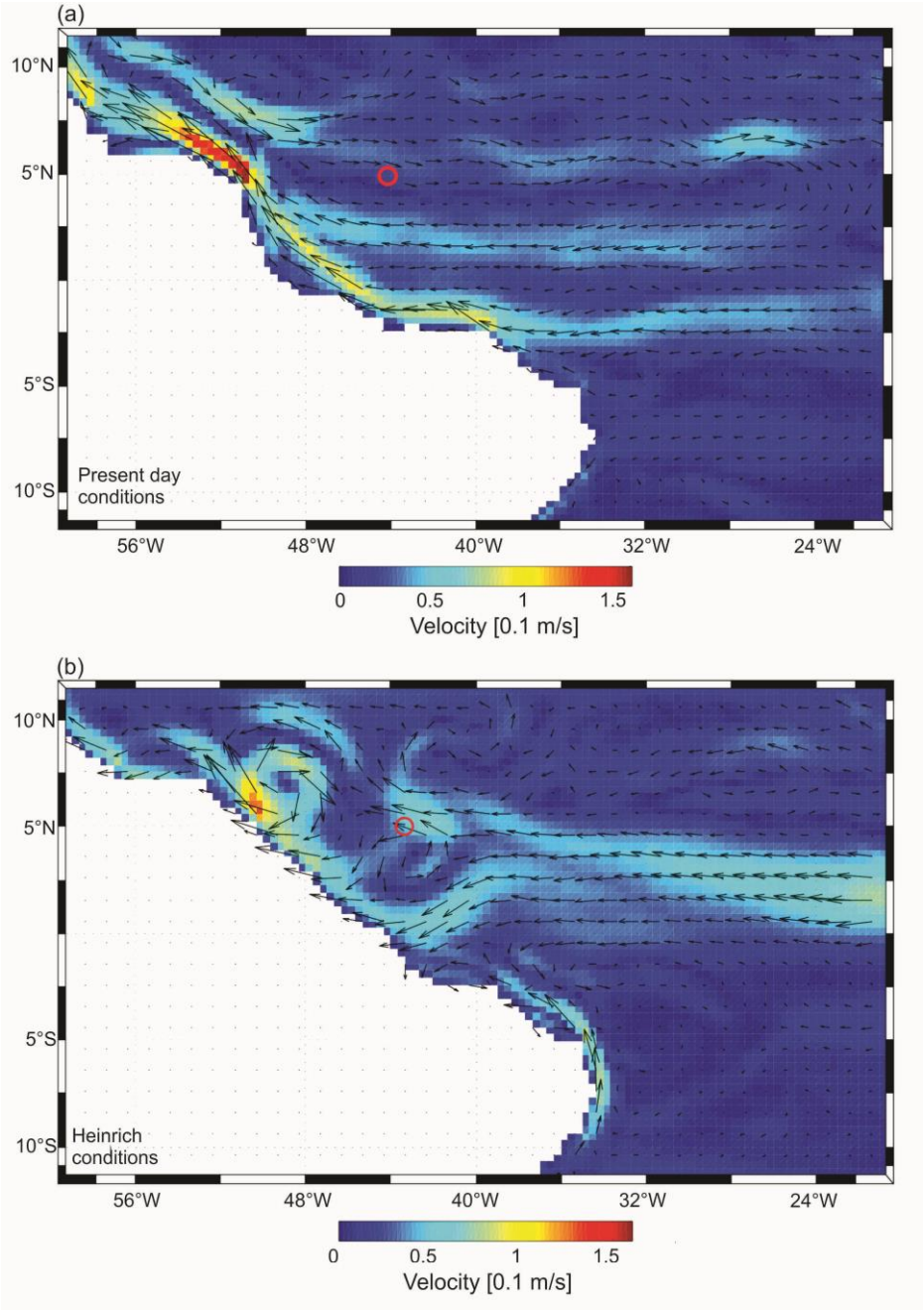

Figure 7.3: Flow velocities along the Equatorial Atlantic off North and Northeast Brazil from Liedtke (2014). (a) simulation 1 for July, (b) simulation 4 for January. Red circle indicates the Ceará Rise.

The inflow of highly coercitive magnetic material sourced by the Parnaiba basin to cores GeoB3913-3 and GeoB3912-1 during Heinrich Events is hard to explain with the present-day

configuration of oceanographic currents, and the high strength of the NBC. Conversely, with the northward shift of SEC predicted by Lietdke (2014) models during Heinrich Events (*Figure 7.3*b), that severely affect the strength of the NBC and eventually promotes a local flow inversion right to the east of the Parnaíba mouth, sediments from the Parnaíba river can effectively reach the sites where cores GeoB3913-3 and GeoB3912-1 were sampled. This configuration also explains the contrasting results observed between these cores and cores GeoB3910-2 and GeoB3911-3, where stadials H1, H4 and H5 are marked by a sudden increase in low-coercivity grains (EM2) sourced by the local rivers or from sources situated in the east and transported westward by the NBC.

8 FINAL CONSIDERATIONS

This thesis describes the longitudinal sediment transport along the margin off NE Brazil for the last 85 kyr BP using environmental magnetism parameters and major element ratios (Fe/Ca, Al/Si, Fe/K, Ti/Al) for four marine cores (GeoB3913-3, geoB3912-1, GeoB3910-2 and GeoB3911-3). These data contribute to a better comprehension about sediment pathways and sources in the margin off NE Brazil, especially concerning differences between abrupt climate events (*i.e.* HE) and interstadials. End-member analysis based on IRM acquisition curves helped in the source sediment study. The models generated from the end-member analysis, resulting only from IRM acquisition curves, require additional substantiation from a detailed magnetic characterization at strategic depths. To support the interpretation, a magnetic characterization using hysteresis and low temperature curves was performed for core GeoB3912-1at strategic depths. The analysis performed here is hindered by the lack of detailed magnetic studies in the potential sources, a study that was out of the scope of the thesis. Magnetic data from sediment sources in Parnaíba Basin and Borborema Province, would be key to compare with the marine sediments from the continental margin. In a broader sense, reference magnetic data, especially IRM and low temperature curves, from soils formed under different climatic conditions in North and NE Brazil would help significantly in improving the interpretation of marine records from adjacent ocean basins.

The interpretation of the data was made in the light of previously published data and climate models for the western tropical Atlantic. Our results suggest a differential deposition of magnetic minerals along the coast, with highly coercive phases (hematite and goethite) further west, and gradually softer phases (like titanomagnetite) to the east. We attributed this difference mainly to differential oxidation over land, but secondarily we suggest a transport of coercive material from W-E during the stadials, caused by the weakness of NBC and possible changes in the coastal currents. Complete XRF scanning along core GeoB3910-2 is missing and could eventually help to support the interpretation suggested here. In addition, a further comprehension about the longitudinal sediment transport along the margin off NE Brazil, requires the study of magnetic and geochemical proxies along cores collected in an W-E transect wider than that studied here. Ideally, this transect would extend from the Parnaíba River mouth down to the coast east of Rio Grande do Norte State, where the SEC splays into the N-S Brazil Current and NW-SE NBC (Figure 5.1). Isotopic data (*i.e.* Sm/Nd and Rb/Sr) from the

continental shelf and from the mouth of the Parnaíba, Jaguaribe, Apodi-Mossoró and Piranhas-Açu rivers could bring new hints about sediment transport and sources, and the influence of the climate on the pathways and weathering on land. It is important to track sources from east, that nowadays transport sediment westward by NBC, especially during July, when this current is stronger due the northward migration of the ITCZ.

Nowadays, the main unsolved problem on the margin off NE Brazil concerns the configuration of the North Brazilian Current (NBC) during the abrupt events that took place during the last glacial. In this thesis, we attempted to address this problem and showed significant variations for a rather small range of longitudes along the coast off NE Brazil which depend on climatic changes on land and on the strength of oceanic currents. Additional magnetic and geochemical data jointly with climate simulations, that consider a set of boundary conditions that permit to understand the fluctuations on the AMOC (*i.e.* fresh water input in North Atlantic), evaporation and southward migration of the ITCZ (*i.e.* ocean-atmosphere interaction), sea-level changes, would be necessary to bring new information on this topic. High-resolution models and more paleoclimate records distributed along a wider longitudinal range would certainly improve our understanding about water exchange between the two hemispheres and help in understanding the mechanisms that control climate change on this region.

9 REFERENCES

Abrajevitch, A., der Voo, R.V., Rea, D.K., 2009. Variations in relative abundances of goethite and hematite in Bengal Fan sediments: Climatic vs. diagenetic signals. Marine Geology 267, 191-206.

Alley, R.B., 2000. The Younger Dryas cold interval as viewed from central Greenland. Quaternary Science Reviews 19, 213-226.

ANA, N.W.A.o.B.-. 2010. Termo de Referência Piranhas-Açu - versão aprovada pelo comite.

ANA, N.W.A.o.B.-. 2014. Região Hidrográfica do Parnaíba.

Archanjo, C.J., Trindade, R., Bouchez, J.L., Ernesto, M., 2002. Granite fabrics and regional-scale strain partitioning in the Serido´ belt (Borborema Province, NE Brazil). Tectonics 21.

Arz, H., Pätzold, J., Wefer, G., 1999. The deglacial history of the western tropical Atlantic as inferred from high resolution stable isotope records off northeastern Brazil. Earth and Planetary Science Letters 167, 105-117.

Arz, H.W., Pätzold, J., Wefer, G., 1998. Correlated Millennial-Scale Changes in Surface Hydrography Terrigenous Sediment Yield Inferred from Last-Glacial Marine Deposits off Northeastern Brazil. Quaternary Research 50, 157-166.

Arz, H.W., Pätzold, J., Wefer, G., 1999. Climate changes during the last deglaciation recorded in sediment cores from the northeastern Brazilian continental Margin. Geo-Marine Letters 19, 209-218.

Baker, P.A., Seltzer, G.O., Fritz, S.C., Dunbar, R.B., Grove, M.J., Tapia, P.M., Cross, S.L., Rowe, H.D., Broda, J.P., 2001. The history of South American tropical precipitation for the past 25,000 years. Science 291, 640-643.

Behling, H., Arz, H., Pa¨tzold, J., Wefer, G., 2000. Late Quaternary vegetational and climate dynamics in northeastern Brazil, inferences from marine core GeoB 3104-1. Quaternary Science Reviews 19, 981-994.

Bloemendal, J., King, J.W., Hall, F.R., Doh, S.-J., 1992. Rock Magnetism of Late Neogene and Pleistocene Deep-Sea Sediments: Relationship of Sediment Source, Diagenetic Processes, and Sediment Lithology. Journal of Geophysical Research 97, 4361-4375.

Blunier, T., Brook, E.J., 2001. Timing of millennial-scale climate change in Antarctica and Greenland during the last glacial period. Science 291, 109-112.

Bond, G.C., Broecker, W.S., Johnsen, S., McManus, J.F., Labeyrie, L., Jouzel, J., Bonani, G., 1993. Correlations between climate records from North Atlantic sediments and Greenland ice. Nature 365, 143-147.

Bond, G.C., Lotti, R., 1995. Iceberg Discharges into the North Atlantic on Millenium Time Scales During the Last Glaciation. Science 267, 1005-1010.

Broecker, W.S., 1998. Paleocean circulation during the last glaciation: A bipolar seesaw? Paleoceanographic currents 13, 119-121.

Broecker, W.S., Denton, G.H., Edwards, R.L., Cheng, H., Alley, R.B., Putnam, A.E., 2010. Putting the Younger Dryas cold event into context. Quaternary Science Reviews 29, 1078-1081.

Carlson, A.E., 2013. PALEOCLIMATE | The Younger Dryas Climate Event, in: Elias, S.A. (Ed.), Encyclopedia of Quaternary Science, 2nd ed, pp. 126-134.

Chang, L., Roberts, A.P., Rowan, C.J., Tang, Y., Pruner, P., Chen, Q., Horng, C.-S., 2009. Low-temperature magnetic properties of greigite (Fe3S4). Geochemistry, Geophysics, Geosystems 10, n/a-n/a.

Cheng, H., Sinha, A., Cruz, F.W., Wang, X., Edwards, R.L., d'Horta, F.M., Ribas, C.C., Vuille, M., Stott, L.D., Auler, A.S., 2013. Climate change patterns in Amazonia and biodiversity. Nature communications 4, 1411.

Chiang, J.C.H., Cheng, W., Bitz, C.M., 2008. Fast teleconnections to the tropical Atlantic sector from Atlantic thermohaline adjustment. Geophysical Research Letters 35, n/a-n/a.

Chiessi, C.M., Mulitza, S., Paul, A., Pätzold, J., Groeneveld, J., Wefer, G., 2008. South Atlantic interocean exchange as the trigger for the Bølling warm event. Geology 36, 919.

Cruz, F.W., Vuille, M., Burns, S.J., Wang, X., Cheng, H., Werner, M., Edwards, R.L., Karmann, I., Auler, A.S., Nguyen, H., 2009. Orbitally driven east–west antiphasing of South American precipitation. Nature Geoscience 2, 1-5.

Day, R., Fuller, M., Schmidt, V.A., 1977. Hysteresis properties of titanomagnetites: grain size and compositional dependence. . Physics of the Earth and Planetary Interiors 13, 260-267.

Dias, F.J.S., Castro, B.M., Lacerda, L.D., 2013. Continental shelf water masses off the Jaguaribe River (4S), northeastern Brazil. Continental Shelf Research 66, 123-135.

Dunlop, D.J., 2002. Theory and application of the Day plot (Mrs/Ms versus Hcr/Hc) 1. Theoretical curves and tests using titanomagnetite data. Journal of Geophysical Research 107.

Dunlop, D.J., Özdemir, Ö., 1997. Rock Magnetism, Fundamentals and Frontiers, Cambridge.

Dupont, L.M., Schlütz, F., Ewah, C.T., Jennerjahn, T.C., Paul, A., Behling, H., 2009. Two-step vegetation response to enhanced precipitation in Northeast Brazil during Heinrich event 1. Global Change Biology 16, 1647-1660.

Egli, R., 2003. Analysis of the field dependence of remanent magnetization curves. Journal of Geophysical Research 108.

Egli, R., 2004. Characterization of individual rock magnetic components by analysis of remanence curves. 3. Bacterial magnetite and natural processes in lakes. Physics and Chemistry of the Earth, Parts A/B/C 29, 869-884.

Evans, M.E., Heller, F., 2003. Environmental Magnetism Principles and Applications of Enviromagnetics. Academic Press, US.

Fairbanks, R.G., 1989. A 17,000-year glacio-eustatic sea level record: influence of glacial melting rates on the Younger Dryas event and deep-ocean circulation. Nature 342, 637-642.
Fischer, G., Arz, H., Baschek, B., Bassek, D., Costa, E., Dierssen, H., Deeken, A., Diekamp, V., Eichner, C., Engelbrecht, I., Elmeking, K., Figueiredo, A., Flechsenhaar, K., Frederichs, T., Freesemalln, A., Gartemicht, U., Herz, M.v., Hübscher, C., Karwath, B., Kasten, S., KinkeI, H., Kölling, M., Miesner, I., Ratmeyer, V., Schlünz, B., Schneider, R., Schmieder, F., Ruhland, G., M., Z., 1996. Report and preliminary results of Meteor cruise M 34/4,

Recife - Bridgetown, 19.3.-15.4.1996. Berichte, Fachbereich Geowissenschaften, Universität Bremen 80, 105 pp.
Fleming, K., Johnston, P., Zwartz, D., Yokoyama, Y., Lambeck, K., Chappell, J., 1998. Refining the eustatic sea-level curve since the Last Glacial Maximum using far- and intermediate-field sites. Earth and Planetary Science Letters 163, 327-342.
Fratantoni, D.M., Richardson, P.L., 2006. The Evolution and Demise of North Brazil Current Rings. Journal of Physical Oceanography 36, 1241-1264.
Garreaud, R.D., Vuille, M., Compagnucci, R., Marengo, J., 2009. Present-day South American climate. Palaeogeography, Palaeoclimatology, Palaeoecology 281, 180-195.
Gatto, L.C.S., Rivas, M.P., Fortunato, F.F., Filho, A.L.S., Oliveira, F.C., Cunha, R.C.M.B., Boas, J.H.V., Pinto, G.C.V.C., Sokolonski, H.H., 1999. Diagnóstico ambiental da Bacia do Jaguaribe.
Geiss, C.E., Egli, R., Zanner, C.W., 2008. Direct estimates of pedogenic magnetite as a tool to reconstruct past climates from buried soils. Journal of Geophysical Research 113.
Gillett, N.P., Kell, T.D., Jones, P.D., 2006. Regional climate impacts of the Southern Annular Mode. Geophysical Research Letters 33.
Gomes, M.P., Vital, H., 2010. Revisão da compartimentação geomorfológica da Plataforma Continental Norte do Rio Grande do Norte, Brasil. Revista Brasileira de Geociências 40, 321-329.
Gomes, M.P., Vital, H., Bezerra, F.H.R., de Castro, D.L., Macedo, J.W.d.P., 2014. The interplay between structural inheritance and morphology in the Equatorial Continental Shelf of Brazil. Marine Geology 355, 150-161.
Govin, A., Holzwarth, U., Heslop, D., Ford Keeling, L., Zabel, M., Mulitza, S., Collins, J.A., Chiessi, C.M., 2012. Distribution of major elements in Atlantic surface sediments (36°N-49°S): Imprint of terrigenous input and continental weathering. Geochemistry, Geophysics, Geosystems 13, n/a-n/a.
Grimm, A.M., 2003. The El Niño Impact on the Summer Monsoon in Brazil: Regional Processes versus Remote Influences. American Meteorological Society, 263-280.
Grimm, A.M., Vera, C.S., Mechoso, C.R., 2005. The South American Monsoon System, in: Chang, C.-P., Wang, B., Lau, N.-C.G. (Eds.), The Global Monsoon System: Research and Forecast World Meteorological Organization, Hangzhou, China, pp. 219-238.

Grousset, F.E., Labeyrie, L., Sinko, J.A., Cremer, M., Bond, G.C., Duprat, J., Cortijo, E., Huon, S., 1993. Patterns of ice-rafted detritus in the glacial North Atlantic. Paleoceanography 8, 175-192.

Gutiérrez, D., Sifeddine, A., Field, D.B., Ortlieb, L., Vargas, G., Chávez, F.P., Velazco, F., Ferreira, V., Tapia, P., Salvatteci, R., Boucher, H., Morales, M.C., Valdés, J., Reyss, J.-L., Campusano, A., Boussafir, M., Mandeng-Yogo, M., García, M., Baumgartner, T., 2009. Rapid reorganization in ocean biogeochemistry off Peru towards the end of the Little Ice Age. Biogeosciences, 6, 835-848.

Heinrich, H., 1988. Origin and Consequences of Cyclic Ice Rafting in the Northeast Atlantic Ocean during the Past 130,000 Years. Quaternary Research 29, 142-152.

Hemming, S.R., 2004. Heinrich events: Massive late Pleistocene detritus layers of the North Atlantic and their global climate imprint. Reviews of Geophysics 42.

Henshaw, J.P.C., Merril, R.T., 1980. Magnetic and Chemical Changes in Marine Sediments. Reviews of Geophysics and Space Physics 18, 483-504.

Heslop, D., Dillon, M., 2007. Unmixing magnetic remanence curves withouta prioriknowledge. Geophysical Journal International 170, 556-566.

Heslop, D., Witt, A., Kleiner, T., Fabian, K., 2006. The role of magnetostatic interactions in sediment suspensions. Geophysical Journal International 165, 775-785.

Hodell, D.A., Anselmetti, F.S., Ariztegui, D., Brenner, M., Curtis, J.H., Gilli, A., Grzesik, D.A., Guilderson, T.J., Müller, A.D., Bush, M.B., 2008. An 85-ka record of climate change in lowland Central America. Quaternary Science Reviews 27, 1152-1165.

Itambi, A.C., von Dobeneck, T., Mulitza, S., Bickert, T., Heslop, D., 2009. Millennial-scale northwest African droughts related to Heinrich events and Dansgaard-Oeschger cycles: Evidence in marine sediments from offshore Senegal. Paleoceanography 24, n/a-n/a.

Jaeschke, A., Rühlemann, C., Arz, H., Heil, G., Lohmann, G., 2007. Coupling of millennial-scale changes in sea surface temperature and precipitation off northeastern Brazil with high-latitude climate shifts during the last glacial period. Paleoceanography 22, n/a-n/a.

Jennerjahn, T.C., Ittekkot, V., Arz, H.W., Behling, H., Pa¨tzold, J., Wefer, G., 2004. Asynchronous Terrestrial and Marine Signals of Climate Change During Heinrich Events. Science 306, 2236-2239.

Journet, E., Balkanski, Y., Harrison, S.P., 2013. A new data set of soil mineralogy for dust-cycle modeling. Atmospheric Chemistry and Physics Discussions 13, 23943-23993.

Journet, E., Balkanski, Y., Harrison, S.P., 2014. A new data set of soil mineralogy for dust-cycle modeling. Atmospheric Chemistry and Physics 14, 3801-3816.

Just, J., Dekkers, M.J., von Dobeneck, T., van Hoesel, A., Bickert, T., 2012a. Signatures and significance of aeolian, fluvial, bacterial and diagenetic magnetic mineral fractions in Late Quaternary marine sediments off Gambia, NW Africa. Geochemistry, Geophysics, Geosystems 13, n/a-n/a.

Just, J., Heslop, D., von Dobeneck, T., Bickert, T., Dekkers, M.J., Frederichs, T., Meyer, I., Zabel, M., 2012b. Multiproxy characterization and budgeting of terrigenous end-members at the NW African continental margin. Geochemistry, Geophysics, Geosystems 13, n/a-n/a.

Just, J., Schefuß, E., Kuhlmann, H., Stuut, J.-B.W., Pätzold, J., 2014. Climate induced sub-basin source-area shifts of Zambezi River sediments over the past 17ka. Palaeogeography, Palaeoclimatology, Palaeoecology.

Kageyama, M., Merkel, U., Otto-Bliesner, B., Prange, M., Abe-Ouchi, A., Lohmann, G., Ohgaito, R., Roche, D.M., Singarayer, J., Swingedouw, D., Zhang, X., 2013a. Climatic impacts of fresh water hosing under Last Glacial Maximum conditions: a multi-model study. Clim. Past 9, 935-953.

Kageyama, M., Merkel, U., Otto-Bliesner, B., Prange, M., Abe-Ouchi, A., Lohmann, G., Ohgaito, R., Roche, D.M., Singarayer, J., Swingedouw, D., Zhang, X., 2013b. Climatic impacts of fresh water hosing under Last Glacial Maximum conditions: a multi-model study. Climate of the Past 9, 935-953.

Kageyama, M., Mignot, J., Swingedouw, D., Marzin, C., Alkama, R., Marti, O., 2009. Glacial climate sensitivity to different states of the Atlantic Meridional Overturning Circulation: results from the IPSL model. Climate of the Past 5, 551–570.

Kasten, S., Zabel, M., Heuer, V., Hensen, C., 2004. Processes and Signals of Nonsteady-State Diagenesis in Deep-Sea Sediments and their Pore Waters., in: Wefer, G., Mulitza, S., Ratmeyer, V. (Eds.), The South Atlantic in the Late Quaternaty

Reconstrution of the Material Budgets and Current Systems. Springer-Verlag Berlin Heidelberg, pp. 431-459.

Kissel, C., Laj, C., Labeyrie, L., Dokken, T., Voelker, A., Blamart, D., 1999. Rapid climatic variations during marine isotopic stage 3: magnetic analysis of sediments from Nordic Seas and North Atlantic. Earth and Planetary Science Letters 171, 489-502.

Kissel, C., Laj, C., Piotrowski, A.M., Goldstein, S.L., Hemming, S.R., 2008. Millennial-scale propagation of Atlantic deep waters to the glacial Southern Ocean. Paleoceanography 23, n/a-n/a.

Kissel, C., Van Toer, A., Laj, C., Cortijo, E., Michel, E., 2013. Variations in the strength of the North Atlantic bottom water during Holocene. Earth and Planetary Science Letters 369-370, 248-259.

Knesel, K.M., Souza, Z.S., Vasconcelos, P.M., Cohen, B.E., Silveira, F.V., 2011. Young volcanism in the Borborema Province, NE Brazil, shows no evidence for a trace of the Fernando de Noronha plume on the continent. Earth and Planetary Science Letters 302, 38-50.

Knoppers, B., Ekau, W., Figueiredo, A.G., 1999. The coast and shelf of east and northeast Brazil and material transport. Geo-Marine Letters 19, 171-178.

Kohler, P., Knorr, G., Bard, E., 2014. Permafrost thawing as a possible source of abrupt carbon release at the onset of the Bolling/Allerod. Nature communications 5, 5520.

Kruiver, P.P., Dekkers, M.J., Heslop, D., 2001. Quantification of magnetic coercivity components by the analysis of acquisition curves of the isothermal remanent magnetisation. Earth and Planetary Science Letters 189, 269-276.

Liedtke, N., 2014. Numerische Simulation der Veränderungen im Nordbrasilstrom während eines Heinrich Ereignisses durch Änderungen im Windfeld, Fachbereich Geowissenschaften. Universität Bremen, Bremen.

Liu, Q., Roberts, A.P., Larrasoaña, J.C., Banerjee, S.K., Guyodo, Y., Tauxe, L., Oldfield, F., 2012. Environmental magnetism: Principles and applications. Reviews of Geophysics 50.

Liu, Z., Otto-Bliesner, B., He, F., Brandy, E.C., Tomas, R., Clark, P.U., Carlson, A.E., Lynch-Stieglitz, J., Curry, W., Brook, E.J., Erickson, D., Jacob, R., Kutzbach, J., Cheng, J., 2009. Transient Simulation of Last Deglaciation with a new mechanism for Bølling-Allerød Warming. Science 325, 310-314.

Mangerud, J., Andersen, S.T., Berglund, B.E., Donner, J.J., 1974. Quaternary stratigraphy of Norden, a proposal for terminology and classification. Boreas 3, 109-127.

McGee, D., Donohoe, A., Marshall, J., Ferreira, D., 2014. Changes in ITCZ location and cross-equatorial heat transport at the Last Glacial Maximum, Heinrich Stadial 1, and the mid-Holocene. Earth and Planetary Science Letters 390, 69-79.

McManus, J.F., Bond, G.C., Broecker, W.S., Johnsen, S., Labeyrie, L., Higgins, S., 1994. High resolution climate records from the North Atlantic during the last Interglacial. Nature 371, 326-329.

McManus, J.F., Francois, R., Gherardi, J.M., Keigwin, L.D., Brown-Leger, S., 2004. Collapse and rapid resumption of Atlantic meridional circulation linked to deglacial climate changes. Nature 428, 834-837.

Meju, M.A., Fontes, S.L., Oliveira, M.F.B., Lima, J.P.R., Ulugergerli, E.U., Carrasquilla, A.A., 1999. Regional aquifer mapping using combined VES-TEM-AMT/EMAP methods in the semiarid eastern margin of Parnaiba Basin, Brazil. Geophysics 64, 337-356.

Milne, G., Long, A., Bassett, S., 2005. Modelling Holocene relative sea-level observations from the Caribbean and South America. Quaternary Science Reviews 24, 1183-1202.

Mulitza, S., Prange, M., Stuut, J.-B., Zabel, M., von Dobeneck, T., Itambi, A.C., Nizou, J., Schulz, M., Wefer, G., 2008. Sahel megadroughts triggered by glacial slowdowns of Atlantic meridional overturning. Paleoceanography 23, n/a-n/a.

Nace, T.E., Baker, P.A., Dwyer, G.S., Silva, C.G., Rigsby, C.A., Burns, S.J., Giosan, L., Otto-Bliesner, B., Liu, Z., Zhu, J., 2014. The role of North Brazil Current transport in the paleoclimate of the Brazilian Nordeste margin and paleoceanography of the western tropical Atlantic during the late Quaternary. Palaeogeography, Palaeoclimatology, Palaeoecology 415, 3-13.

Nobre, P., Shukla, J., 1996. Variations of sea surface temperature, wind stress, and rainfall over the tropical Atlantic and South America. Journal of Climate 9, 2464-2479.

Nogués-Paegle, J., Mo, K.C., 1997. Alternating Wet and Dry Conditions over South America during Summer. American Meteorological Society, 279-291.
Nogués-Paegle, J., Mo, K.C., 2002. Linkages between Summer Rainfall Variability over South America and Sea Surface Temperarure Anomalies. Journal of Climate 15, 1389-1407.
Oliveira, R.G., Medeiros, W.E., 2012. Evidences of buried loads in the base of the crust of Borborema Plateau (NE Brazil) from Bouguer admittance estimates. Journal of South American Earth Sciences 37, 60-76.
Özdemir, Ö., 2002. Thermoremanence and stable memory of single-domain hematites. Geophysical Research Letters 29.
Özdemir, Ö., Dunlop, D.J., 2014. Hysteresis and coercivity of hematite. Journal of Geophysical Research: Solid Earth 119, 2582-2594.
Poveda, G., Waylen, P.R., Pulwarty, R.S., 2006. Annual and inter-annual variability of the present climate in northern South America and southern Mesoamerica. Palaeogeography, Palaeoclimatology, Palaeoecology 234, 3-27.
Prado, L.F., Wainer, I., Chiessi, C.M., Ledru, M.P., Turcq, B., 2013. A mid-Holocene climate reconstruction for eastern South America. Climate of the Past 9, 2117-2133.
Rahmstorf, S., 2001. Abrupt Climate Change. 1-6.
Razik, S., Chiessi, C.M., Romero, O.E., von Dobeneck, T., 2013. Interaction of the South American Monsoon System and the Southern Westerly Wind Belt during the last 14kyr. Palaeogeography, Palaeoclimatology, Palaeoecology 374, 28-40.
Roberts, A.P., Chang, L., Rowan, C.J., Horng, C.-S., Florindo, F., 2011. Magnetic properties of sedimentary greigite (Fe3S4): An update. Reviews of Geophysics 49.
Robertson, A.W., Mechoso, C.R., 2000. Interannual and Interdecadal Variability of the South Atlantic Convergence Zone. Monthly Weather Review 128, 2947-2957.
Robertson, D.J., France, D.E., 1994. Discrimination of remanence-carrying minerals in mixtures, using isothermal remanent magnetisation acquisition curves. Physics of the Earth and Planetary Interiors 82, 223-234.
Rochette, P., Fillion, G., Mattéi, J.-L., Dekkers, M.J., 1990. Margnetic transition at 30-34 Kelvin in pyrrhotite: insight into a widespread occurence of this mineral in rocks. Earth and Planetary Science Letters 98, 319-328.
Roud, S.C., 2014. Magnetic mineral inventory of late Quaternary sediments from the tropical Atlantic off North Brazil: indicator for paleoenvironmental conditions and early diagenesis, Fachbereich Geowissenschaften. Universität Bremen, Bremen, p. 66.
Rowan, C.J., Roberts, A.P., Broadbent, T., 2009. Reductive diagenesis, magnetite dissolution, greigite growth and paleomagnetic smoothing in marine sediments: A new view. Earth and Planetary Science Letters 277, 223-235.

Ruddiman, W.F., 1977. North Atlantic Ice-Rafting: A Major Change at 75,000 Years Before the Present. Science 196, 1208-1211.

Ruddinam, W.F., 2008. Earth's Climate: Past and Future, 2nd ed. Clancy Marshall, New York.

Sarnthein, M., Stattegger, K., Dreger, D., Erlenkeuser, H., Grootes, P.M., Haupt, B.J., Jung, S., Kiefer, T., Kuhnt, W., Pflaumann, U., Schäfer-Neth, C., Schulz, H.D., Schulz, M., Seidov, D., Simstich, J., van Kreveld, S., Vogelsang, E., Völker, A., Weinelt, M., 2001. Fundamental Modes and Abrupt Changes in North Atlantic Circulation and Climate over the last 60 ky — Concepts, Reconstruction and Numerical Modeling. Springer, Berlin.

Schmitt, J., Schneider, R., Elsig, J., Leuenberger, D., Lourantou, A., ChappellazJ., Köhler, P., Joos, F., Stocker, T.F., Leuenberger, M., Fischer, H., 2012. Carbon Isotope Constraints on the Deglacial CO2 Rise from Ice Cores. Science 336, 711-714.

Schulz, H.D., Zabel, M., 2006. Marine Geochemistry. Springer.

Shchepetkin, A.F., 2003. A method for computing horizontal pressure-gradient force in an oceanic model with a nonaligned vertical coordinate. Journal of Geophysical Research 108.

Shchepetkin, A.F., McWilliams, J.C., 2005. The regional oceanic modeling system (ROMS): a split-explicit, free-surface, topography-following-coordinate oceanic model. Ocean Modelling 9, 347-404.

Sifeddine, A., Gutiérrez, D., Ortlieb, L., Boucher, H., Velazco, F., Field, D., Vargas, G., Boussafir, M., Salvatteci, R., Ferreira, V., García, M., Valdés, J., Caquineau, S., Mandeng Yogo, M., Cetin, F., Solis, J., Soler, P., Baumgartner, T., 2008. Laminated sediments from the central Peruvian continental slope: A 500 year record of upwelling system productivity, terrestrial runoff and redox conditions. Progress in Oceanography 79, 190-197.

Souza, A.C.M., Silva, M.R.F., Dias, N.S., 2012. Gestão de recursos hídricos: o caso da Bacia Hidrográfica de Apodi/Mossoro (RN). Irriga, Botucatu, 280-296.

Stocker, T.F., 2000. Past and future reorganizations in the climate system. Quaternary Science Reviews 19, 301-319.

Stocker, T.F., Marchal, O., 2000. Abrupt climate change in the computer:Is it real? Proceedings of the National Academy of Sciences of USA 97, 1362-1365.

Stoner, J.S., Channell, J.E.T., Hillaire-Marcel, C., 1996. The magnetic signature of rapidly deposited detrital layers from the deep Labrador Sea: Relationship to North Atlantic Heinrich layers. Paleoceanography 11, 309-325.

Stramma, L., England, M., 1999. On the water masses and mean circulation of the South Atlantic Ocean. Journal of Geophysical Research 104, 20,863-820,883.

Tauxe, L., 2008. Essentials of Rock and Paleomagnetism, La Jolla, CA.

Thiagarajan, N., Subhas, A.V., Southon, J.R., Eiler, J.M., Adkins, J.F., 2014. Abrupt pre-Bolling-Allerod warming and circulation changes in the deep ocean. Nature 511, 75-78.

Thompson, R., Oldfield, F., 1986. Environmental magnetism. Allen & Unwin, London.

Trindade, R., Dagrellafilho, M., Epof, I., Britoneves, B., 2006. Paleomagnetism of Early Cambrian Itabaiana mafic dikes (NE Brazil) and the final assembly of Gondwana. Earth and Planetary Science Letters 244, 361-377.

Verosub, K.L., Roberts, A.P., 1995. Environmental magnetism- Past, present, and future. Journal of Geophysical Research 1000, 2175-2192.

Vidal, L., Labeyrie, L., Cortijo, E., Arnold, M., Duplessy, J.C., Michel, E., Becqué, S., van Weering, T.C.E., 1997. Evidence for changes in the North Atlantic Deep Water linked to meltwater surges during the Heinrich events. Earth and Planetary Science Letters 146, 13-27.

Vital, H., Furtado, S.F.L., Gomes, M.P., 2010a. Response of the Apodi-Mossoró estuary- incised valley system (NE Brazil) to sea-level fluctuations. Brazilian Journal of Oceanography 58, 13-24.

Vital, H., Gomes, M.P., Tabosa, W.F., Frazão, E.P., Santos, C.L.S., Plácido Junior, J.S., 2010b. Characterization of the Brazilian continental shelf adjacent to Rio Grande State, NE Brazil. Brazilian Journal of Oceanography 58, 43-54.

Vital, H., Stattegger, K., Amaro, V.E., Schwarzer, K., Frazão, E.P., Tabosa, W.F., Silveira, I.M., 2008. A modern high-energy siliciclastic-carbonate platform: continental shelf adjacent to Northern Rio Grande do Norte State, Northeastern Brazil. Recent Advances in Models of Siliciclastic Shallow-MarineStratigraphy 90, 175-188.

Wang, X., Auler, A.S., Edwards, R.L., Cheng, H., Cristalli, P.S., Smart, P.L., Richards, D.A., Shen, C.C., 2004. Wet periods in northeastern Brazil over the past 210 kyr linked to distant climate anomalies. Nature 432, 740-743.

Weldeab, S., Schneider, R.R., Kolling, M., 2006. Deglacial sea surface temperature and salinity increase in the western tropical Atlantic in synchrony with high latitude climate instabilities. Earth and Planetary Science Letters 241, 699-706.

Weltje, G.J., Tjallingii, R., 2008. Calibration of XRF core scanners for quantitative geochemical logging of sediment cores: Theory and application. Earth and Planetary Science Letters 274, 423-438.

Wilson, K.E., Maslin, M.A., Burns, S.J., 2011. Evidence for a prolonged retroflection of the North Brazil Current during glacial stages. Palaeogeography, Palaeoclimatology, Palaeoecology 301, 86-96.

WRB, 2006. World reference base for soil resources 2006.

Zabel, M., Schneider, R.R., Wagner, T., Adegbie, A.T., de Vries, U., Kolonic, S., 2001. Late Quaternary Climate Changes in Central Africa as Inferred from Terrigenous Input to the Niger Fan. Quaternary Research 56, 207-217.

Zhou, J., Lau, K.-M., 1998. Does a Monsoon Climate Exist over South America? Journal of Climate 11, 1020-1040.

ANNEX I – Age Model

Radiocarbon ages used for the age models calibration

GeoB3910-2[a]			
Laboratory ID[b]	Core depth (cm)	14C Age (yr BP) ± 1σ	Age (cal yr BP)
KIA 6800	0	165 ± 30	170
KIA 6799	13	3530 ± 35	3800
KIA 6798	23	5760 ± 40	6560
KIA 7225	38	8030 ± 40	8900
KIA 6815	58	9690 ± 60	11020
KIA 6814	73	10540 ± 70	12460
KIA 6813	88	12440 ± 110	14550
KIA 25825	103	13150 ± 70	16100
KIA 25824	113	13600 ± 70	16800
KIA 6812	148	15380 ± 110	18300
KIA 6811	173	19600 ± 170	22800
KIA 25822	183	20180 ± 150	23400
KIA 6808	193	22080 ± 220	25700
KIA 25821	213	24730 ± 260	28600
KIA 25820	233	26760 ± 310	30200
KIA 6806	238	27880 ± 430	31500
KIA 22411	268	30460 ± 430	35000
	302		38500*
KIA 6804	328	38200 ± 1480	41800
KIA 21829	348	40600 ± 820	42800
KIA 21830	373	44080 ± 1250	45400
	400		46900*
	435		52100*
	453		54600*
	478		58000*

* correlation points to the GISP2 ice core [Grootes at el., 1993]

GeoB3129-1[c]			
Laboratory ID[b]	Core depth (cm)	14C Age (yr BP) ± 1σ	Age (cal yr BP)
KIA 2576	22	1830 ± 30	1910
KIA 2575	52	3610 ± 50	3980
KIA 2574	62	3820 ± 30	4230
KIA 2573	90	5880 ± 40	6610
KIA 655	119	6510 ± 60	7330
KIA 654	207	9160 ± 80	10200
KIA 1872	241	9650 ± 60	11130

KIA 1871	307	9910 ± 60	11450
KIA 1861	329	10430 ± 60	12090
KIA 1860	452	10610 ± 70	12320
KIA 1859	491	11600 ± 70	13540
KIA 2614	523	12040 ± 70	14090
KIA 2612	548	12380 ± 50	14510

GeoB3911-3[d]

Laboratory ID[b]	Core depth (cm)	14C Age (yr BP) ± 1σ	Age (cal yr BP)
KIA 2613	543	12680 ± 80	14880
KIA 2611	648	14610 ± 110	16720
KIA 1858	665	16920 ± 90	20140

GeoB3104-1[c]

Laboratory ID[b]	Core depth (cm)	14C Age (yr BP) ± 1σ	Age (cal yr BP)
KIA 653	8	2660 ± 50	2880
KIA 1857	20	5740 ± 60	6450
KIA 1856	52	9660 ± 50	11140
GrA 3719	87	12580 ± 100	14760
KIA 1855	97	12960 ± 90	15230
GrA 3720	172	16120 ± 160	19150
KIA 651	209	20540 + 350/-330	24280
GrA 3721	274	25050 ± 200	29340
KIA 1853	292	27820 + 290/-280	32340
KIA 1852	337	31690 + 450/-420	36370
KIA 650	384	33400 +1840/-149	38100
GrA 3722	462	38600 +900/-800	43130

GeoB3912-1[a]		GeoB3913-3	
SPECMAP $\delta^{18}O$[c]	Age (cal yr BP)	Stratigraphic tie points from core GeoB3912-1 (yr BP)	Age (cal yr BP)
538	65000	17	11034
568	71000	24	15341
633	80000	25	15707
		26	16212
		29	17058
		32	1737
		33	177
		34	17947
		37	18235
		40	18797
		48	19339

51	20146
55	21291
56	22316
59	22673
60	23046
63	23414
64	23777
68	24139
69	25021
70	25208
74	26607
76	27731
82	29262
86	30358
91	30956
96	32093
100	34153
104	37001
106	37348
108	37757
113	37893
115	38217
116	38668
117	39141
118	39759
121	40791
127	4207
129	42608
131	43429
132	44204
134	45776
136	46696
137	46923
140	47799
143	48089
147	48434
150	49443
151	50022
152	50603
154	53517
158	54678
161	56127
162	56415
165	57285
170	58752

171	59622
172	60057
174	60492
177	60782
180	61362
182	63394
185	64562
192	656
218	66802
239	67606
249	6961
253	7001
254	7041
266	70755
291	72537
297	73089
300	73641
301	75022
308	76404
350	84696

[a] Jaechke *et al* [2007]

[b] GrA Groningen; KIA Kiel.

[c] see Arz *et al* [1998] for detailed information

[d] see Arz *et al* [1999] for detailed information

ANNEX II – Protocols for magnetic mineralogy measurements

PROTOCOL 1 – Demagnetization of the NRM

Step by step demagnetization of the Natural Remanent Magnetization (NRM) up to 100 mT.

Steps:

- 5 mT, between 0-30 mT
- 10 mT, between 30-80 mT
- 20 mT, between 80-100 mT

PROTOCOL 2 – Acquisition of the ARM

Step by step acquisition of the Anisteretic Remanent Magnetization (ARM). This is an artificial magnetization acquired in laboratory through imparting an alternated field concomitant to a direct field (DC). We used field of 0.5μT.

Steps:

- 5 mT, between 0-30 mT
- 10 mT, between 30-80 mT
- 20 mT, between 80-100 mT

PROTOCOL 3 – Demagnetization of the ARM

Step by step demagnetization of the Anisteretic Remanent Magnetization (ARM).

Steps:

- 5 mT, between 0-30 mT
- 10 mT, between 30-80 mT
- 20 mT, between 80-100 mT

PROTOCOL 4 – IRM acquisition in low fields

Acquisition of Isotermal Remanent Magnetization (IRM) in low fields (up to 700 mT).

Steps:

- 5 mT, between 0-30 mT
- 10 mT, between 30-50 mT

- 20 mT, between 50-100 mT
- 25 mT, between 100-150 mT
- 50 mT, between 150-300 mT
- 200 mT, between 300-700 mT

PROTOCOL 5 – IRM acquisition in high fields

Acquisition of Isotermal Remanent Magnetization (IRM) in high fields (between 1000 and 2500 mT).

Steps:

- 250 mT, between 1000-1500 mT
- 200 mT, between 1500-2000 mT
- 500 mT, between 2000-2500 mT

ANNEX III – Rock magnetic parameters

GeoB3913-3

Depth	Age	kappa	IRM_{300mT}	ARM_{100}/IRM_{100}	$HIRM_{[300\&2700]}$	$S\text{-ratio}_{[300\&2700]}$	Fe/kappa
[cm]	*cal [kyr]*	*[10**-6 SI]*	*[mA/m]*	-	-	-	*[cps/10**-6 SI]*
5	3.3397	14.2	3.48E+02	1.47E-01	28.30	0.92	5.21E+02
10	6.6794	21.2	4.48E+02	1.52E-01	29.66	0.94	4.18E+02
15	10.0191	36.2	6.93E+02	1.42E-01	89.29	0.89	1.10E+03
20	13.7525	59.4	7.50E+02	1.22E-01	179.01	0.81	1.24E+03
25	14.8788	78.3	8.65E+02	1.01E-01	332.64	0.72	1.26E+03
30	15.8405	92.8	6.70E+02	9.90E-02	190.85	0.78	1.76E+03
35	16.7612	91.2	8.32E+02	8.70E-02	243.01	0.77	1.34E+03
40	17.6818	98.8	1.08E+03	6.86E-02	242.65	0.82	1.35E+03
45	18.6025	88.3	1.25E+03	5.85E-02	210.76	0.86	8.81E+02
50	19.6349	76.1	1.14E+03	5.43E-02	174.32	0.87	9.74E+02
55	21.1142	88.2	1.25E+03	5.74E-02	196.05	0.86	1.04E+03
60	22.5935	105	1.10E+03	5.97E-02	218.89	0.83	7.17E+02
65	23.9478	117.1	1.30E+03	5.75E-02	250.12	0.84	1.01E+03
70	24.8018	116.2	1.28E+03	5.36E-02	245.50	0.84	9.61E+02
75	26.608	108.3	1.01E+03	5.89E-02	150.82	0.87	7.45E+02
80	28.7009	104.2	1.01E+03	8.43E-02	214.66	0.83	1.28E+03
85	29.9133	110.8	9.32E+02	9.16E-02	203.03	0.82	1.47E+03
90	31.1256	88.4	9.40E+02	7.27E-02	182.42	0.84	1.21E+03
95	32.338	70.2	7.73E+02	7.07E-02	130.57	0.86	1.03E+03
100	34.3699	67.2	7.70E+02	7.37E-02	131.95	0.85	8.16E+02
105	36.4018	69.7	9.17E+02	7.34E-02	166.86	0.85	8.62E+02
110	37.8395	68.9	7.23E+02	8.99E-02	106.16	0.87	9.58E+02

Depth	Age	kappa	IRM_{300mT}	ARM_{100}/IRM_{100}	$HIRM_{[300\&2700]}$	$S\text{-}ratio_{[300\&2700]}$	Fe/kappa
[cm]	*cal [kyr]*	*[10**-6 SI]*	*[mA/m]*	-	-	-	*[cps/10**-6 SI]*
115	38.3858	100.8	9.44E+02	9.05E-02	226.85	0.81	1.46E+03
120	40.2543	79.5	8.43E+02	8.26E-02	176.72	0.83	8.21E+02
125	41.6504	56	6.42E+02	8.12E-02	111.01	0.85	8.88E+02
130	42.981	60.6	7.55E+02	8.37E-02	121.81	0.86	1.30E+03
135	45.7709	77.4	6.80E+02	8.89E-02	127.62	0.84	1.23E+03
140	46.8805	110.4	1.11E+03	7.98E-02	280.66	0.80	1.39E+03
145	47.9902	93	1.05E+03	7.58E-02	187.23	0.85	8.80E+02
150	50.6124	53.1	8.02E+02	8.17E-02	108.64	0.88	7.16E+02
155	53.8464	60	5.98E+02	1.01E-01	113.63	0.84	6.77E+02
160	55.4934	73.8	8.72E+02	8.26E-02	148.12	0.85	1.18E+03
165	57.1404	71.5	8.04E+02	8.45E-02	102.61	0.89	6.60E+02
170	58.5925	88.8	7.99E+02	9.80E-02	173.45	0.82	1.21E+03
175	59.265	105.7	8.71E+02	1.08E-01	214.19	0.80	1.41E+03
180	59.9376	112.3	7.99E+02	1.06E-01	189.41	0.81	2.21E+03
185	60.6101	107.1	7.95E+02	9.76E-02	196.77	0.80	1.87E+03
190	61.2826	100.9	5.13E+02	7.33E-02	185.07	0.73	1.37E+03
195	61.9552	98.9	8.44E+02	7.18E-02	212.80	0.80	1.27E+03
200	62.6277	94.3	1.09E+03	6.46E-02	231.11	0.83	1.07E+03
205	63.3003	101.1	1.06E+03	6.89E-02	199.85	0.84	1.07E+03
210	63.9728	100	1.12E+03	6.85E-02	230.87	0.83	1.04E+03
215	64.6453	105.3	1.30E+03	6.56E-02	233.46	0.85	9.07E+02
220	65.3179	107.5	1.27E+03	7.00E-02	241.27	0.84	8.42E+02
225	65.9904	95.6	1.08E+03	7.65E-02	196.24	0.85	9.21E+02
230	66.6629	90.7	1.04E+03	8.27E-02	148.94	0.87	8.56E+02
235	67.3355	86.4	8.53E+02	1.02E-01	134.32	0.86	9.43E+02
240	68.008	65.9	7.23E+02	1.21E-01	74.16	0.91	5.97E+02

Depth	Age	kappa	IRM_{300mT}	ARM_{100}/IRM_{100}	$HIRM_{[300\&2700]}$	$S\text{-ratio}_{[300\&2700]}$	Fe/kappa
[cm]	*cal [kyr]*	*[10**-6 SI]*	*[mA/m]*	-	-	-	*[cps/10**-6 SI]*
245	68.5363	77.2	8.56E+02	1.17E-01	138.05	0.86	8.93E+02
250	69.0645	104	9.87E+02	1.22E-01	222.84	0.82	1.18E+03
256	69.6985	90.8	7.55E+02	1.28E-01	160.12	0.83	1.29E+03
260	70.1211	72	7.32E+02	1.21E-01	155.72	0.82	1.56E+03
265	70.6493	51.5	6.34E+02	1.21E-01	96.57	0.87	7.15E+02
270	71.0621	46	7.57E+02	1.22E-01	84.30	0.90	1.06E+03
275	71.4459	56.2	9.67E+02	1.27E-01	115.95	0.89	1.00E+03
280	71.8297	50.2	7.38E+02	1.33E-01	83.41	0.90	8.05E+02
285	72.2135	50.2	8.41E+02	1.45E-01	89.70	0.90	8.46E+02
290	72.5974	42.6	7.60E+02	1.57E-01	74.59	0.91	1.01E+03
295	72.9812	58.1	7.98E+02	1.41E-01	94.10	0.89	1.44E+03
300	73.365	75.8	9.56E+02	1.14E-01	186.41	0.84	1.19E+03
305	74.8989	70.9	9.38E+02	1.03E-01	102.13	0.90	7.82E+02
310	76.3444	49	8.10E+02	1.12E-01	101.65	0.89	4.13E+02
315	77.4365	27.7	5.73E+02	1.40E-01	53.57	0.91	5.22E+02
320	78.5286	19.3	3.65E+02	1.60E-01	27.10	0.93	3.06E+02
325	79.6207	28	2.54E+02	1.66E-01	18.13	0.93	3.75E+03
330	80.7316	73.9	1.11E+03	7.89E-02	242.32	0.82	1.24E+03
335	81.8708	85.4	1.20E+03	8.11E-02	269.17	0.82	1.12E+03
340	83.0099	64	6.53E+02	9.39E-02	129.69	0.83	1.07E+03
345	84.149	57.1	7.91E+02	9.12E-02	156.76	0.83	1.65E+03
350	85.2881	83	9.03E+02	8.91E-02	217.13	0.81	1.28E+03

GeoB3912-1

Depth	Age	kappa	IRM_{300mT}	ARM_{100}/IRM_{100}	$HIRM_{[300\&2700]}$	S-ratio $_{[300\&2700]}$	Fe/kappa	Age
[cm]	*cal [kyr]*	*[10**-6 SI]*	*[mA/m]*	-	-	-	*[cps/10**-6 SI]*	*cal [kyr]*
5	2.45	48.66	9.72E+02	6.86E-02	63.03	0.94	4.26E+02	1.27
10.5	4.64	61.83	1.16E+03	8.68E-02	68.50	0.94	3.28E+02	2.05
15	6.83	45.97	1.01E+03	8.06E-02	63.60	0.94	4.72E+02	2.84
20	9.54	120.70	1.12E+03	7.20E-02	135.40	0.89	3.99E+02	3.66
25	10.19	106.72	9.73E+02	7.01E-02	130.44	0.88	5.56E+02	4.44
30	10.57	113.71	9.88E+02	6.90E-02	148.84	0.87	6.30E+02	5.23
35	10.95	104.57	8.77E+02	6.90E-02	133.55	0.87	5.38E+02	6.21
40.5	11.39	105.65	8.11E+02	6.93E-02	122.58	0.87	3.45E+02	7.39
45	11.95	87.90	6.54E+02	7.08E-02	86.74	0.88	5.64E+02	8.54
50	12.56	80.11	7.11E+02	7.29E-02	64.91	0.92	8.20E+02	9.43
55	13.18	82.53	7.60E+02	7.08E-02	77.13	0.91	7.55E+02	9.85
61	13.92	91.67	8.49E+02	6.61E-02	107.81	0.89	9.22E+02	10.09
65	14.41	112.10	1.15E+03	6.24E-02	164.20	0.87	8.78E+02	10.27
70	14.88	105.65	1.19E+03	5.86E-02	157.00	0.88	8.57E+02	10.42
75	15.16	120.70	1.03E+03	6.32E-02	211.90	0.83	9.36E+02	10.57
81	15.52	110.48	9.73E+02	6.28E-02	204.73	0.83	9.07E+02	10.72
85	15.77	118.28	1.01E+03	6.07E-02	180.10	0.85	1.03E+03	10.88
90.5	16.12	114.52	9.41E+02	6.31E-02	165.21	0.85	1.07E+03	11.02
95	16.40	111.56	9.09E+02	6.22E-02	172.71	0.84	1.01E+03	11.15
100.5	16.74	112.90	7.51E+02	5.79E-02	179.71	0.81	1.07E+03	11.34
105	17.01	114.52	6.79E+02	6.38E-02	138.16	0.83	1.15E+03	11.58
110.5	17.29	113.98	5.65E+02	6.20E-02	123.01	0.82	1.21E+03	11.82
115	17.53	111.56	6.13E+02	6.36E-02	111.93	0.85	1.14E+03	12.07
121	17.87	99.73	4.78E+02	6.15E-02	115.09	0.81	1.12E+03	12.32

Depth	Age	kappa	IRM_{300mT}	ARM_{100}/IRM_{100}	$HIRM_{[300\&2700]}$	S-ratio $_{[300\&2700]}$	Fe/kappa	Age
[cm]	*cal [kyr]*	*[10**-6 SI]*	*[mA/m]*	-	-	-	*[cps/10**-6 SI]*	*cal [kyr]*
125	18.17	115.59	5.70E+02	6.13E-02	117.93	0.83	9.87E+02	12.56
130.5	18.55	114.52	4.68E+02	6.18E-02	99.20	0.83	9.68E+02	12.81
135	18.87	109.95	4.63E+02	6.02E-02	91.75	0.83	8.87E+02	13.05
141	19.43	79.03	6.47E+02	6.72E-02	76.65	0.89	8.12E+02	13.30
145	20.00	83.06	6.09E+02	6.22E-02	80.80	0.88	9.68E+02	13.55
150.5	20.79	82.80	7.01E+02	6.69E-02	87.68	0.89	7.48E+02	13.79
155	21.44	80.65	6.97E+02	6.44E-02	83.20	0.89	9.32E+02	14.04
161.5	22.58	121.51	8.67E+02	6.42E-02	119.38	0.88	9.38E+02	14.28
165	23.23	123.39	8.00E+02	5.95E-02	122.22	0.87	1.01E+03	14.52
170.5	24.23	132.26	7.81E+02	6.06E-02	123.53	0.86	7.95E+02	14.74
175	24.74	110.75	6.15E+02	6.24E-02	116.60	0.84	1.04E+03	14.87
182	25.40	109.95	6.32E+02	6.52E-02	108.68	0.85	1.02E+03	14.99
185	25.66	90.86	5.82E+02	6.28E-02	89.38	0.87	1.13E+03	15.11
190.5	26.16	89.52	7.57E+02	6.95E-02	92.40	0.89	1.20E+03	15.22
195	26.61	103.49	6.78E+02	6.59E-02	95.41	0.88	1.26E+03	15.34
200.5	27.22	100.54	7.39E+02	6.68E-02	106.05	0.87	1.03E+03	15.46
205	27.73	101.88	7.40E+02	6.94E-02	86.99	0.89	9.41E+02	15.59
210	28.29	106.18	7.28E+02	7.01E-02	86.50	0.89	1.29E+03	15.83
215	28.85	105.11	6.50E+02	7.02E-02	86.06	0.88	1.28E+03	15.96
220	29.37	102.96	6.46E+02	7.02E-02	94.48	0.87	1.29E+03	16.09
225	30.06	109.68	5.89E+02	6.37E-02	106.17	0.85	1.30E+03	16.21
230.5	30.88	113.17	5.63E+02	6.56E-02	121.62	0.82	1.27E+03	16.33
235	31.55	110.75	5.70E+02	6.19E-02	100.90	0.85	1.32E+03	16.46
240.5	32.30	98.39	6.42E+02	6.63E-02	94.66	0.87	1.32E+03	16.58
245	32.67	81.72	6.67E+02	6.64E-02	68.63	0.91	1.45E+03	16.71
250.5	33.08	83.33	7.04E+02	6.79E-02	74.11	0.90	1.42E+03	16.83

Depth	Age	kappa	IRM_{300mT}	ARM_{100}/IRM_{100}	$HIRM_{[300\&2700]}$	S-ratio $_{[300\&2700]}$	Fe/kappa	Age
[cm]	*cal [kyr]*	*[10**-6 SI]*	*[mA/m]*	-	-	-	*[cps/10**-6 SI]*	*cal [kyr]*
255	33.41	79.84	6.22E+02	6.86E-02	68.88	0.90	1.46E+03	16.95
260	33.78	83.06	5.93E+02	6.82E-02	71.38	0.89	1.48E+03	17.06
265	34.15	84.68	5.97E+02	7.01E-02	71.05	0.89	1.50E+03	17.16
270	34.52	98.12	6.06E+02	6.76E-02	87.14	0.87	1.54E+03	17.26
275	34.89	79.30	6.48E+02	6.48E-02	70.67	0.90	1.41E+03	17.37
280	35.40	78.49	8.11E+02	6.70E-02	78.44	0.91	1.41E+03	17.47
285	36.12	102.96	6.51E+02	7.00E-02	86.99	0.88	1.42E+03	17.58
290	36.56	98.12	6.54E+02	6.71E-02	91.53	0.88	1.40E+03	17.68
295	36.86	76.61	7.66E+02	6.82E-02	90.01	0.89	1.38E+03	17.81
300	37.04	70.16	8.34E+02	6.77E-02	89.99	0.90	1.36E+03	17.95
305	37.21	90.05	8.43E+02	6.44E-02	104.17	0.89	1.34E+03	18.09
310	37.38	106.99	8.80E+02	6.78E-02	128.11	0.87	1.40E+03	18.24
315	37.55	106.45	9.09E+02	6.56E-02	127.78	0.88	1.41E+03	18.38
321.5	37.77	101.61	8.16E+02	6.36E-02	142.11	0.85	1.40E+03	18.52
325	37.89	105.65	8.04E+02	6.05E-02	158.05	0.84	1.34E+03	18.66
330.5	38.09	111.02	7.55E+02	6.06E-02	167.35	0.82	1.30E+03	18.80
335	38.32	104.03	6.64E+02	5.42E-02	165.01	0.80	1.28E+03	18.94
340	38.75	105.11	6.50E+02	5.61E-02	182.27	0.78	1.07E+03	19.08
345	39.40	69.89	6.55E+02	6.64E-02	63.27	0.91	9.54E+02	19.30
350.5	39.89	76.08	7.03E+02	6.23E-02	62.95	0.92	9.20E+02	19.58
355	40.28	88.71	6.63E+02	6.25E-02	81.80	0.89	9.56E+02	19.86
359	40.62	93.01	6.93E+02	6.64E-02	81.15	0.90	1.08E+03	20.15
365	41.13	83.87	7.39E+02	6.54E-02	71.65	0.91	9.74E+02	20.43
370.5	41.73	97.31	7.14E+02	6.59E-02	93.11	0.88	9.02E+02	20.72
375	42.34	91.67	7.92E+02	6.55E-02	97.25	0.89	9.61E+02	21.01
380	43.01	84.68	8.30E+02	6.52E-02	95.11	0.90	8.46E+02	21.29

Depth	Age	kappa	IRM_{300mT}	ARM_{100}/IRM_{100}	$HIRM_{[300\&2700]}$	S-ratio $_{[300\&2700]}$	Fe/kappa	Age
[cm]	*cal [kyr]*	*[10**-6 SI]*	*[mA/m]*	-	-	-	*[cps/10**-6 SI]*	*cal [kyr]*
385	44.20	90.32	8.20E+02	6.36E-02	98.22	0.89	8.81E+02	21.58
390	45.21	97.85	8.06E+02	6.60E-02	113.77	0.88	9.63E+02	21.92
395	45.78	101.61	9.33E+02	6.40E-02	122.85	0.88	9.35E+02	22.30
399.5	46.30	93.01	7.88E+02	6.45E-02	120.78	0.87	1.23E+03	22.67
405	46.92	109.41	8.65E+02	6.03E-02	147.49	0.85	1.12E+03	23.05
410	47.50	108.87	7.57E+02	6.15E-02	154.47	0.83	1.22E+03	23.42
415	48.00	117.20	7.54E+02	5.78E-02	158.73	0.83	7.23E+02	23.79
420	48.23	104.84	8.30E+02	6.38E-02	110.96	0.88	1.19E+03	24.14
425	48.57	104.84	8.68E+02	6.08E-02	100.16	0.90	1.18E+03	24.41
430	49.30	104.57	8.73E+02	6.13E-02	102.75	0.89	1.14E+03	24.63
435	50.02	98.92	8.49E+02	6.29E-02	100.06	0.89	1.15E+03	24.84
440	50.75	87.90	8.19E+02	6.28E-02	87.12	0.90	8.73E+02	25.03
445	51.47	93.82	8.23E+02	6.31E-02	84.03	0.91	9.31E+02	25.21
450	52.21	85.75	8.07E+02	6.21E-02	86.10	0.90	1.11E+03	25.39
455	52.94	89.25	8.14E+02	6.23E-02	90.99	0.90	1.15E+03	26.38
460	53.66	101.34	7.81E+02	6.80E-02	87.42	0.90	9.12E+02	26.60
465	54.39	105.11	6.84E+02	6.57E-02	101.18	0.87	1.01E+03	26.83
470	55.11	112.10	6.46E+02	6.48E-02	105.60	0.86	1.08E+03	27.06
475	55.84	103.49	7.71E+02	6.38E-02	96.54	0.89	9.67E+02	27.28
479.5	56.49	101.88	8.19E+02	6.56E-02	97.90	0.89	1.06E+03	27.50
485	57.29	97.85	9.91E+02	6.25E-02	93.43	0.91	1.21E+03	27.73
490.5	58.09	107.53	8.17E+02	6.68E-02	108.31	0.88	1.18E+03	27.95
495	58.75	110.75	9.46E+02	6.69E-02	136.20	0.87	1.18E+03	28.17
500.5	59.55	108.87	8.59E+02	6.71E-02	154.33	0.85	1.24E+03	28.40
505	60.20	120.97	8.43E+02	6.53E-02	160.76	0.84	1.23E+03	28.62
510.5	61.00	122.85	8.76E+02	6.81E-02	150.45	0.85	1.22E+03	28.84

Depth	Age	kappa	IRM_{300mT}	ARM_{100}/IRM_{100}	$HIRM_{[300\&2700]}$	S-ratio $_{[300\&2700]}$	Fe/kappa	Age
[cm]	*cal [kyr]*	*[10**-6 SI]*	*[mA/m]*	-	-	-	*[cps/10**-6 SI]*	*cal [kyr]*
515	61.65	119.89	8.18E+02	6.39E-02	134.19	0.86	1.30E+03	29.06
520.5	62.45	122.04	8.37E+02	6.58E-02	141.09	0.86	1.30E+03	29.27
525	63.10	126.34	8.03E+02	6.64E-02	128.92	0.86	1.25E+03	29.50
530.5	63.91	123.39	7.72E+02	6.64E-02	123.26	0.86	1.30E+03	29.76
535	64.56	125.54	6.41E+02	6.44E-02	135.21	0.83	1.27E+03	30.06
541	65.60	131.72	5.95E+02	6.60E-02	130.01	0.82	1.34E+03	30.36
545	66.40	128.23	5.84E+02	5.89E-02	135.73	0.81	1.24E+03	30.66
550.5	67.51	112.90	8.07E+02	6.35E-02	122.58	0.87	1.32E+03	30.95
555	68.41	118.01	1.11E+03	6.71E-02	113.90	0.91	1.13E+03	31.25
560.5	69.51	132.26	9.09E+02	6.63E-02	169.98	0.84	1.15E+03	31.55
565	70.41	129.03	9.07E+02	6.20E-02	134.90	0.87	1.16E+03	31.85
570.5	71.36	102.96	1.33E+03	7.55E-02	85.40	0.94	1.16E+03	32.12
575	71.99	86.56	1.28E+03	7.52E-02	74.90	0.94	9.23E+02	32.34
579.5	72.61	94.62	1.09E+03	7.83E-02	71.20	0.94	9.31E+02	32.52
585	73.37	113.17	1.13E+03	7.21E-02	101.70	0.92	8.31E+02	32.67
591	74.19	117.47	1.16E+03	7.26E-02	120.00	0.91	9.24E+02	32.82
595	74.75	123.39	1.14E+03	6.76E-02	120.90	0.90	9.39E+02	32.97
600.5	75.51	125.54	9.46E+02	7.18E-02	132.55	0.88	8.94E+02	33.12
605	76.13	87.10	1.19E+03	7.28E-02	97.30	0.92	9.66E+02	33.26
610.5	76.89	88.98	1.35E+03	8.11E-02	93.10	0.94	8.94E+02	33.40
615	77.52	86.02	1.35E+03	7.78E-02	94.80	0.93	9.76E+02	33.55
620	78.21	86.02	1.52E+03	8.12E-02	69.10	0.96	1.01E+03	33.71
625	78.90	75.27	1.37E+03	7.86E-02	64.20	0.96	1.13E+03	33.86
630	79.59	98.66	1.63E+03	8.03E-02	73.00	0.96	1.05E+03	34.00
635	80.28	92.47	1.25E+03	7.82E-02	68.00	0.95	9.84E+02	34.15
640	80.97	84.68	1.23E+03	7.35E-02	69.30	0.95	1.04E+03	34.30

Depth	Age	kappa	IRM_{300mT}	ARM_{100}/IRM_{100}	$HIRM_{[300\&2700]}$	S-ratio $_{[300\&2700]}$	Fe/kappa	Age
[cm]	*cal [kyr]*	*[10**-6 SI]*	*[mA/m]*	-	-	-	*[cps/10**-6 SI]*	*cal [kyr]*
645	81.66	97.31	1.19E+03	6.68E-02	91.00	0.93	1.02E+03	34.45
650.5	82.42	146.51	1.44E+03	6.29E-02	148.00	0.91	9.78E+02	34.60
655	83.04	125.81	1.17E+03	7.00E-02	127.20	0.90	9.44E+02	34.74
661	83.87	121.24	9.57E+02	7.58E-02	118.37	0.89	9.71E+02	34.89
665	84.42	122.85	9.73E+02	7.22E-02	113.66	0.90	8.72E+02	35.04
670	85.11	72.85	1.25E+03	7.91E-02	74.70	0.94	9.28E+02	35.25
							9.49E+02	35.54
							6.81E+02	36.12
							7.00E+02	36.34
							7.29E+02	36.50
							7.90E+02	36.62
							1.03E+03	36.74
							9.80E+02	36.85
							1.05E+03	36.93
							1.18E+03	37.00
							1.13E+03	37.07
							9.29E+02	37.15
							8.40E+02	37.21
							9.59E+02	37.28
							9.72E+02	37.35
							1.03E+03	37.42
							9.74E+02	37.49
							9.30E+02	37.55
							9.74E+02	37.62
							1.04E+03	37.69
							8.16E+02	37.76

Depth	Age	kappa	IRM_{300mT}	ARM_{100}/IRM_{100}	$HIRM_{[300\&2700]}$	S-ratio $_{[300\&2700]}$	Fe/kappa	Age
[cm]	*cal [kyr]*	*[10**-6 SI]*	*[mA/m]*	-	-	-	*[cps/10**-6 SI]*	*cal [kyr]*
							1.02E+03	37.83
							1.21E+03	37.89
							1.27E+03	37.96
							1.30E+03	38.03
							1.29E+03	38.11
							1.28E+03	38.21
							1.31E+03	38.32
							1.28E+03	38.45
							1.21E+03	38.63
							1.26E+03	38.87
							1.30E+03	39.13
							1.30E+03	39.39
							1.34E+03	39.59
							1.29E+03	39.77
							9.79E+02	39.94
							1.19E+03	40.11
							1.21E+03	40.28
							1.04E+03	40.45
							1.02E+03	40.62
							9.89E+02	40.79
							9.56E+02	40.96
							8.89E+02	41.14
							8.67E+02	41.32
							8.28E+02	41.54
							8.69E+02	41.81
							1.04E+03	42.07

Depth	Age	kappa	IRM_{300mT}	ARM_{100}/IRM_{100}	$HIRM_{[300\&2700]}$	S-ratio $_{[300\&2700]}$	Fe/kappa	Age
[cm]	*cal [kyr]*	*[10**-6 SI]*	*[mA/m]*	-	-	-	*[cps/10**-6 SI]*	*cal [kyr]*
							1.19E+03	42.33
							1.13E+03	42.60
							1.15E+03	42.88
							1.07E+03	43.22
							1.05E+03	44.20
							8.29E+02	44.68
							9.61E+02	45.05
							9.97E+02	45.32
							1.01E+03	45.55
							9.89E+02	45.78
							1.19E+03	46.01
							1.20E+03	46.24
							1.27E+03	46.47
							1.29E+03	46.69
							1.26E+03	46.93
							1.38E+03	47.16
							1.43E+03	47.39
							1.36E+03	47.61
							1.39E+03	47.80
							1.42E+03	47.99
							1.33E+03	48.13
							1.30E+03	48.21
							1.11E+03	48.23
							1.04E+03	48.28
							1.09E+03	48.58
							1.15E+03	48.87

Depth	Age	kappa	IRM_{300mT}	ARM_{100}/IRM_{100}	$HIRM_{[300\&2700]}$	S-ratio $_{[300\&2700]}$	Fe/kappa	Age
[cm]	*cal [kyr]*	*[10**-6 SI]*	*[mA/m]*	-	-	-	*[cps/10**-6 SI]*	*cal [kyr]*
							1.10E+03	49.15
							1.24E+03	49.44
							1.18E+03	49.73
							1.00E+03	50.03
							1.08E+03	50.32
							9.90E+02	50.60
							9.14E+02	50.89
							1.01E+03	51.18
							9.49E+02	51.48
							9.48E+02	51.77
							9.06E+02	52.06
							9.56E+02	52.35
							8.77E+02	52.65
							9.01E+02	52.94
							8.86E+02	53.23
							8.52E+02	53.52
							9.62E+02	53.81
							1.24E+03	54.10
							1.27E+03	54.39
							1.39E+03	54.68
							1.39E+03	54.97
							1.30E+03	55.26
							1.21E+03	55.55
							1.20E+03	55.84
							1.07E+03	56.13
							1.09E+03	56.41

Depth	Age	kappa	IRM_{300mT}	ARM_{100}/IRM_{100}	$HIRM_{[300\&2700]}$	S-ratio $_{[300\&2700]}$	Fe/kappa	Age
[cm]	*cal [kyr]*	*[10**-6 SI]*	*[mA/m]*	-	-	-	*[cps/10**-6 SI]*	*cal [kyr]*
							1.09E+03	56.75
							7.35E+02	57.31
							7.09E+02	57.58
							8.87E+02	57.87
							9.32E+02	58.16
							1.07E+03	58.46
							1.02E+03	58.76
							1.15E+03	58.90
							1.27E+03	59.62
							1.29E+03	60.06
							1.34E+03	60.21
							1.38E+03	60.50
							1.33E+03	60.78
							1.35E+03	61.07
							1.38E+03	61.36
							1.38E+03	61.66
							1.38E+03	61.95
							1.34E+03	62.23
							1.26E+03	62.52
							1.34E+03	62.81
							1.32E+03	63.11
							1.18E+03	63.40
							1.29E+03	63.69
							1.30E+03	63.98
							1.25E+03	64.27
							1.36E+03	64.57

Depth	Age	kappa	IRM_{300mT}	ARM_{100}/IRM_{100}	$HIRM_{[300\&2700]}$	S-ratio $_{[300\&2700]}$	Fe/kappa	Age
[cm]	*cal [kyr]*	*[10**-6 SI]*	*[mA/m]*	-	-	-	*[cps/10**-6 SI]*	*cal [kyr]*
							1.40E+03	64.86
							1.06E+03	65.20
							1.04E+03	65.60
							1.38E+03	66.00
							1.32E+03	66.40
							1.20E+03	66.80
							1.03E+03	67.20
							1.01E+03	67.61
							8.21E+02	68.01
							6.74E+02	68.41
							1.13E+03	68.81
							1.19E+03	69.21
							1.30E+03	69.61
							1.25E+03	70.01
							1.34E+03	70.41
							7.09E+02	70.81
							7.74E+02	71.15
							8.39E+02	71.43
							6.21E+02	71.71
							6.88E+02	71.99
							6.75E+02	72.26
							7.65E+02	72.54
							9.39E+02	72.86
							9.68E+02	73.38
							1.04E+03	73.64
							1.21E+03	73.92

Depth	Age	kappa	IRM_{300mT}	ARM_{100}/IRM_{100}	$HIRM_{[300\&2700]}$	S-ratio $_{[300\&2700]}$	Fe/kappa	Age
[cm]	*cal [kyr]*	*[10**-6 SI]*	*[mA/m]*	-	-	-	*[cps/10**-6 SI]*	*cal [kyr]*
							1.10E+03	74.20
							1.12E+03	74.47
							1.13E+03	74.75
							1.20E+03	75.02
							1.26E+03	75.30
							1.22E+03	75.58
							1.15E+03	75.85
							6.40E+02	76.13
							7.24E+02	76.40
							7.92E+02	76.68
							7.71E+02	76.96
							7.90E+02	77.24
							7.74E+02	77.52
							7.22E+02	77.79
							6.36E+02	78.07
							6.12E+02	78.35
							6.32E+02	78.62
							6.94E+02	78.90
							7.67E+02	79.17
							6.92E+02	79.45
							7.42E+02	79.73
							6.83E+02	80.00
							6.69E+02	80.28
							9.26E+02	80.55
							9.16E+02	80.83
							6.69E+02	81.11

Depth	Age	kappa	IRM_{300mT}	ARM_{100}/IRM_{100}	HIRM [300&2700]	S-ratio [300&2700]	Fe/kappa	Age
[cm]	*cal [kyr]*	*[10**-6 SI]*	*[mA/m]*	-	-	-	*[cps/10**-6 SI]*	*cal [kyr]*
							6.12E+02	81.38
							6.98E+02	81.66
							6.22E+02	81.93
							6.90E+02	82.21
							7.14E+02	82.49
							8.41E+02	82.76
							9.17E+02	83.04
							1.06E+03	83.32
							8.97E+02	83.60
							1.13E+03	83.88
							1.26E+03	84.15
							1.30E+03	84.42
							1.20E+03	84.69

GeoB3911-3

Depth	Age	kappa	IRM_{300mT}	ARM_{100}/IRM_{100}	HIRM [300&2700]	S-ratio [300&2700]	Fe/kappa	Age
[cm]	*cal [kyr]*	*[10**-6 SI]*	*[mA/m]*	-	-	-	*[cps/10**-6 SI]*	*cal [kyr]*
5	0.43	61.10	1.22E+03	1.67E-01	5.12E+01	0.96	8.42E+02	0.087
15	1.30	66.20	1.28E+03	1.69E-01	5.41E+01	0.96	6.30E+02	0.174
25	2.12	70.30	1.33E+03	1.69E-01	6.21E+01	0.96	6.17E+02	0.260
35	2.81	66.30	1.55E+03	1.71E-01	7.82E+01	0.95	6.71E+02	0.347
45	3.50	64.40	1.54E+03	1.72E-01	6.32E+01	0.96	8.73E+02	0.434
55	4.06	58.30	1.37E+03	1.73E-01	5.60E+01	0.96	7.87E+02	0.521
65	4.49	62.20	1.67E+03	1.76E-01	7.21E+01	0.96	5.53E+02	0.608
75	5.34	66.10	1.71E+03	1.81E-01	9.43E+01	0.95	5.78E+02	0.695
85	6.19	71.60	1.51E+03	1.78E-01	5.95E+01	0.96	5.26E+02	0.781

Depth	**Age**	**kappa**	**IRM_{300mT}**	**ARM_{100}/IRM_{100}**	**HIRM [300&2700]**	**S-ratio [300&2700]**	**Fe/kappa**	**Age**
[cm]	*cal [kyr]*	*[10**-6 SI]*	*[mA/m]*	-	-	-	*[cps/10**-6 SI]*	*cal [kyr]*
95	6.73	85.30	1.60E+03	1.78E-01	6.86E+01	0.96	5.32E+02	0.868
105	6.98	71.00	1.21E+03	1.77E-01	4.39E+01	0.97	5.15E+02	0.955
115	7.23	76.70	1.34E+03	1.75E-01	4.15E+01	0.97	5.56E+02	1.042
125	7.53	75.10	1.40E+03	1.74E-01	4.27E+01	0.97	5.51E+02	1.129
135	7.85	71.50	1.34E+03	1.70E-01	4.97E+01	0.96	4.92E+02	1.215
145	8.18	78.50	1.24E+03	1.66E-01	5.20E+01	0.96	4.48E+02	1.302
155	8.50	85.00	1.12E+03	1.57E-01	6.05E+01	0.95	4.84E+02	1.389
165	8.83	97.40	1.13E+03	1.50E-01	5.67E+01	0.95	4.85E+02	1.476
175	9.16	90.70	1.09E+03	1.40E-01	6.21E+01	0.95	4.77E+02	1.563
185	9.48	96.20	9.79E+02	1.42E-01	6.42E+01	0.94	4.86E+02	1.650
195	9.81	111.20	8.59E+02	1.28E-01	5.96E+01	0.94	4.75E+02	1.736
205	10.13	102.10	9.95E+02	1.36E-01	6.84E+01	0.94	4.54E+02	1.823
215	10.42	112.20	9.36E+02	1.31E-01	7.89E+01	0.92	4.84E+02	1.910
225	10.69	111.40	9.04E+02	1.28E-01	8.07E+01	0.92	4.22E+02	1.979
235	10.97	131.60	9.52E+02	1.23E-01	9.67E+01	0.91	4.99E+02	2.048
245	11.15	135.60	9.73E+02	1.17E-01	9.40E+01	0.91	4.45E+02	2.117
255	11.20	123.20	9.57E+02	1.11E-01	1.01E+02	0.90	3.52E+02	2.186
265	11.25	106.00	9.40E+02	1.18E-01	9.95E+01	0.90	4.65E+02	2.255
275	11.29	90.40	9.91E+02	1.23E-01	9.13E+01	0.92	4.99E+02	2.324
285	11.34	91.90	9.40E+02	1.18E-01	8.94E+01	0.91	4.39E+02	2.393
295	11.39	89.10	9.88E+02	1.25E-01	9.54E+01	0.91	4.67E+02	2.462
305	11.44	84.20	9.01E+02	1.29E-01	8.65E+01	0.91	3.87E+02	2.531
315	11.68	90.10	7.99E+02	1.24E-01	9.07E+01	0.90	4.19E+02	2.600
325	11.97	85.20	6.93E+02	1.12E-01	8.09E+01	0.90	4.78E+02	2.669
335	12.10	83.00	5.73E+02	1.09E-01	6.51E+01	0.90	4.69E+02	2.738
345	12.12	83.50	4.84E+02	1.13E-01	6.60E+01	0.88	4.94E+02	2.807

Depth	**Age**	**kappa**	**IRM_{300mT}**	**ARM_{100}/IRM_{100}**	**HIRM [300&2700]**	**S-ratio [300&2700]**	**Fe/kappa**	**Age**
[cm]	*cal [kyr]*	*[10**-6 SI]*	*[mA/m]*	-	-	-	*[cps/10**-6 SI]*	*cal [kyr]*
355	12.14	81.30	4.85E+02	1.09E-01	6.94E+01	0.87	5.26E+02	2.876
365	12.16	85.00	4.42E+02	1.02E-01	5.60E+01	0.89	5.28E+02	2.945
375	12.18	85.00	4.63E+02	1.10E-01	5.74E+01	0.89	5.08E+02	3.014
385	12.19	95.70	5.50E+02	1.09E-01	6.10E+01	0.90	4.63E+02	3.083
395	12.21	108.40	6.92E+02	1.15E-01	7.02E+01	0.91	4.38E+02	3.152
405	12.23	100.80	7.26E+02	1.24E-01	7.59E+01	0.91	4.04E+02	3.221
415	12.25	103.00	6.07E+02	1.35E-01	7.77E+01	0.89	3.70E+02	3.290
425	12.27	100.80	6.12E+02	1.46E-01	6.91E+01	0.90	4.56E+02	3.359
435	12.29	96.90	7.35E+02	1.40E-01	7.54E+01	0.91	4.50E+02	3.428
445	12.31	112.50	8.35E+02	1.13E-01	1.11E+02	0.88	4.37E+02	3.497
455	12.41	133.20	1.09E+03	8.70E-02	1.42E+02	0.88	4.39E+02	3.566
465	12.73	149.30	1.11E+03	7.65E-02	1.63E+02	0.87	4.72E+02	3.635
475	13.04	160.60	1.19E+03	7.22E-02	1.76E+02	0.87	4.74E+02	3.704
485	13.35	168.90	1.16E+03	7.03E-02	1.90E+02	0.86	4.98E+02	3.773
495	13.61	172.30	1.15E+03	7.32E-02	1.79E+02	0.86	5.05E+02	3.842
505	13.78	141.20	7.68E+02	1.69E-01	1.53E+02	0.83	5.32E+02	3.911
515	13.95	115.50	1.18E+03	4.47E-03	1.21E+02	0.91	5.51E+02	3.980
525	14.17	83.90	2.33E+02	9.14E-03	3.93E+01	0.86	5.76E+02	4.005
535	14.56	68.00	6.75E+01	3.91E-02	9.53E+00	0.88	5.29E+02	4.030
545	14.92	70.30	6.47E+01	4.85E-02	8.73E+00	0.88	5.21E+02	4.055
555	15.09	72.20	8.15E+01	5.41E-02	1.10E+01	0.88	5.60E+02	4.080
565	15.27	97.30	1.90E+02	8.31E-02	2.20E+01	0.90	5.87E+02	4.105
575	15.44	123.90	5.63E+02	6.06E-02	7.64E+01	0.88	6.25E+02	4.130
585	15.62	135.00	6.81E+02	1.49E-01	8.71E+01	0.89	6.12E+02	4.155
595	15.79	143.3	1.09E+03	8.57E-02	1.15E+02	0.90	5.82E+02	4.180
605	15.97	135	1.07E+03	7.20E-02	1.28E+02	0.89	6.05E+02	4.205

Depth	**Age**	**kappa**	**IRM_{300mT}**	**ARM_{100}/IRM_{100}**	**HIRM [300&2700]**	**S-ratio [300&2700]**	**Fe/kappa**	**Age**
[cm]	*cal [kyr]*	*[10**-6 SI]*	*[mA/m]*	-	-	-	*[cps/10**-6 SI]*	*cal [kyr]*
615	16.14	143.4	1.09E+03	4.86E-02	1.27E+02	0.90	6.92E+02	4.230
625	16.32	150.3	8.11E+02	6.92E-02	8.63E+01	0.90	6.36E+02	4.315
635	16.49	158.8	8.44E+02	6.78E-02	9.67E+01	0.90	6.18E+02	4.400
645	16.67	156	7.22E+02	5.76E-02	8.02E+01	0.90	7.39E+02	4.485
655	18.13	179.5	1.51E+03	9.32E-03	1.09E+02	0.93	6.58E+02	4.570
665	20.14	133	4.61E+02	2.57E-02	7.23E+01	0.86	6.67E+02	4.655
675	22.17	131.30	3.99E+02	3.03E-05	7.86E+01	0.84	7.12E+02	4.740
							7.65E+02	4.825
							7.78E+02	4.910
							7.51E+02	4.995
							6.72E+02	5.080
							7.08E+02	5.165
							7.49E+02	5.250
							7.93E+02	5.335
							8.52E+02	5.420
							5.57E+02	5.505
							6.50E+02	5.590
							8.47E+02	5.675
							9.00E+02	5.760
							5.58E+02	5.845
							8.56E+02	5.930
							1.06E+03	6.015
							1.02E+03	6.100
							1.07E+03	6.185
							1.10E+03	6.270
							1.12E+03	6.355

Depth	Age	kappa	IRM_{300mT}	ARM_{100}/IRM_{100}	$HIRM_{[300\&2700]}$	$S\text{-}ratio_{[300\&2700]}$	Fe/kappa	Age
[cm]	*cal [kyr]*	*[10**-6 SI]*	*[mA/m]*	-	-	-	*[cps/10**-6 SI]*	*cal [kyr]*
							1.09E+03	6.440
							9.29E+02	6.525
							9.35E+02	6.610
							9.95E+02	6.635
							8.55E+02	6.660
							8.40E+02	6.684
							8.74E+02	6.709
							8.00E+02	6.734
							8.23E+02	6.759
							7.00E+02	6.809
							8.28E+02	6.833
							9.00E+02	6.858
							8.88E+02	6.883
							8.91E+02	6.908
							9.32E+02	6.933
							9.98E+02	6.958
							1.08E+03	6.982
							1.08E+03	7.007
							9.28E+02	7.032
							9.46E+02	7.057
							1.04E+03	7.082
							1.06E+03	7.107
							1.13E+03	7.131
							1.11E+03	7.156
							1.18E+03	7.181
							1.08E+03	7.206

Depth	Age	kappa	IRM_{300mT}	ARM_{100}/IRM_{100}	$HIRM_{[300\&2700]}$	$S\text{-}ratio_{[300\&2700]}$	Fe/kappa	Age
[cm]	*cal [kyr]*	*[10**-6 SI]*	*[mA/m]*	-	-	-	*[cps/10**-6 SI]*	*cal [kyr]*
							1.11E+03	7.231
							1.10E+03	7.256
							1.16E+03	7.280
							1.12E+03	7.305
							1.10E+03	7.330
							1.12E+03	7.363
							1.11E+03	7.395
							1.19E+03	7.428
							1.19E+03	7.460
							1.18E+03	7.493
							1.15E+03	7.526
							1.18E+03	7.558
							1.19E+03	7.591
							1.14E+03	7.624
							1.09E+03	7.656
							9.83E+02	7.689
							1.03E+03	7.721
							1.11E+03	7.754
							1.15E+03	7.787
							1.11E+03	7.819
							1.16E+03	7.852
							1.15E+03	7.884
							1.05E+03	7.917
							1.11E+03	7.950
							1.07E+03	7.982
							1.09E+03	8.015

Depth	Age	kappa	IRM_{300mT}	ARM_{100}/IRM_{100}	$HIRM_{[300\&2700]}$	$S\text{-}ratio_{[300\&2700]}$	Fe/kappa	Age
[cm]	*cal [kyr]*	*[10**-6 SI]*	*[mA/m]*	-	-	-	*[cps/10**-6 SI]*	*cal [kyr]*
							1.09E+03	8.048
							1.10E+03	8.080
							1.14E+03	8.113
							1.18E+03	8.145
							1.13E+03	8.178
							1.25E+03	8.211
							1.27E+03	8.243
							1.16E+03	8.276
							1.12E+03	8.308
							1.06E+03	8.341
							1.03E+03	8.374
							1.09E+03	8.406
							1.09E+03	8.439
							1.08E+03	8.471
							1.11E+03	8.504
							1.15E+03	8.537
							1.16E+03	8.569
							1.15E+03	8.602
							1.22E+03	8.635
							1.28E+03	8.667
							1.23E+03	8.700
							1.27E+03	8.732
							1.16E+03	8.765
							1.13E+03	8.798
							9.91E+02	8.830
							9.80E+02	8.863

Depth	Age	kappa	IRM_{300mT}	ARM_{100}/IRM_{100}	$HIRM_{[300\&2700]}$	$S\text{-}ratio_{[300\&2700]}$	Fe/kappa	Age
[cm]	*cal [kyr]*	*[10**-6 SI]*	*[mA/m]*	*-*	*-*	*-*	*[cps/10**-6 SI]*	*cal [kyr]*
							9.88E+02	8.895
							1.11E+03	8.928
							1.13E+03	8.961
							1.15E+03	8.993
							1.12E+03	9.026
							1.10E+03	9.059
							1.09E+03	9.091
							1.04E+03	9.124
							1.13E+03	9.156
							1.04E+03	9.189
							1.06E+03	9.222
							1.10E+03	9.254
							1.08E+03	9.287
							1.08E+03	9.319
							1.06E+03	9.352
							1.11E+03	9.385
							1.10E+03	9.417
							1.10E+03	9.483
							1.07E+03	9.515
							1.13E+03	9.548
							1.22E+03	9.580
							1.30E+03	9.613
							1.28E+03	9.646
							1.21E+03	9.678
							1.20E+03	9.711
							1.23E+03	9.743

Depth	Age	kappa	IRM_{300mT}	ARM_{100}/IRM_{100}	$HIRM_{[300\&2700]}$	$S\text{-}ratio_{[300\&2700]}$	Fe/kappa	Age
[cm]	*cal [kyr]*	*[10**-6 SI]*	*[mA/m]*	-	-	-	*[cps/10**-6 SI]*	*cal [kyr]*
							1.10E+03	9.776
							1.10E+03	9.809
							1.16E+03	9.841
							1.08E+03	9.874
							9.64E+02	9.906
							1.19E+03	9.939
							1.20E+03	9.972
							1.13E+03	10.004
							1.09E+03	10.037
							1.12E+03	10.070
							1.19E+03	10.102
							1.24E+03	10.135
							1.31E+03	10.167
							1.24E+03	10.200
							1.23E+03	10.227
							1.11E+03	10.255
							1.14E+03	10.282
							1.05E+03	10.309
							1.16E+03	10.337
							1.16E+03	10.364
							1.17E+03	10.391
							1.14E+03	10.419
							1.17E+03	10.446
							1.24E+03	10.474
							1.14E+03	10.501
							1.25E+03	10.528

Depth	Age	kappa	IRM_{300mT}	ARM_{100}/IRM_{100}	$HIRM_{[300\&2700]}$	$S\text{-}ratio_{[300\&2700]}$	Fe/kappa	Age
[cm]	*cal [kyr]*	*[10**-6 SI]*	*[mA/m]*	-	-	-	*[cps/10**-6 SI]*	*cal [kyr]*
							1.30E+03	10.556
							1.26E+03	10.583
							1.28E+03	10.610
							1.27E+03	10.638
							1.34E+03	10.665
							1.22E+03	10.692
							1.18E+03	10.720
							1.11E+03	10.747
							1.08E+03	10.774
							1.09E+03	10.802
							1.20E+03	10.829
							1.09E+03	10.856
							1.06E+03	10.884
							1.12E+03	10.911
							1.12E+03	10.939
							1.15E+03	10.966
							1.22E+03	10.993
							1.09E+03	11.021
							1.12E+03	11.048
							1.18E+03	11.075
							1.18E+03	11.103
							1.07E+03	11.130
							1.23E+03	11.135
							1.32E+03	11.140
							1.15E+03	11.145
							1.15E+03	11.149

Depth	Age	kappa	IRM_{300mT}	ARM_{100}/IRM_{100}	$HIRM_{[300\&2700]}$	$S\text{-}ratio_{[300\&2700]}$	Fe/kappa	Age
[cm]	*cal [kyr]*	*[10**-6 SI]*	*[mA/m]*	-	-	-	*[cps/10**-6 SI]*	*cal [kyr]*
							1.15E+03	11.154
							1.13E+03	11.159
							1.12E+03	11.164
							9.80E+02	11.169
							9.86E+02	11.174
							1.09E+03	11.178
							1.17E+03	11.183
							1.18E+03	11.188
							1.19E+03	11.193
							1.29E+03	11.198
							1.30E+03	11.203
							1.35E+03	11.208
							1.37E+03	11.212
							1.38E+03	11.217
							1.32E+03	11.222
							1.32E+03	11.227
							1.39E+03	11.232
							1.37E+03	11.237
							1.42E+03	11.242
							1.34E+03	11.246
							1.39E+03	11.251
							1.40E+03	11.256
							1.34E+03	11.261
							1.45E+03	11.266
							1.56E+03	11.271
							1.44E+03	11.275

Depth	**Age**	**kappa**	**IRM_{300mT}**	**ARM_{100}/IRM_{100}**	**HIRM [300&2700]**	**S-ratio [300&2700]**	**Fe/kappa**	**Age**
[cm]	*cal [kyr]*	*[10**-6 SI]*	*[mA/m]*	*-*	*-*	*-*	*[cps/10**-6 SI]*	*cal [kyr]*
							1.60E+03	11.280
							1.60E+03	11.285
							1.58E+03	11.290
							1.61E+03	11.295
							1.63E+03	11.300
							1.62E+03	11.305
							1.61E+03	11.309
							1.67E+03	11.314
							1.60E+03	11.319
							1.56E+03	11.324
							1.56E+03	11.329
							1.57E+03	11.334
							1.69E+03	11.338
							1.62E+03	11.343
							1.67E+03	11.348
							1.75E+03	11.353
							1.71E+03	11.358
							1.75E+03	11.363
							1.63E+03	11.368
							1.64E+03	11.372
							1.67E+03	11.377
							1.73E+03	11.382
							1.74E+03	11.387
							1.76E+03	11.392
							1.70E+03	11.397
							1.68E+03	11.402

Depth	Age	kappa	IRM_{300mT}	ARM_{100}/IRM_{100}	$HIRM_{[300\&2700]}$	$S\text{-}ratio_{[300\&2700]}$	Fe/kappa	Age
[cm]	*cal [kyr]*	*[10**-6 SI]*	*[mA/m]*	-	-	-	*[cps/10**-6 SI]*	*cal [kyr]*
							1.73E+03	11.406
							1.71E+03	11.411
							1.69E+03	11.416
							1.82E+03	11.421
							1.80E+03	11.426
							1.75E+03	11.431
							1.77E+03	11.435
							1.81E+03	11.440
							1.83E+03	11.445
							1.83E+03	11.450
							1.88E+03	11.479
							1.86E+03	11.508
							1.94E+03	11.537
							1.90E+03	11.566
							1.90E+03	11.595
							1.75E+03	11.625
							1.72E+03	11.654
							1.75E+03	11.683
							1.79E+03	11.712
							1.73E+03	11.741
							1.79E+03	11.770
							1.81E+03	11.799
							1.85E+03	11.828
							1.93E+03	11.857
							1.85E+03	11.886
							1.82E+03	11.915

Depth	Age	kappa	IRM_{300mT}	ARM_{100}/IRM_{100}	$HIRM_{[300\&2700]}$	$S\text{-}ratio_{[300\&2700]}$	Fe/kappa	Age
[cm]	*cal [kyr]*	*[10**-6 SI]*	*[mA/m]*	-	-	-	*[cps/10**-6 SI]*	*cal [kyr]*
							1.83E+03	11.945
							1.85E+03	11.974
							1.90E+03	12.003
							1.90E+03	12.032
							1.90E+03	12.061
							1.95E+03	12.090
							1.89E+03	12.092
							1.90E+03	12.094
							1.89E+03	12.096
							1.94E+03	12.097
							1.89E+03	12.099
							1.84E+03	12.101
							1.85E+03	12.103
							1.88E+03	12.105
							1.94E+03	12.107
							1.86E+03	12.109
							1.90E+03	12.111
							1.87E+03	12.112
							1.92E+03	12.114
							1.94E+03	12.116
							1.92E+03	12.118
							1.85E+03	12.120
							1.76E+03	12.122
							1.75E+03	12.124
							1.77E+03	12.126
							1.85E+03	12.127

Depth	Age	kappa	IRM_{300mT}	ARM_{100}/IRM_{100}	$HIRM_{[300\&2700]}$	$S\text{-}ratio_{[300\&2700]}$	Fe/kappa	Age
[cm]	*cal [kyr]*	*[10**-6 SI]*	*[mA/m]*	-	-	-	*[cps/10**-6 SI]*	*cal [kyr]*
							1.78E+03	12.129
							1.74E+03	12.131
							1.80E+03	12.133
							1.82E+03	12.135
							1.90E+03	12.137
							1.97E+03	12.139
							2.09E+03	12.140
							2.06E+03	12.142
							1.99E+03	12.144
							1.90E+03	12.146
							1.95E+03	12.148
							1.95E+03	12.150
							1.95E+03	12.152
							1.97E+03	12.154
							1.88E+03	12.155
							2.00E+03	12.157
							1.98E+03	12.159
							2.02E+03	12.161
							1.98E+03	12.163
							2.15E+03	12.165
							2.03E+03	12.167
							1.92E+03	12.169
							1.95E+03	12.170
							1.98E+03	12.172
							2.01E+03	12.174
							1.98E+03	12.176

Depth	Age	kappa	IRM_{300mT}	ARM_{100}/IRM_{100}	$HIRM_{[300\&2700]}$	$S\text{-}ratio_{[300\&2700]}$	Fe/kappa	Age
[cm]	*cal [kyr]*	*[10**-6 SI]*	*[mA/m]*	-	-	-	*[cps/10**-6 SI]*	*cal [kyr]*
							1.93E+03	12.178
							1.90E+03	12.180
							1.83E+03	12.182
							1.86E+03	12.183
							1.91E+03	12.185
							1.86E+03	12.187
							1.84E+03	12.189
							1.76E+03	12.191
							1.93E+03	12.193
							1.80E+03	12.195
							1.87E+03	12.197
							1.92E+03	12.198
							1.99E+03	12.200
							1.86E+03	12.202
							1.62E+03	12.204
							1.49E+03	12.206
							1.44E+03	12.208
							1.40E+03	12.210
							1.41E+03	12.212
							1.53E+03	12.213
							1.67E+03	12.215
							1.73E+03	12.217
							1.77E+03	12.219
							1.76E+03	12.221
							1.83E+03	12.223
							1.86E+03	12.225

Depth	Age	kappa	IRM_{300mT}	ARM_{100}/IRM_{100}	$HIRM_{[300\&2700]}$	$S\text{-}ratio_{[300\&2700]}$	Fe/kappa	Age
[cm]	*cal [kyr]*	*[10**-6 SI]*	*[mA/m]*	-	-	-	*[cps/10**-6 SI]*	*cal [kyr]*
							1.88E+03	12.227
							1.77E+03	12.228
							1.84E+03	12.230
							1.91E+03	12.232
							1.86E+03	12.234
							1.82E+03	12.236
							1.92E+03	12.238
							1.77E+03	12.240
							1.72E+03	12.241
							1.77E+03	12.243
							1.75E+03	12.245
							1.72E+03	12.247
							1.82E+03	12.249
							1.87E+03	12.251
							1.86E+03	12.253
							1.86E+03	12.255
							1.88E+03	12.256
							1.87E+03	12.258
							1.90E+03	12.260
							1.95E+03	12.262
							1.86E+03	12.264
							1.75E+03	12.266
							1.83E+03	12.268
							1.78E+03	12.270
							1.90E+03	12.271
							2.03E+03	12.273

Depth	Age	kappa	IRM_{300mT}	ARM_{100}/IRM_{100}	$HIRM_{[300\&2700]}$	$S\text{-}ratio_{[300\&2700]}$	Fe/kappa	Age
[cm]	*cal [kyr]*	*[10**-6 SI]*	*[mA/m]*	-	-	-	*[cps/10**-6 SI]*	*cal [kyr]*
							1.92E+03	12.275
							1.75E+03	12.277
							1.56E+03	12.279
							1.45E+03	12.281
							1.52E+03	12.283
							1.55E+03	12.284
							1.68E+03	12.286
							1.62E+03	12.288
							1.66E+03	12.290
							1.57E+03	12.292
							1.62E+03	12.294
							1.55E+03	12.296
							1.51E+03	12.298
							1.49E+03	12.299
							1.53E+03	12.301
							1.46E+03	12.303
							1.46E+03	12.305
							1.48E+03	12.307
							1.48E+03	12.309
							1.48E+03	12.311
							1.40E+03	12.313
							1.40E+03	12.314
							1.30E+03	12.316
							1.37E+03	12.318
							1.37E+03	12.320
							1.32E+03	12.351

Depth	**Age**	**kappa**	**IRM_{300mT}**	**ARM_{100}/IRM_{100}**	**HIRM [300&2700]**	**S-ratio [300&2700]**	**Fe/kappa**	**Age**
[cm]	*cal [kyr]*	*[10**-6 SI]*	*[mA/m]*	*-*	*-*	*-*	*[cps/10**-6 SI]*	*cal [kyr]*
							1.28E+03	12.383
							1.28E+03	12.414
							1.25E+03	12.445
							1.25E+03	12.476
							1.31E+03	12.508
							1.31E+03	12.539
							1.28E+03	12.570
							1.29E+03	12.602
							1.25E+03	12.633
							1.25E+03	12.664
							1.30E+03	12.695
							1.31E+03	12.727
							1.27E+03	12.758
							1.32E+03	12.789
							1.25E+03	12.821
							1.20E+03	12.852
							1.19E+03	12.883
							1.17E+03	12.914
							1.27E+03	12.946
							1.31E+03	12.977
							1.40E+03	13.008
							1.37E+03	13.039
							1.27E+03	13.071
							1.32E+03	13.102
							1.28E+03	13.133
							1.33E+03	13.165

Depth	Age	kappa	IRM_{300mT}	ARM_{100}/IRM_{100}	$HIRM_{[300\&2700]}$	$S\text{-}ratio_{[300\&2700]}$	Fe/kappa	Age
[cm]	*cal [kyr]*	*[10**-6 SI]*	*[mA/m]*	-	-	-	*[cps/10**-6 SI]*	*cal [kyr]*
							1.40E+03	13.196
							1.42E+03	13.227
							1.37E+03	13.258
							1.34E+03	13.290
							1.31E+03	13.321
							1.30E+03	13.352
							1.25E+03	13.384
							1.32E+03	13.415
							1.37E+03	13.446
							1.34E+03	13.477
							1.23E+03	13.509
							1.34E+03	13.626
							1.46E+03	13.643
							1.24E+03	13.660
							1.30E+03	13.678
							1.40E+03	13.695
							1.50E+03	13.712
							1.54E+03	13.729
							1.57E+03	13.746
							1.56E+03	13.763
							1.50E+03	13.781
							1.41E+03	13.798
							1.41E+03	13.815
							1.47E+03	13.832
							1.49E+03	13.849
							1.43E+03	13.867

Depth	**Age**	**kappa**	**IRM_{300mT}**	**ARM_{100}/IRM_{100}**	**HIRM [300&2700]**	**S-ratio [300&2700]**	**Fe/kappa**	**Age**
[cm]	*cal [kyr]*	*[10**-6 SI]*	*[mA/m]*	*-*	*-*	*-*	*[cps/10**-6 SI]*	*cal [kyr]*
							1.50E+03	13.884
							1.58E+03	13.901
							1.55E+03	13.918
							1.55E+03	13.935
							1.50E+03	13.953
							1.57E+03	13.970
							1.59E+03	13.987
							1.53E+03	14.004
							1.52E+03	14.021
							1.53E+03	14.038
							1.69E+03	14.056
							1.84E+03	14.073
							2.02E+03	14.090
							2.04E+03	14.130
							1.84E+03	14.169
							2.05E+03	14.209
							2.15E+03	14.248
							2.15E+03	14.288
							2.21E+03	14.327
							2.39E+03	14.367
							2.34E+03	14.406
							2.45E+03	14.446
							2.34E+03	14.485
							2.35E+03	14.525
							2.42E+03	14.564
							2.71E+03	14.604

Depth	Age	kappa	IRM_{300mT}	ARM_{100}/IRM_{100}	$HIRM_{[300\&2700]}$	$S\text{-}ratio_{[300\&2700]}$	Fe/kappa	Age
[cm]	*cal [kyr]*	*[10**-6 SI]*	*[mA/m]*	-	-	-	*[cps/10**-6 SI]*	*cal [kyr]*
							2.61E+03	14.643
							2.42E+03	14.683
							2.32E+03	14.722
							2.16E+03	14.762
							2.05E+03	14.801
							2.19E+03	14.841
							2.27E+03	14.880
							2.30E+03	14.898
							2.43E+03	14.915
							2.29E+03	14.933
							2.11E+03	14.950
							1.99E+03	14.968
							2.03E+03	14.985
							2.10E+03	15.003
							2.11E+03	15.020
							2.26E+03	15.038
							2.29E+03	15.055
							2.36E+03	15.073
							2.18E+03	15.090
							2.21E+03	15.108
							2.29E+03	15.125
							2.02E+03	15.143
							1.88E+03	15.160
							1.99E+03	15.178
							1.95E+03	15.195
							1.83E+03	15.213

Depth	**Age**	**kappa**	**IRM_{300mT}**	**ARM_{100}/IRM_{100}**	**HIRM [300&2700]**	**S-ratio [300&2700]**	**Fe/kappa**	**Age**
[cm]	*cal [kyr]*	*[10**-6 SI]*	*[mA/m]*	*-*	*-*	*-*	*[cps/10**-6 SI]*	*cal [kyr]*
							1.73E+03	15.230
							1.69E+03	15.248
							1.67E+03	15.266
							1.72E+03	15.283
							1.55E+03	15.301
							1.52E+03	15.318
							1.62E+03	15.336
							1.43E+03	15.353
							1.40E+03	15.371
							1.38E+03	15.388
							1.32E+03	15.406
							1.33E+03	15.423
							1.34E+03	15.441
							1.36E+03	15.458
							1.42E+03	15.476
							1.55E+03	15.493
							1.51E+03	15.511
							1.48E+03	15.528
							1.42E+03	15.546
							1.29E+03	15.563
							1.31E+03	15.581
							1.41E+03	15.598
							1.31E+03	15.616
							1.34E+03	15.634
							1.33E+03	15.651
							1.27E+03	15.669

Depth	Age	kappa	IRM_{300mT}	ARM_{100}/IRM_{100}	$HIRM_{[300\&2700]}$	$S\text{-}ratio_{[300\&2700]}$	Fe/kappa	Age
[cm]	*cal [kyr]*	*[10**-6 SI]*	*[mA/m]*	*-*	*-*	*-*	*[cps/10**-6 SI]*	*cal [kyr]*
							1.33E+03	15.686
							1.35E+03	15.704
							1.24E+03	15.721
							1.25E+03	15.739
							1.27E+03	15.756
							1.37E+03	15.774
							1.42E+03	15.791
							1.34E+03	15.809
							1.16E+03	15.826
							1.36E+03	15.844
							1.44E+03	15.861
							1.30E+03	15.879
							1.22E+03	15.896
							1.30E+03	15.914
							1.37E+03	15.931
							1.38E+03	15.949
							1.52E+03	15.966
							1.47E+03	15.984
							1.44E+03	16.002
							1.48E+03	16.019
							1.44E+03	16.037
							1.49E+03	16.054
							1.41E+03	16.072
							1.39E+03	16.089
							1.44E+03	16.107
							1.38E+03	16.124

Depth	**Age**	**kappa**	**IRM_{300mT}**	**ARM_{100}/IRM_{100}**	**HIRM [300&2700]**	**S-ratio [300&2700]**	**Fe/kappa**	**Age**
[cm]	*cal [kyr]*	*[10**-6 SI]*	*[mA/m]*	*-*	*-*	*-*	*[cps/10**-6 SI]*	*cal [kyr]*
							1.48E+03	16.142
							1.52E+03	16.159
							1.67E+03	16.177
							1.59E+03	16.194
							1.62E+03	16.212
							1.52E+03	16.229
							1.50E+03	16.247
							1.34E+03	16.264
							1.29E+03	16.282
							1.26E+03	16.299
							1.35E+03	16.317
							1.45E+03	16.334
							1.47E+03	16.352
							1.56E+03	16.370
							1.63E+03	16.387
							1.71E+03	16.405
							1.62E+03	16.422
							1.59E+03	16.440
							1.54E+03	16.457
							1.49E+03	16.475
							1.43E+03	16.492
							1.38E+03	16.510
							1.45E+03	16.527
							1.48E+03	16.545
							1.52E+03	16.562
							1.49E+03	16.580

Depth	Age	kappa	IRM_{300mT}	ARM_{100}/IRM_{100}	$HIRM_{[300\&2700]}$	$S\text{-}ratio_{[300\&2700]}$	Fe/kappa	Age
[cm]	*cal [kyr]*	*[10**-6 SI]*	*[mA/m]*	-	-	-	*[cps/10**-6 SI]*	*cal [kyr]*
							1.52E+03	16.597
							1.46E+03	16.615
							1.51E+03	16.632
							1.51E+03	16.650
							1.45E+03	16.667
							1.45E+03	16.685
							1.46E+03	16.702
							1.48E+03	16.720
							1.37E+03	16.921
							1.28E+03	17.122
							1.28E+03	17.324
							1.29E+03	17.525
							1.30E+03	17.726
							1.25E+03	17.927
							1.27E+03	18.128
							1.32E+03	18.329
							1.30E+03	18.531
							1.30E+03	18.732
							1.28E+03	18.933
							1.30E+03	19.134
							1.29E+03	19.335
							1.16E+03	19.536
							1.27E+03	19.738
							1.32E+03	19.939
							1.35E+03	20.140
							1.35E+03	20.359

Depth	**Age**	**kappa**	**IRM_{300mT}**	**ARM_{100}/IRM_{100}**	**HIRM [300&2700]**	**S-ratio [300&2700]**	**Fe/kappa**	**Age**
[cm]	*cal [kyr]*	*[10**-6 SI]*	*[mA/m]*	-	-	-	*[cps/10**-6 SI]*	*cal [kyr]*
							1.26E+03	20.560
							1.35E+03	20.762
							1.38E+03	20.963
							1.37E+03	21.164
							1.42E+03	21.365
							1.39E+03	21.566
							1.47E+03	21.768
							1.40E+03	21.969
							1.57E+03	22.170

GeoB3910-2

Depth	Age	kappa	IRM_{300mT}	ARM_{100}/IRM_{100}	$HIRM_{[300\&2700]}$	S-ratio $_{[300\&2700]}$	Fe/kappa
[cm]	*cal [kyr]*	*[10**-6 SI]*	*[mA/m]*	-	-	-	*[cps/10**-6 SI]*
6.5	1.99	80.65	1.42E+03	1.56E-01	1.12E+02	0.93	1.64E+01
11	3.24	85.48	1.45E+03	1.59E-01	1.21E+02	0.92	1.58E+01
15	4.35	75.81	1.42E+03	1.62E-01	1.16E+02	0.92	1.73E+01
20	5.73	79.03	1.62E+03	1.69E-01	1.18E+02	0.93	1.55E+01
25	6.87	79.03	1.69E+03	1.72E-01	1.07E+02	0.94	1.94E+01
30	7.65	91.94	1.71E+03	1.85E-01	8.79E+01	0.95	2.41E+01
35	8.43	98.39	1.60E+03	1.81E-01	8.35E+01	0.95	2.26E+01
39.5	9.06	100.00	1.54E+03	1.87E-01	9.89E+01	0.94	3.74E+01
45	9.64	108.06	1.31E+03	1.69E-01	7.55E+01	0.95	7.85E+00
50.5	10.23	108.06	1.31E+03	1.63E-01	8.70E+01	0.94	8.92E+00
55	10.70	114.52	1.23E+03	1.61E-01	1.14E+02	0.92	1.11E+01
60.5	11.26	119.35	1.05E+03	1.51E-01	1.19E+02	0.90	1.17E+01
65	11.69	122.58	9.31E+02	1.33E-01	1.05E+02	0.90	1.31E+01
70	12.17	117.74	8.29E+02	1.26E-01	1.02E+02	0.89	1.29E+01
75	12.74	88.71	6.97E+02	1.40E-01	9.27E+01	0.88	1.41E+01
80.5	13.51	95.16	8.26E+02	1.44E-01	1.26E+02	0.87	1.21E+01
85	14.13	90.32	8.73E+02	1.33E-01	1.18E+02	0.88	1.41E+01
90	14.76	130.65	1.08E+03	1.32E-01	1.66E+02	0.87	1.30E+01
95	15.27	133.87	1.07E+03	1.36E-01	1.76E+02	0.86	1.55E+01
100	15.79	130.65	9.56E+02	1.47E-01	1.94E+02	0.83	1.62E+01
105	16.24	141.94	1.05E+03	1.46E-01	2.10E+02	0.83	1.51E+01
111	16.66	138.71	1.17E+03	1.47E-01	2.29E+02	0.84	1.34E+01
115	16.89	174.19	2.74E+03	7.26E-02	2.53E+02	0.92	1.29E+01
120	17.10	127.42	7.75E+02	1.58E-01	1.79E+02	0.81	1.91E+01

Depth	Age	kappa	IRM_{300mT}	ARM_{100}/IRM_{100}	$HIRM_{[300\&2700]}$	$S\text{-ratio}_{[300\&2700]}$	Fe/kappa
[cm]	*cal [kyr]*	*[10**-6 SI]*	*[mA/m]*	-	-	-	*[cps/10**-6 SI]*
125	17.31	135.48	9.86E+02	1.07E-01	1.26E+02	0.89	1.65E+01
130	17.53	140.32	1.54E+03	7.69E-02	1.23E+02	0.93	1.64E+01
135	17.74	133.87	1.37E+03	7.31E-02	1.00E+02	0.93	1.75E+01
140	17.96	145.16	1.54E+03	7.83E-02	1.24E+02	0.93	1.60E+01
145	18.17	153.23	1.85E+03	7.38E-02	1.54E+02	0.92	1.43E+01
150	18.66	122.58	1.28E+03	1.03E-01	1.69E+02	0.88	1.30E+01
155	19.56	125.81	1.23E+03	1.07E-01	1.61E+02	0.88	1.01E+01
160	20.46	116.13	1.26E+03	1.09E-01	1.83E+02	0.87	8.31E+00
165	21.36	114.52	1.18E+03	1.08E-01	1.75E+02	0.87	1.05E+01
170	22.26	127.42	1.21E+03	1.12E-01	1.78E+02	0.87	1.12E+01
174.5	22.92	129.03	1.19E+03	1.13E-01	1.77E+02	0.87	1.11E+01
180	23.22	156.45	1.09E+03	1.21E-01	1.72E+02	0.86	1.24E+01
185	23.86	166.13	8.91E+02	1.28E-01	1.62E+02	0.85	1.61E+01
190	25.01	166.13	8.74E+02	1.18E-01	1.38E+02	0.86	1.36E+01
195.5	25.99	116.13	8.91E+02	1.21E-01	1.46E+02	0.86	1.06E+01
200	26.72	127.42	1.21E+03	1.04E-01	1.86E+02	0.87	1.03E+01
205	27.44	129.03	1.33E+03	1.03E-01	1.76E+02	0.88	8.44E+00
211	28.31	138.71	1.15E+03	1.06E-01	1.42E+02	0.89	1.43E+01
214.5	28.76	127.42	9.19E+02	1.25E-01	1.42E+02	0.87	1.37E+01
220.5	29.20	127.42	1.10E+03	1.13E-01	1.61E+02	0.87	1.49E+01
224.5	29.56	137.10	8.41E+02	1.35E-01	1.49E+02	0.85	1.46E+01
230	29.96	154.84	7.78E+02	1.44E-01	1.49E+02	0.84	1.83E+01
234.5	30.72	124.19	7.63E+02	1.34E-01	1.42E+02	0.84	1.38E+01
240	31.73	109.68	1.01E+03	1.13E-01	1.45E+02	0.87	1.13E+01
244	32.32	106.45	1.04E+03	1.10E-01	1.44E+02	0.88	8.82E+00
250	32.90	127.42	1.09E+03	1.12E-01	1.46E+02	0.88	1.07E+01

Depth	Age	kappa	IRM_{300mT}	ARM_{100}/IRM_{100}	$HIRM_{[300\&2700]}$	$S\text{-ratio}_{[300\&2700]}$	Fe/kappa
[cm]	*cal [kyr]*	*[10**-6 SI]*	*[mA/m]*	-	-	-	*[cps/10**-6 SI]*
254.5	33.48	114.52	8.44E+02	1.22E-01	1.33E+02	0.86	1.46E+01
260	34.07	117.74	1.15E+03	1.04E-01	1.50E+02	0.88	9.35E+00
264.5	34.65	100.00	7.85E+02	1.21E-01	1.27E+02	0.86	1.42E+01
270	35.21	117.74	1.16E+03	1.07E-01	1.40E+02	0.89	8.27E+00
274	35.72	122.58	1.25E+03	1.07E-01	1.44E+02	0.90	9.81E+00
280	36.24	103.23	7.97E+02	1.33E-01	1.41E+02	0.85	1.49E+01
284.5	36.75	103.23	9.61E+02	1.26E-01	1.33E+02	0.88	9.57E+00
290	37.26	103.23	1.13E+03	1.15E-01	1.41E+02	0.89	8.69E+00
294.5	37.78	122.58	1.07E+03	1.30E-01	1.55E+02	0.87	1.01E+01
300.5	38.35	133.87	8.76E+02	1.58E-01	1.61E+02	0.84	1.48E+01
304	38.88	141.94	8.76E+02	1.43E-01	1.52E+02	0.85	1.76E+01
310	39.52	159.68	1.08E+03	1.32E-01	1.55E+02	0.87	1.42E+01
315	40.15	179.03	2.44E+03	8.20E-02	1.89E+02	0.93	1.32E+01
320	40.78	140.32	9.65E+02	1.28E-01	1.27E+02	0.88	1.64E+01
325	41.42	124.19	1.65E+03	8.94E-02	1.41E+02	0.92	1.21E+01
330	41.90	108.06	1.06E+03	1.19E-01	1.38E+02	0.89	1.09E+01
335	42.15	122.58	1.04E+03	1.07E-01	1.38E+02	0.88	8.14E+00
340	42.40	129.03	9.50E+02	1.21E-01	1.48E+02	0.87	1.13E+01
345	42.65	119.35	1.16E+03	1.08E-01	1.36E+02	0.89	1.02E+01
350	43.01	127.42	1.19E+03	1.10E-01	1.55E+02	0.89	9.68E+00
355	43.53	143.55	1.03E+03	1.28E-01	1.51E+02	0.87	1.17E+01
360	44.05	109.68	1.07E+03	1.20E-01	1.57E+02	0.87	1.13E+01
365	44.57	106.45	1.13E+03	1.12E-01	1.36E+02	0.89	9.19E+00
370	45.09	122.58	1.15E+03	1.17E-01	1.46E+02	0.89	8.72E+00
375	45.51	143.55	1.12E+03	1.34E-01	1.59E+02	0.88	1.13E+01
380	45.79	146.77	1.09E+03	1.36E-01	1.56E+02	0.87	1.53E+01

Depth	**Age**	**kappa**	**IRM_{300mT}**	**ARM_{100}/IRM_{100}**	**HIRM [300&2700]**	**S-ratio [300&2700]**	**Fe/kappa**
[cm]	*cal [kyr]*	*[10**-6 SI]*	*[mA/m]*	-	-	-	*[cps/10**-6 SI]*
385	46.07	146.77	1.62E+03	1.04E-01	1.64E+02	0.91	1.68E+01
390	46.34	179.03	2.19E+03	9.68E-02	2.11E+02	0.91	1.31E+01
395	46.62	198.39	3.95E+03	5.26E-02	2.38E+02	0.94	1.22E+01
400	46.90	145.16	2.35E+03	7.75E-02	1.76E+02	0.93	1.23E+01
405	47.64	133.87	1.29E+03	1.12E-01	1.65E+02	0.89	9.52E+00
410.5	48.46	124.19	1.12E+03	1.17E-01	1.55E+02	0.88	9.49E+00
415	49.13	120.97	1.09E+03	1.13E-01	1.58E+02	0.87	9.20E+00
420	49.87	129.03	1.08E+03	1.12E-01	1.53E+02	0.88	8.47E+00
425	50.61	111.29	1.08E+03	1.20E-01	1.60E+02	0.87	9.58E+00
430	51.36	117.74	1.06E+03	1.24E-01	1.65E+02	0.86	9.47E+00
435	52.10	135.48	9.82E+02	1.31E-01	1.55E+02	0.86	1.09E+01
440	52.79	124.19	8.91E+02	1.29E-01	1.44E+02	0.86	1.58E+01
445	53.49	129.03	1.09E+03	1.14E-01	1.56E+02	0.88	1.21E+01
450	54.18	138.71	1.04E+03	1.08E-01	1.46E+02	0.88	1.05E+01
455	54.99	112.90	1.17E+03	1.09E-01	1.59E+02	0.88	9.48E+00
460	55.72	133.87	1.04E+03	1.22E-01	1.53E+02	0.87	1.34E+01
465	56.45	129.03	9.68E+02	1.26E-01	1.53E+02	0.86	1.28E+01
470	57.18	140.32	8.98E+02	1.44E-01	1.64E+02	0.85	1.51E+01
475	57.91	146.77	7.82E+02	1.48E-01	1.33E+02	0.85	1.50E+01
480	58.64	169.35	1.09E+03	9.75E-02	1.09E+02	0.91	1.42E+01

ANNEX IV – Element ratios

GeoB3913-3

Depth *[cm]*	Age *[cal kyr]*	Fe/Ca *[cps]*	Al/Si *[cps]*	Fe/K *[cps]*	Ti/Al *[cps]*
2	1.34	1.81E-02	5.40E-02	3.02E+00	3.63E+00
3	2.00	1.87E-02	8.59E-02	3.99E+00	2.13E+00
4	2.67	1.67E-02	5.74E-02	3.09E+00	3.06E+00
5	3.34	1.40E-02	6.45E-02	3.98E+00	3.17E+00
6	4.01	1.09E-02	7.79E-02	1.33E+01	2.91E+00
7	4.68	1.27E-02	5.63E-02	4.72E+00	2.65E+00
8	5.34	1.36E-02	8.42E-02	6.03E+00	2.00E+00
9	6.01	1.98E-02	8.79E-02	4.30E+00	2.00E+00
10	6.68	2.05E-02	6.33E-02	5.17E+00	3.32E+00
11	7.35	3.56E-02	7.77E-02	4.86E+00	3.19E+00
12	8.02	5.34E-02	8.96E-02	3.98E+00	3.17E+00
13	8.68	5.93E-02	8.33E-02	4.33E+00	3.80E+00
14	9.35	8.63E-02	1.07E-01	4.01E+00	2.68E+00
15	10.02	1.06E-01	1.11E-01	4.42E+00	2.86E+00
16	10.69	1.34E-01	1.18E-01	4.14E+00	2.59E+00
17	11.36	1.52E-01	1.19E-01	4.66E+00	2.59E+00
18	13.30	1.17E-01	1.10E-01	4.37E+00	2.68E+00
19	13.53	1.41E-01	1.20E-01	4.59E+00	2.42E+00
20	13.75	2.67E-01	1.20E-01	5.07E+00	2.54E+00
21	13.98	2.66E-01	1.24E-01	4.96E+00	2.53E+00
22	14.20	2.82E-01	1.25E-01	4.88E+00	2.35E+00
23	14.43	2.59E-01	1.26E-01	5.29E+00	2.66E+00
24	14.65	6.03E-01	1.25E-01	6.15E+00	3.12E+00
25	14.88	5.79E-01	1.28E-01	6.20E+00	3.14E+00
26	15.10	6.95E-01	1.38E-01	6.57E+00	3.05E+00
27	15.29	6.81E-01	1.28E-01	6.85E+00	3.13E+00
28	15.47	7.48E-01	1.17E-01	8.16E+00	3.47E+00
29	15.66	1.13E+00	1.05E-01	9.97E+00	4.28E+00
30	15.84	8.28E-01	1.11E-01	8.21E+00	3.12E+00
31	16.02	7.74E-01	1.31E-01	5.96E+00	2.94E+00
32	16.21	6.36E-01	1.29E-01	5.46E+00	3.03E+00
33	16.39	8.97E-01	1.27E-01	5.58E+00	3.19E+00
34	16.58	7.43E-01	1.28E-01	5.61E+00	3.25E+00
35	16.76	9.25E-01	1.28E-01	5.89E+00	2.94E+00
36	16.95	1.10E+00	1.35E-01	6.75E+00	3.19E+00
37	17.13	1.17E+00	1.25E-01	6.92E+00	3.51E+00
38	17.31	9.04E-01	1.25E-01	6.00E+00	3.40E+00
39	17.50	7.22E-01	1.27E-01	5.82E+00	3.32E+00
40	17.68	6.51E-01	1.28E-01	5.50E+00	3.02E+00

Depth	Age	Fe/Ca	Al/Si	Fe/K	Ti/Al
[cm]	*[cal kyr]*	*[cps]*	*[cps]*	*[cps]*	*[cps]*
41	17.87	4.82E-01	1.21E-01	5.52E+00	3.13E+00
42	18.05	3.91E-01	1.26E-01	4.96E+00	2.87E+00
43	18.23	3.66E-01	1.19E-01	4.85E+00	2.81E+00
44	18.42	3.46E-01	1.28E-01	4.32E+00	2.43E+00
45	18.60	2.92E-01	1.15E-01	4.23E+00	2.60E+00
46	18.79	2.62E-01	1.12E-01	4.20E+00	2.66E+00
47	18.97	2.41E-01	1.04E-01	4.25E+00	2.91E+00
48	19.15	2.15E-01	1.08E-01	4.22E+00	2.92E+00
49	19.34	2.07E-01	1.07E-01	4.02E+00	2.54E+00
50	19.63	2.44E-01	1.16E-01	4.24E+00	2.58E+00
51	19.93	2.50E-01	1.13E-01	4.49E+00	2.56E+00
52	20.23	2.64E-01	1.18E-01	4.19E+00	2.18E+00
54	20.82	2.61E-01	1.07E-01	4.23E+00	3.03E+00
55	21.11	2.61E-01	1.10E-01	3.99E+00	2.87E+00
56	21.41	3.32E-01	1.13E-01	4.57E+00	2.97E+00
57	21.71	3.59E-01	1.19E-01	4.42E+00	2.84E+00
58	22.00	5.04E-01	1.20E-01	5.01E+00	2.82E+00
59	22.30	5.05E-01	1.14E-01	5.03E+00	3.35E+00
60	22.59	4.61E-01	1.19E-01	5.19E+00	3.16E+00
61	22.89	5.97E-01	1.17E-01	5.40E+00	3.39E+00
62	23.19	6.16E-01	1.08E-01	6.19E+00	3.72E+00
63	23.48	7.35E-01	1.24E-01	5.86E+00	2.80E+00
64	23.78	3.79E-01	1.35E-01	3.86E+00	2.22E+00
65	23.95	4.79E-01	1.25E-01	4.07E+00	2.65E+00
66	24.12	5.38E-01	1.29E-01	4.31E+00	2.40E+00
67	24.29	5.89E-01	1.28E-01	4.80E+00	2.61E+00
68	24.46	9.32E-01	1.36E-01	4.68E+00	2.97E+00
69	24.63	3.70E-01	1.25E-01	4.03E+00	2.25E+00
70	24.80	4.59E-01	1.31E-01	4.14E+00	2.15E+00
71	24.97	2.95E-01	1.26E-01	3.76E+00	2.39E+00
72	25.14	2.52E-01	1.19E-01	3.62E+00	2.35E+00
73	25.31	2.46E-01	1.23E-01	3.63E+00	2.42E+00
74	25.49	2.31E-01	1.27E-01	3.65E+00	2.34E+00
75	26.61	2.93E-01	1.20E-01	3.92E+00	2.82E+00
76	27.73	4.24E-01	1.32E-01	4.26E+00	2.49E+00
77	27.97	4.02E-01	1.30E-01	4.35E+00	2.65E+00
78	28.22	4.50E-01	1.30E-01	4.56E+00	2.56E+00
79	28.46	5.51E-01	1.34E-01	4.72E+00	2.45E+00
80	28.70	7.29E-01	1.38E-01	5.10E+00	3.00E+00
81	28.94	8.65E-01	1.39E-01	5.44E+00	2.68E+00
82	29.19	1.01E+00	1.36E-01	5.27E+00	2.96E+00
83	29.43	5.06E-01	1.32E-01	4.58E+00	2.88E+00
84	29.67	7.69E-01	1.36E-01	5.07E+00	2.84E+00

Depth	Age	Fe/Ca	Al/Si	Fe/K	Ti/Al
[cm]	*[cal kyr]*	*[cps]*	*[cps]*	*[cps]*	*[cps]*
85	29.91	9.91E-01	1.29E-01	5.74E+00	3.00E+00
86	30.16	1.04E+00	1.30E-01	6.14E+00	3.38E+00
87	30.40	5.73E-01	1.29E-01	4.88E+00	3.26E+00
88	30.64	3.41E-01	1.21E-01	4.49E+00	2.94E+00
89	30.88	3.51E-01	1.27E-01	4.42E+00	2.81E+00
90	31.13	3.56E-01	1.17E-01	5.01E+00	3.12E+00
91	31.37	4.22E-01	1.15E-01	7.48E+00	3.03E+00
92	31.61	2.65E-01	1.15E-01	5.14E+00	2.46E+00
93	31.85	1.70E-01	1.10E-01	3.83E+00	2.47E+00
94	32.10	1.59E-01	1.12E-01	3.84E+00	2.60E+00
95	32.34	1.94E-01	1.11E-01	4.03E+00	2.72E+00
96	32.74	2.11E-01	1.17E-01	4.19E+00	2.49E+00
97	33.15	2.37E-01	1.13E-01	4.74E+00	2.52E+00
98	33.56	1.58E-01	1.07E-01	3.80E+00	2.78E+00
99	33.96	1.27E-01	1.13E-01	3.24E+00	2.51E+00
100	34.37	1.35E-01	1.11E-01	3.38E+00	2.69E+00
101	34.78	1.46E-01	1.08E-01	3.49E+00	2.94E+00
102	35.18	1.36E-01	1.17E-01	3.51E+00	2.58E+00
103	35.59	1.63E-01	1.19E-01	3.57E+00	2.58E+00
104	36.00	2.70E-01	1.32E-01	3.58E+00	2.21E+00
105	36.40	1.66E-01	1.20E-01	3.85E+00	2.65E+00
106	36.81	1.55E-01	1.20E-01	3.56E+00	2.37E+00
107	37.21	1.03E-01	1.01E-01	3.30E+00	2.73E+00
108	37.62	9.63E-02	1.03E-01	3.20E+00	2.40E+00
109	37.73	1.05E-01	1.07E-01	3.17E+00	2.50E+00
110	37.84	1.79E-01	1.17E-01	3.89E+00	2.80E+00
111	37.95	2.14E-01	1.24E-01	4.00E+00	2.66E+00
112	38.06	3.51E-01	1.21E-01	4.20E+00	2.63E+00
113	38.17	7.05E-01	1.35E-01	4.91E+00	2.64E+00
114	38.28	8.43E-01	1.35E-01	5.06E+00	2.85E+00
115	38.39	8.91E-01	1.28E-01	5.31E+00	3.28E+00
116	38.50	6.51E-01	1.28E-01	4.68E+00	3.02E+00
117	38.93	6.98E-01	1.34E-01	4.88E+00	2.98E+00
118	39.37	4.26E-01	1.26E-01	4.26E+00	2.87E+00
119	39.81	3.15E-01	1.26E-01	3.99E+00	2.85E+00
120	40.25	1.76E-01	1.16E-01	3.76E+00	2.65E+00
121	40.69	1.60E-01	1.20E-01	3.57E+00	2.50E+00
122	41.13	1.08E-01	1.15E-01	3.43E+00	2.57E+00
123	41.31	1.02E-01	1.07E-01	3.54E+00	2.53E+00
124	41.48	1.07E-01	1.06E-01	3.19E+00	2.59E+00
125	41.65	1.21E-01	1.14E-01	3.58E+00	2.56E+00
126	41.82	1.32E-01	1.19E-01	3.28E+00	2.26E+00
127	41.99	1.31E-01	1.10E-01	3.37E+00	2.47E+00

Depth	Age	Fe/Ca	Al/Si	Fe/K	Ti/Al
[cm]	*[cal kyr]*	*[cps]*	*[cps]*	*[cps]*	*[cps]*
128	42.17	2.17E-01	1.17E-01	4.05E+00	2.59E+00
129	42.34	2.59E-01	1.09E-01	4.65E+00	3.15E+00
130	42.98	2.04E-01	1.09E-01	4.27E+00	3.02E+00
131	43.62	2.65E-01	1.11E-01	4.72E+00	3.49E+00
132	44.27	1.19E-01	1.02E-01	3.89E+00	3.15E+00
133	44.91	1.35E-01	9.13E-02	4.14E+00	4.14E+00
134	45.55	1.69E-01	1.12E-01	3.81E+00	3.25E+00
135	45.77	4.46E-01	1.18E-01	4.67E+00	3.57E+00
136	45.99	7.77E-01	1.26E-01	5.53E+00	3.78E+00
137	46.21	5.19E-01	1.26E-01	4.58E+00	2.87E+00
138	46.44	9.66E-01	1.31E-01	5.53E+00	3.40E+00
139	46.66	1.09E+00	1.34E-01	6.00E+00	3.67E+00
140	46.88	1.16E+00	1.26E-01	6.06E+00	3.97E+00
141	47.10	9.05E-01	1.22E-01	5.92E+00	4.11E+00
142	47.32	7.06E-01	1.15E-01	5.56E+00	4.60E+00
143	47.55	5.60E-01	1.17E-01	5.11E+00	4.24E+00
144	47.77	4.46E-01	1.24E-01	4.81E+00	4.25E+00
145	47.99	3.25E-01	1.08E-01	4.33E+00	4.12E+00
146	48.21	1.74E-01	1.13E-01	3.40E+00	2.99E+00
147	48.43	1.37E-01	1.08E-01	3.18E+00	2.82E+00
148	49.16	1.39E-01	1.03E-01	3.31E+00	2.94E+00
149	49.89	1.32E-01	1.23E-01	3.36E+00	2.44E+00
150	50.61	1.49E-01	9.99E-02	3.74E+00	4.03E+00
151	51.34	1.11E-01	9.64E-02	3.59E+00	3.16E+00
152	52.06	8.83E-02	8.00E-02	4.14E+00	3.92E+00
153	52.79	8.71E-02	8.77E-02	3.53E+00	3.69E+00
154	53.52	4.48E-02	1.05E-01	2.97E+00	1.66E+00
155	53.85	8.10E-02	1.17E-01	3.27E+00	1.66E+00
156	54.18	1.76E-01	1.24E-01	3.58E+00	1.95E+00
157	54.51	2.30E-01	1.28E-01	3.74E+00	2.06E+00
158	54.83	2.83E-01	1.31E-01	4.05E+00	1.99E+00
159	55.16	2.73E-01	1.31E-01	4.07E+00	2.08E+00
160	55.49	2.42E-01	1.26E-01	3.92E+00	2.08E+00
161	55.82	1.84E-01	1.27E-01	3.56E+00	1.92E+00
162	56.15	1.94E-01	1.30E-01	3.80E+00	1.88E+00
163	56.48	1.92E-01	1.26E-01	3.69E+00	1.89E+00
164	56.81	1.42E-01	1.23E-01	3.44E+00	1.89E+00
165	57.14	1.11E-01	1.15E-01	3.07E+00	1.79E+00
166	57.47	1.42E-01	1.26E-01	3.36E+00	1.75E+00
167	57.80	1.60E-01	1.21E-01	3.49E+00	1.78E+00
168	58.13	2.03E-01	1.30E-01	3.65E+00	1.82E+00
169	58.46	3.39E-01	1.38E-01	4.22E+00	1.95E+00
170	58.59	3.65E-01	1.32E-01	4.37E+00	2.09E+00

Depth	Age	Fe/Ca	Al/Si	Fe/K	Ti/Al
[cm]	*[cal kyr]*	*[cps]*	*[cps]*	*[cps]*	*[cps]*
171	58.73	6.85E-01	1.32E-01	5.15E+00	2.34E+00
172	58.86	8.79E-01	1.31E-01	5.35E+00	2.40E+00
173	59.00	9.06E-01	1.43E-01	5.36E+00	2.28E+00
174	59.13	9.38E-01	1.37E-01	5.45E+00	2.31E+00
175	59.27	8.00E-01	1.39E-01	4.95E+00	2.27E+00
176	59.40	8.30E-01	1.43E-01	4.85E+00	2.13E+00
177	59.53	8.22E-01	1.40E-01	4.78E+00	2.30E+00
178	59.67	1.07E+00	1.41E-01	5.64E+00	2.32E+00
179	59.80	1.22E+00	1.38E-01	6.24E+00	2.46E+00
180	59.94	1.69E+00	1.35E-01	7.85E+00	2.51E+00
181	60.07	1.60E+00	1.34E-01	7.02E+00	2.55E+00
182	60.21	1.13E+00	1.43E-01	5.01E+00	2.26E+00
183	60.34	1.17E+00	1.42E-01	5.55E+00	2.29E+00
184	60.48	1.38E+00	1.41E-01	6.09E+00	2.41E+00
185	60.61	1.45E+00	1.41E-01	6.26E+00	2.41E+00
186	60.74	1.37E+00	1.42E-01	5.83E+00	2.45E+00
187	60.88	1.35E+00	1.37E-01	5.58E+00	2.54E+00
188	61.01	1.43E+00	1.38E-01	5.56E+00	2.60E+00
189	61.15	1.18E+00	1.43E-01	4.87E+00	2.42E+00
190	61.28	9.49E-01	1.49E-01	4.19E+00	2.31E+00
191	61.42	9.05E-01	1.45E-01	4.23E+00	2.44E+00
192	61.55	8.84E-01	1.49E-01	4.20E+00	2.27E+00
193	61.69	8.24E-01	1.50E-01	4.14E+00	2.27E+00
194	61.82	7.65E-01	1.42E-01	4.08E+00	2.38E+00
195	61.96	6.69E-01	1.43E-01	4.05E+00	2.26E+00
196	62.09	6.39E-01	1.44E-01	4.10E+00	2.33E+00
197	62.22	4.93E-01	1.40E-01	3.83E+00	2.17E+00
198	62.36	4.50E-01	1.37E-01	3.85E+00	2.12E+00
199	62.49	4.26E-01	1.42E-01	3.74E+00	2.03E+00
200	62.63	3.51E-01	1.35E-01	3.59E+00	2.07E+00
201	62.76	3.66E-01	1.39E-01	3.70E+00	2.00E+00
202	62.90	3.53E-01	1.35E-01	3.55E+00	2.00E+00
203	63.03	3.46E-01	1.32E-01	3.63E+00	2.03E+00
204	63.17	3.63E-01	1.39E-01	3.73E+00	1.92E+00
205	63.30	3.87E-01	1.38E-01	3.85E+00	1.95E+00
206	63.43	3.85E-01	1.38E-01	3.79E+00	1.85E+00
207	63.57	3.88E-01	1.38E-01	3.91E+00	1.97E+00
208	63.70	3.94E-01	1.36E-01	4.02E+00	2.04E+00
209	63.84	3.75E-01	1.34E-01	3.94E+00	1.98E+00
210	63.97	3.79E-01	1.33E-01	4.02E+00	2.00E+00
211	64.11	3.68E-01	1.36E-01	3.99E+00	1.91E+00
212	64.24	3.61E-01	1.34E-01	3.91E+00	2.03E+00
213	64.38	2.98E-01	1.28E-01	3.84E+00	1.98E+00

Depth	Age	Fe/Ca	Al/Si	Fe/K	Ti/Al
[cm]	*[cal kyr]*	*[cps]*	*[cps]*	*[cps]*	*[cps]*
214	64.51	3.05E-01	1.26E-01	3.84E+00	1.95E+00
215	64.65	3.06E-01	1.30E-01	3.88E+00	2.02E+00
216	64.78	2.76E-01	1.22E-01	3.73E+00	2.12E+00
217	64.91	2.90E-01	1.29E-01	3.75E+00	1.92E+00
218	65.05	3.04E-01	1.31E-01	3.74E+00	1.87E+00
219	65.18	2.87E-01	1.26E-01	3.72E+00	2.00E+00
220	65.32	2.81E-01	1.30E-01	3.64E+00	1.92E+00
221	65.45	2.56E-01	1.29E-01	3.60E+00	1.84E+00
222	65.59	2.17E-01	1.29E-01	3.34E+00	1.77E+00
223	65.72	2.28E-01	1.23E-01	3.42E+00	1.93E+00
224	65.86	2.36E-01	1.23E-01	3.58E+00	1.93E+00
225	65.99	2.79E-01	1.30E-01	3.77E+00	1.97E+00
226	66.12	2.21E-01	1.23E-01	3.57E+00	2.02E+00
227	66.26	2.78E-01	1.28E-01	3.79E+00	2.01E+00
228	66.39	2.85E-01	1.29E-01	3.81E+00	2.00E+00
229	66.53	1.75E-01	1.18E-01	3.43E+00	2.07E+00
230	66.66	2.02E-01	1.19E-01	3.49E+00	2.14E+00
231	66.80	1.99E-01	1.21E-01	3.45E+00	1.99E+00
232	66.93	3.11E-01	1.31E-01	4.05E+00	2.11E+00
233	67.07	2.47E-01	1.24E-01	3.89E+00	2.23E+00
234	67.20	3.95E-01	1.36E-01	4.54E+00	2.15E+00
235	67.34	2.52E-01	1.28E-01	4.06E+00	2.24E+00
236	67.47	1.66E-01	1.33E-01	3.39E+00	1.76E+00
237	67.60	1.47E-01	1.20E-01	3.45E+00	2.09E+00
238	67.74	1.16E-01	1.19E-01	3.13E+00	1.83E+00
239	67.87	9.40E-02	1.21E-01	2.93E+00	1.72E+00
240	68.01	9.37E-02	1.16E-01	3.14E+00	2.15E+00
241	68.11	8.51E-02	1.11E-01	2.99E+00	2.15E+00
242	68.22	9.79E-02	1.11E-01	3.13E+00	2.15E+00
243	68.33	1.01E-01	1.11E-01	3.27E+00	2.23E+00
244	68.43	1.40E-01	1.16E-01	3.50E+00	2.21E+00
245	68.54	1.87E-01	1.28E-01	3.71E+00	1.96E+00
246	68.64	2.46E-01	1.32E-01	3.85E+00	1.81E+00
247	68.75	2.78E-01	1.40E-01	4.07E+00	1.79E+00
248	68.85	3.06E-01	1.38E-01	4.04E+00	1.90E+00
249	68.96	4.31E-01	1.39E-01	4.80E+00	2.10E+00
250	69.06	4.50E-01	1.37E-01	4.64E+00	2.05E+00
251	69.17	4.17E-01	1.35E-01	4.56E+00	2.11E+00
252	69.28	4.19E-01	1.32E-01	4.59E+00	2.15E+00
253	69.38	3.90E-01	1.39E-01	4.65E+00	2.03E+00
254	69.49	4.74E-01	1.30E-01	5.62E+00	2.54E+00
256	69.70	4.33E-01	1.25E-01	5.10E+00	2.63E+00
257	69.80	4.10E-01	1.27E-01	4.86E+00	2.46E+00

Depth	Age	Fe/Ca	Al/Si	Fe/K	Ti/Al
[cm]	*[cal kyr]*	*[cps]*	*[cps]*	*[cps]*	*[cps]*
258	69.91	3.69E-01	1.31E-01	4.79E+00	2.36E+00
259	70.02	3.28E-01	1.26E-01	4.94E+00	2.46E+00
260	70.12	3.35E-01	1.26E-01	4.65E+00	2.48E+00
261	70.23	3.05E-01	1.30E-01	4.17E+00	2.33E+00
262	70.33	1.78E-01	1.21E-01	3.62E+00	2.07E+00
263	70.44	2.19E-01	1.31E-01	3.77E+00	2.01E+00
264	70.54	2.48E-01	1.23E-01	4.12E+00	2.26E+00
265	70.65	1.12E-01	1.11E-01	3.29E+00	2.20E+00
266	70.76	6.54E-02	9.29E-02	3.05E+00	2.37E+00
267	70.83	7.69E-02	1.09E-01	2.90E+00	2.13E+00
268	70.91	7.92E-02	1.17E-01	3.19E+00	2.04E+00
269	70.99	9.09E-02	1.08E-01	3.15E+00	2.05E+00
270	71.06	9.70E-02	1.16E-01	3.16E+00	1.90E+00
271	71.14	1.05E-01	1.13E-01	3.35E+00	2.18E+00
272	71.22	1.18E-01	1.14E-01	3.54E+00	2.11E+00
273	71.29	1.25E-01	1.18E-01	3.51E+00	1.96E+00
274	71.37	1.16E-01	1.22E-01	3.47E+00	1.93E+00
275	71.45	1.21E-01	1.18E-01	3.58E+00	2.09E+00
276	71.52	1.10E-01	1.22E-01	3.45E+00	1.94E+00
277	71.60	1.04E-01	1.29E-01	3.31E+00	1.74E+00
278	71.68	1.12E-01	1.22E-01	3.35E+00	2.02E+00
279	71.75	8.76E-02	1.20E-01	3.49E+00	1.70E+00
280	71.83	8.44E-02	1.19E-01	3.61E+00	1.85E+00
281	71.91	8.59E-02	1.11E-01	3.34E+00	2.00E+00
282	71.98	1.10E-01	1.19E-01	3.86E+00	2.24E+00
283	72.06	9.75E-02	1.21E-01	3.80E+00	2.26E+00
284	72.14	8.49E-02	1.19E-01	3.50E+00	1.89E+00
285	72.21	8.51E-02	1.12E-01	3.50E+00	2.03E+00
286	72.29	7.03E-02	1.21E-01	3.26E+00	1.72E+00
287	72.37	8.19E-02	1.20E-01	3.35E+00	1.83E+00
288	72.44	8.85E-02	1.20E-01	3.47E+00	1.96E+00
289	72.52	8.86E-02	1.18E-01	3.47E+00	2.16E+00
290	72.60	8.57E-02	1.10E-01	3.48E+00	2.16E+00
291	72.67	1.08E-01	1.22E-01	3.53E+00	2.03E+00
292	72.75	1.77E-01	1.30E-01	4.00E+00	1.97E+00
293	72.83	1.36E-01	1.15E-01	3.47E+00	2.16E+00
294	72.90	1.54E-01	1.22E-01	3.62E+00	2.18E+00
295	72.98	2.09E-01	1.17E-01	4.03E+00	2.33E+00
296	73.06	3.19E-01	1.27E-01	4.54E+00	2.21E+00
297	73.13	4.27E-01	1.23E-01	4.90E+00	2.39E+00
298	73.21	3.62E-01	1.26E-01	4.60E+00	2.31E+00
299	73.29	2.86E-01	1.28E-01	4.30E+00	1.93E+00
300	73.37	2.56E-01	1.21E-01	4.13E+00	2.03E+00

Depth	Age	Fe/Ca	Al/Si	Fe/K	Ti/Al
[cm]	*[cal kyr]*	*[cps]*	*[cps]*	*[cps]*	*[cps]*
301	73.67	3.49E-01	1.25E-01	4.71E+00	2.20E+00
302	73.98	1.49E-01	1.14E-01	3.47E+00	2.06E+00
303	74.29	1.36E-01	1.10E-01	3.37E+00	2.20E+00
304	74.59	1.40E-01	1.15E-01	3.37E+00	2.19E+00
305	74.90	1.35E-01	1.26E-01	3.08E+00	1.89E+00
306	75.21	1.43E-01	1.11E-01	3.12E+00	1.86E+00
307	75.51	1.14E-01	1.18E-01	3.09E+00	1.82E+00
308	75.82	5.78E-02	1.13E-01	2.73E+00	1.60E+00
309	76.13	4.09E-02	1.13E-01	2.76E+00	1.38E+00
310	76.34	3.82E-02	9.26E-02	2.80E+00	1.89E+00
311	76.56	4.22E-02	9.91E-02	2.68E+00	1.68E+00
312	76.78	3.34E-02	9.50E-02	2.88E+00	1.62E+00
313	77.00	2.45E-02	7.30E-02	2.49E+00	1.67E+00
314	77.22	2.13E-02	7.95E-02	2.93E+00	1.98E+00
315	77.44	2.56E-02	6.76E-02	2.15E+00	1.79E+00
316	77.65	2.29E-02	6.64E-02	2.49E+00	2.08E+00
317	77.87	2.25E-02	3.75E-02	1.61E+00	2.55E+00
318	78.09	1.68E-02	2.91E-02	6.13E-01	8.50E-01
319	78.31	2.08E-02	2.87E-02	7.35E-01	9.18E-01
320	78.53	2.22E-02	2.78E-02	6.06E-01	1.09E+00
321	78.75	1.38E-02	4.33E-02	2.59E+00	2.12E+00
322	78.97	1.41E-02	6.56E-02	5.13E+00	2.36E+00
323	79.18	4.69E-02	6.79E-02	4.60E+00	1.93E+00
324	79.40	3.35E-01	1.34E-01	4.44E+00	1.89E+00
325	79.62	3.18E-01	1.27E-01	3.99E+00	2.09E+00
326	79.84	2.54E-01	1.29E-01	3.68E+00	2.00E+00
327	80.06	2.32E-01	1.25E-01	3.86E+00	2.10E+00
328	80.28	1.88E-01	1.20E-01	3.32E+00	2.05E+00
329	80.50	2.94E-01	1.28E-01	3.80E+00	2.04E+00
330	80.73	2.87E-01	1.29E-01	3.89E+00	2.24E+00
331	80.96	2.72E-01	1.24E-01	3.74E+00	2.20E+00
332	81.19	3.21E-01	1.24E-01	3.94E+00	2.24E+00
333	81.42	3.10E-01	1.27E-01	4.07E+00	2.25E+00
334	81.64	2.66E-01	1.29E-01	3.74E+00	2.13E+00
335	81.87	2.85E-01	1.25E-01	3.91E+00	2.20E+00
336	82.10	2.60E-01	1.24E-01	3.95E+00	2.14E+00
337	82.33	1.27E-01	1.08E-01	3.55E+00	2.16E+00
338	82.55	9.03E-02	1.02E-01	3.07E+00	2.12E+00
339	82.78	7.44E-02	1.03E-01	3.06E+00	1.98E+00
340	83.01	1.62E-01	1.14E-01	5.36E+00	1.94E+00
341	83.24	1.79E-01	1.16E-01	4.13E+00	1.99E+00
342	83.47	2.84E-01	1.25E-01	4.41E+00	2.11E+00
343	83.69	3.41E-01	1.29E-01	4.54E+00	2.08E+00

Depth	**Age**	**Fe/Ca**	**Al/Si**	**Fe/K**	**Ti/Al**
[cm]	*[cal kyr]*	*[cps]*	*[cps]*	*[cps]*	*[cps]*
344	83.92	3.34E-01	1.27E-01	4.36E+00	2.21E+00
345	84.15	3.12E-01	1.29E-01	3.95E+00	2.25E+00
346	84.38	3.49E-01	1.33E-01	4.06E+00	2.26E+00
347	84.60	3.46E-01	1.28E-01	4.04E+00	2.32E+00
348	84.83	3.43E-01	1.32E-01	3.73E+00	2.22E+00
349	85.06	4.06E-01	1.34E-01	4.04E+00	2.25E+00
350	85.29	3.89E-01	1.35E-01	4.08E+00	2.18E+00

GeoB3912-1

Depth	Age	Fe/Ca	Al/Si	Fe/K	Ti/Al
[cm]	*[cal kyr]*	*[cps]*	*[cps]*	*[cps]*	*[cps]*
2	1.27	5.20E-02	1.01E-01	2.85E+00	2.68E+00
4	2.05	5.38E-02	9.88E-02	2.98E+00	2.79E+00
6	2.85	5.91E-02	1.03E-01	2.97E+00	2.46E+00
8	3.64	5.38E-02	9.75E-02	2.80E+00	2.60E+00
10	4.44	7.35E-02	1.01E-01	3.45E+00	2.56E+00
12	5.37	9.03E-02	1.17E-01	3.30E+00	2.44E+00
14	6.34	5.84E-02	9.20E-02	2.73E+00	3.64E+00
16	7.37	1.02E-01	1.01E-01	3.21E+00	3.39E+00
18	8.45	2.63E-01	1.19E-01	4.12E+00	2.86E+00
20	9.54	7.51E-01	1.29E-01	4.99E+00	3.21E+00
22	9.80	4.70E-01	1.33E-01	3.96E+00	2.84E+00
24	10.06	6.35E-01	1.41E-01	4.11E+00	2.36E+00
26	10.27	6.39E-01	1.32E-01	4.57E+00	2.89E+00
28	10.42	6.06E-01	1.38E-01	4.39E+00	2.66E+00
30	10.57	9.79E-01	1.36E-01	5.33E+00	3.13E+00
32	10.73	9.89E-01	1.31E-01	5.30E+00	3.08E+00
34	10.88	1.20E+00	1.36E-01	5.40E+00	2.98E+00
36	11.03	1.26E+00	1.34E-01	5.57E+00	2.96E+00
38	11.19	1.15E+00	1.39E-01	5.31E+00	2.81E+00
40	11.35	1.30E+00	1.39E-01	5.85E+00	3.17E+00
42	11.58	1.17E+00	1.36E-01	5.42E+00	2.97E+00
44	11.83	1.21E+00	1.40E-01	5.53E+00	3.02E+00
46	12.07	1.05E+00	1.38E-01	5.58E+00	2.95E+00
48	12.32	8.36E-01	1.32E-01	5.26E+00	3.17E+00
50	12.56	8.16E-01	1.38E-01	5.39E+00	3.08E+00
52	12.81	4.39E-01	1.39E-01	4.16E+00	2.64E+00
54	13.05	3.72E-01	1.29E-01	4.03E+00	2.89E+00
56	13.30	3.44E-01	1.31E-01	3.86E+00	2.86E+00
58	13.55	5.82E-01	1.28E-01	4.72E+00	3.45E+00
60	13.80	4.01E-01	1.27E-01	3.92E+00	2.93E+00
62	14.04	1.10E+00	1.24E-01	4.84E+00	3.23E+00
64	14.29	1.18E+00	1.31E-01	4.87E+00	3.11E+00
66	14.51	1.24E+00	1.22E-01	5.19E+00	3.62E+00
68	14.69	5.90E-01	1.32E-01	4.87E+00	2.92E+00
70	14.88	1.39E+00	1.25E-01	5.77E+00	3.48E+00
72	14.99	1.26E+00	1.31E-01	5.47E+00	3.09E+00
74	15.10	1.59E+00	1.23E-01	5.87E+00	4.02E+00
76	15.22	2.29E+00	1.19E-01	6.33E+00	4.25E+00
78	15.34	2.32E+00	1.24E-01	6.04E+00	3.54E+00
80	15.46	2.19E+00	1.21E-01	6.12E+00	3.99E+00
82	15.58	2.43E+00	1.29E-01	6.01E+00	3.44E+00
84	15.71	1.70E+00	1.26E-01	5.49E+00	3.24E+00

Depth	Age	Fe/Ca	Al/Si	Fe/K	Ti/Al
[cm]	*[cal kyr]*	*[cps]*	*[cps]*	*[cps]*	*[cps]*
86	15.83	2.63E+00	1.24E-01	6.12E+00	3.76E+00
88	15.96	3.13E+00	1.31E-01	6.47E+00	3.52E+00
90	16.09	2.58E+00	1.29E-01	5.84E+00	3.22E+00
92	16.21	2.76E+00	1.30E-01	6.06E+00	3.24E+00
94	16.34	2.97E+00	1.34E-01	6.02E+00	3.00E+00
96	16.46	2.94E+00	1.35E-01	5.99E+00	2.93E+00
98	16.58	3.15E+00	1.36E-01	6.19E+00	3.11E+00
100	16.71	3.49E+00	1.34E-01	6.42E+00	3.21E+00
102	16.83	4.13E+00	1.36E-01	6.36E+00	3.28E+00
104	16.95	4.23E+00	1.33E-01	6.69E+00	3.47E+00
106	17.06	5.62E+00	1.39E-01	6.58E+00	3.06E+00
108	17.16	3.51E+00	1.46E-01	6.35E+00	2.71E+00
110	17.27	3.92E+00	1.47E-01	6.57E+00	2.89E+00
112	17.37	2.27E+00	1.44E-01	6.39E+00	2.88E+00
114	17.47	2.51E+00	1.42E-01	6.35E+00	2.96E+00
116	17.58	4.24E+00	1.42E-01	6.65E+00	3.07E+00
118	17.70	4.09E+00	1.42E-01	6.19E+00	3.07E+00
120	17.82	3.85E+00	1.42E-01	6.34E+00	2.94E+00
122	17.95	3.67E+00	1.43E-01	6.57E+00	3.09E+00
124	18.09	4.36E+00	1.37E-01	6.61E+00	3.40E+00
126	18.24	5.04E+00	1.44E-01	6.80E+00	3.50E+00
128	18.38	4.64E+00	1.47E-01	6.98E+00	3.44E+00
130	18.52	4.74E+00	1.46E-01	6.80E+00	3.53E+00
132	18.66	3.55E+00	1.45E-01	6.42E+00	3.35E+00
134	18.80	2.78E+00	1.48E-01	6.32E+00	3.07E+00
136	18.96	1.32E+00	1.38E-01	5.56E+00	3.09E+00
138	19.15	5.36E-01	1.32E-01	4.26E+00	2.66E+00
140	19.34	3.16E-01	1.25E-01	3.93E+00	2.55E+00
142	19.58	3.59E-01	1.26E-01	3.98E+00	2.75E+00
144	19.86	3.78E-01	1.26E-01	4.08E+00	2.67E+00
146	20.15	4.44E-01	1.30E-01	4.26E+00	2.54E+00
148	20.43	3.03E-01	1.29E-01	3.68E+00	2.42E+00
150	20.71	2.93E-01	1.26E-01	3.65E+00	2.46E+00
152	21.00	3.23E-01	1.41E-01	3.69E+00	2.10E+00
154	21.29	2.55E-01	1.29E-01	3.43E+00	2.22E+00
156	21.61	3.68E-01	1.33E-01	3.67E+00	2.33E+00
158	21.96	5.02E-01	1.33E-01	3.91E+00	2.42E+00
160	22.32	7.29E-01	1.40E-01	4.32E+00	2.40E+00
162	22.67	2.32E+00	1.49E-01	5.70E+00	2.62E+00
164	23.05	1.90E+00	1.42E-01	5.51E+00	2.85E+00
166	23.41	2.24E+00	1.47E-01	5.79E+00	2.68E+00
168	23.78	3.53E-01	1.30E-01	3.85E+00	2.53E+00
170	24.14	2.44E+00	1.45E-01	6.03E+00	2.84E+00

Depth	Age	Fe/Ca	Al/Si	Fe/K	Ti/Al
[cm]	*[cal kyr]*	*[cps]*	*[cps]*	*[cps]*	*[cps]*
172	24.40	1.67E+00	1.40E-01	5.71E+00	3.08E+00
174	24.63	1.04E+00	1.41E-01	5.11E+00	2.73E+00
176	24.83	1.19E+00	1.36E-01	4.98E+00	2.91E+00
178	25.02	7.97E-01	1.30E-01	5.03E+00	3.37E+00
180	25.21	1.35E+00	1.28E-01	5.78E+00	3.81E+00
182	25.40	9.83E-01	1.40E-01	5.01E+00	2.98E+00
183	25.48	8.47E-01	1.39E-01	5.09E+00	2.99E+00
185	25.66	5.93E-01	1.34E-01	4.54E+00	3.07E+00
187	25.84	3.81E-01	1.32E-01	4.25E+00	2.89E+00
189	26.02	4.07E-01	1.25E-01	4.44E+00	3.35E+00
191	26.21	5.08E-01	1.31E-01	4.48E+00	3.17E+00
193	26.41	8.26E-01	1.38E-01	4.96E+00	2.99E+00
195	26.61	4.93E-01	1.34E-01	4.38E+00	2.79E+00
197	26.83	6.79E-01	1.36E-01	5.16E+00	3.53E+00
199	27.06	8.97E-01	1.45E-01	5.24E+00	2.91E+00
201	27.28	6.09E-01	1.21E-01	4.86E+00	3.71E+00
203	27.51	7.91E-01	1.41E-01	4.91E+00	3.02E+00
205	27.73	1.41E+00	1.42E-01	5.69E+00	2.95E+00
207	27.95	1.39E+00	1.42E-01	5.64E+00	2.93E+00
209	28.18	1.35E+00	1.38E-01	5.81E+00	3.10E+00
211	28.40	1.68E+00	1.44E-01	5.84E+00	2.83E+00
213	28.62	2.21E+00	1.45E-01	5.87E+00	2.70E+00
215	28.85	2.68E+00	1.34E-01	6.52E+00	3.21E+00
217	29.05	3.92E+00	1.45E-01	6.24E+00	2.84E+00
219	29.26	4.13E+00	1.38E-01	6.34E+00	3.14E+00
221	29.50	3.00E+00	1.46E-01	5.97E+00	2.72E+00
223	29.78	4.11E+00	1.45E-01	6.23E+00	2.88E+00
225	30.06	2.74E+00	1.42E-01	6.10E+00	3.02E+00
227	30.36	3.66E+00	1.41E-01	6.20E+00	3.06E+00
229	30.66	2.08E+00	1.45E-01	5.88E+00	2.92E+00
231	30.96	2.91E+00	1.45E-01	6.16E+00	3.13E+00
233	31.25	1.36E+00	1.40E-01	5.73E+00	3.24E+00
235	31.55	1.30E+00	1.38E-01	5.66E+00	3.71E+00
237	31.82	4.70E-01	1.31E-01	4.59E+00	3.41E+00
239	32.09	4.30E-01	1.23E-01	4.63E+00	3.65E+00
241	32.34	4.45E-01	1.31E-01	4.51E+00	3.08E+00
243	32.51	3.92E-01	1.26E-01	4.44E+00	3.40E+00
245	32.67	3.44E-01	1.24E-01	4.16E+00	3.31E+00
247	32.82	3.34E-01	1.25E-01	4.39E+00	3.44E+00
249	32.97	3.44E-01	1.27E-01	4.34E+00	3.21E+00
251	33.12	2.91E-01	1.22E-01	3.88E+00	2.77E+00
253	33.26	3.53E-01	1.31E-01	4.08E+00	2.77E+00
255	33.41	3.70E-01	1.24E-01	4.40E+00	3.37E+00

Depth	Age	Fe/Ca	Al/Si	Fe/K	Ti/Al
[cm]	*[cal kyr]*	*[cps]*	*[cps]*	*[cps]*	*[cps]*
257	33.56	4.24E-01	1.33E-01	4.14E+00	2.79E+00
259	33.71	4.57E-01	1.40E-01	4.20E+00	2.54E+00
261	33.86	5.43E-01	1.36E-01	4.35E+00	2.65E+00
263	34.01	4.79E-01	1.36E-01	4.49E+00	2.77E+00
265	34.15	4.44E-01	1.35E-01	4.46E+00	3.05E+00
267	34.30	4.85E-01	1.36E-01	4.43E+00	2.69E+00
269	34.45	5.35E-01	1.38E-01	4.52E+00	2.81E+00
271	34.59	5.15E-01	1.37E-01	4.49E+00	2.80E+00
273	34.74	3.85E-01	1.34E-01	4.20E+00	2.75E+00
275	34.89	4.30E-01	1.41E-01	4.36E+00	2.71E+00
277	35.10	2.58E-01	1.19E-01	4.16E+00	3.18E+00
279	35.30	2.62E-01	1.28E-01	4.05E+00	2.80E+00
281	35.54	3.15E-01	1.31E-01	4.21E+00	2.71E+00
285	36.12	2.84E-01	1.22E-01	4.09E+00	3.13E+00
287	36.29	2.83E-01	1.12E-01	4.22E+00	3.42E+00
289	36.47	2.97E-01	1.30E-01	4.32E+00	2.85E+00
291	36.62	3.47E-01	1.37E-01	4.31E+00	2.49E+00
293	36.74	4.68E-01	1.47E-01	4.47E+00	2.41E+00
295	36.86	5.16E-01	1.41E-01	4.62E+00	2.61E+00
297	36.93	6.84E-01	1.44E-01	4.71E+00	2.58E+00
299	37.00	9.41E-01	1.42E-01	4.98E+00	2.80E+00
301	37.07	5.62E-01	1.38E-01	4.89E+00	2.68E+00
303	37.14	3.35E-01	1.34E-01	4.08E+00	2.50E+00
305	37.21	2.35E-01	1.27E-01	3.73E+00	2.46E+00
307	37.28	3.91E-01	1.40E-01	4.09E+00	2.15E+00
309	37.35	4.90E-01	1.43E-01	4.41E+00	2.32E+00
311	37.42	5.76E-01	1.43E-01	4.43E+00	2.34E+00
313	37.48	3.15E-01	1.29E-01	3.98E+00	2.38E+00
315	37.55	2.71E-01	1.41E-01	4.31E+00	2.16E+00
317	37.62	2.37E-01	1.37E-01	3.83E+00	2.01E+00
319	37.69	2.63E-01	1.30E-01	3.93E+00	2.46E+00
321	37.76	2.36E-01	1.29E-01	3.85E+00	2.53E+00
323	37.83	6.68E-01	1.43E-01	4.75E+00	2.34E+00
325	37.89	1.99E+00	1.48E-01	5.59E+00	2.53E+00
327	37.96	2.32E+00	1.47E-01	5.80E+00	2.59E+00
329	38.03	2.24E+00	1.47E-01	5.77E+00	2.47E+00
331	38.11	2.41E+00	1.44E-01	5.74E+00	2.65E+00
333	38.22	2.62E+00	1.44E-01	5.74E+00	2.56E+00
335	38.32	2.38E+00	1.43E-01	5.64E+00	2.64E+00
337	38.49	2.22E+00	1.46E-01	5.63E+00	2.58E+00
339	38.67	1.52E+00	1.42E-01	5.28E+00	2.70E+00
341	38.88	1.78E+00	1.41E-01	5.59E+00	2.67E+00
343	39.14	2.69E+00	1.38E-01	5.70E+00	2.86E+00

Depth	Age	Fe/Ca	Al/Si	Fe/K	Ti/Al
[cm]	*[cal kyr]*	*[cps]*	*[cps]*	*[cps]*	*[cps]*
345	39.40	2.39E+00	1.39E-01	5.61E+00	2.67E+00
347	39.58	2.16E+00	1.40E-01	5.62E+00	2.70E+00
349	39.76	2.01E+00	1.38E-01	5.45E+00	2.69E+00
351	39.94	4.92E-01	1.41E-01	4.55E+00	2.34E+00
353	40.11	1.51E+00	1.43E-01	5.43E+00	2.55E+00
355	40.28	1.39E+00	1.42E-01	5.35E+00	2.59E+00
357	40.45	6.52E-01	1.37E-01	4.59E+00	2.62E+00
359	40.62	5.17E-01	1.44E-01	4.27E+00	2.43E+00
361	40.79	4.03E-01	1.33E-01	3.90E+00	2.50E+00
363	40.96	2.91E-01	1.28E-01	3.81E+00	2.50E+00
365	41.13	2.19E-01	1.28E-01	3.73E+00	2.33E+00
367	41.35	2.19E-01	1.22E-01	3.73E+00	2.58E+00
369	41.57	2.02E-01	1.33E-01	3.74E+00	2.42E+00
371	41.80	2.03E-01	1.32E-01	3.76E+00	2.51E+00
373	42.07	3.14E-01	1.38E-01	4.14E+00	2.41E+00
375	42.34	7.43E-01	1.51E-01	4.86E+00	2.39E+00
377	42.61	8.15E-01	1.46E-01	5.09E+00	2.68E+00
379	42.88	9.33E-01	1.45E-01	5.23E+00	2.89E+00
381	43.25	8.60E-01	1.49E-01	4.85E+00	2.50E+00
383	43.73	8.42E-01	1.51E-01	4.92E+00	2.45E+00
385	44.20	3.31E-01	1.37E-01	4.01E+00	2.32E+00
387	44.61	3.30E-01	1.32E-01	3.98E+00	2.39E+00
389	45.01	4.25E-01	1.40E-01	4.33E+00	2.40E+00
391	45.32	4.93E-01	1.42E-01	4.42E+00	2.31E+00
393	45.55	4.90E-01	1.35E-01	4.08E+00	2.37E+00
395	45.78	5.59E-01	1.30E-01	4.19E+00	2.44E+00
397	46.01	1.10E+00	1.42E-01	5.04E+00	2.49E+00
399	46.24	1.47E+00	1.43E-01	5.40E+00	2.60E+00
401	46.47	1.70E+00	1.39E-01	5.53E+00	2.61E+00
403	46.70	1.96E+00	1.48E-01	5.67E+00	2.37E+00
405	46.92	1.50E+00	1.45E-01	5.37E+00	2.45E+00
407	47.15	2.26E+00	1.44E-01	5.77E+00	2.61E+00
409	47.39	2.79E+00	1.37E-01	5.83E+00	2.88E+00
411	47.60	2.53E+00	1.38E-01	5.83E+00	2.97E+00
413	47.80	2.87E+00	1.41E-01	5.71E+00	2.84E+00
415	48.00	2.96E+00	1.47E-01	6.05E+00	2.76E+00
417	48.09	1.74E+00	1.35E-01	5.53E+00	2.99E+00
419	48.18	1.20E+00	1.37E-01	5.52E+00	2.76E+00
420	48.23	7.13E-01	1.43E-01	4.53E+00	2.39E+00
423	48.43	5.00E-01	1.32E-01	4.29E+00	2.57E+00
425	48.57	4.94E-01	1.35E-01	4.24E+00	2.45E+00
427	48.86	5.48E-01	1.29E-01	4.42E+00	2.67E+00
429	49.15	5.86E-01	1.36E-01	4.27E+00	2.56E+00

Depth	Age	Fe/Ca	Al/Si	Fe/K	Ti/Al
[cm]	*[cal kyr]*	*[cps]*	*[cps]*	*[cps]*	*[cps]*
431	49.44	6.87E-01	1.36E-01	4.97E+00	2.57E+00
433	49.73	5.00E-01	1.39E-01	4.38E+00	2.41E+00
435	50.02	4.33E-01	1.38E-01	4.16E+00	2.47E+00
437	50.31	5.04E-01	1.30E-01	4.39E+00	2.95E+00
439	50.60	4.12E-01	1.26E-01	4.19E+00	3.02E+00
441	50.89	3.32E-01	1.27E-01	4.10E+00	2.85E+00
443	51.18	3.88E-01	1.35E-01	4.32E+00	2.74E+00
445	51.47	3.54E-01	1.20E-01	3.96E+00	3.05E+00
447	51.77	3.24E-01	1.24E-01	3.85E+00	2.73E+00
449	52.06	2.97E-01	1.27E-01	3.83E+00	2.43E+00
451	52.35	2.74E-01	1.33E-01	3.76E+00	2.25E+00
453	52.65	2.62E-01	1.27E-01	3.71E+00	2.17E+00
455	52.94	3.17E-01	1.33E-01	3.82E+00	2.19E+00
457	53.23	3.23E-01	1.34E-01	3.63E+00	2.06E+00
459	53.52	2.98E-01	1.30E-01	3.63E+00	2.24E+00
461	53.81	3.94E-01	1.37E-01	4.17E+00	2.15E+00
463	54.10	1.20E+00	1.42E-01	5.36E+00	2.53E+00
465	54.39	1.68E+00	1.45E-01	5.57E+00	2.75E+00
467	54.68	2.23E+00	1.50E-01	5.67E+00	2.50E+00
469	54.97	1.92E+00	1.50E-01	5.88E+00	2.52E+00
471	55.26	1.33E+00	1.43E-01	5.50E+00	2.83E+00
473	55.55	8.91E-01	1.45E-01	5.11E+00	2.64E+00
475	55.84	8.62E-01	1.46E-01	5.13E+00	2.56E+00
477	56.13	6.78E-01	1.43E-01	4.79E+00	2.70E+00
479	56.42	8.58E-01	1.40E-01	4.85E+00	2.67E+00
481	56.71	7.04E-01	1.37E-01	5.10E+00	2.71E+00
483	57.00	6.82E-01	1.24E-01	5.18E+00	3.87E+00
485	57.29	3.53E-01	1.27E-01	4.10E+00	2.84E+00
487	57.58	3.96E-01	1.31E-01	4.26E+00	2.87E+00
489	57.87	3.99E-01	1.32E-01	4.16E+00	2.51E+00
491	58.16	5.50E-01	1.38E-01	4.41E+00	2.47E+00
493	58.46	9.48E-01	1.45E-01	5.00E+00	2.50E+00
495	58.75	1.04E+00	1.47E-01	5.18E+00	2.44E+00
496	58.90	1.64E+00	1.42E-01	5.44E+00	2.60E+00
501	59.62	2.63E+00	1.42E-01	5.79E+00	2.66E+00
504	60.06	2.98E+00	1.45E-01	6.05E+00	2.66E+00
505	60.20	2.97E+00	1.40E-01	6.14E+00	2.70E+00
507	60.49	3.16E+00	1.43E-01	6.27E+00	2.70E+00
509	60.78	2.94E+00	1.48E-01	5.98E+00	2.61E+00
511	61.07	3.30E+00	1.45E-01	5.96E+00	2.57E+00
513	61.36	3.98E+00	1.46E-01	6.20E+00	2.65E+00
515	61.65	3.66E+00	1.46E-01	6.41E+00	2.79E+00
517	61.94	3.68E+00	1.43E-01	6.42E+00	2.79E+00

Depth	Age	Fe/Ca	Al/Si	Fe/K	Ti/Al
[cm]	*[cal kyr]*	*[cps]*	*[cps]*	*[cps]*	*[cps]*
519	62.23	3.51E+00	1.44E-01	6.33E+00	2.75E+00
521	62.52	1.77E+00	1.53E-01	5.89E+00	2.46E+00
523	62.81	3.39E+00	1.49E-01	6.49E+00	2.59E+00
525	63.10	3.72E+00	1.49E-01	6.37E+00	2.68E+00
527	63.39	1.50E+00	1.48E-01	5.86E+00	2.49E+00
529	63.69	3.52E+00	1.47E-01	6.49E+00	2.68E+00
531	63.98	3.36E+00	1.49E-01	6.51E+00	2.80E+00
533	64.27	2.00E+00	1.45E-01	6.31E+00	2.92E+00
535	64.56	4.26E+00	1.49E-01	6.43E+00	2.90E+00
537	64.91	3.73E+00	1.51E-01	6.70E+00	2.83E+00
539	65.25	9.46E-01	1.43E-01	5.32E+00	2.67E+00
541	65.60	3.58E+00	1.54E-01	6.34E+00	2.72E+00
543	66.00	3.10E+00	1.58E-01	5.89E+00	2.52E+00
545	66.40	2.38E+00	1.49E-01	5.70E+00	2.56E+00
547	66.80	1.81E+00	1.48E-01	5.26E+00	2.51E+00
549	67.20	7.70E-01	1.47E-01	4.52E+00	2.32E+00
551	67.61	6.28E-01	1.43E-01	4.43E+00	2.26E+00
553	68.01	2.98E-01	1.35E-01	3.75E+00	2.19E+00
555	68.41	3.57E-01	1.15E-01	3.58E+00	2.37E+00
557	68.81	1.49E+00	1.35E-01	5.64E+00	2.75E+00
559	69.21	2.45E+00	1.41E-01	6.21E+00	2.83E+00
561	69.61	3.53E+00	1.42E-01	6.21E+00	2.77E+00
563	70.01	3.36E+00	1.53E-01	6.14E+00	2.54E+00
565	70.41	4.44E+00	1.51E-01	6.39E+00	2.66E+00
567	70.76	2.26E-01	1.19E-01	3.76E+00	2.27E+00
569	71.10	3.09E-01	1.22E-01	3.99E+00	2.50E+00
571	71.43	2.76E-01	1.32E-01	4.05E+00	2.36E+00
573	71.71	1.34E-01	1.25E-01	3.35E+00	2.22E+00
575	71.99	1.68E-01	1.24E-01	3.56E+00	2.23E+00
577	72.26	2.13E-01	1.20E-01	3.41E+00	2.32E+00
579	72.54	2.91E-01	1.21E-01	3.72E+00	2.63E+00
581	72.81	4.09E-01	1.24E-01	4.33E+00	2.73E+00
583	73.09	1.67E+00	1.32E-01	5.47E+00	3.26E+00
585	73.37	6.52E-01	1.26E-01	4.76E+00	3.24E+00
587	73.64	5.77E-01	1.23E-01	4.92E+00	3.03E+00
589	73.92	1.31E+00	1.31E-01	5.13E+00	2.94E+00
591	74.19	1.45E+00	1.35E-01	5.29E+00	3.02E+00
593	74.47	1.45E+00	1.33E-01	5.30E+00	3.03E+00
595	74.75	1.56E+00	1.34E-01	5.42E+00	2.86E+00
597	75.02	1.90E+00	1.34E-01	5.61E+00	3.09E+00
599	75.30	1.77E+00	1.37E-01	5.84E+00	2.85E+00
601	75.57	1.59E+00	1.38E-01	5.62E+00	2.90E+00
603	75.85	7.95E-01	1.43E-01	5.21E+00	2.67E+00

Depth	Age	Fe/Ca	Al/Si	Fe/K	Ti/Al
[cm]	*[cal kyr]*	*[cps]*	*[cps]*	*[cps]*	*[cps]*
605	76.13	1.52E-01	1.21E-01	3.38E+00	2.50E+00
607	76.40	1.65E-01	1.25E-01	3.67E+00	2.50E+00
609	76.68	2.12E-01	1.28E-01	4.11E+00	2.32E+00
611	76.96	1.92E-01	1.26E-01	4.13E+00	2.33E+00
613	77.24	1.80E-01	1.25E-01	3.90E+00	2.44E+00
615	77.52	1.85E-01	1.30E-01	4.00E+00	2.27E+00
617	77.79	1.67E-01	1.28E-01	4.01E+00	2.28E+00
619	78.07	1.44E-01	1.22E-01	3.55E+00	2.15E+00
621	78.34	1.35E-01	1.29E-01	3.38E+00	1.97E+00
623	78.62	1.38E-01	1.20E-01	3.46E+00	2.13E+00
625	78.90	1.41E-01	1.24E-01	3.42E+00	2.21E+00
627	79.17	1.42E-01	1.28E-01	3.43E+00	2.13E+00
629	79.45	1.69E-01	1.28E-01	3.44E+00	2.31E+00
631	79.72	2.73E-01	1.22E-01	3.83E+00	2.44E+00
633	80.00	1.71E-01	1.22E-01	3.34E+00	2.36E+00
635	80.28	1.68E-01	1.23E-01	3.36E+00	2.38E+00
637	80.55	3.73E-01	1.36E-01	4.05E+00	2.28E+00
639	80.83	3.75E-01	1.40E-01	3.99E+00	2.19E+00
641	81.10	2.07E-01	1.24E-01	3.36E+00	2.33E+00
643	81.38	1.95E-01	1.25E-01	2.92E+00	2.34E+00
645	81.66	2.64E-01	1.26E-01	3.19E+00	2.36E+00
647	81.93	3.30E-01	1.27E-01	3.33E+00	2.55E+00
649	82.21	4.71E-01	1.28E-01	3.80E+00	2.69E+00
651	82.48	4.15E-01	1.31E-01	3.66E+00	2.40E+00
653	82.76	7.63E-01	1.37E-01	4.30E+00	2.46E+00
655	83.04	7.70E-01	1.37E-01	4.56E+00	2.47E+00
657	83.32	1.23E+00	1.45E-01	5.16E+00	2.56E+00
659	83.60	6.48E-01	1.43E-01	4.05E+00	2.29E+00
661	83.87	1.72E+00	1.43E-01	5.03E+00	2.44E+00
663	84.15	1.60E+00	1.49E-01	5.23E+00	2.36E+00
665	84.42	1.79E+00	1.48E-01	5.54E+00	2.54E+00
667	84.70	1.41E+00	1.48E-01	5.19E+00	2.40E+00

GeoB3911-3

Depth	Age	Fe/Ca	Al/Si	Fe/K	Ti/Al
[cm]	*[cal kyr]*	*[cps]*	*[cps]*	*[cps]*	*[cps]*
1	0.09	8.07E-02	9.89E-02	3.85E+00	3.30E+00
2	0.17	6.51E-02	9.30E-02	3.12E+00	3.21E+00
3	0.26	6.99E-02	1.07E-01	3.29E+00	2.69E+00
4	0.35	8.04E-02	9.78E-02	4.00E+00	2.92E+00
5	0.43	1.22E-01	9.30E-02	5.38E+00	3.27E+00
6	0.52	1.02E-01	8.84E-02	4.52E+00	3.38E+00
7	0.61	6.23E-02	8.48E-02	2.67E+00	3.16E+00
8	0.69	6.13E-02	8.48E-02	2.84E+00	3.98E+00
9	0.78	6.46E-02	9.56E-02	3.17E+00	3.45E+00
10	0.87	5.91E-02	9.80E-02	2.91E+00	2.87E+00
11	0.96	5.59E-02	1.17E-01	2.87E+00	2.49E+00
12	1.04	6.17E-02	1.08E-01	3.03E+00	2.49E+00
13	1.13	6.62E-02	1.03E-01	3.54E+00	2.95E+00
14	1.22	5.36E-02	1.08E-01	3.08E+00	2.30E+00
15	1.30	5.06E-02	1.05E-01	2.76E+00	2.31E+00
16	1.39	5.60E-02	1.04E-01	2.77E+00	2.45E+00
17	1.48	5.69E-02	9.50E-02	2.67E+00	2.34E+00
18	1.56	5.54E-02	1.00E-01	2.58E+00	2.64E+00
19	1.65	5.40E-02	1.02E-01	2.57E+00	2.62E+00
20	1.74	5.49E-02	9.31E-02	2.75E+00	2.95E+00
21	1.82	5.50E-02	9.31E-02	2.53E+00	2.81E+00
22	1.91	5.71E-02	1.01E-01	2.83E+00	2.62E+00
23	1.98	5.91E-02	8.81E-02	2.88E+00	3.01E+00
24	2.05	9.60E-02	7.82E-02	2.59E+00	3.74E+00
25	2.12	8.16E-02	8.02E-02	2.54E+00	3.46E+00
26	2.19	8.45E-02	6.10E-02	2.06E+00	3.12E+00
27	2.26	1.17E-01	6.43E-02	2.47E+00	5.03E+00
28	2.32	9.81E-02	8.00E-02	2.73E+00	4.21E+00
29	2.39	6.53E-02	9.37E-02	3.01E+00	3.38E+00
30	2.46	6.06E-02	1.04E-01	3.39E+00	2.52E+00
31	2.53	5.42E-02	1.07E-01	2.97E+00	2.19E+00
32	2.60	5.38E-02	1.03E-01	3.06E+00	2.39E+00
33	2.67	5.56E-02	9.50E-02	3.02E+00	2.70E+00
34	2.74	5.16E-02	9.52E-02	2.93E+00	2.91E+00
35	2.81	5.76E-02	9.24E-02	3.19E+00	3.21E+00
36	2.88	6.09E-02	9.49E-02	3.30E+00	3.24E+00
37	2.95	6.06E-02	1.08E-01	3.32E+00	2.70E+00
38	3.01	5.77E-02	9.63E-02	3.24E+00	3.00E+00
39	3.08	5.50E-02	1.11E-01	2.97E+00	2.71E+00
40	3.15	5.92E-02	8.66E-02	2.91E+00	3.21E+00
41	3.22	5.47E-02	9.20E-02	3.48E+00	3.21E+00

Depth	Age	Fe/Ca	Al/Si	Fe/K	Ti/Al
[cm]	*[cal kyr]*	*[cps]*	*[cps]*	*[cps]*	*[cps]*
42	3.29	5.00E-02	9.46E-02	3.43E+00	2.73E+00
43	3.36	6.38E-02	9.47E-02	3.15E+00	3.19E+00
44	3.43	5.85E-02	1.12E-01	3.43E+00	2.40E+00
45	3.50	5.68E-02	9.72E-02	3.54E+00	3.14E+00
46	3.57	5.16E-02	9.34E-02	2.90E+00	2.88E+00
47	3.64	5.43E-02	1.08E-01	3.29E+00	2.41E+00
48	3.70	5.42E-02	9.61E-02	3.03E+00	2.59E+00
49	3.77	5.61E-02	1.06E-01	3.37E+00	2.34E+00
50	3.84	5.50E-02	1.04E-01	3.30E+00	2.25E+00
51	3.91	5.46E-02	1.14E-01	3.31E+00	2.27E+00
52	3.98	5.48E-02	1.03E-01	3.22E+00	2.57E+00
53	4.01	5.58E-02	1.17E-01	3.14E+00	2.28E+00
54	4.03	5.76E-02	1.00E-01	3.21E+00	3.11E+00
55	4.06	6.43E-02	7.73E-02	3.13E+00	3.54E+00
56	4.08	6.45E-02	9.52E-02	3.06E+00	2.96E+00
57	4.11	6.18E-02	8.96E-02	3.33E+00	3.13E+00
58	4.13	6.40E-02	1.10E-01	3.23E+00	2.50E+00
59	4.16	5.86E-02	1.10E-01	3.21E+00	2.41E+00
60	4.18	5.41E-02	1.23E-01	2.96E+00	1.91E+00
61	4.21	5.66E-02	1.13E-01	3.28E+00	2.10E+00
62	4.23	7.08E-02	1.17E-01	4.10E+00	2.30E+00
63	4.32	6.71E-02	1.11E-01	3.79E+00	2.36E+00
64	4.40	7.07E-02	1.17E-01	3.78E+00	2.40E+00
65	4.49	8.54E-02	1.23E-01	4.02E+00	2.10E+00
66	4.57	8.01E-02	1.21E-01	3.74E+00	2.24E+00
67	4.66	8.12E-02	1.21E-01	3.93E+00	2.14E+00
68	4.74	8.24E-02	1.30E-01	3.82E+00	1.98E+00
69	4.83	9.28E-02	1.18E-01	4.14E+00	2.28E+00
70	4.91	9.36E-02	1.21E-01	4.09E+00	2.26E+00
71	5.00	9.63E-02	1.22E-01	3.98E+00	2.25E+00
72	5.08	8.77E-02	1.22E-01	3.85E+00	2.14E+00
73	5.17	9.22E-02	1.33E-01	3.91E+00	2.06E+00
74	5.25	1.17E-01	1.35E-01	4.37E+00	2.02E+00
75	5.34	1.31E-01	1.34E-01	4.50E+00	2.04E+00
76	5.42	1.41E-01	1.34E-01	4.38E+00	2.22E+00
77	5.51	7.44E-02	1.15E-01	3.39E+00	2.36E+00
78	5.59	9.29E-02	1.18E-01	3.87E+00	2.49E+00
79	5.68	1.48E-01	1.38E-01	4.55E+00	2.20E+00
80	5.76	1.55E-01	1.40E-01	4.39E+00	2.07E+00
81	5.85	7.08E-02	1.11E-01	3.37E+00	2.35E+00
82	5.93	1.27E-01	1.36E-01	4.07E+00	1.98E+00
83	6.02	2.10E-01	1.36E-01	4.36E+00	2.24E+00
84	6.10	2.08E-01	1.41E-01	4.29E+00	2.20E+00

Depth	Age	Fe/Ca	Al/Si	Fe/K	Ti/Al
[cm]	*[cal kyr]*	*[cps]*	*[cps]*	*[cps]*	*[cps]*
85	6.19	2.24E-01	1.35E-01	4.22E+00	2.29E+00
86	6.27	2.39E-01	1.38E-01	4.16E+00	2.13E+00
87	6.36	2.33E-01	1.36E-01	4.18E+00	2.02E+00
88	6.44	2.43E-01	1.36E-01	4.09E+00	2.14E+00
89	6.53	2.00E-01	1.39E-01	4.42E+00	2.21E+00
90	6.61	1.70E-01	1.33E-01	4.40E+00	2.14E+00
91	6.63	1.76E-01	1.39E-01	4.28E+00	2.01E+00
92	6.66	1.72E-01	1.42E-01	4.37E+00	1.94E+00
93	6.68	1.83E-01	1.41E-01	4.55E+00	2.12E+00
94	6.71	1.86E-01	1.33E-01	4.51E+00	2.29E+00
95	6.73	1.65E-01	1.39E-01	4.32E+00	2.09E+00
96	6.76	1.75E-01	1.46E-01	4.50E+00	1.85E+00
98	6.81	1.46E-01	1.31E-01	4.38E+00	2.53E+00
99	6.83	2.05E-01	1.33E-01	4.65E+00	2.60E+00
100	6.86	2.17E-01	1.33E-01	4.73E+00	2.40E+00
101	6.88	2.09E-01	1.44E-01	4.61E+00	2.22E+00
102	6.91	2.21E-01	1.49E-01	4.72E+00	2.28E+00
103	6.93	2.18E-01	1.42E-01	4.45E+00	2.20E+00
104	6.96	2.24E-01	1.46E-01	4.61E+00	2.17E+00
105	6.98	2.49E-01	1.46E-01	4.51E+00	2.09E+00
106	7.01	2.49E-01	1.41E-01	4.48E+00	2.15E+00
107	7.03	1.92E-01	1.37E-01	4.24E+00	2.05E+00
108	7.06	2.02E-01	1.38E-01	4.41E+00	2.20E+00
109	7.08	2.40E-01	1.37E-01	4.47E+00	2.43E+00
110	7.11	2.39E-01	1.36E-01	4.50E+00	2.54E+00
111	7.13	2.76E-01	1.43E-01	4.60E+00	2.36E+00
112	7.16	2.76E-01	1.35E-01	4.53E+00	2.39E+00
113	7.18	3.08E-01	1.34E-01	4.75E+00	2.52E+00
114	7.21	2.77E-01	1.43E-01	4.45E+00	2.26E+00
115	7.23	3.03E-01	1.35E-01	4.51E+00	2.27E+00
116	7.26	3.17E-01	1.39E-01	4.78E+00	2.22E+00
117	7.28	3.56E-01	1.35E-01	4.65E+00	2.31E+00
118	7.31	3.43E-01	1.40E-01	4.56E+00	2.25E+00
119	7.33	3.32E-01	1.38E-01	4.37E+00	2.23E+00
120	7.36	3.33E-01	1.35E-01	4.57E+00	2.30E+00
121	7.40	3.10E-01	1.35E-01	4.34E+00	2.26E+00
122	7.43	3.38E-01	1.32E-01	4.54E+00	2.42E+00
123	7.46	3.16E-01	1.43E-01	4.70E+00	2.35E+00
124	7.49	3.06E-01	1.35E-01	4.53E+00	2.27E+00
125	7.53	2.98E-01	1.41E-01	4.44E+00	2.25E+00
126	7.56	3.31E-01	1.25E-01	4.67E+00	2.65E+00
127	7.59	3.34E-01	1.36E-01	4.61E+00	2.50E+00
128	7.62	2.93E-01	1.38E-01	4.18E+00	2.18E+00

Depth	Age	Fe/Ca	Al/Si	Fe/K	Ti/Al
[cm]	*[cal kyr]*	*[cps]*	*[cps]*	*[cps]*	*[cps]*
129	7.66	2.87E-01	1.31E-01	4.16E+00	2.33E+00
130	7.69	2.66E-01	1.23E-01	3.96E+00	2.45E+00
131	7.72	2.85E-01	1.26E-01	4.00E+00	2.27E+00
132	7.75	2.85E-01	1.33E-01	4.27E+00	2.22E+00
133	7.79	2.65E-01	1.35E-01	4.21E+00	2.30E+00
134	7.82	2.75E-01	1.26E-01	4.20E+00	2.33E+00
135	7.85	2.69E-01	1.37E-01	4.09E+00	2.17E+00
136	7.88	2.76E-01	1.28E-01	4.10E+00	2.33E+00
137	7.92	2.58E-01	1.25E-01	3.97E+00	2.48E+00
138	7.95	2.81E-01	1.35E-01	4.06E+00	2.23E+00
139	7.98	2.94E-01	1.31E-01	4.04E+00	2.49E+00
140	8.01	2.98E-01	1.35E-01	3.99E+00	2.28E+00
141	8.05	3.02E-01	1.32E-01	4.20E+00	2.48E+00
142	8.08	2.98E-01	1.35E-01	4.03E+00	2.15E+00
143	8.11	3.46E-01	1.25E-01	4.34E+00	2.54E+00
144	8.15	3.66E-01	1.23E-01	4.35E+00	2.66E+00
145	8.18	3.58E-01	1.28E-01	4.47E+00	2.89E+00
146	8.21	3.97E-01	1.29E-01	4.39E+00	2.67E+00
147	8.24	4.25E-01	1.30E-01	4.58E+00	2.48E+00
148	8.28	3.65E-01	1.29E-01	4.26E+00	2.67E+00
149	8.31	3.26E-01	1.30E-01	4.19E+00	2.46E+00
150	8.34	3.27E-01	1.29E-01	4.07E+00	2.38E+00
151	8.37	3.40E-01	1.26E-01	3.77E+00	2.30E+00
152	8.41	3.76E-01	1.33E-01	3.95E+00	2.32E+00
153	8.44	3.76E-01	1.23E-01	3.84E+00	2.50E+00
154	8.47	3.56E-01	1.25E-01	3.78E+00	2.53E+00
155	8.50	3.70E-01	1.33E-01	4.00E+00	2.44E+00
156	8.54	3.72E-01	1.33E-01	3.97E+00	2.40E+00
157	8.57	3.80E-01	1.27E-01	3.92E+00	2.40E+00
158	8.60	3.73E-01	1.27E-01	3.99E+00	2.52E+00
159	8.63	3.91E-01	1.33E-01	4.22E+00	2.49E+00
160	8.67	4.48E-01	1.31E-01	4.48E+00	2.56E+00
161	8.70	4.21E-01	1.25E-01	4.26E+00	2.61E+00
162	8.73	4.83E-01	1.33E-01	4.41E+00	2.45E+00
163	8.77	5.12E-01	1.33E-01	4.82E+00	2.92E+00
164	8.80	4.62E-01	1.30E-01	4.31E+00	2.45E+00
165	8.83	4.20E-01	1.33E-01	4.03E+00	2.31E+00
166	8.86	3.87E-01	1.34E-01	3.94E+00	2.15E+00
167	8.90	4.16E-01	1.30E-01	3.94E+00	2.45E+00
168	8.93	4.59E-01	1.31E-01	4.16E+00	2.42E+00
169	8.96	4.63E-01	1.31E-01	4.10E+00	2.49E+00
170	8.99	4.83E-01	1.29E-01	4.01E+00	2.43E+00
171	9.03	4.74E-01	1.34E-01	4.17E+00	2.37E+00

Depth	Age	Fe/Ca	Al/Si	Fe/K	Ti/Al
[cm]	*[cal kyr]*	*[cps]*	*[cps]*	*[cps]*	*[cps]*
172	9.06	4.76E-01	1.31E-01	4.22E+00	2.47E+00
173	9.09	4.81E-01	1.24E-01	4.08E+00	2.54E+00
174	9.12	4.78E-01	1.30E-01	4.11E+00	2.47E+00
175	9.16	5.00E-01	1.32E-01	4.13E+00	2.54E+00
176	9.19	5.12E-01	1.31E-01	4.19E+00	2.61E+00
177	9.22	5.32E-01	1.28E-01	4.15E+00	2.60E+00
178	9.25	5.18E-01	1.27E-01	4.20E+00	2.79E+00
179	9.29	5.14E-01	1.32E-01	4.22E+00	2.56E+00
180	9.32	5.58E-01	1.25E-01	4.52E+00	2.99E+00
181	9.35	5.21E-01	1.27E-01	4.35E+00	2.84E+00
182	9.38	6.42E-01	1.29E-01	4.53E+00	2.98E+00
183	9.42	6.28E-01	1.34E-01	4.60E+00	2.94E+00
184	9.45	6.26E-01	1.27E-01	4.49E+00	2.92E+00
185	9.48	5.77E-01	1.28E-01	4.52E+00	2.87E+00
186	9.52	5.97E-01	1.33E-01	4.51E+00	2.73E+00
187	9.55	7.70E-01	1.35E-01	4.42E+00	2.78E+00
188	9.58	8.31E-01	1.42E-01	4.79E+00	2.51E+00
189	9.61	8.16E-01	1.42E-01	4.61E+00	2.43E+00
190	9.65	8.55E-01	1.41E-01	4.54E+00	2.44E+00
191	9.68	8.00E-01	1.40E-01	4.62E+00	2.37E+00
192	9.71	9.45E-01	1.35E-01	4.68E+00	2.79E+00
193	9.74	9.05E-01	1.36E-01	4.58E+00	2.67E+00
194	9.78	9.18E-01	1.31E-01	4.38E+00	2.76E+00
195	9.81	8.57E-01	1.26E-01	4.23E+00	2.85E+00
196	9.84	9.32E-01	1.30E-01	4.63E+00	2.86E+00
197	9.87	8.14E-01	1.34E-01	4.63E+00	2.94E+00
198	9.91	8.91E-01	1.24E-01	5.34E+00	3.62E+00
199	9.94	9.02E-01	1.29E-01	5.55E+00	3.61E+00
200	9.97	7.45E-01	1.31E-01	4.85E+00	3.01E+00
201	10.00	8.03E-01	1.29E-01	5.30E+00	3.42E+00
202	10.04	8.90E-01	1.29E-01	4.82E+00	3.26E+00
203	10.07	7.55E-01	1.27E-01	4.84E+00	3.00E+00
204	10.10	7.70E-01	1.35E-01	4.74E+00	2.74E+00
205	10.13	8.04E-01	1.31E-01	4.90E+00	3.09E+00
206	10.17	7.07E-01	1.30E-01	4.70E+00	2.92E+00
207	10.20	7.32E-01	1.22E-01	5.00E+00	3.27E+00
208	10.23	6.95E-01	1.37E-01	4.67E+00	2.67E+00
209	10.25	6.18E-01	1.28E-01	4.21E+00	2.84E+00
210	10.28	7.26E-01	1.33E-01	4.49E+00	2.43E+00
211	10.31	6.95E-01	1.36E-01	4.22E+00	2.43E+00
212	10.34	8.89E-01	1.35E-01	4.65E+00	2.68E+00
213	10.36	8.59E-01	1.39E-01	4.67E+00	2.55E+00
214	10.39	8.97E-01	1.29E-01	4.66E+00	2.85E+00

Depth	Age	Fe/Ca	Al/Si	Fe/K	Ti/Al
[cm]	*[cal kyr]*	*[cps]*	*[cps]*	*[cps]*	*[cps]*
215	10.42	8.83E-01	1.41E-01	4.52E+00	2.63E+00
216	10.45	8.80E-01	1.35E-01	4.51E+00	2.50E+00
217	10.47	9.12E-01	1.41E-01	4.66E+00	2.35E+00
218	10.50	8.24E-01	1.36E-01	4.67E+00	2.67E+00
219	10.53	9.35E-01	1.44E-01	5.01E+00	2.61E+00
220	10.56	1.02E+00	1.39E-01	5.16E+00	2.73E+00
221	10.58	1.01E+00	1.40E-01	5.04E+00	2.90E+00
222	10.61	9.30E-01	1.38E-01	4.90E+00	2.71E+00
223	10.64	1.00E+00	1.38E-01	5.02E+00	2.73E+00
224	10.67	1.12E+00	1.44E-01	5.31E+00	2.53E+00
225	10.69	1.10E+00	1.41E-01	4.89E+00	2.48E+00
226	10.72	1.02E+00	1.35E-01	5.01E+00	2.50E+00
227	10.75	8.86E-01	1.36E-01	4.81E+00	2.54E+00
228	10.77	9.13E-01	1.39E-01	4.62E+00	2.48E+00
229	10.80	1.15E+00	1.36E-01	5.22E+00	2.78E+00
230	10.83	1.26E+00	1.44E-01	5.04E+00	2.44E+00
231	10.86	1.12E+00	1.44E-01	4.90E+00	2.38E+00
232	10.88	1.32E+00	1.47E-01	5.13E+00	2.47E+00
233	10.91	1.95E+00	1.47E-01	5.61E+00	2.62E+00
234	10.94	1.96E+00	1.46E-01	6.07E+00	2.80E+00
235	10.97	2.08E+00	1.44E-01	6.01E+00	2.89E+00
236	10.99	2.57E+00	1.49E-01	6.13E+00	2.74E+00
237	11.02	1.79E+00	1.48E-01	5.75E+00	2.80E+00
238	11.05	1.68E+00	1.46E-01	5.94E+00	2.91E+00
239	11.08	2.56E+00	1.45E-01	5.92E+00	3.13E+00
240	11.10	2.31E+00	1.48E-01	5.64E+00	2.79E+00
241	11.13	1.43E+00	1.38E-01	5.29E+00	2.95E+00
242	11.13	2.30E+00	1.46E-01	6.09E+00	2.91E+00
243	11.14	3.12E+00	1.45E-01	6.15E+00	3.03E+00
244	11.14	1.64E+00	1.43E-01	5.85E+00	2.86E+00
245	11.15	1.56E+00	1.44E-01	5.62E+00	2.71E+00
246	11.15	1.79E+00	1.52E-01	5.59E+00	2.45E+00
247	11.16	2.08E+00	1.51E-01	5.51E+00	2.44E+00
248	11.16	2.12E+00	1.46E-01	5.80E+00	2.51E+00
249	11.17	1.58E+00	1.49E-01	5.82E+00	2.60E+00
250	11.17	1.36E+00	1.48E-01	5.56E+00	2.48E+00
251	11.18	1.88E+00	1.45E-01	5.86E+00	2.83E+00
252	11.18	2.22E+00	1.47E-01	5.53E+00	2.55E+00
253	11.19	2.04E+00	1.49E-01	5.28E+00	2.56E+00
254	11.19	2.05E+00	1.46E-01	5.70E+00	2.88E+00
255	11.20	2.16E+00	1.49E-01	5.67E+00	2.81E+00
256	11.20	2.10E+00	1.44E-01	5.74E+00	2.85E+00
257	11.21	2.12E+00	1.36E-01	5.90E+00	2.92E+00

Depth	Age	Fe/Ca	Al/Si	Fe/K	Ti/Al
[cm]	*[cal kyr]*	*[cps]*	*[cps]*	*[cps]*	*[cps]*
258	11.21	2.24E+00	1.45E-01	5.64E+00	2.71E+00
259	11.22	2.20E+00	1.46E-01	5.47E+00	2.72E+00
260	11.22	2.11E+00	1.42E-01	5.26E+00	2.70E+00
261	11.23	1.95E+00	1.44E-01	5.16E+00	2.47E+00
262	11.23	2.03E+00	1.48E-01	5.58E+00	2.45E+00
263	11.24	1.98E+00	1.41E-01	5.37E+00	2.58E+00
264	11.24	2.08E+00	1.45E-01	5.80E+00	2.54E+00
265	11.25	1.86E+00	1.43E-01	5.36E+00	2.55E+00
266	11.25	1.74E+00	1.38E-01	5.17E+00	2.69E+00
267	11.26	1.35E+00	1.34E-01	5.28E+00	2.68E+00
268	11.26	1.51E+00	1.36E-01	5.05E+00	2.81E+00
269	11.27	1.66E+00	1.31E-01	5.39E+00	2.85E+00
270	11.27	2.01E+00	1.30E-01	5.67E+00	2.66E+00
271	11.28	1.78E+00	1.32E-01	5.18E+00	2.81E+00
272	11.28	1.87E+00	1.33E-01	5.51E+00	2.75E+00
273	11.29	1.87E+00	1.33E-01	5.34E+00	2.89E+00
274	11.29	1.92E+00	1.25E-01	5.57E+00	3.19E+00
275	11.29	1.78E+00	1.22E-01	5.38E+00	3.14E+00
276	11.30	1.80E+00	1.25E-01	5.21E+00	3.12E+00
277	11.30	1.86E+00	1.25E-01	5.21E+00	3.21E+00
278	11.31	1.88E+00	1.25E-01	5.48E+00	3.31E+00
279	11.31	1.96E+00	1.20E-01	5.45E+00	3.35E+00
280	11.32	2.04E+00	1.26E-01	5.44E+00	3.25E+00
281	11.32	2.12E+00	1.22E-01	5.58E+00	3.33E+00
282	11.33	2.09E+00	1.23E-01	5.22E+00	3.03E+00
283	11.33	2.13E+00	1.29E-01	5.08E+00	2.87E+00
284	11.34	3.01E+00	1.47E-01	5.76E+00	2.67E+00
285	11.34	1.99E+00	1.24E-01	5.18E+00	3.16E+00
286	11.35	2.16E+00	1.25E-01	5.06E+00	2.87E+00
287	11.35	2.28E+00	1.28E-01	5.19E+00	2.81E+00
288	11.36	2.06E+00	1.26E-01	4.98E+00	2.77E+00
289	11.36	2.24E+00	1.24E-01	5.13E+00	2.90E+00
290	11.37	2.00E+00	1.25E-01	5.01E+00	2.99E+00
291	11.37	2.08E+00	1.27E-01	5.02E+00	2.81E+00
292	11.38	1.98E+00	1.31E-01	5.16E+00	2.81E+00
293	11.38	2.00E+00	1.25E-01	5.32E+00	2.93E+00
294	11.39	2.00E+00	1.25E-01	5.30E+00	3.03E+00
295	11.39	1.94E+00	1.25E-01	5.00E+00	3.13E+00
296	11.40	1.95E+00	1.31E-01	5.04E+00	2.88E+00
297	11.40	1.86E+00	1.25E-01	5.13E+00	3.10E+00
298	11.41	2.03E+00	1.32E-01	5.11E+00	2.74E+00
299	11.41	2.15E+00	1.27E-01	5.08E+00	2.83E+00
300	11.42	2.06E+00	1.32E-01	4.98E+00	2.64E+00

Depth	Age	Fe/Ca	Al/Si	Fe/K	Ti/Al
[cm]	*[cal kyr]*	*[cps]*	*[cps]*	*[cps]*	*[cps]*
301	11.42	2.19E+00	1.30E-01	5.53E+00	2.69E+00
302	11.43	1.89E+00	1.30E-01	5.09E+00	2.64E+00
303	11.43	1.78E+00	1.28E-01	4.94E+00	2.52E+00
304	11.44	1.87E+00	1.32E-01	4.91E+00	2.58E+00
305	11.44	1.79E+00	1.29E-01	4.78E+00	2.56E+00
306	11.45	1.83E+00	1.28E-01	4.89E+00	2.58E+00
307	11.45	1.86E+00	1.24E-01	4.94E+00	2.67E+00
308	11.48	1.89E+00	1.29E-01	4.95E+00	2.59E+00
309	11.51	1.85E+00	1.28E-01	4.88E+00	2.50E+00
310	11.54	1.84E+00	1.30E-01	5.09E+00	2.52E+00
311	11.57	1.91E+00	1.26E-01	5.06E+00	2.62E+00
312	11.60	1.92E+00	1.24E-01	5.00E+00	2.62E+00
313	11.62	1.76E+00	1.30E-01	4.78E+00	2.57E+00
314	11.65	1.75E+00	1.29E-01	4.84E+00	2.43E+00
315	11.68	1.82E+00	1.31E-01	4.86E+00	2.46E+00
316	11.71	1.79E+00	1.30E-01	4.85E+00	2.55E+00
317	11.74	1.75E+00	1.28E-01	4.85E+00	2.57E+00
318	11.77	1.76E+00	1.27E-01	4.77E+00	2.50E+00
319	11.80	1.87E+00	1.25E-01	4.64E+00	2.65E+00
320	11.83	1.97E+00	1.28E-01	4.68E+00	2.55E+00
321	11.86	2.08E+00	1.26E-01	4.92E+00	2.56E+00
322	11.89	2.08E+00	1.24E-01	4.85E+00	2.59E+00
323	11.92	2.20E+00	1.30E-01	4.79E+00	2.48E+00
324	11.94	2.02E+00	1.27E-01	4.60E+00	2.53E+00
325	11.97	2.14E+00	1.22E-01	4.77E+00	2.78E+00
326	12.00	2.23E+00	1.22E-01	5.04E+00	2.76E+00
327	12.03	2.19E+00	1.21E-01	4.78E+00	2.70E+00
328	12.06	2.08E+00	1.25E-01	4.80E+00	2.76E+00
329	12.09	2.18E+00	1.28E-01	4.85E+00	2.56E+00
330	12.09	1.96E+00	1.29E-01	4.76E+00	2.62E+00
331	12.09	2.01E+00	1.25E-01	4.73E+00	2.58E+00
332	12.10	1.96E+00	1.28E-01	4.88E+00	2.50E+00
333	12.10	2.25E+00	1.30E-01	4.95E+00	2.53E+00
334	12.10	2.11E+00	1.31E-01	5.01E+00	2.60E+00
335	12.10	2.00E+00	1.28E-01	4.79E+00	2.62E+00
336	12.10	2.13E+00	1.28E-01	4.85E+00	2.56E+00
337	12.10	2.08E+00	1.25E-01	4.95E+00	2.72E+00
338	12.11	2.02E+00	1.26E-01	5.10E+00	2.70E+00
339	12.11	1.99E+00	1.27E-01	4.96E+00	2.76E+00
340	12.11	1.82E+00	1.25E-01	5.09E+00	2.74E+00
341	12.11	1.97E+00	1.31E-01	5.01E+00	2.59E+00
342	12.11	2.01E+00	1.27E-01	5.03E+00	2.64E+00
343	12.12	1.92E+00	1.26E-01	5.17E+00	2.74E+00

Depth	Age	Fe/Ca	Al/Si	Fe/K	Ti/Al
[cm]	*[cal kyr]*	*[cps]*	*[cps]*	*[cps]*	*[cps]*
344	12.12	2.01E+00	1.24E-01	5.07E+00	2.64E+00
345	12.12	1.90E+00	1.33E-01	4.85E+00	2.34E+00
346	12.12	1.95E+00	1.25E-01	4.89E+00	2.69E+00
347	12.12	2.06E+00	1.26E-01	4.85E+00	2.69E+00
348	12.13	2.30E+00	1.31E-01	4.72E+00	2.56E+00
349	12.13	2.52E+00	1.29E-01	5.07E+00	2.60E+00
350	12.13	2.39E+00	1.32E-01	5.03E+00	2.54E+00
351	12.13	2.28E+00	1.31E-01	4.91E+00	2.64E+00
352	12.13	2.54E+00	1.32E-01	5.04E+00	2.68E+00
353	12.13	2.42E+00	1.37E-01	4.81E+00	2.56E+00
354	12.14	2.27E+00	1.36E-01	5.01E+00	2.64E+00
355	12.14	2.22E+00	1.36E-01	4.99E+00	2.52E+00
356	12.14	2.45E+00	1.35E-01	5.18E+00	2.64E+00
357	12.14	2.23E+00	1.31E-01	5.23E+00	2.77E+00
358	12.14	2.32E+00	1.33E-01	5.06E+00	2.62E+00
359	12.15	2.18E+00	1.38E-01	4.92E+00	2.56E+00
360	12.15	2.37E+00	1.30E-01	5.19E+00	2.75E+00
361	12.15	2.38E+00	1.34E-01	5.35E+00	2.70E+00
362	12.15	2.34E+00	1.33E-01	4.94E+00	2.68E+00
363	12.15	2.52E+00	1.32E-01	5.21E+00	2.61E+00
364	12.16	2.38E+00	1.36E-01	4.89E+00	2.53E+00
365	12.16	2.74E+00	1.34E-01	5.49E+00	2.63E+00
366	12.16	2.61E+00	1.33E-01	5.33E+00	2.67E+00
367	12.16	2.64E+00	1.33E-01	5.49E+00	2.67E+00
368	12.16	2.62E+00	1.31E-01	5.55E+00	2.85E+00
369	12.16	3.00E+00	1.35E-01	5.89E+00	2.72E+00
370	12.17	2.77E+00	1.35E-01	5.61E+00	2.69E+00
371	12.17	2.48E+00	1.37E-01	5.23E+00	2.67E+00
372	12.17	2.67E+00	1.34E-01	5.43E+00	2.86E+00
373	12.17	2.61E+00	1.35E-01	5.51E+00	2.82E+00
374	12.17	2.93E+00	1.32E-01	5.61E+00	2.84E+00
375	12.18	2.81E+00	1.38E-01	5.39E+00	2.70E+00
376	12.18	2.91E+00	1.31E-01	5.42E+00	2.79E+00
377	12.18	2.70E+00	1.38E-01	5.23E+00	2.65E+00
378	12.18	2.65E+00	1.31E-01	5.35E+00	2.75E+00
379	12.18	2.63E+00	1.34E-01	5.33E+00	2.85E+00
380	12.19	2.83E+00	1.31E-01	5.57E+00	2.84E+00
381	12.19	2.67E+00	1.36E-01	5.27E+00	2.73E+00
382	12.19	2.91E+00	1.34E-01	5.59E+00	2.82E+00
383	12.19	2.80E+00	1.36E-01	5.26E+00	2.66E+00
384	12.19	3.32E+00	1.33E-01	6.08E+00	2.79E+00
385	12.19	2.97E+00	1.33E-01	5.32E+00	2.69E+00
386	12.20	3.70E+00	1.37E-01	5.39E+00	2.69E+00

Depth	Age	Fe/Ca	Al/Si	Fe/K	Ti/Al
[cm]	*[cal kyr]*	*[cps]*	*[cps]*	*[cps]*	*[cps]*
387	12.20	3.86E+00	1.31E-01	5.46E+00	2.87E+00
388	12.20	5.63E+00	1.29E-01	5.54E+00	2.98E+00
389	12.20	5.39E+00	1.35E-01	5.47E+00	2.91E+00
390	12.20	3.50E+00	1.36E-01	5.24E+00	2.88E+00
391	12.21	3.46E+00	1.31E-01	5.24E+00	2.88E+00
392	12.21	3.49E+00	1.31E-01	5.39E+00	3.04E+00
393	12.21	3.13E+00	1.34E-01	5.58E+00	3.06E+00
394	12.21	3.33E+00	1.32E-01	5.59E+00	2.95E+00
395	12.21	3.42E+00	1.33E-01	5.41E+00	2.91E+00
396	12.22	3.89E+00	1.32E-01	5.42E+00	2.84E+00
397	12.22	4.07E+00	1.33E-01	5.29E+00	2.88E+00
398	12.22	3.89E+00	1.37E-01	5.56E+00	3.04E+00
399	12.22	3.64E+00	1.38E-01	5.47E+00	2.90E+00
400	12.22	3.72E+00	1.39E-01	5.43E+00	2.82E+00
401	12.22	3.95E+00	1.36E-01	5.78E+00	2.82E+00
402	12.23	3.63E+00	1.37E-01	5.81E+00	2.89E+00
403	12.23	3.41E+00	1.37E-01	5.66E+00	2.89E+00
404	12.23	3.54E+00	1.43E-01	5.71E+00	2.69E+00
405	12.23	3.78E+00	1.43E-01	5.68E+00	2.67E+00
406	12.23	3.53E+00	1.41E-01	5.93E+00	2.81E+00
407	12.24	3.19E+00	1.45E-01	5.60E+00	2.65E+00
408	12.24	3.73E+00	1.43E-01	6.04E+00	2.57E+00
409	12.24	3.36E+00	1.52E-01	5.67E+00	2.50E+00
410	12.24	2.98E+00	1.47E-01	5.66E+00	2.52E+00
411	12.24	3.39E+00	1.42E-01	5.76E+00	2.70E+00
412	12.25	3.40E+00	1.47E-01	5.74E+00	2.58E+00
413	12.25	2.86E+00	1.49E-01	5.58E+00	2.59E+00
414	12.25	2.81E+00	1.50E-01	5.73E+00	2.50E+00
415	12.25	2.67E+00	1.50E-01	5.62E+00	2.56E+00
416	12.25	2.43E+00	1.49E-01	5.74E+00	2.56E+00
417	12.25	2.60E+00	1.47E-01	5.83E+00	2.55E+00
418	12.26	2.55E+00	1.51E-01	5.81E+00	2.45E+00
419	12.26	2.47E+00	1.58E-01	5.70E+00	2.30E+00
420	12.26	2.59E+00	1.53E-01	5.76E+00	2.40E+00
421	12.26	2.68E+00	1.54E-01	5.89E+00	2.41E+00
422	12.26	2.22E+00	1.49E-01	5.83E+00	2.54E+00
423	12.27	1.50E+00	1.54E-01	5.72E+00	2.36E+00
424	12.27	1.84E+00	1.57E-01	5.84E+00	2.33E+00
425	12.27	1.58E+00	1.58E-01	5.55E+00	2.29E+00
426	12.27	1.56E+00	1.54E-01	5.70E+00	2.29E+00
427	12.27	2.06E+00	1.54E-01	6.10E+00	2.41E+00
428	12.28	1.85E+00	1.57E-01	6.05E+00	2.41E+00
429	12.28	1.49E+00	1.60E-01	5.82E+00	2.30E+00

Depth	Age	Fe/Ca	Al/Si	Fe/K	Ti/Al
[cm]	*[cal kyr]*	*[cps]*	*[cps]*	*[cps]*	*[cps]*
430	12.28	1.20E+00	1.53E-01	5.34E+00	2.26E+00
431	12.28	9.27E-01	1.50E-01	5.23E+00	2.25E+00
432	12.28	1.05E+00	1.52E-01	5.27E+00	2.28E+00
433	12.28	1.04E+00	1.54E-01	5.20E+00	2.26E+00
434	12.29	1.05E+00	1.51E-01	5.51E+00	2.36E+00
435	12.29	9.05E-01	1.54E-01	4.99E+00	2.21E+00
436	12.29	9.30E-01	1.53E-01	5.07E+00	2.25E+00
437	12.29	8.23E-01	1.52E-01	4.91E+00	2.28E+00
438	12.29	8.71E-01	1.46E-01	5.14E+00	2.32E+00
439	12.30	9.21E-01	1.47E-01	5.11E+00	2.41E+00
440	12.30	9.53E-01	1.51E-01	5.10E+00	2.38E+00
441	12.30	9.15E-01	1.50E-01	5.16E+00	2.32E+00
442	12.30	9.09E-01	1.50E-01	5.17E+00	2.34E+00
443	12.30	9.39E-01	1.54E-01	4.93E+00	2.27E+00
444	12.31	9.18E-01	1.54E-01	4.89E+00	2.34E+00
445	12.31	1.05E+00	1.49E-01	4.88E+00	2.40E+00
446	12.31	1.22E+00	1.54E-01	4.84E+00	2.37E+00
447	12.31	1.48E+00	1.51E-01	4.85E+00	2.43E+00
448	12.31	1.20E+00	1.51E-01	4.88E+00	2.31E+00
449	12.31	1.20E+00	1.51E-01	4.99E+00	2.43E+00
450	12.32	1.11E+00	1.51E-01	4.74E+00	2.38E+00
451	12.32	1.22E+00	1.51E-01	4.91E+00	2.47E+00
452	12.32	1.27E+00	1.47E-01	4.88E+00	2.49E+00
453	12.35	1.20E+00	1.51E-01	4.96E+00	2.48E+00
454	12.38	1.43E+00	1.48E-01	4.90E+00	2.45E+00
455	12.41	1.57E+00	1.51E-01	5.03E+00	2.49E+00
456	12.45	1.50E+00	1.49E-01	4.94E+00	2.52E+00
457	12.48	1.54E+00	1.55E-01	5.02E+00	2.40E+00
458	12.51	1.87E+00	1.49E-01	5.20E+00	2.60E+00
459	12.54	1.91E+00	1.52E-01	5.10E+00	2.46E+00
460	12.57	1.94E+00	1.50E-01	5.13E+00	2.50E+00
461	12.60	2.01E+00	1.53E-01	5.20E+00	2.54E+00
462	12.63	2.05E+00	1.53E-01	5.12E+00	2.50E+00
463	12.66	2.08E+00	1.52E-01	5.18E+00	2.56E+00
464	12.70	2.28E+00	1.54E-01	5.14E+00	2.54E+00
465	12.73	2.29E+00	1.48E-01	5.30E+00	2.65E+00
466	12.76	2.42E+00	1.47E-01	5.25E+00	2.65E+00
467	12.79	3.56E+00	1.48E-01	5.24E+00	2.77E+00
468	12.82	2.95E+00	1.52E-01	5.21E+00	2.66E+00
469	12.85	2.46E+00	1.51E-01	5.11E+00	2.65E+00
470	12.88	3.13E+00	1.54E-01	5.18E+00	2.56E+00
471	12.91	3.37E+00	1.49E-01	5.07E+00	2.67E+00
472	12.95	5.50E+00	1.50E-01	5.26E+00	2.77E+00

Depth	Age	Fe/Ca	Al/Si	Fe/K	Ti/Al
[cm]	*[cal kyr]*	*[cps]*	*[cps]*	*[cps]*	*[cps]*
473	12.98	4.64E+00	1.45E-01	5.29E+00	2.78E+00
474	13.01	7.25E+00	1.54E-01	5.47E+00	2.73E+00
475	13.04	6.70E+00	1.49E-01	5.36E+00	2.89E+00
476	13.07	3.40E+00	1.50E-01	5.34E+00	2.75E+00
477	13.10	4.92E+00	1.55E-01	5.42E+00	2.70E+00
478	13.13	3.88E+00	1.54E-01	5.25E+00	2.63E+00
479	13.16	4.98E+00	1.53E-01	5.39E+00	2.72E+00
480	13.20	8.79E+00	1.57E-01	5.39E+00	2.71E+00
481	13.23	8.34E+00	1.56E-01	5.49E+00	2.68E+00
482	13.26	8.75E+00	1.52E-01	5.45E+00	2.86E+00
483	13.29	8.18E+00	1.55E-01	5.55E+00	2.78E+00
484	13.32	9.11E+00	1.53E-01	5.42E+00	2.78E+00
485	13.35	7.71E+00	1.53E-01	5.40E+00	2.85E+00
486	13.38	7.17E+00	1.53E-01	5.43E+00	2.84E+00
487	13.41	9.59E+00	1.51E-01	5.47E+00	2.96E+00
488	13.45	1.40E+01	1.56E-01	5.47E+00	2.75E+00
489	13.48	1.56E+01	1.53E-01	5.58E+00	2.81E+00
490	13.51	1.52E+01	1.52E-01	5.49E+00	2.97E+00
496	13.63	1.10E+01	1.53E-01	5.38E+00	2.94E+00
497	13.64	9.96E+00	1.55E-01	5.39E+00	2.94E+00
498	13.66	1.05E+01	1.54E-01	5.29E+00	2.97E+00
499	13.68	1.29E+01	1.53E-01	5.29E+00	2.86E+00
500	13.69	1.13E+01	1.52E-01	5.23E+00	2.97E+00
501	13.71	1.27E+01	1.55E-01	5.34E+00	2.88E+00
502	13.73	1.01E+01	1.55E-01	5.39E+00	2.84E+00
503	13.75	9.16E+00	1.59E-01	5.35E+00	2.79E+00
504	13.76	5.87E+00	1.55E-01	5.16E+00	2.82E+00
505	13.78	4.81E+00	1.55E-01	5.16E+00	2.67E+00
506	13.80	4.55E+00	1.53E-01	5.16E+00	2.73E+00
507	13.82	4.37E+00	1.55E-01	4.96E+00	2.62E+00
508	13.83	4.01E+00	1.55E-01	5.08E+00	2.66E+00
509	13.85	3.76E+00	1.47E-01	5.28E+00	2.65E+00
510	13.87	3.52E+00	1.46E-01	4.92E+00	2.77E+00
511	13.88	3.61E+00	1.45E-01	5.07E+00	2.89E+00
512	13.90	4.16E+00	1.45E-01	5.02E+00	2.83E+00
513	13.92	3.07E+00	1.35E-01	5.15E+00	2.93E+00
514	13.94	2.66E+00	1.34E-01	5.18E+00	2.94E+00
515	13.95	2.43E+00	1.29E-01	5.12E+00	3.02E+00
516	13.97	3.16E+00	1.35E-01	4.82E+00	2.98E+00
517	13.99	3.02E+00	1.35E-01	4.97E+00	2.91E+00
518	14.00	2.17E+00	1.29E-01	5.23E+00	2.94E+00
519	14.02	2.22E+00	1.28E-01	5.19E+00	3.10E+00
520	14.04	2.46E+00	1.27E-01	5.00E+00	3.16E+00

Depth	Age	Fe/Ca	Al/Si	Fe/K	Ti/Al
[cm]	*[cal kyr]*	*[cps]*	*[cps]*	*[cps]*	*[cps]*
521	14.06	2.94E+00	1.31E-01	5.02E+00	2.97E+00
522	14.07	2.96E+00	1.28E-01	4.87E+00	3.03E+00
523	14.09	3.87E+00	1.38E-01	5.08E+00	2.99E+00
524	14.13	3.69E+00	1.35E-01	5.07E+00	3.00E+00
525	14.17	2.45E+00	1.22E-01	5.06E+00	3.16E+00
526	14.21	2.17E+00	1.26E-01	5.12E+00	2.81E+00
527	14.25	2.09E+00	1.22E-01	5.27E+00	3.13E+00
528	14.29	2.13E+00	1.21E-01	5.05E+00	3.14E+00
529	14.33	2.52E+00	1.17E-01	4.92E+00	3.46E+00
530	14.37	2.59E+00	1.17E-01	5.10E+00	3.29E+00
531	14.41	2.43E+00	1.20E-01	4.99E+00	3.20E+00
532	14.45	2.51E+00	1.22E-01	5.10E+00	3.14E+00
533	14.49	2.42E+00	1.24E-01	4.71E+00	2.93E+00
534	14.52	2.42E+00	1.23E-01	4.92E+00	3.02E+00
535	14.56	2.43E+00	1.23E-01	5.02E+00	3.00E+00
536	14.60	2.46E+00	1.25E-01	5.48E+00	2.91E+00
537	14.64	2.55E+00	1.22E-01	5.11E+00	3.03E+00
538	14.68	2.34E+00	1.24E-01	4.78E+00	2.96E+00
539	14.72	2.45E+00	1.21E-01	4.79E+00	3.05E+00
540	14.76	2.28E+00	1.22E-01	4.54E+00	2.90E+00
541	14.80	2.50E+00	1.19E-01	4.43E+00	2.99E+00
542	14.84	2.40E+00	1.24E-01	4.54E+00	2.85E+00
543	14.88	2.49E+00	1.26E-01	4.68E+00	2.85E+00
544	14.90	2.23E+00	1.21E-01	4.71E+00	3.15E+00
545	14.92	2.65E+00	1.28E-01	4.80E+00	3.05E+00
546	14.93	2.26E+00	1.22E-01	4.50E+00	3.00E+00
547	14.95	2.37E+00	1.28E-01	4.47E+00	2.74E+00
548	14.97	2.80E+00	1.22E-01	4.63E+00	2.93E+00
549	14.99	2.74E+00	1.21E-01	4.58E+00	2.94E+00
550	15.00	2.39E+00	1.22E-01	4.78E+00	3.03E+00
551	15.02	2.48E+00	1.18E-01	4.58E+00	3.12E+00
552	15.04	2.77E+00	1.17E-01	4.80E+00	3.27E+00
553	15.06	2.79E+00	1.22E-01	4.76E+00	3.00E+00
554	15.07	2.56E+00	1.22E-01	4.82E+00	2.99E+00
555	15.09	2.75E+00	1.21E-01	4.59E+00	3.06E+00
556	15.11	2.81E+00	1.21E-01	4.51E+00	2.86E+00
557	15.13	2.94E+00	1.21E-01	4.88E+00	2.92E+00
558	15.14	2.74E+00	1.20E-01	4.38E+00	2.89E+00
559	15.16	3.14E+00	1.21E-01	4.19E+00	2.65E+00
560	15.18	3.69E+00	1.27E-01	4.89E+00	2.85E+00
561	15.20	4.24E+00	1.26E-01	5.00E+00	2.85E+00
562	15.21	3.45E+00	1.24E-01	4.95E+00	3.01E+00
563	15.23	3.51E+00	1.22E-01	4.72E+00	2.99E+00

Depth	Age	Fe/Ca	Al/Si	Fe/K	Ti/Al
[cm]	*[cal kyr]*	*[cps]*	*[cps]*	*[cps]*	*[cps]*
564	15.25	3.31E+00	1.24E-01	4.46E+00	2.86E+00
565	15.27	3.19E+00	1.25E-01	4.55E+00	2.80E+00
566	15.28	3.57E+00	1.24E-01	4.97E+00	2.93E+00
567	15.30	4.82E+00	1.23E-01	4.41E+00	2.87E+00
568	15.32	3.55E+00	1.26E-01	4.44E+00	2.72E+00
569	15.34	5.16E+00	1.24E-01	4.94E+00	2.83E+00
570	15.35	3.70E+00	1.25E-01	4.50E+00	2.82E+00
571	15.37	3.51E+00	1.28E-01	4.44E+00	2.73E+00
572	15.39	3.80E+00	1.25E-01	4.37E+00	2.79E+00
573	15.41	3.20E+00	1.27E-01	4.30E+00	2.61E+00
574	15.42	3.36E+00	1.28E-01	4.34E+00	2.72E+00
575	15.44	4.02E+00	1.27E-01	4.26E+00	2.69E+00
576	15.46	3.83E+00	1.28E-01	4.22E+00	2.73E+00
577	15.48	3.93E+00	1.28E-01	4.38E+00	2.87E+00
578	15.49	4.23E+00	1.25E-01	4.72E+00	2.93E+00
579	15.51	3.46E+00	1.27E-01	4.66E+00	2.81E+00
580	15.53	3.63E+00	1.29E-01	4.79E+00	2.78E+00
581	15.55	3.12E+00	1.30E-01	4.68E+00	2.79E+00
582	15.56	3.44E+00	1.24E-01	4.60E+00	2.93E+00
583	15.58	4.66E+00	1.24E-01	4.61E+00	2.82E+00
584	15.60	3.48E+00	1.22E-01	5.10E+00	2.85E+00
585	15.62	3.30E+00	1.25E-01	4.45E+00	2.77E+00
586	15.63	2.86E+00	1.22E-01	4.72E+00	2.81E+00
587	15.65	4.07E+00	1.28E-01	4.43E+00	2.88E+00
588	15.67	3.48E+00	1.26E-01	4.56E+00	2.84E+00
589	15.69	4.22E+00	1.25E-01	4.61E+00	2.88E+00
590	15.70	3.93E+00	1.24E-01	4.75E+00	2.80E+00
591	15.72	3.63E+00	1.28E-01	4.62E+00	2.78E+00
592	15.74	4.56E+00	1.27E-01	4.48E+00	2.80E+00
593	15.76	3.97E+00	1.29E-01	4.65E+00	2.75E+00
594	15.77	3.73E+00	1.28E-01	4.94E+00	2.86E+00
595	15.79	4.16E+00	1.28E-01	5.42E+00	2.79E+00
596	15.81	4.28E+00	1.29E-01	5.01E+00	2.81E+00
597	15.83	3.71E+00	1.25E-01	5.18E+00	3.06E+00
598	15.84	5.51E+00	1.26E-01	4.92E+00	2.85E+00
599	15.86	7.76E+00	1.29E-01	4.99E+00	2.98E+00
600	15.88	8.53E+00	1.21E-01	5.07E+00	3.08E+00
601	15.90	9.66E+00	1.26E-01	5.12E+00	3.16E+00
602	15.91	9.96E+00	1.27E-01	5.10E+00	2.85E+00
603	15.93	8.62E+00	1.28E-01	4.88E+00	2.68E+00
604	15.95	6.20E+00	1.31E-01	4.72E+00	2.60E+00
605	15.97	7.56E+00	1.29E-01	5.38E+00	2.77E+00
606	15.98	4.46E+00	1.26E-01	5.07E+00	2.74E+00

Depth	Age	Fe/Ca	Al/Si	Fe/K	Ti/Al
[cm]	*[cal kyr]*	*[cps]*	*[cps]*	*[cps]*	*[cps]*
607	16.00	4.34E+00	1.30E-01	4.86E+00	2.70E+00
608	16.02	4.99E+00	1.32E-01	5.03E+00	2.71E+00
609	16.04	4.41E+00	1.30E-01	4.85E+00	2.63E+00
610	16.05	3.82E+00	1.30E-01	5.17E+00	2.71E+00
611	16.07	4.68E+00	1.30E-01	5.08E+00	2.70E+00
612	16.09	4.19E+00	1.32E-01	4.96E+00	2.70E+00
613	16.11	4.19E+00	1.30E-01	5.26E+00	2.63E+00
614	16.12	4.83E+00	1.32E-01	4.86E+00	2.61E+00
615	16.14	6.21E+00	1.36E-01	5.18E+00	2.65E+00
616	16.16	7.83E+00	1.28E-01	5.21E+00	2.79E+00
617	16.18	7.41E+00	1.36E-01	5.55E+00	2.62E+00
618	16.19	7.67E+00	1.35E-01	5.09E+00	2.68E+00
619	16.21	7.61E+00	1.33E-01	5.16E+00	2.62E+00
620	16.23	7.30E+00	1.35E-01	4.88E+00	2.61E+00
621	16.25	6.52E+00	1.34E-01	4.98E+00	2.64E+00
622	16.26	7.89E+00	1.38E-01	4.97E+00	2.65E+00
623	16.28	9.67E+00	1.39E-01	5.12E+00	2.53E+00
624	16.30	1.01E+01	1.32E-01	5.25E+00	2.85E+00
625	16.32	9.80E+00	1.40E-01	5.06E+00	2.58E+00
626	16.33	9.95E+00	1.39E-01	5.19E+00	2.62E+00
627	16.35	9.10E+00	1.44E-01	5.26E+00	2.53E+00
628	16.37	9.28E+00	1.37E-01	5.28E+00	2.81E+00
629	16.39	9.98E+00	1.37E-01	5.57E+00	2.78E+00
630	16.40	9.28E+00	1.41E-01	5.83E+00	2.86E+00
631	16.42	6.20E+00	1.41E-01	5.47E+00	2.80E+00
632	16.44	6.68E+00	1.39E-01	5.67E+00	2.86E+00
633	16.46	6.69E+00	1.38E-01	5.63E+00	2.89E+00
634	16.47	5.68E+00	1.45E-01	5.61E+00	2.66E+00
635	16.49	4.94E+00	1.43E-01	5.27E+00	2.60E+00
636	16.51	4.38E+00	1.40E-01	5.14E+00	2.69E+00
637	16.53	7.30E+00	1.42E-01	5.37E+00	2.77E+00
638	16.54	7.79E+00	1.48E-01	5.26E+00	2.71E+00
639	16.56	5.94E+00	1.43E-01	5.65E+00	2.78E+00
640	16.58	8.10E+00	1.44E-01	5.52E+00	2.68E+00
641	16.60	8.30E+00	1.46E-01	5.60E+00	2.65E+00
642	16.61	6.11E+00	1.43E-01	5.42E+00	2.76E+00
643	16.63	8.29E+00	1.45E-01	5.51E+00	2.72E+00
644	16.65	1.00E+01	1.42E-01	5.64E+00	2.84E+00
645	16.67	8.55E+00	1.44E-01	5.51E+00	2.72E+00
646	16.68	8.76E+00	1.51E-01	5.65E+00	2.69E+00
647	16.70	9.73E+00	1.46E-01	5.69E+00	2.78E+00
648	16.72	8.24E+00	1.47E-01	5.93E+00	2.70E+00
649	16.92	8.86E+00	1.48E-01	5.47E+00	2.68E+00

Depth	Age	Fe/Ca	Al/Si	Fe/K	Ti/Al
[cm]	*[cal kyr]*	*[cps]*	*[cps]*	*[cps]*	*[cps]*
650	17.12	6.45E+00	1.47E-01	5.30E+00	2.65E+00
651	17.32	7.15E+00	1.53E-01	5.39E+00	2.53E+00
652	17.52	1.14E+01	1.47E-01	5.17E+00	2.73E+00
653	17.73	1.08E+01	1.47E-01	5.30E+00	2.72E+00
654	17.93	1.05E+01	1.49E-01	5.31E+00	2.74E+00
655	18.13	1.08E+01	1.49E-01	5.26E+00	2.70E+00
656	18.33	1.07E+01	1.51E-01	5.42E+00	2.64E+00
657	18.53	9.57E+00	1.47E-01	5.07E+00	2.70E+00
658	18.73	8.84E+00	1.52E-01	4.88E+00	2.70E+00
659	18.93	5.71E+00	1.45E-01	4.74E+00	2.84E+00
660	19.13	4.16E+00	1.39E-01	4.94E+00	2.93E+00
661	19.34	2.96E+00	1.43E-01	4.95E+00	2.80E+00
662	19.54	1.52E+00	1.37E-01	4.60E+00	2.81E+00
663	19.74	1.94E+00	1.39E-01	4.49E+00	2.77E+00
664	19.94	1.99E+00	1.38E-01	4.34E+00	2.77E+00
665	20.14	1.75E+00	1.40E-01	4.28E+00	2.73E+00
666	20.36	1.56E+00	1.38E-01	4.44E+00	2.75E+00
667	20.56	1.16E+00	1.37E-01	4.24E+00	2.65E+00
668	20.76	1.41E+00	1.38E-01	4.38E+00	2.73E+00
669	20.96	1.55E+00	1.39E-01	4.46E+00	2.65E+00
670	21.16	1.47E+00	1.37E-01	4.42E+00	2.68E+00
671	21.37	1.56E+00	1.45E-01	4.53E+00	2.57E+00
672	21.57	1.44E+00	1.41E-01	4.45E+00	2.58E+00
673	21.77	1.73E+00	1.42E-01	4.49E+00	2.69E+00
674	21.97	1.50E+00	1.41E-01	4.44E+00	2.65E+00
675	22.17	2.54E+00	1.45E-01	4.27E+00	2.64E+00
676	22.37	1.94E+00	1.42E-01	4.37E+00	2.62E+00
681	23.38	2.82E+00	1.49E-01	4.78E+00	2.64E+00
682	23.58	1.24E+00	1.35E-01	4.62E+00	2.83E+00
683	23.78	2.33E+00	1.34E-01	5.09E+00	3.33E+00

GeoB3910-2

Depth	Age	Fe/Ca	Fe/K
[cm]	*[cal kyr]*	*[cps]*	*[cps]*
1	0.45	2.48E-01	7.01E+00
2	0.73	2.54E-01	7.06E+00
3	1.01	2.58E-01	7.46E+00
4	1.29	2.54E-01	7.26E+00
5	1.57	2.64E-01	7.22E+00
8	2.40	2.29E-01	6.87E+00
9	2.68	2.30E-01	6.57E+00
10	2.96	2.20E-01	6.39E+00
11	3.24	2.20E-01	6.80E+00
12	3.52	2.23E-01	6.94E+00
13	3.80	2.25E-01	7.34E+00
14	4.08	2.28E-01	7.82E+00
15	4.35	2.35E-01	7.47E+00
16	4.63	2.26E-01	7.54E+00
17	4.90	2.19E-01	7.18E+00
18	5.18	2.20E-01	6.98E+00
19	5.46	2.11E-01	7.05E+00
20	5.73	2.10E-01	7.16E+00
21	6.01	2.06E-01	6.75E+00
22	6.28	2.20E-01	7.20E+00
23	6.56	2.37E-01	7.66E+00
24	6.72	2.57E-01	7.62E+00
25	6.87	2.53E-01	7.97E+00
26	7.03	2.50E-01	7.72E+00
27	7.18	2.58E-01	7.46E+00
28	7.34	2.77E-01	7.80E+00
29	7.50	3.32E-01	8.58E+00
30	7.65	3.67E-01	9.21E+00
31	7.81	3.94E-01	9.85E+00
32	7.96	4.35E-01	1.08E+01
33	8.12	4.10E-01	9.83E+00
34	8.28	3.80E-01	9.07E+00
35	8.43	3.92E-01	8.97E+00
36	8.59	4.22E-01	9.91E+00
37	8.74	4.36E-01	1.02E+01
38	8.90	4.15E-01	9.44E+00
39	9.01	5.55E-01	1.19E+01
40	9.11	1.06E+00	2.02E+01
41	9.22	5.98E-01	2.12E+01
41.2	9.24	6.85E-01	2.71E+01
41.6	9.28	9.93E-01	2.58E+01

Depth	Age	Fe/Ca	Fe/K
[cm]	*[cal kyr]*	*[cps]*	*[cps]*
42	9.32	1.46E+00	3.67E+01
42.4	9.37	1.77E+00	3.50E+01
42.8	9.41	2.06E+00	3.62E+01
43.2	9.45	1.46E+00	2.66E+01
43.6	9.49	1.13E+00	2.11E+01
44	9.54	9.23E-01	1.59E+01
44.4	9.58	6.16E-01	1.21E+01
44.8	9.62	6.87E-01	1.24E+01
45.2	9.66	6.06E-01	1.15E+01
45.6	9.71	6.64E-01	1.32E+01
46	9.75	7.67E-01	1.44E+01
46.4	9.79	6.60E-01	1.26E+01
46.8	9.83	6.29E-01	1.27E+01
47.2	9.88	5.71E-01	1.11E+01
47.6	9.92	6.56E-01	1.29E+01
48	9.96	7.17E-01	1.33E+01
48.4	10.00	7.17E-01	1.37E+01
48.8	10.04	7.76E-01	1.35E+01
49.2	10.09	6.62E-01	1.26E+01
49.6	10.13	8.26E-01	1.46E+01
50	10.17	7.54E-01	1.36E+01
50.4	10.21	6.79E-01	1.34E+01
50.8	10.26	8.91E-01	1.64E+01
51.2	10.30	7.72E-01	1.34E+01
51.6	10.34	8.69E-01	1.45E+01
52	10.38	1.21E+00	1.81E+01
52.4	10.43	1.47E+00	2.17E+01
52.8	10.47	8.63E-01	1.36E+01
53.2	10.51	7.11E-01	1.21E+01
53.6	10.55	8.28E-01	1.46E+01
54	10.60	9.49E-01	1.40E+01
54.4	10.64	1.21E+00	1.66E+01
54.8	10.68	1.34E+00	1.81E+01
55.2	10.72	1.16E+00	1.61E+01
55.6	10.77	1.04E+00	1.71E+01
56	10.81	1.05E+00	1.63E+01
56.4	10.85	1.16E+00	1.66E+01
56.8	10.89	1.23E+00	1.73E+01
57.2	10.94	1.33E+00	1.78E+01
57.6	10.98	1.47E+00	1.93E+01
58	11.02	2.04E+00	2.36E+01
58.4	11.06	2.18E+00	2.28E+01
58.8	11.10	1.49E+00	1.65E+01

Depth	Age	Fe/Ca	Fe/K
[cm]	*[cal kyr]*	*[cps]*	*[cps]*
59.2	11.14	2.06E+00	2.15E+01
59.6	11.17	2.12E+00	2.07E+01
60	11.21	1.68E+00	2.05E+01
60.4	11.25	1.73E+00	1.78E+01
60.8	11.29	2.38E+00	2.18E+01
61.2	11.33	1.88E+00	1.89E+01
61.6	11.37	1.91E+00	1.93E+01
62	11.40	2.70E+00	2.37E+01
62.4	11.44	1.96E+00	1.92E+01
62.8	11.48	2.23E+00	1.98E+01
63.2	11.52	2.59E+00	2.15E+01
63.6	11.56	3.70E+00	2.37E+01
64	11.60	4.51E+00	2.41E+01
64.4	11.63	4.26E+00	2.25E+01
64.8	11.67	3.72E+00	2.20E+01
65.2	11.71	3.92E+00	2.27E+01
65.6	11.75	3.30E+00	2.19E+01
66	11.79	3.30E+00	2.18E+01
66.4	11.83	3.01E+00	2.15E+01
66.8	11.86	2.81E+00	2.09E+01
67.2	11.90	3.22E+00	2.13E+01
67.6	11.94	3.08E+00	2.05E+01
68	11.98	3.71E+00	2.10E+01
68.4	12.02	3.87E+00	2.22E+01
68.8	12.06	3.69E+00	2.29E+01
69.2	12.10	4.19E+00	2.09E+01
69.6	12.13	3.82E+00	2.08E+01
70	12.17	4.03E+00	1.81E+01
70.4	12.21	4.93E+00	2.05E+01
70.8	12.25	4.56E+00	1.99E+01
71.2	12.29	4.70E+00	1.94E+01
71.6	12.33	5.29E+00	2.20E+01
72	12.36	3.66E+00	1.83E+01
72.4	12.40	3.50E+00	2.00E+01
72.8	12.44	2.69E+00	1.74E+01
73.2	12.49	2.49E+00	1.83E+01
73.6	12.54	1.81E+00	1.76E+01
74	12.60	1.58E+00	1.67E+01
74.4	12.66	1.55E+00	1.78E+01
74.8	12.71	1.64E+00	1.75E+01
75.2	12.77	1.57E+00	1.67E+01
75.6	12.82	1.74E+00	1.85E+01
76	12.88	1.87E+00	1.78E+01

Depth	Age	Fe/Ca	Fe/K
[cm]	*[cal kyr]*	*[cps]*	*[cps]*
76.4	12.93	1.54E+00	1.71E+01
76.8	12.99	1.62E+00	1.97E+01
77.2	13.05	1.39E+00	1.66E+01
77.6	13.10	1.46E+00	1.80E+01
78	13.16	1.31E+00	1.94E+01
78.4	13.21	1.31E+00	1.67E+01
78.8	13.27	1.16E+00	1.63E+01
79.2	13.32	1.17E+00	1.37E+01
79.6	13.38	1.10E+00	1.61E+01
80	13.44	1.14E+00	1.65E+01
80.4	13.49	1.03E+00	1.45E+01
80.8	13.55	1.02E+00	1.45E+01
81.2	13.60	1.09E+00	1.59E+01
81.6	13.66	1.14E+00	1.73E+01
82	13.71	1.19E+00	1.54E+01
82.4	13.77	1.19E+00	1.52E+01
82.8	13.83	1.14E+00	1.42E+01
83.2	13.88	1.09E+00	1.49E+01
83.6	13.94	9.67E-01	1.41E+01
84	13.99	9.67E-01	1.46E+01
84.4	14.05	1.02E+00	1.48E+01
84.8	14.10	1.28E+00	1.59E+01
85.2	14.16	1.42E+00	1.68E+01
85.6	14.22	1.37E+00	1.73E+01
86	14.27	1.41E+00	1.63E+01
86.4	14.33	1.74E+00	1.87E+01
86.8	14.38	2.18E+00	1.80E+01
87.2	14.44	2.33E+00	1.97E+01
87.6	14.49	2.24E+00	1.94E+01
88	14.55	2.42E+00	2.22E+01
88.4	14.59	2.95E+00	2.40E+01
88.8	14.63	3.57E+00	2.30E+01
89.2	14.67	3.49E+00	2.25E+01
89.6	14.72	2.82E+00	2.19E+01
90.6	14.82	4.32E+00	2.46E+01
90.8	14.84	3.93E+00	2.27E+01
91.2	14.88	3.84E+00	2.35E+01
91.6	14.92	3.79E+00	2.16E+01
92	14.96	4.17E+00	2.35E+01
92.4	15.00	6.01E+00	2.53E+01
92.8	15.05	5.91E+00	2.82E+01
93.2	15.09	6.64E+00	2.67E+01
93.6	15.13	6.67E+00	2.72E+01

Depth	Age	Fe/Ca	Fe/K
[cm]	*[cal kyr]*	*[cps]*	*[cps]*
94	15.17	8.08E+00	2.99E+01
94.4	15.21	6.28E+00	2.98E+01
94.8	15.25	6.36E+00	2.81E+01
95.2	15.29	5.76E+00	2.71E+01
95.6	15.34	6.50E+00	2.97E+01
96	15.38	5.86E+00	2.68E+01
96.4	15.42	8.09E+00	2.84E+01
96.8	15.46	7.64E+00	2.68E+01
97.2	15.50	9.31E+00	2.89E+01
97.6	15.54	9.43E+00	3.03E+01
98	15.58	7.10E+00	2.87E+01
98.4	15.62	8.04E+00	3.13E+01
98.8	15.67	9.16E+00	2.88E+01
99.2	15.71	8.83E+00	2.78E+01
99.6	15.75	7.93E+00	2.68E+01
100	15.79	9.38E+00	2.90E+01
100.4	15.83	9.65E+00	2.70E+01
100.8	15.87	1.01E+01	2.93E+01
101.2	15.91	9.99E+00	2.77E+01
101.6	15.96	9.36E+00	2.73E+01
102	16.00	8.77E+00	2.68E+01
102.4	16.04	8.27E+00	2.49E+01
102.8	16.08	9.22E+00	2.59E+01
103.2	16.11	8.95E+00	2.59E+01
103.6	16.14	8.38E+00	2.56E+01
104	16.17	7.46E+00	2.33E+01
104.4	16.20	8.90E+00	2.52E+01
104.8	16.23	7.04E+00	2.44E+01
105.2	16.25	6.68E+00	2.80E+01
105.6	16.28	5.68E+00	2.44E+01
106	16.31	6.74E+00	2.78E+01
108.8	16.51	7.19E+00	2.56E+01
109.2	16.53	5.52E+00	2.36E+01
109.6	16.56	7.04E+00	2.66E+01
110	16.59	9.50E+00	2.89E+01
110.4	16.62	1.06E+01	2.99E+01
110.8	16.65	1.02E+01	3.20E+01
111.2	16.67	5.55E+00	2.65E+01
111.6	16.70	6.34E+00	2.77E+01
112	16.73	9.00E+00	2.58E+01
112.4	16.76	9.01E+00	2.80E+01
112.8	16.79	9.28E+00	2.57E+01
113.2	16.81	9.84E+00	2.76E+01

Depth	Age	Fe/Ca	Fe/K
[cm]	*[cal kyr]*	*[cps]*	*[cps]*
113.6	16.83	1.17E+01	2.51E+01
114	16.84	1.00E+01	2.62E+01
114.4	16.86	9.29E+00	2.57E+01
114.8	16.88	1.50E+01	2.65E+01
115.2	16.89	1.19E+01	2.49E+01
115.6	16.91	9.25E+00	2.46E+01
116	16.93	1.01E+01	2.61E+01
116.4	16.95	1.22E+01	2.59E+01
116.8	16.96	1.49E+01	2.80E+01
117.2	16.98	1.07E+01	2.82E+01
117.6	17.00	1.42E+01	2.87E+01
118	17.01	1.33E+01	2.51E+01
118.4	17.03	1.36E+01	2.80E+01
118.8	17.05	1.62E+01	2.73E+01
119.2	17.07	1.41E+01	2.85E+01
119.6	17.08	1.26E+01	2.79E+01
120	17.10	1.38E+01	2.72E+01
120.4	17.12	1.50E+01	2.90E+01
120.8	17.13	1.22E+01	2.64E+01
121.2	17.15	1.26E+01	2.72E+01
121.6	17.17	8.48E+00	2.55E+01
122	17.19	1.83E+01	2.84E+01
122.4	17.20	2.11E+01	2.93E+01
122.8	17.22	2.82E+01	3.26E+01
123.2	17.24	1.52E+01	2.53E+01
123.6	17.25	4.24E+01	2.48E+01
124	17.27	3.33E+01	2.65E+01
124.4	17.29	2.00E+01	2.43E+01
124.8	17.31	2.11E+01	2.42E+01
125.2	17.32	1.63E+01	2.45E+01
125.6	17.34	1.31E+01	2.39E+01
126	17.36	1.53E+01	2.39E+01
126.4	17.37	1.65E+01	2.51E+01
126.8	17.39	1.41E+01	2.43E+01
127.2	17.41	1.66E+01	3.92E+01
127.6	17.43	1.58E+01	2.41E+01
128	17.44	1.54E+01	2.60E+01
128.4	17.46	1.13E+01	2.38E+01
128.8	17.48	1.54E+01	2.44E+01
129.2	17.49	1.61E+01	2.50E+01
129.6	17.51	1.74E+01	2.55E+01
130	17.53	1.74E+01	2.47E+01
130.4	17.55	2.02E+01	2.79E+01

Depth	Age	Fe/Ca	Fe/K
[cm]	*[cal kyr]*	*[cps]*	*[cps]*
130.8	17.56	1.74E+01	2.59E+01
131.2	17.58	1.74E+01	2.58E+01
131.6	17.60	1.77E+01	2.43E+01
132	17.61	1.78E+01	2.39E+01
132.4	17.63	1.73E+01	2.67E+01
132.8	17.65	1.64E+01	2.65E+01
133.2	17.67	1.55E+01	2.48E+01
133.6	17.68	1.68E+01	2.65E+01
134	17.70	1.61E+01	2.63E+01
134.4	17.72	1.75E+01	4.83E+01
134.8	17.73	1.49E+01	2.58E+01
135.2	17.75	1.41E+01	2.57E+01
135.6	17.77	1.30E+01	2.59E+01
136	17.79	1.41E+01	2.52E+01
136.4	17.80	1.96E+01	2.57E+01
136.8	17.82	2.45E+01	4.41E+01
137.2	17.84	1.67E+01	2.46E+01
137.6	17.85	1.58E+01	2.47E+01
138	17.87	1.38E+01	2.33E+01
138.4	17.89	1.03E+01	2.35E+01
138.8	17.91	1.26E+01	2.46E+01
139.2	17.92	1.47E+01	2.49E+01
139.6	17.94	1.37E+01	2.44E+01
140	17.96	1.19E+01	2.35E+01
140.4	17.97	1.19E+01	2.37E+01
140.8	17.99	1.25E+01	2.22E+01
141.2	18.01	1.17E+01	2.35E+01
141.6	18.03	1.33E+01	2.46E+01
142	18.04	1.24E+01	2.29E+01
142.4	18.06	9.81E+00	2.21E+01
142.8	18.08	1.06E+01	2.19E+01
143.2	18.09	1.03E+01	2.36E+01
143.6	18.11	1.03E+01	2.38E+01
144	18.13	1.00E+01	2.32E+01
144.4	18.15	9.68E+00	2.28E+01
144.8	18.16	8.61E+00	2.31E+01
145.2	18.18	7.92E+00	2.29E+01
145.6	18.20	4.80E+00	2.16E+01
146	18.21	3.51E+00	1.98E+01
146.4	18.23	3.42E+00	2.11E+01
146.8	18.25	2.44E+00	2.14E+01
147.2	18.27	2.14E+00	1.92E+01
147.6	18.28	1.46E+00	1.64E+01

Depth	Age	Fe/Ca	Fe/K
[cm]	*[cal kyr]*	*[cps]*	*[cps]*
148	18.30	1.38E+00	1.58E+01
148.4	18.37	1.32E+00	1.49E+01
148.8	18.44	1.41E+00	1.69E+01
149.2	18.52	1.36E+00	1.63E+01
149.6	18.59	1.15E+00	1.50E+01
150	18.66	2.28E+00	1.80E+01
150.4	18.73	1.43E+00	1.54E+01
150.8	18.80	1.27E+00	1.59E+01
151.2	18.88	1.39E+00	1.57E+01
151.6	18.95	1.42E+00	1.61E+01
152	19.02	1.38E+00	1.60E+01
152.4	19.09	1.49E+00	1.63E+01
152.8	19.16	1.34E+00	1.51E+01
153.2	19.24	1.41E+00	1.59E+01
153.6	19.31	1.59E+00	1.59E+01
154	19.38	1.70E+00	1.78E+01
154.4	19.45	1.73E+00	1.63E+01
154.8	19.52	1.43E+00	1.53E+01
155.2	19.60	1.48E+00	1.56E+01
155.6	19.67	1.53E+00	1.57E+01
156	19.74	1.44E+00	1.53E+01
156.4	19.81	1.31E+00	1.43E+01
156.8	19.88	1.35E+00	1.49E+01
157.2	19.96	1.20E+00	1.46E+01
157.6	20.03	1.14E+00	1.40E+01
158	20.10	1.02E+00	1.46E+01
158.4	20.17	9.88E-01	1.50E+01
158.8	20.24	1.14E+00	1.43E+01
159.2	20.32	1.18E+00	1.58E+01
159.6	20.39	1.23E+00	1.51E+01
160	20.46	1.12E+00	1.50E+01
160.4	20.53	1.12E+00	1.49E+01
160.8	20.60	9.80E-01	1.40E+01
161.2	20.68	1.06E+00	1.46E+01
161.6	20.75	1.00E+00	1.42E+01
162	20.82	1.04E+00	1.41E+01
162.4	20.89	1.22E+00	1.50E+01
162.8	20.96	1.26E+00	1.64E+01
163.2	21.04	1.19E+00	1.50E+01
163.6	21.11	1.46E+00	1.62E+01
164	21.18	1.35E+00	1.63E+01
164.4	21.25	1.20E+00	1.49E+01
164.8	21.32	1.37E+00	1.63E+01

Depth	Age	Fe/Ca	Fe/K
[cm]	*[cal kyr]*	*[cps]*	*[cps]*
165.2	21.40	1.22E+00	1.48E+01
165.6	21.47	1.28E+00	1.48E+01
166	21.54	1.44E+00	1.70E+01
166.4	21.61	1.38E+00	1.68E+01
166.8	21.68	1.35E+00	1.69E+01
167.2	21.76	1.29E+00	1.50E+01
167.6	21.83	1.32E+00	1.63E+01
168	21.90	1.19E+00	1.53E+01
168.4	21.97	1.47E+00	1.58E+01
168.8	22.04	1.40E+00	1.58E+01
169.2	22.12	1.53E+00	1.64E+01
169.6	22.19	1.50E+00	1.68E+01
170	22.26	1.74E+00	1.86E+01
170.4	22.33	1.79E+00	1.76E+01
170.8	22.40	1.80E+00	1.73E+01
171.2	22.48	1.71E+00	1.73E+01
171.6	22.55	1.93E+00	1.87E+01
172	22.62	2.07E+00	1.86E+01
172.4	22.69	2.19E+00	1.96E+01
172.8	22.76	1.93E+00	1.75E+01
173.2	22.81	1.67E+00	1.61E+01
173.6	22.84	1.84E+00	1.68E+01
174	22.86	1.86E+00	1.78E+01
174.4	22.88	1.98E+00	1.88E+01
174.8	22.91	1.73E+00	1.70E+01
175.2	22.93	1.68E+00	1.64E+01
175.6	22.96	1.83E+00	1.76E+01
176	22.98	1.74E+00	1.67E+01
176.4	23.00	2.07E+00	1.76E+01
176.8	23.03	2.32E+00	1.74E+01
177.2	23.05	2.41E+00	1.68E+01
177.6	23.08	2.44E+00	1.71E+01
178	23.10	2.48E+00	1.71E+01
178.4	23.12	3.36E+00	1.82E+01
178.8	23.15	4.47E+00	2.08E+01
179.2	23.17	4.88E+00	2.04E+01
179.6	23.20	3.24E+00	1.93E+01
180	23.22	3.32E+00	1.98E+01
180.4	23.24	3.93E+00	2.13E+01
180.8	23.27	3.38E+00	2.02E+01
181.2	23.29	5.25E+00	2.44E+01
181.6	23.32	6.14E+00	2.84E+01
182	23.34	6.70E+00	2.79E+01

Depth	Age	Fe/Ca	Fe/K
[cm]	*[cal kyr]*	*[cps]*	*[cps]*
182.4	23.36	6.40E+00	2.54E+01
182.8	23.39	8.46E+00	2.67E+01
183.2	23.45	9.37E+00	2.63E+01
183.6	23.54	9.39E+00	2.73E+01
184	23.63	1.03E+01	2.71E+01
184.4	23.72	8.53E+00	2.65E+01
184.8	23.81	1.04E+01	2.82E+01
185.2	23.91	1.06E+01	2.78E+01
185.6	24.00	1.54E+01	3.68E+01
186	24.09	1.14E+01	2.48E+01
186.4	24.18	9.88E+00	2.48E+01
186.8	24.27	1.05E+01	2.43E+01
187.2	24.37	1.23E+01	2.49E+01
187.6	24.46	1.09E+01	2.36E+01
188	24.55	2.00E+01	2.85E+01
188.4	24.64	1.96E+01	3.46E+01
188.8	24.73	2.52E+01	4.42E+01
189.2	24.83	1.22E+01	2.47E+01
189.6	24.92	1.28E+01	2.08E+01
190	25.01	1.79E+01	2.07E+01
190.4	25.10	2.02E+01	2.06E+01
190.8	25.19	1.25E+01	2.32E+01
191.2	25.29	1.08E+01	2.30E+01
191.6	25.38	1.32E+01	2.26E+01
192	25.47	1.28E+01	2.22E+01
192.4	25.56	1.11E+01	2.31E+01
192.8	25.65	6.53E+00	2.07E+01
193.2	25.73	5.14E+00	2.01E+01
193.6	25.79	5.25E+00	1.94E+01
194	25.85	4.97E+00	2.14E+01
194.4	25.90	3.71E+00	1.99E+01
194.8	25.96	1.62E+00	1.48E+01
195.2	26.02	1.75E+00	1.63E+01
195.6	26.08	1.71E+00	1.68E+01
196	26.14	1.71E+00	1.66E+01
196.4	26.19	2.07E+00	1.87E+01
196.8	26.25	2.33E+00	1.87E+01
197.2	26.31	2.64E+00	1.83E+01
197.6	26.37	2.28E+00	1.80E+01
198	26.43	2.45E+00	1.87E+01
198.4	26.48	2.05E+00	1.70E+01
198.8	26.54	2.02E+00	1.75E+01
199.2	26.60	2.04E+00	1.74E+01

Depth	Age	Fe/Ca	Fe/K
[cm]	*[cal kyr]*	*[cps]*	*[cps]*
199.6	26.66	1.45E+00	1.48E+01
200	26.72	1.72E+00	1.67E+01
200.4	26.77	1.39E+00	1.51E+01
200.8	26.83	1.29E+00	1.51E+01
201.2	26.89	1.60E+00	1.54E+01
201.6	26.95	1.37E+00	1.63E+01
202	27.01	1.30E+00	1.52E+01
202.4	27.06	1.39E+00	1.41E+01
202.8	27.12	1.34E+00	1.38E+01
203.2	27.18	1.36E+00	1.49E+01
203.6	27.24	1.24E+00	1.55E+01
204	27.30	1.25E+00	1.46E+01
204.4	27.35	1.25E+00	1.50E+01
204.8	27.41	1.24E+00	1.61E+01
205.2	27.47	1.29E+00	1.53E+01
205.6	27.53	1.37E+00	1.55E+01
206	27.59	1.32E+00	1.53E+01
206.4	27.64	1.37E+00	1.53E+01
206.8	27.70	1.64E+00	1.64E+01
207.2	27.76	1.62E+00	1.61E+01
207.6	27.82	1.71E+00	1.87E+01
208.8	27.99	1.96E+00	1.91E+01
209.2	28.05	1.92E+00	1.67E+01
209.6	28.11	2.18E+00	1.79E+01
210	28.17	2.91E+00	2.06E+01
210.4	28.22	2.99E+00	2.22E+01
210.8	28.28	3.24E+00	2.47E+01
211.2	28.34	3.32E+00	2.04E+01
211.6	28.40	3.06E+00	1.94E+01
212	28.46	3.01E+00	2.05E+01
212.4	28.51	4.47E+00	2.43E+01
212.8	28.57	2.66E+00	2.19E+01
213.2	28.62	4.39E+00	2.50E+01
213.6	28.65	3.58E+00	2.18E+01
214	28.68	4.21E+00	2.07E+01
214.4	28.71	2.68E+00	1.95E+01
214.8	28.74	2.93E+00	1.96E+01
215.2	28.78	3.19E+00	2.06E+01
215.6	28.81	2.94E+00	2.10E+01
216	28.84	2.35E+00	1.96E+01
216.4	28.87	3.25E+00	2.61E+01
216.8	28.90	3.15E+00	2.18E+01
217.2	28.94	2.57E+00	2.14E+01

Depth	Age	Fe/Ca	Fe/K
[cm]	*[cal kyr]*	*[cps]*	*[cps]*
217.6	28.97	2.66E+00	2.12E+01
218	29.00	2.82E+00	2.34E+01
218.4	29.03	2.35E+00	2.08E+01
218.8	29.06	2.84E+00	2.28E+01
219.2	29.10	2.97E+00	2.67E+01
219.6	29.13	3.97E+00	3.12E+01
220	29.16	3.34E+00	2.77E+01
220.4	29.19	3.18E+00	2.56E+01
220.8	29.22	1.79E+00	1.69E+01
221.2	29.26	1.89E+00	1.76E+01
221.6	29.29	2.44E+00	1.74E+01
222	29.32	2.50E+00	1.92E+01
222.4	29.35	4.28E+00	2.05E+01
222.8	29.38	3.95E+00	2.06E+01
223.2	29.42	4.16E+00	2.19E+01
223.6	29.45	3.83E+00	2.36E+01
224	29.48	4.90E+00	2.14E+01
224.4	29.51	5.05E+00	2.08E+01
224.8	29.54	5.18E+00	2.27E+01
225.2	29.58	6.09E+00	2.17E+01
225.6	29.61	8.09E+00	2.31E+01
226	29.64	7.12E+00	2.16E+01
226.4	29.67	8.16E+00	2.44E+01
226.8	29.70	1.03E+01	2.58E+01
227.2	29.74	1.01E+01	2.70E+01
227.6	29.77	7.07E+00	2.42E+01
228	29.80	5.17E+00	2.25E+01
228.4	29.83	1.77E+01	3.19E+01
228.8	29.86	1.30E+01	2.59E+01
229.2	29.90	1.40E+01	2.64E+01
229.6	29.93	2.37E+01	4.12E+01
230	29.96	1.79E+01	3.08E+01
230.4	29.99	1.44E+01	2.67E+01
230.8	30.02	1.49E+01	2.58E+01
231.2	30.06	1.21E+01	2.37E+01
231.6	30.09	1.13E+01	2.30E+01
232	30.12	8.32E+00	2.18E+01
232.4	30.15	8.18E+00	2.28E+01
232.8	30.18	5.48E+00	2.28E+01
233.2	30.25	5.87E+00	2.34E+01
233.6	30.36	5.03E+00	2.21E+01
234	30.46	4.31E+00	2.33E+01
234.4	30.56	3.00E+00	2.03E+01

Depth	Age	Fe/Ca	Fe/K
[cm]	*[cal kyr]*	*[cps]*	*[cps]*
234.8	30.67	2.87E+00	2.05E+01
235.2	30.77	2.84E+00	2.06E+01
235.6	30.88	3.21E+00	2.00E+01
236	30.98	5.31E+00	2.20E+01
236.4	31.08	2.47E+00	1.84E+01
236.8	31.19	3.02E+00	2.04E+01
237.2	31.29	2.79E+00	2.01E+01
237.6	31.40	1.82E+00	1.81E+01
238	31.50	1.52E+00	1.67E+01
238.4	31.55	9.95E-01	1.56E+01
238.8	31.59	1.04E+00	1.57E+01
239.2	31.64	1.11E+00	1.61E+01
239.6	31.69	1.38E+00	1.63E+01
240	31.73	1.30E+00	1.72E+01
240.4	31.78	1.24E+00	1.70E+01
240.8	31.83	1.21E+00	1.75E+01
241.2	31.87	1.32E+00	1.68E+01
241.6	31.92	1.29E+00	1.70E+01
242	31.97	1.16E+00	1.61E+01
242.4	32.01	1.15E+00	1.72E+01
242.8	32.06	1.05E+00	1.61E+01
243.2	32.11	9.43E-01	1.64E+01
243.6	32.15	1.05E+00	1.59E+01
244	32.20	9.67E-01	1.62E+01
244.4	32.25	1.04E+00	1.60E+01
244.8	32.29	8.36E-01	1.26E+01
245.2	32.34	8.41E-01	1.38E+01
245.6	32.39	1.07E+00	1.43E+01
246	32.43	1.14E+00	1.47E+01
246.4	32.48	9.67E-01	1.41E+01
246.8	32.53	1.07E+00	1.65E+01
247.2	32.57	1.05E+00	1.56E+01
247.6	32.62	1.13E+00	1.55E+01
248	32.67	1.15E+00	1.61E+01
248.4	32.71	1.44E+00	1.59E+01
248.8	32.76	1.59E+00	1.80E+01
249.2	32.81	1.39E+00	1.71E+01
249.6	32.85	1.52E+00	1.60E+01
250	32.90	1.68E+00	1.72E+01
250.4	32.95	1.53E+00	1.68E+01
250.8	32.99	2.16E+00	1.85E+01
251.2	33.04	2.22E+00	1.94E+01
251.6	33.09	2.73E+00	2.28E+01

Depth	Age	Fe/Ca	Fe/K
[cm]	*[cal kyr]*	*[cps]*	*[cps]*
252	33.13	2.83E+00	2.37E+01
252.4	33.18	2.81E+00	1.97E+01
252.8	33.23	2.67E+00	2.01E+01
253.2	33.27	3.94E+00	2.60E+01
253.6	33.32	2.18E+00	1.92E+01
254	33.37	2.56E+00	2.04E+01
254.4	33.41	2.24E+00	1.93E+01
254.8	33.46	2.90E+00	2.23E+01
255.2	33.51	1.92E+00	1.92E+01
255.6	33.55	1.59E+00	1.81E+01
256	33.60	1.60E+00	1.92E+01
256.4	33.65	2.36E+00	2.29E+01
256.8	33.69	2.40E+00	2.14E+01
257.2	33.74	1.77E+00	1.88E+01
257.6	33.79	1.47E+00	1.74E+01
258	33.83	1.36E+00	1.94E+01
258.4	33.88	1.15E+00	1.80E+01
258.8	33.93	1.55E+00	2.13E+01
259.2	33.97	1.31E+00	1.75E+01
259.6	34.02	1.04E+00	1.41E+01
260	34.07	9.80E-01	1.46E+01
260.4	34.11	1.28E+00	1.37E+01
260.8	34.16	1.29E+00	1.50E+01
261.2	34.21	1.32E+00	1.61E+01
261.6	34.25	1.42E+00	1.61E+01
262	34.30	1.81E+00	1.85E+01
262.4	34.35	2.09E+00	1.74E+01
262.8	34.39	1.77E+00	1.72E+01
263.2	34.44	1.66E+00	1.73E+01
263.6	34.49	1.90E+00	1.81E+01
264	34.53	1.72E+00	1.95E+01
264.4	34.58	1.87E+00	1.82E+01
264.8	34.63	1.85E+00	1.71E+01
265.2	34.67	1.54E+00	1.78E+01
265.6	34.72	1.49E+00	1.73E+01
266	34.77	1.37E+00	1.64E+01
266.4	34.81	8.25E-01	1.35E+01
266.8	34.86	1.04E+00	1.60E+01
267.2	34.91	1.07E+00	1.59E+01
267.6	34.95	9.75E-01	1.55E+01
268	35.00	8.13E-01	1.60E+01
268.4	35.04	8.21E-01	1.49E+01
268.8	35.08	7.46E-01	1.42E+01

Depth	Age	Fe/Ca	Fe/K
[cm]	*[cal kyr]*	*[cps]*	*[cps]*
269.2	35.12	9.04E-01	1.56E+01
269.6	35.16	8.20E-01	1.56E+01
270	35.21	8.14E-01	1.37E+01
270.4	35.25	1.03E+00	1.58E+01
270.8	35.29	1.24E+00	1.69E+01
271.2	35.33	1.06E+00	1.61E+01
271.6	35.37	8.01E-01	1.26E+01
272	35.41	8.70E-01	1.39E+01
272.4	35.45	9.25E-01	1.48E+01
272.8	35.49	9.83E-01	1.42E+01
273.2	35.54	1.11E+00	1.45E+01
273.6	35.58	1.07E+00	1.41E+01
274	35.62	1.26E+00	1.49E+01
274.4	35.66	1.18E+00	1.52E+01
274.8	35.70	1.37E+00	1.65E+01
275.2	35.74	1.11E+00	1.55E+01
275.6	35.78	1.07E+00	1.35E+01
276	35.82	1.24E+00	1.60E+01
276.4	35.86	1.44E+00	1.68E+01
276.8	35.91	1.51E+00	1.72E+01
277.2	35.95	1.72E+00	1.76E+01
277.6	35.99	1.80E+00	1.98E+01
278	36.03	1.85E+00	1.88E+01
278.4	36.07	1.59E+00	1.78E+01
278.8	36.11	1.84E+00	1.73E+01
279.2	36.15	1.78E+00	1.76E+01
279.6	36.19	1.71E+00	1.79E+01
280	36.24	1.95E+00	1.86E+01
280.4	36.28	2.13E+00	1.96E+01
280.8	36.32	1.88E+00	1.82E+01
281.2	36.36	1.57E+00	1.64E+01
281.6	36.40	1.68E+00	1.82E+01
282	36.44	1.44E+00	1.59E+01
282.4	36.48	1.38E+00	1.71E+01
282.8	36.52	1.43E+00	1.70E+01
283.2	36.56	1.66E+00	1.72E+01
283.6	36.61	2.04E+00	2.18E+01
284	36.65	1.86E+00	2.08E+01
284.4	36.69	1.17E+00	1.76E+01
284.8	36.73	9.12E-01	1.51E+01
285.2	36.77	6.44E-01	1.12E+01
285.6	36.81	6.87E-01	1.35E+01
286	36.85	1.13E+00	1.63E+01

Depth	Age	Fe/Ca	Fe/K
[cm]	*[cal kyr]*	*[cps]*	*[cps]*
286.4	36.89	9.69E-01	1.45E+01
286.8	36.94	5.58E-01	1.08E+01
287.2	36.98	6.78E-01	1.29E+01
287.6	37.02	6.11E-01	1.07E+01
288	37.06	6.78E-01	1.23E+01
288.4	37.10	5.58E-01	9.92E+00
288.8	37.14	6.45E-01	1.21E+01
289.2	37.18	6.84E-01	1.30E+01
289.6	37.22	7.94E-01	1.27E+01
290	37.26	7.60E-01	1.53E+01
290.4	37.31	7.27E-01	1.30E+01
290.8	37.35	6.92E-01	1.26E+01
291.2	37.39	7.46E-01	1.36E+01
291.6	37.43	9.52E-01	1.57E+01
292	37.47	9.34E-01	1.44E+01
292.4	37.51	1.08E+00	1.66E+01
292.8	37.55	1.04E+00	1.47E+01
293.2	37.59	1.01E+00	1.53E+01
293.6	37.64	1.03E+00	1.53E+01
294	37.68	1.07E+00	1.55E+01
294.4	37.72	1.21E+00	1.64E+01
294.8	37.76	1.10E+00	1.55E+01
295.2	37.80	1.26E+00	1.66E+01
295.6	37.84	1.47E+00	1.57E+01
296	37.88	1.98E+00	1.83E+01
296.4	37.92	1.81E+00	1.66E+01
296.8	37.96	2.71E+00	1.94E+01
297.2	38.01	3.14E+00	2.07E+01
297.6	38.05	2.63E+00	2.23E+01
298	38.09	2.76E+00	2.03E+01
298.4	38.13	3.17E+00	2.17E+01
298.8	38.17	3.39E+00	2.29E+01
299.2	38.21	3.51E+00	2.36E+01
299.6	38.25	1.93E+00	1.70E+01
300	38.29	1.91E+00	1.75E+01
300.4	38.34	3.80E+00	1.96E+01
300.8	38.38	7.32E+00	2.38E+01
301.2	38.42	8.32E+00	2.68E+01
301.6	38.46	6.52E+00	2.37E+01
302	38.50	5.96E+00	2.30E+01
302.4	38.55	4.77E+00	2.20E+01
302.8	38.60	5.16E+00	2.31E+01
303.2	38.65	8.92E+00	2.56E+01

Depth	Age	Fe/Ca	Fe/K
[cm]	*[cal kyr]*	*[cps]*	*[cps]*
303.6	38.70	8.78E+00	2.72E+01
304	38.75	8.49E+00	2.60E+01
304.4	38.80	1.17E+01	2.80E+01
304.8	38.86	1.21E+01	2.88E+01
305.2	38.91	2.63E+01	3.33E+01
305.6	38.96	1.76E+01	3.38E+01
306	39.01	1.54E+01	2.66E+01
306.4	39.06	1.74E+01	2.74E+01
306.8	39.11	1.61E+01	2.52E+01
307.2	39.16	1.64E+01	2.55E+01
307.6	39.21	1.53E+01	2.58E+01
307.8	39.24	1.37E+01	2.23E+01
308.2	39.29	1.43E+01	2.69E+01
308.6	39.34	1.59E+01	2.46E+01
309	39.39	1.77E+01	2.64E+01
309.4	39.44	2.02E+01	2.66E+01
309.8	39.49	1.24E+01	2.55E+01
310.2	39.54	7.94E+00	2.51E+01
310.6	39.59	1.33E+01	2.80E+01
311	39.64	1.74E+01	2.43E+01
311.4	39.69	1.71E+01	2.71E+01
311.8	39.74	1.63E+01	2.73E+01
312.2	39.79	1.87E+01	2.66E+01
312.6	39.85	2.07E+01	2.76E+01
313	39.90	1.97E+01	2.65E+01
313.4	39.95	2.11E+01	2.80E+01
313.8	40.00	1.55E+01	2.54E+01
314.2	40.05	1.65E+01	2.69E+01
314.6	40.10	1.79E+01	2.58E+01
315	40.15	1.94E+01	2.60E+01
315.4	40.20	1.87E+01	2.57E+01
315.8	40.25	1.59E+01	2.72E+01
316.2	40.30	1.48E+01	2.56E+01
316.6	40.35	7.56E+00	2.33E+01
317	40.40	7.58E+00	2.35E+01
317.4	40.45	1.60E+01	2.33E+01
317.8	40.51	1.61E+01	2.46E+01
318.2	40.56	1.27E+01	2.45E+01
318.6	40.61	1.32E+01	2.67E+01
319	40.66	1.12E+01	2.66E+01
319.4	40.71	1.16E+01	2.53E+01
319.8	40.76	1.24E+01	2.53E+01
320.2	40.81	9.39E+00	2.41E+01

Depth	Age	Fe/Ca	Fe/K
[cm]	*[cal kyr]*	*[cps]*	*[cps]*
320.6	40.86	1.03E+01	2.50E+01
321	40.91	7.98E+00	2.38E+01
321.4	40.96	8.42E+00	2.56E+01
321.8	41.01	7.07E+00	2.20E+01
322.2	41.06	6.95E+00	2.23E+01
322.6	41.11	5.05E+00	2.01E+01
323	41.17	6.91E+00	2.24E+01
323.4	41.22	7.17E+00	2.47E+01
323.8	41.27	7.56E+00	2.42E+01
324.2	41.32	6.91E+00	2.33E+01
324.6	41.37	2.40E+00	1.90E+01
325	41.42	2.42E+00	2.02E+01
325.4	41.47	2.41E+00	1.99E+01
325.8	41.52	1.55E+00	1.71E+01
326.2	41.57	1.44E+00	1.77E+01
326.6	41.62	1.32E+00	1.64E+01
327	41.67	9.93E-01	1.36E+01
327.4	41.72	1.11E+00	1.63E+01
327.8	41.77	1.28E+00	1.63E+01
328.2	41.81	9.90E-01	1.51E+01
328.6	41.83	9.03E-01	1.39E+01
329	41.85	8.83E-01	1.46E+01
329.4	41.87	1.07E+00	1.52E+01
329.8	41.89	1.35E+00	1.79E+01
330.2	41.91	8.43E-01	1.44E+01
330.6	41.93	7.18E-01	1.40E+01
331	41.95	8.37E-01	1.32E+01
331.4	41.97	8.15E-01	1.40E+01
331.8	41.99	8.72E-01	1.54E+01
332.2	42.01	6.83E-01	1.14E+01
332.6	42.03	7.06E-01	1.13E+01
333	42.05	7.37E-01	1.25E+01
333.4	42.07	9.49E-01	1.51E+01
333.8	42.09	7.06E-01	1.36E+01
334.2	42.11	5.34E-01	1.03E+01
334.6	42.13	7.77E-01	1.20E+01
335	42.15	9.17E-01	1.57E+01
335.4	42.17	1.12E+00	1.53E+01
335.8	42.19	1.37E+00	1.48E+01
336.2	42.21	1.52E+00	1.62E+01
336.6	42.23	1.48E+00	1.55E+01
337	42.25	1.58E+00	1.58E+01
337.4	42.27	1.98E+00	1.85E+01

Depth	Age	Fe/Ca	Fe/K
[cm]	*[cal kyr]*	*[cps]*	*[cps]*
337.8	42.29	1.88E+00	2.01E+01
338.2	42.31	1.52E+00	1.76E+01
338.6	42.33	2.04E+00	2.00E+01
339	42.35	2.27E+00	1.97E+01
339.4	42.37	1.87E+00	1.80E+01
339.8	42.39	1.68E+00	1.74E+01
340.2	42.41	1.72E+00	1.83E+01
340.6	42.43	1.92E+00	1.96E+01
341	42.45	2.18E+00	1.79E+01
341.4	42.47	2.51E+00	1.89E+01
341.8	42.49	2.73E+00	1.93E+01
342.2	42.51	2.74E+00	1.89E+01
342.6	42.53	2.66E+00	2.06E+01
343	42.55	2.41E+00	1.93E+01
343.4	42.57	2.50E+00	1.95E+01
343.8	42.59	2.22E+00	2.02E+01
344.2	42.61	1.41E+00	1.70E+01
344.6	42.63	1.40E+00	1.77E+01
345	42.65	1.21E+00	1.64E+01
345.4	42.67	1.13E+00	1.46E+01
345.8	42.69	1.14E+00	1.58E+01
346.2	42.71	1.20E+00	1.55E+01
346.6	42.73	1.14E+00	1.76E+01
347	42.75	1.06E+00	1.64E+01
347.4	42.77	1.04E+00	1.46E+01
347.8	42.79	8.62E-01	1.34E+01
348.2	42.82	7.81E-01	1.15E+01
348.6	42.86	9.52E-01	1.42E+01
349	42.90	1.05E+00	1.49E+01
349.4	42.95	1.12E+00	1.41E+01
349.8	42.99	1.12E+00	1.43E+01
350.2	43.03	1.07E+00	1.35E+01
350.6	43.07	1.16E+00	1.49E+01
351	43.11	1.50E+00	1.57E+01
351.4	43.15	1.37E+00	1.57E+01
351.8	43.20	1.70E+00	1.66E+01
352.2	43.24	1.82E+00	1.74E+01
352.6	43.28	2.23E+00	1.87E+01
353	43.32	2.73E+00	1.90E+01
353.4	43.36	2.42E+00	1.86E+01
353.8	43.40	2.89E+00	1.99E+01
354.2	43.44	3.26E+00	2.09E+01
354.6	43.49	3.30E+00	1.93E+01

Depth	Age	Fe/Ca	Fe/K
[cm]	*[cal kyr]*	*[cps]*	*[cps]*
355	43.53	2.59E+00	1.82E+01
355.4	43.57	3.30E+00	1.90E+01
355.8	43.61	3.56E+00	2.00E+01
356.2	43.65	4.01E+00	2.07E+01
356.6	43.69	3.91E+00	2.27E+01
357	43.74	3.83E+00	2.30E+01
357.4	43.78	3.47E+00	2.11E+01
357.8	43.82	3.63E+00	2.17E+01
358.2	43.86	4.73E+00	2.91E+01
358.6	43.90	3.60E+00	2.26E+01
359	43.94	2.65E+00	2.13E+01
359.4	43.99	1.99E+00	1.76E+01
359.8	44.03	1.64E+00	1.60E+01
360.2	44.07	1.26E+00	1.53E+01
360.6	44.11	8.94E-01	1.35E+01
361	44.15	8.61E-01	1.37E+01
361.4	44.19	8.93E-01	1.38E+01
361.8	44.24	8.10E-01	1.49E+01
362.2	44.28	8.40E-01	1.33E+01
362.6	44.32	8.80E-01	1.42E+01
363	44.36	9.04E-01	1.43E+01
363.4	44.40	9.36E-01	1.35E+01
363.8	44.44	8.89E-01	1.41E+01
364.2	44.48	8.14E-01	1.42E+01
364.6	44.53	7.95E-01	1.44E+01
365	44.57	7.83E-01	1.34E+01
365.4	44.61	7.35E-01	1.33E+01
365.8	44.65	7.74E-01	1.31E+01
366.2	44.69	8.00E-01	1.32E+01
366.6	44.73	9.19E-01	1.53E+01
367	44.78	8.59E-01	1.44E+01
367.4	44.82	9.09E-01	1.46E+01
367.8	44.86	9.78E-01	1.49E+01
368.2	44.90	9.52E-01	1.70E+01
368.6	44.94	9.96E-01	1.47E+01
369	44.98	9.66E-01	1.51E+01
369.4	45.03	8.73E-01	1.41E+01
369.8	45.07	1.14E+00	1.57E+01
370.2	45.11	1.12E+00	1.61E+01
370.6	45.15	1.33E+00	1.65E+01
371	45.19	1.67E+00	1.89E+01
371.4	45.23	1.23E+00	1.54E+01
371.8	45.28	1.08E+00	1.58E+01

Depth	Age	Fe/Ca	Fe/K
[cm]	*[cal kyr]*	*[cps]*	*[cps]*
372.2	45.32	1.51E+00	1.79E+01
372.6	45.36	1.87E+00	1.86E+01
373	45.40	1.79E+00	1.90E+01
373.4	45.42	1.51E+00	1.78E+01
373.8	45.44	1.26E+00	1.60E+01
374.2	45.47	1.58E+00	1.51E+01
374.6	45.49	2.23E+00	1.77E+01
375	45.51	2.25E+00	1.87E+01
375.4	45.53	2.68E+00	1.94E+01
375.8	45.56	3.38E+00	2.17E+01
376.2	45.58	4.05E+00	2.20E+01
376.6	45.60	4.89E+00	2.23E+01
377	45.62	6.35E+00	2.52E+01
377.4	45.64	6.03E+00	2.34E+01
377.8	45.67	7.49E+00	2.59E+01
378.2	45.69	7.07E+00	2.60E+01
378.6	45.71	7.00E+00	2.45E+01
379	45.73	1.02E+01	2.86E+01
379.4	45.76	9.72E+00	2.92E+01
379.8	45.78	1.13E+01	2.93E+01
380.2	45.80	5.01E+00	2.29E+01
380.6	45.82	1.14E+01	2.95E+01
381	45.84	1.13E+01	3.02E+01
381.4	45.87	8.62E+00	2.56E+01
381.8	45.89	7.72E+00	2.45E+01
382.2	45.91	1.07E+01	2.37E+01
382.6	45.93	8.52E+00	2.32E+01
383	45.96	9.39E+00	2.41E+01
383.4	45.98	1.16E+01	2.56E+01
383.8	46.00	2.28E+01	2.86E+01
384.2	46.02	1.54E+01	2.61E+01
384.6	46.04	2.15E+01	2.44E+01
385	46.07	2.15E+01	2.35E+01
385.4	46.09	2.09E+01	2.52E+01
385.8	46.11	1.61E+01	2.47E+01
386.2	46.13	6.14E+00	2.10E+01
386.6	46.16	4.96E+00	2.26E+01
387	46.18	1.58E+01	2.39E+01
387.4	46.20	1.20E+01	2.59E+01
387.8	46.22	5.92E+00	2.11E+01
388.2	46.24	1.46E+01	2.38E+01
388.6	46.27	1.44E+01	2.49E+01
389	46.29	9.73E+00	2.45E+01

Depth	Age	Fe/Ca	Fe/K
[cm]	*[cal kyr]*	*[cps]*	*[cps]*
389.4	46.31	1.09E+01	2.46E+01
389.8	46.33	1.40E+01	2.56E+01
390.2	46.36	1.45E+01	2.51E+01
390.6	46.38	1.86E+01	2.45E+01
391	46.40	1.73E+01	2.60E+01
391.4	46.42	1.82E+01	2.61E+01
391.8	46.44	1.66E+01	2.52E+01
392.2	46.47	1.64E+01	2.57E+01
392.6	46.49	1.30E+01	2.49E+01
393	46.51	1.08E+01	2.62E+01
393.4	46.53	1.85E+01	2.42E+01
393.8	46.56	1.55E+01	2.34E+01
394.2	46.58	1.70E+01	2.33E+01
394.6	46.60	1.65E+01	2.42E+01
395	46.62	1.69E+01	2.34E+01
395.4	46.64	1.83E+01	2.25E+01
395.8	46.67	1.89E+01	2.20E+01
396.2	46.69	1.69E+01	2.41E+01
396.6	46.71	1.46E+01	2.33E+01
397	46.73	1.30E+01	2.34E+01
397.4	46.76	1.33E+01	2.25E+01
397.8	46.78	1.31E+01	2.23E+01
398.2	46.80	1.26E+01	2.20E+01
398.6	46.82	1.21E+01	2.21E+01
399	46.84	8.78E+00	2.20E+01
399.4	46.87	6.49E+00	2.00E+01
399.8	46.89	3.22E+00	1.96E+01
400.2	46.93	2.26E+00	1.71E+01
400.6	46.99	2.11E+00	1.72E+01
401	47.05	3.35E+00	1.99E+01
401.4	47.11	3.22E+00	1.98E+01
401.8	47.17	2.35E+00	1.66E+01
402.2	47.23	1.79E+00	1.55E+01
402.6	47.29	1.84E+00	1.68E+01
403	47.35	1.81E+00	1.77E+01
403.4	47.41	1.08E+00	1.56E+01
403.8	47.46	1.13E+00	1.55E+01
404.2	47.52	1.08E+00	1.43E+01
404.6	47.58	1.32E+00	1.48E+01
405	47.64	1.40E+00	1.55E+01
405.4	47.70	1.60E+00	1.56E+01
405.8	47.76	1.53E+00	1.54E+01
406.2	47.82	1.44E+00	1.39E+01

Depth	Age	Fe/Ca	Fe/K
[cm]	*[cal kyr]*	*[cps]*	*[cps]*
406.6	47.88	2.68E+00	1.71E+01
407.8	48.06	1.64E+00	1.67E+01
408.2	48.12	1.43E+00	1.51E+01
408.6	48.18	1.04E+00	1.42E+01
409	48.24	1.12E+00	1.59E+01
409.4	48.30	1.10E+00	1.51E+01
409.8	48.36	1.21E+00	1.58E+01
410.2	48.42	1.27E+00	1.73E+01
410.6	48.47	1.16E+00	1.47E+01
411	48.53	1.13E+00	1.46E+01
411.4	48.59	1.23E+00	1.72E+01
411.8	48.65	1.31E+00	1.69E+01
412.2	48.71	1.30E+00	1.53E+01
412.6	48.77	1.19E+00	1.34E+01
413	48.83	1.25E+00	1.66E+01
413.4	48.89	1.20E+00	1.38E+01
413.8	48.95	1.12E+00	1.46E+01
414.2	49.01	9.40E-01	1.26E+01
414.6	49.07	9.84E-01	1.44E+01
415	49.13	9.56E-01	1.46E+01
415.4	49.19	9.79E-01	1.39E+01
415.8	49.25	9.80E-01	1.39E+01
416.2	49.31	1.12E+00	1.50E+01
416.6	49.37	1.02E+00	1.57E+01
417	49.43	1.35E+00	1.53E+01
417.4	49.49	1.22E+00	1.45E+01
417.8	49.54	1.62E+00	1.70E+01
418.2	49.60	1.78E+00	1.96E+01
418.6	49.66	1.54E+00	1.78E+01
419	49.72	1.41E+00	1.48E+01
419.4	49.78	1.14E+00	1.37E+01
419.8	49.84	1.04E+00	1.34E+01
420.2	49.90	1.01E+00	1.29E+01
420.6	49.96	1.17E+00	1.45E+01
421	50.02	1.35E+00	1.53E+01
421.4	50.08	1.35E+00	1.60E+01
421.8	50.14	1.50E+00	1.63E+01
422.2	50.20	1.45E+00	1.62E+01
422.6	50.26	1.62E+00	1.66E+01
423	50.32	1.64E+00	1.80E+01
423.4	50.38	1.20E+00	1.43E+01
423.8	50.44	1.17E+00	1.41E+01
424.2	50.50	1.11E+00	1.52E+01

Depth	Age	Fe/Ca	Fe/K
[cm]	*[cal kyr]*	*[cps]*	*[cps]*
424.6	50.55	1.20E+00	1.50E+01
425	50.61	1.02E+00	1.45E+01
425.4	50.67	8.95E-01	1.41E+01
425.8	50.73	9.89E-01	1.43E+01
426.2	50.79	9.65E-01	1.61E+01
426.6	50.85	8.41E-01	1.26E+01
427	50.91	8.27E-01	1.22E+01
427.4	50.97	8.41E-01	1.38E+01
427.8	51.03	1.03E+00	1.49E+01
428.2	51.09	9.54E-01	1.31E+01
428.6	51.15	9.65E-01	1.42E+01
429	51.21	8.51E-01	1.38E+01
429.4	51.27	9.18E-01	1.45E+01
429.8	51.33	8.67E-01	1.38E+01
430.2	51.39	9.18E-01	1.36E+01
430.6	51.45	9.00E-01	1.41E+01
431	51.51	9.22E-01	1.45E+01
431.4	51.57	8.59E-01	1.47E+01
431.8	51.62	1.12E+00	1.64E+01
432.2	51.68	1.21E+00	1.59E+01
432.6	51.74	1.12E+00	1.59E+01
433	51.80	1.18E+00	1.65E+01
433.4	51.86	1.28E+00	1.62E+01
433.8	51.92	1.50E+00	1.50E+01
434.2	51.98	1.72E+00	1.73E+01
434.6	52.04	2.20E+00	1.90E+01
435	52.10	1.85E+00	1.77E+01
435.4	52.16	2.94E+00	2.20E+01
435.8	52.21	3.40E+00	2.09E+01
436.2	52.27	3.12E+00	2.18E+01
436.6	52.32	3.79E+00	2.14E+01
437	52.38	3.99E+00	2.19E+01
437.4	52.43	4.21E+00	2.39E+01
437.8	52.49	2.67E+00	1.90E+01
438.2	52.54	3.32E+00	2.03E+01
438.6	52.60	5.08E+00	2.68E+01
439	52.66	4.79E+00	2.55E+01
439.4	52.71	4.01E+00	2.22E+01
439.8	52.77	3.37E+00	2.16E+01
440.2	52.82	3.64E+00	2.16E+01
440.6	52.88	2.97E+00	1.97E+01
441	52.93	2.63E+00	1.83E+01
441.4	52.99	2.58E+00	1.78E+01

Depth	Age	Fe/Ca	Fe/K
[cm]	*[cal kyr]*	*[cps]*	*[cps]*
441.8	53.04	2.32E+00	1.90E+01
442.2	53.10	2.38E+00	1.91E+01
442.6	53.16	2.55E+00	1.80E+01
443	53.21	2.06E+00	1.85E+01
443.4	53.27	2.41E+00	1.95E+01
443.8	53.32	1.97E+00	1.79E+01
444.2	53.38	1.83E+00	1.67E+01
444.6	53.43	1.86E+00	1.77E+01
445	53.49	2.03E+00	1.76E+01
445.4	53.54	1.96E+00	1.84E+01
445.8	53.60	2.07E+00	1.75E+01
446.2	53.66	3.14E+00	2.03E+01
446.6	53.71	2.56E+00	1.82E+01
447	53.77	2.66E+00	1.91E+01
447.4	53.82	2.42E+00	1.89E+01
447.8	53.88	2.02E+00	1.77E+01
448.2	53.93	2.18E+00	1.83E+01
448.6	53.99	2.82E+00	1.89E+01
449	54.04	2.65E+00	1.89E+01
449.4	54.10	3.68E+00	2.28E+01
449.8	54.16	4.18E+00	2.77E+01
450.2	54.21	2.71E+00	1.94E+01
450.6	54.27	2.65E+00	1.81E+01
451	54.32	2.76E+00	1.85E+01
451.4	54.38	2.54E+00	1.77E+01
451.8	54.43	2.45E+00	1.76E+01
452.2	54.49	2.35E+00	1.75E+01
452.6	54.54	1.26E+00	1.59E+01
453	54.60	1.26E+00	1.68E+01
453.4	54.65	1.35E+00	1.76E+01
453.8	54.71	1.30E+00	2.03E+01
454.2	54.76	9.72E-01	1.52E+01
454.6	54.82	7.30E-01	1.22E+01
455	54.87	8.24E-01	1.49E+01
455.4	54.93	7.72E-01	1.18E+01
455.8	54.98	8.39E-01	1.24E+01
456.2	55.04	8.33E-01	1.36E+01
456.6	55.09	9.09E-01	1.38E+01
457	55.14	9.18E-01	1.31E+01
457.4	55.20	1.37E+00	1.71E+01
457.8	55.25	1.48E+00	1.73E+01
458.2	55.31	1.42E+00	1.62E+01
458.6	55.36	1.41E+00	1.52E+01

Depth	Age	Fe/Ca	Fe/K
[cm]	*[cal kyr]*	*[cps]*	*[cps]*
459	55.42	1.55E+00	1.67E+01
459.4	55.47	1.64E+00	1.54E+01
459.8	55.52	1.65E+00	1.71E+01
460.2	55.58	1.81E+00	1.89E+01
460.6	55.63	1.87E+00	1.92E+01
461	55.69	2.17E+00	2.05E+01
461.4	55.74	2.43E+00	2.31E+01
461.8	55.80	2.26E+00	2.07E+01
462.2	55.85	1.90E+00	1.76E+01
462.6	55.91	1.76E+00	1.68E+01
463	55.96	2.45E+00	1.84E+01
463.4	56.01	2.25E+00	1.73E+01
463.8	56.07	1.55E+00	1.60E+01
464.2	56.12	1.80E+00	1.69E+01
464.6	56.18	1.86E+00	1.71E+01
465	56.23	1.89E+00	1.64E+01
465.4	56.29	1.53E+00	1.58E+01
465.8	56.34	1.55E+00	1.77E+01
466.2	56.40	2.21E+00	1.98E+01
466.6	56.45	2.15E+00	2.00E+01
467	56.50	2.39E+00	1.92E+01
467.4	56.56	2.16E+00	1.98E+01
467.8	56.61	2.55E+00	1.97E+01
468.2	56.67	3.01E+00	1.94E+01
468.6	56.72	3.96E+00	2.32E+01
469	56.78	3.91E+00	2.15E+01
469.4	56.83	4.44E+00	2.25E+01
469.8	56.88	5.32E+00	2.30E+01
470.2	56.94	5.04E+00	2.11E+01
470.6	56.99	5.43E+00	2.29E+01
471	57.05	5.47E+00	2.18E+01
471.4	57.10	5.09E+00	2.25E+01
471.8	57.16	5.20E+00	2.32E+01
472.2	57.21	6.35E+00	2.68E+01
472.6	57.27	1.05E+01	3.15E+01
473	57.32	8.76E+00	2.76E+01
473.4	57.37	1.12E+01	2.68E+01
473.8	57.43	6.86E+00	2.42E+01
474.2	57.48	1.66E+01	2.55E+01
474.6	57.54	7.09E+00	2.17E+01
475	57.59	1.39E+01	2.35E+01
475.4	57.65	1.46E+01	2.28E+01
475.8	57.70	1.61E+01	2.30E+01

Depth	**Age**	**Fe/Ca**	**Fe/K**
[cm]	*[cal kyr]*	*[cps]*	*[cps]*
476.2	57.76	1.31E+01	2.19E+01
476.6	57.81	1.47E+01	2.29E+01
477	57.86	1.30E+01	2.33E+01
477.4	57.92	1.73E+01	2.28E+01
477.8	57.97	2.30E+01	2.45E+01
478.2	58.36	2.08E+01	2.57E+01
478.6	58.42	2.49E+01	2.40E+01
479	58.48	2.62E+01	2.48E+01
479.4	58.54	2.58E+01	2.58E+01
479.8	58.59	3.09E+01	2.43E+01
480.2	58.65	2.97E+01	2.65E+01
480.6	58.71	2.78E+01	4.07E+01

ANNEX V – Input data for the end-member modelling. Data only in digital format. Media in the library of IAG/USP.

ANNEX VI - R-Square data from unmixing of cores

	R^2			
Number of end-members	**GeoB3913-3**	**GeoB3912-1**	**GeoB3910-2**	**GeoB3911-3**
2	0.94446	0.96881	0.92075	0.94419
3	0.96584	0.98195	0.94021	0.97522
4	0.97784	0.9864	0.95372	0.98092
5	0.98445	0.9895	0.96616	0.98689
6	0.99098	0.99132	0.97949	0.99082
7	0.99464	0.99378	0.9847	0.99508
8	0.99606	0.99517	0.98943	0.99652
9	0.99731	0.99623	0.99237	0.9975

ANNEX VII – End-member contribution and IRM "synthetic" curve for core GeoB3911-3

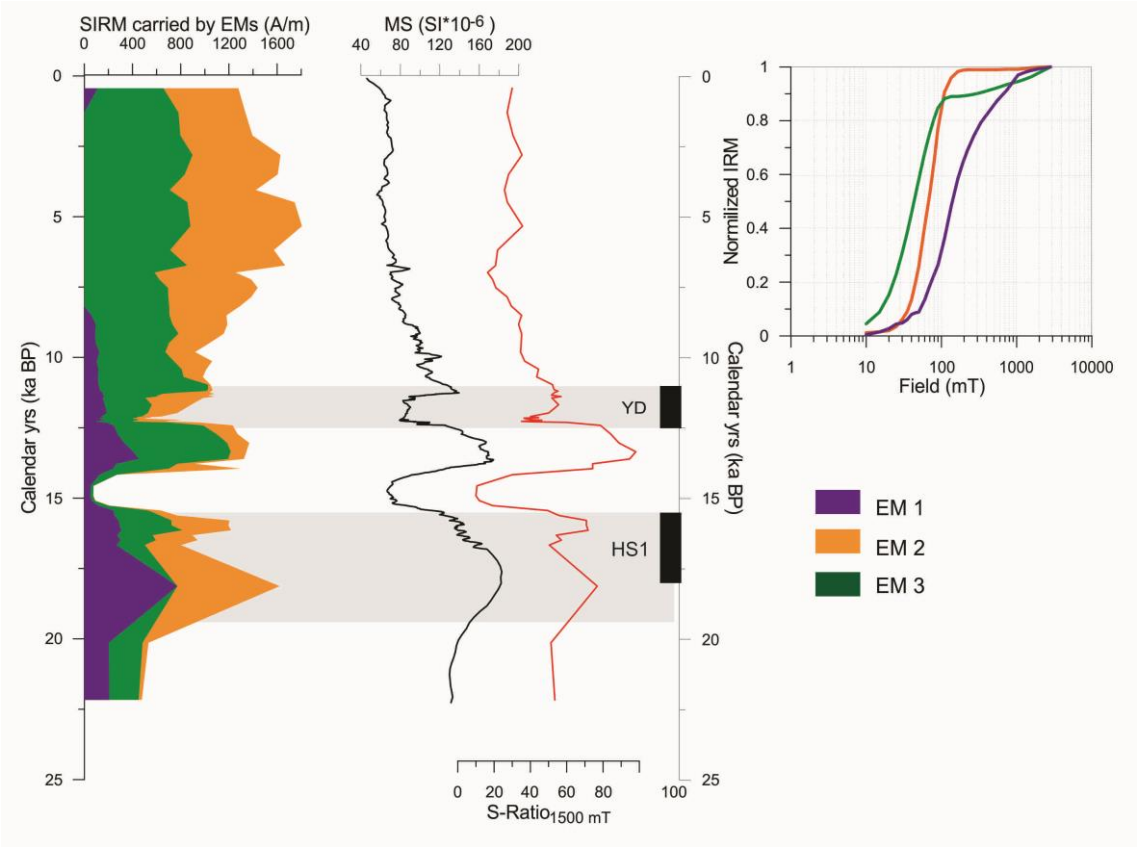

ANNEX VIII – Output data from the end-member analysis.

GeoB3913-3							
IRM "synthetic" curves				End-member total contributions			
Field	**EM1**	**EM2**	**EM3**	**Age**	**IRM EM1**	**IRM EM2**	**IRM EM3**
[mT]				*cal [kyr]*			
0	0	0	0	3.3397	0	197.1728	176.9172
10	0.012277	0.025645	0.032073	6.6794	0	226.2026	253.2674
15	0.03254	0.047311	0.072131	10.0191	149.255	252.676	383.109
20	0.060776	0.076563	0.115379	13.7525	442.9035	232.079	257.6175
25	0.100948	0.113907	0.173435	14.8788	941.459	219.9387	38.53237
30	0.147156	0.146989	0.244893	15.8405	543.799	255.9896	61.76138
35	0.195099	0.190956	0.309131	16.7612	628.2554	385.7265	62.62805
40	0.233689	0.222896	0.380378	17.6818	546.071	625.4361	146.0829
45	0.271651	0.246861	0.448538	18.6025	329.7993	949.7094	181.8513
50	0.313851	0.272823	0.500066	19.6349	255.1937	807.2301	253.9362
60	0.387292	0.338143	0.627261	21.1142	314.2598	858.722	280.8782
70	0.446356	0.371587	0.718092	22.5935	428.7799	659.7667	225.1734
80	0.486171	0.416573	0.789719	23.9478	677.3262	233.3497	631.644
90	0.520785	0.45059	0.850925	24.8018	668.6396	239.1512	612.3592
110	0.567805	0.514801	0.919292	26.608	381.9629	196.115	578.2121
140	0.610478	0.619969	0.951177	28.7009	636.3274	115.7399	473.2727
165	0.630532	0.694415	0.958179	29.9133	610.0133	132.0979	390.8688
190	0.645023	0.74842	0.961829	31.1256	553.4863	121.3518	453.0819
220	0.659533	0.794164	0.964942	32.338	382.7588	109.7772	414.484
275	0.681596	0.843164	0.969959	34.3699	384.4762	108.9865	410.3473
335	0.700793	0.873121	0.974669	36.4018	462.5938	123.7777	493.1685
430	0.727406	0.897125	0.981292	37.8395	318.7454	69.83107	446.0135
550	0.756266	0.916852	0.987338	38.3858	670.4207	66.40869	432.9006
750	0.798433	0.937721	0.993214	40.2543	519.803	90.28083	406.0362
1045	0.839358	0.949829	0.998623	41.6504	326.563	106.5294	318.6375
1255	0.86626	0.960727	0.99899	42.981	341.8202	88.47608	445.2137
1580	0.902485	0.972956	1	45.7709	367.0637	53.49847	385.8478
2090	0.950186	0.986752	1	46.8805	814.8933	67.22981	512.3069
2845	1	1	1	47.9902	524.6107	118.1989	592.3904
				50.6124	293.771	98.38875	517.9402
				53.8464	334.3718	41.87081	334.7274
				55.4934	421.7407	85.16091	511.7484
				57.1404	327.3741	104.4058	487.3302
				58.5925	565.2729	33.88084	380.7163
				59.265	741.449	4.204522	347.0264
				59.9376	645.6957	26.61	320.7643
				60.6101	674.6012	31.05335	292.9255
				61.2826	643.5322	62.3778	0
				61.9552	678.8314	103.1502	276.8283

62.6277	690.7155	177.4909	453.7236
63.3003	617.8925	223.6916	434.8258
63.9728	678.0859	192.6359	488.2082
64.6453	650.9615	243.1145	647.034
65.3179	696.5114	232.8604	594.1282
65.9904	567.6276	183.2349	535.5876
66.6629	407.1588	162.4329	626.6283
67.3355	361.1729	75.9834	551.9537
68.008	189.7548	57.11402	551.7112
68.5363	392.4622	71.66172	530.0561
69.0645	681.59	17.39122	511.1988
69.6985	505.2395	0.809919	409.7206
70.1211	500.1059	10.14127	377.3729
70.6493	300.0504	13.6234	416.8862
71.0621	244.6671	30.15057	565.6023
71.4459	329.2952	22.38235	731.0025
71.8297	231.9705	21.66459	565.4149
72.2135	221.5146	60.10341	654.372
72.5974	170.6147	17.12341	646.2619
72.9812	232.7528	40.88387	617.9133
73.365	535.6436	75.15741	531.119
74.8989	240.3179	126.8529	673.5493
76.3444	256.1228	99.0763	556.3409
77.4365	114.5701	41.38418	469.2658
78.5286	47.44926	27.89354	314.9872
79.6207	35.56917	35.98605	201.9648
80.7316	701.9493	150.1067	501.224
81.8708	783.2817	168.5683	514.1199
83.0099	386.2578	98.22289	297.4993
84.149	475.6898	84.65396	386.2063
85.2881	688.9781	95.30692	336.7049

GeoB3912-1							
IRM "synthetic" curves				End-member total contributions			
Field	**EM1**	**EM2**	**EM3**	**Age**	**IRM EM1**	**IRM EM2**	**IRM EM3**
[mT]				*cal [kyr]*			
0	0	0	0	2.446	0	0	0
10	0.044895	0.004667	0.018448	4.643	684.0858	271.9317	50.84244
15	0.082749	0.012152	0.036489	6.828	905.4458	0	323.8342
20	0.136161	0.022718	0.067742	9.537	623.6384	9.625281	439.1663
25	0.197236	0.041006	0.105795	10.190	1109.109	126.0982	23.08301
30	0.26594	0.05929	0.152182	10.573	924.6968	157.225	15.74819
35	0.330284	0.089516	0.205348	10.954	838.7367	233.251	61.4623
40	0.386466	0.126213	0.270283	11.395	673.9042	251.1558	82.19004
45	0.451657	0.164686	0.33958	11.951	553.2923	242.4354	132.8223
50	0.509421	0.210282	0.404377	12.560	226.5623	229.0989	279.4888
60	0.598211	0.321597	0.553949	13.178	447.6811	77.68221	248.8767
70	0.675558	0.39232	0.669113	13.920	485.2201	100.4442	249.3958
80	0.73753	0.457589	0.773465	14.412	376.7834	239.9238	337.9528
90	0.788969	0.507147	0.8466	14.879	226.4138	479.2977	595.7286
110	0.840331	0.582493	0.937442	15.161	194.1086	361.1626	724.0788
135	0.862978	0.619998	0.971417	15.522	313.5242	609.8346	303.2512
160	0.877257	0.638827	0.979851	15.769	273.3258	591.2849	301.3893
185	0.885992	0.653127	0.982749	16.119	142.0945	597.8606	438.1749
215	0.894114	0.667243	0.984252	16.397	212.6132	493.5148	391.902
265	0.903762	0.687558	0.985963	16.738	217.9003	523.6658	330.9838
325	0.91073	0.708985	0.987519	17.006	257.1938	528.2825	137.3538
420	0.91913	0.737338	0.989653	17.292	185.8345	408.9877	212.4078
530	0.925536	0.766322	0.990995	17.526	208.4542	324.5674	153.0085
720	0.934964	0.809326	0.992543	17.874	185.3706	306.0621	229.0272
1060	0.955673	0.861258	1.000529	18.165	156.6939	328.624	100.4821
1325	0.961784	0.88543	1.000813	18.551	73.24312	398.4757	207.2812
1595	0.97327	0.910602	0.997128	18.867	174.7319	274.6706	113.9575
2105	0.983115	0.954492	0.999776	19.434	195.6946	265.7948	87.62062
2870	1	1	1	20.004	330.6199	166.7213	223.9989
				20.786	277.306	201.9232	205.5409
				21.435	403.2549	147.3884	236.9066
				22.580	371.5101	161.0442	238.6356
				23.233	479.7618	235.3699	264.2783
				24.230	359.9343	331.0028	223.1829
				24.740	516.0388	276.2381	106.2331
				25.395	445.4721	270.6211	10.22681
				25.663	390.172	243.3376	104.8505
				26.159	363.8684	190.5289	109.7027
				26.607	346.5508	190.4784	311.0409
				27.224	213.968	231.6146	320.7874
				27.731	229.0003	260.2881	347.2016

28.288	38.10489	291.2997	491.6254
28.846	153.9635	236.4109	419.8156
29.366	121.7339	242.0408	367.3853
30.059	77.35641	277.6728	383.6908
30.881	96.41512	329.1833	259.9216
31.552	171.1953	352.9655	157.0792
32.296	210.3082	298.2908	151.531
32.674	250.7068	257.814	222.8192
33.083	112.0282	213.7973	404.2446
33.410	227.13	173.3399	374.5301
33.783	158.0531	174.7414	354.5455
34.153	144.0403	187.8143	330.8553
34.519	220.6231	167.7718	274.355
34.892	200.4108	221.6438	266.9555
35.402	192.4339	178.0481	344.358
36.116	143.3896	206.2578	532.3126
36.561	59.73637	291.8462	379.4274
36.859	171.7044	253.9976	314.6679
37.037	196.2833	232.5959	421.2508
37.212	112.3435	254.2111	554.7954
37.382	266.3796	275.7915	395.1089
37.552	247.1807	352.1925	400.9068
37.774	177.4642	395.0544	454.4714
37.893	136.0177	454.0934	355.8789
38.086	81.98122	586.8257	286.4031
38.322	258.3362	528.6379	133.6559
38.754	307.1416	517.7784	0
39.398	260.6362	570.9338	0
39.895	135.4105	181.32	397.2695
40.279	146.1787	133.5633	461.198
40.620	204.8226	229.5093	310.1281
41.134	141.3033	239.1962	389.6805
41.734	51.75814	240.9057	513.5761
42.339	189.9847	251.3058	362.9095
43.011	251.42	246.9527	385.6672
44.204	275.4562	227.7557	421.9581
45.207	344.1549	226.3285	342.8765
45.776	335.6824	275.6321	303.1055
46.297	247.1844	336.7383	465.5873
46.923	111.1575	370.5797	420.3128
47.502	49.42492	502.95	450.6651
47.996	235.298	442.011	230.301
48.227	342.5965	434.495	127.7685
48.572	219.6192	291.6241	428.8067
49.298	302.678	239.6294	418.7726

50.022	249.5293	248.5729	474.0478
50.748	251.935	231.2511	457.0239
51.472	273.8083	198.72	427.9717
52.206	118.0789	257.5089	526.4522
52.938	259.2478	201.9668	428.9453
53.662	220.7517	227.2969	454.1714
54.388	115.1878	235.5729	517.6694
55.112	32.37031	318.7706	427.9591
55.838	144.4998	292.0228	312.3374
56.488	189.2612	241.673	427.7858
57.285	184.8406	262.1996	462.0098
58.090	173.6058	267.8595	634.0148
58.752	330.044	249.9474	340.9686
59.550	59.46909	404.7524	609.3085
60.202	0	502.0879	505.0821
61.000	42.51998	511.2873	441.8927
61.652	2.096045	480.7777	535.4263
62.450	80.8875	421.1959	440.2966
63.102	101.8117	413.0417	458.3866
63.905	0	449.6232	474.9568
64.562	120.5403	372.8069	398.6528
65.600	127.6586	421.9717	222.3997
66.400	188.5133	381.6672	150.0895
67.505	276.8293	401.5775	31.96318
68.410	436.5252	291.5647	197.7601
69.510	384.9215	268.9164	553.1721
70.410	204.882	516.9767	350.4713
71.360	207.2768	448.3709	376.8323
71.986	438.4834	138.6003	832.8763
72.606	416.2103	107.9878	819.3519
73.365	262.3527	156.4594	740.3779
74.194	120.2844	299.0873	804.2082
74.746	77.09015	371.7194	825.2504
75.505	115.5088	378.7772	757.704
76.126	226.7914	364.7653	484.8233
76.890	257.1668	232.5762	797.847
77.516	484.9471	116.8039	835.129
78.206	591.1368	86.65005	767.3231
78.896	454.1157	32.7562	1089.608
79.586	465.949	26.00267	935.8383
80.276	393.7949	65.46749	1243.248
80.966	452.1655	50.97582	806.0487
81.656	237.3685	140.9976	920.5139
82.415	188.2453	250.5955	841.9791
83.040	586.6843	306.3862	686.3694

				83.874	248.5695	299.8108	738.8797
				84.423	63.2846	348.8466	656.8388

GeoB3911-3

IRM "synthetic" curves				End-member total contributions			
Field	**EM1**	**EM2**	**EM3**	**Age**	**IRM EM1**	**IRM EM2**	**IRM EM3**
[mT]				*cal [kyr]*			
0	0	0	0	0.434	544.7771	112.3132	621.1598
10	0.004975	0.045352	0.012136	1.302	781.6955	0	554.9245
15	0.014744	0.088741	0.015209	2.117	797.6968	0	597.8832
20	0.027216	0.152378	0.019723	2.807	898.9558	0	728.9742
25	0.04402	0.228665	0.034648	3.497	834.1714	0	770.7386
30	0.047686	0.308577	0.060898	4.055	708.043	0	714.817
35	0.060444	0.383581	0.090297	4.485	855.362	0	889.338
40	0.079735	0.455747	0.133511	5.335	881.0864	0	925.1936
45	0.086065	0.522299	0.196932	6.185	711.8231	0	861.3169
50	0.088724	0.581327	0.25747	6.734	853.6721	0	813.4179
60	0.134742	0.681689	0.409172	6.982	583.6376	0	670.8024
70	0.187244	0.755063	0.529381	7.231	623.1474	0	762.4926
80	0.228714	0.809271	0.650627	7.526	693.7931	0	744.6769
90	0.263259	0.847702	0.771789	7.852	697.1128	0	688.5572
110	0.362939	0.881697	0.906921	8.178	703.6025	1.305173	587.5823
135	0.48231	0.890182	0.959584	8.504	647.9112	58.46641	473.1224
165	0.583009	0.890182	0.982608	8.830	635.9247	95.84051	454.5948
190	0.639249	0.891978	0.987607	9.156	690.856	90.45653	375.7975
220	0.687719	0.89387	0.989637	9.483	609.0316	94.51628	338.8821
270	0.74439	0.898313	0.989637	9.809	546.9815	125.2558	246.8028
335	0.793431	0.904286	0.989637	10.135	639.5115	103.4031	317.7853
545	0.873067	0.922	0.989637	10.419	691.8197	116.3865	204.7838
745	0.914726	0.934806	0.991247	10.692	711.2298	112.4587	159.5915
1040	0.969629	0.945525	0.991247	10.966	908.2017	118.4687	20.18958
1305	0.980569	0.95467	0.99405	11.149	896.4082	130.4362	37.42563
1570	0.986769	0.963439	0.996708	11.198	873.4754	136.1082	45.56645
2075	0.994294	0.981145	0.99905	11.246	651.0103	152.3154	234.0143
2825	1	1	1	11.295	496.3479	153.9821	429.88
				11.343	456.982	157.361	412.2569
				11.392	434.2088	167.6363	478.9349
				11.440	352.9305	155.242	477.4974
				11.683	390.338	169.7718	327.3101
				11.974	340.5653	187.1948	245.0599
				12.101	334.5219	144.4358	157.6624
				12.120	286.3575	148.3135	114.469
				12.139	293.0421	154.921	105.8069
				12.157	277.453	132.0768	86.75014
				12.176	272.8446	129.3359	117.3695
				12.195	303.0915	134.8435	172.0951

12.213	295.1139	155.4947	310.7014
12.232	274.4442	172.7016	354.4642
12.251	280.5479	133.1511	271.491
12.270	298.3424	102.9748	279.5127
12.288	375.2665	112.1321	322.8113
12.307	515.4712	182.8685	246.4703
12.414	739.6812	244.8781	247.2506
12.727	822.6342	276.6413	173.1945
13.039	854.4974	331.8658	182.6968
13.352	807.3919	407.5403	129.8778
13.609	739.3415	453.6176	131.4109
13.781	504.4965	266.6847	147.6288
13.953	462.3497	239.3685	596.2818
14.169	146.2275	124.8121	0.060347
14.564	22.9841	53.76832	0.697586
14.915	24.53266	49.91734	0
15.090	26.01936	62.20414	4.966502
15.266	81.77857	115.326	14.53547
15.441	290.216	244.358	103.7061
15.616	379.3089	250.3003	137.0709
15.791	437.3991	285.3583	481.0426
15.966	433.8415	290.6657	471.0728
16.142	505.5753	308.6823	403.4324
16.317	294.8663	272.7143	328.5693
16.492	291.811	302.3525	345.6465
16.667	235.2107	267.3432	298.7261
18.128	0	772.6585	847.8115
20.140	279.7791	203.6883	49.00258
22.170	243.2877	207.8333	26.13902

GeoB3910-2							
IRM "synthetic" curves				End-member total contributions			
Field	**EM1**	**EM2**	**EM3**	**Age**	**IRM EM1**	**IRM EM2**	**IRM EM3**
[mT]				*cal [kyr]*			
0	0	0	0	1.985	369.0038	698.9196	418.4566
10	0	0.005786	0.047499	3.242	384.6172	672.7945	466.3383
15	0.010437	0.005876	0.102055	4.352	345.1646	691.0379	457.1075
20	0.031515	0.009399	0.152825	5.732	298.3371	841.1937	556.5091
25	0.068635	0.020057	0.232356	6.872	219.1175	913.9949	626.6176
30	0.112745	0.035516	0.345135	7.652	213.7625	385.058	1164.39
40	0.214351	0.053208	0.47332	8.432	210.1096	221.5531	1211.537
45	0.271482	0.072769	0.516687	9.059	396.6688	60.97451	1144.227
50	0.314687	0.106862	0.596476	9.642	414.6185	0	934.2915
55	0.370581	0.115693	0.642764	10.225	497.1793	0	864.7407
65	0.465221	0.159506	0.769942	10.702	555.0627	0	736.0973
75	0.52833	0.231422	0.85132	11.260	554.4971	0	574.3129
85	0.573869	0.314419	0.935403	11.692	529.1138	0	466.3662
95	0.629851	0.396487	0.948922	12.172	492.7106	23.73011	370.5093
115	0.686343	0.575239	0.955749	12.739	458.1225	84.37	207.2275
140	0.725548	0.719978	0.955749	13.505	623.9714	36.83832	237.9103
170	0.751826	0.822137	0.957164	14.132	658.8709	53.74249	230.2966
200	0.767254	0.870858	0.965685	14.757	917.4062	62.82495	193.0088
230	0.77786	0.898677	0.974018	15.273	933.0446	58.68636	174.909
280	0.793692	0.922932	0.979977	15.790	972.805	53.80127	33.35368
345	0.809252	0.940602	0.985724	16.240	1006.897	107.4111	35.24168
450	0.8304	0.954173	0.989598	16.660	917.7482	377.4218	0
570	0.849551	0.962938	0.991574	16.886	887.9124	1827.095	190.6729
785	0.877655	0.972329	0.993434	17.100	819.5699	49.87012	0
1020	0.901371	0.977644	0.995918	17.314	613.8113	379.8809	70.64778
1230	0.917971	0.981832	0.995918	17.529	473.3196	1159.34	0
1550	0.939529	0.986964	0.996707	17.743	372.0272	1046.538	33.61506
2045	0.968225	0.992921	0.999151	17.957	409.8342	1204.866	14.78021
2790	1	1	1	18.171	334.1324	1620.668	0
				18.660	797.4888	333.0303	240.5809
				19.560	809.1372	263.4792	241.2436
				20.460	852.2892	241.0038	255.777
				21.360	843.9363	190.6595	226.9441
				22.260	869.725	178.9233	243.6517
				22.920	859.6902	141.1048	275.815
				23.220	861.2518	133.3343	183.1739
				23.860	799.6926	10.25902	165.9083
				25.010	659.2792	125.8332	156.2376
				25.990	711.9158	133.877	122.1672
				26.715	921.7434	148.1896	241.1269
				27.440	963.6188	182.7563	270.2149

28.310	815.6266	158.4485	255.9949
28.760	739.5698	123.1215	131.5987
29.200	858.1978	97.41488	231.2673
29.560	786.9261	0.23023	133.9037
29.960	744.9173	52.2778	57.48493
30.720	702.879	59.51817	74.32279
31.733	733.1261	130.7955	228.4284
32.317	765.5923	88.79712	259.6106
32.900	818.4227	144.5084	206.9789
33.483	708.5984	54.50344	153.7682
34.067	828.3568	131.8374	271.6457
34.650	653.0219	71.50218	129.7459
35.206	770.2875	144.927	317.7055
35.721	803.231	155.1432	364.7558
36.235	709.1872	21.91081	141.112
36.750	688.8877	145.7121	197.7802
37.265	760.9403	123.0235	326.7161
37.779	809.7732	84.20469	249.0721
38.346	806.6367	11.82007	133.0533
38.881	730.5657	105.2336	111.8507
39.515	668.7619	437.2742	49.2439
40.150	435.514	2103.2	12.20588
40.785	511.3392	493.4928	20.50802
41.419	529.678	1144.641	61.3713
41.900	757.1623	197.1097	174.248
42.150	739.2554	127.4074	252.7771
42.400	775.6572	81.6819	172.0609
42.650	741.6913	177.3791	309.9097
43.008	803.711	159.7938	307.0852
43.528	753.8384	206.4149	155.5768
44.048	780.1673	118.6463	250.9063
44.568	709.8627	140.0781	348.4092
45.088	746.91	138.5448	333.5052
45.511	822.9597	55.42946	305.2008
45.789	772.6903	204.5618	177.8778
46.067	585.6905	1013.366	100.1738
46.344	516.7456	1788.874	0
46.622	0.531019	4085.325	17.4439
46.900	342.9973	1976.381	130.0118
47.643	781.6231	265.2675	317.4593
48.460	751.1826	125.4239	316.9635
49.129	753.0288	71.86646	355.6048
49.871	721.8912	112.4892	329.6897
50.614	850.9968	116.2947	208.2986
51.357	886.9966	15.04182	252.7615

52.100	845.3367	28.63105	195.0723
52.794	774.3237	61.24639	138.2599
53.489	824.8914	184.826	167.8926
54.183	800.2864	85.16146	232.4221
54.988	881.2706	52.83335	324.466
55.717	869.6601	112.9668	71.00312
56.447	849.6965	57.91415	67.41937
57.176	861.6183	37.98174	0
57.906	649.7434	135.1466	0
58.635	469.8503	586.2562	39.67352